SURFACE CHARACTERIZATION OF ALKALI AND ALKALINE EARTH METALS ON SINGLE CRYSTAL REFRACTORY METALS

Gerald Glenn Magera
B.S., Linfield College, 1989

A dissertation submitted to the faculty
of the Oregon Graduate Institute of
Science & Technology in partial
fulfillment of the requirements
for the degree
Doctor of Philosophy
in
Electrical Engineering

October, 1995

The dissertation "Surface Characterization of Alkali and Alkaline Earth Metals on Single Crystal Refractory Metals" by Gerald Glenn Magera has been examined and approved by the following Examination Committee:

Paul Davis, Thesis Advisor
Professor

Anthony Bell
Professor

Rao Gudimetla
Assistant Professor

William Mackie
Professor, Linfield College

Jean-Louis Desplat
Rasor Associates

ACKNOWLEDGMENTS

The research activities were carried out under Subcontract Number S-273-005-004 to UES, Inc. whose Contract Number F33615-92-C-2284 was sponsored by SDIO/IST and the Thermionic Facilities of the Areo Propulsion and Power Directorate, Wright Laboratory, Wright-Patterson AFB, OH 45433-6563.

I would also like to give special thanks to Dr. Paul Davis, my thesis advisor, for all the advise, assistance and friendship throughout this research project. In addition, I would like to give thanks to the students and staff of Linfield College and LRI, especially Mark Hinrichs, Dr. Clarence Hinrichs, Dr. Ira Cohen and Gary Cabe, for there many grateful contributions.

Lastly, I would like to thank my wife and family for the love, support and encouragement which made this all worthwhile.

TABLE OF CONTENTS

LIST OF TABLES

LIST OF FIGURES

ABSTRACT

Surface Characterization of Alkali and alkaline Earth Metals on Single Crystal Refractory Metals

Gerald G. Magera
Oregon Graduate of Science & Technology, 1995

Supervising Professor: Paul R. Davis

The aim of this investigation was to study the interaction of barium and cesium with surfaces of model thermionic converter collectors. We successfully showed how submonolayer coverages of cesium, barium and cesium/barium interacted with the surface of W(110), Mo(110) and Nb(110) by measuring the changes in the work functions, dipole moments, activation energies for desorption and surface structure versus adsorbate coverage. These fundamental results are important in determining whether the use of a second vapor (barium) leads to substantial improvements over a high-pressure cesium thermionic converter.

The experiments were conducted on the clean surfaces of W(110), Mo(110) and Nb(110) under ultrahigh vacuum conditions using techniques of line-of-sight thermal desorption mass spectrometry, Auger electron spectroscopy and retarding potential work function measurement. The clean work functions for W(110), Mo(110) and Nb(110) were found to be 5.38 eV, 5.08 eV and 4.62 eV, respectively. The behavior of the work function was characteristic of alkali and alkaline earth metal adsorption onto refractory metal surfaces with the minimum work function for the three surfaces of approximately 1.50 eV for cesium and 2.20 eV for barium. The results of the change in work function versus adsorption of cesium onto the bariated surfaces of W(110), Mo(110) and Nb(110) were similar.

The energies of desorption for the different binding states were calculated for the various adsorbate-metal systems using first order desorption kinetics, that is, the adsorbates desorb at a rate linearly dependent on coverage. The desorption spectra for cesium from the various metal surfaces showed three distinct desorption sites, while

barium had a more continuous decrease in activation energy of desorption up to a monolayer of coverage. The main difference between the desorption of the two adsorbates was the temperature of the terminal (lowest coverage) desorption energy site. The highest terminal desorption energy for cesium occurred on the W(110) surface at a temperature of 1200 K, while barium does not start to desorb from the W(110) surface until the temperature reaches approximately 1700 K. The temperature difference between the binding states of cesium and barium on all three of the substrates allowed for the adsorption and desorption of cesium without altering the barium adlayer. The desorption behavior of cesium from the various barium/substrate surfaces, like the work function change, was also very similar. As the coverage of pre-adsorbed barium increased, the activation energy of the cesium decreased.

Chapter 1

Introduction

The adsorption of alkali and alkaline earth atoms on metal surfaces is of theoretical and experimental interest because it represents one of the basic forms of chemisorption and has shown great potential in many different technological applications. The alteration of the electron and ion emission properties of a metal with the adsorption of a fraction of a monolayer of alkali or alkaline earth atoms has important implications in the development of thermionic energy converters and other physical electronic devices. The advancement of energy conversion and ion propulsion devices which require low-energy plasmas and ion beams has been connected to the continued understanding of the emission properties of alkali and alkaline earth metal coated surfaces. An advanced understanding of the atomic physics of the unique emission behavior of alkali and alkaline earth coated metal surfaces should lead to new areas of device development.

In addition to the technological interest of alkali and alkaline earth metal adsorption, there has been considerable theoretical and experimental work done to try to understand the basic physical processes occurring when an electropositive atom chemisorbs on a metal surface. In the early work of Langmuir and Kingdon,[1] it was discovered that the electron emission rate of a tungsten surface was greatly enhanced by the adsorption of cesium onto its surface. Additionally, Becker[2] discovered the electron emission rate of cesiated tungsten could even be further enhanced by the presence of oxygen. Further experiments by Taylor and Langmuir[3,4] performed with cesium on polycrystalline tungsten, led to clarification of desorption rates, coverages and surface mobilities as functions of temperature and pressure. Binding energies were found to decrease with increasing coverage from a zero coverage binding energy of 2.83 eV to 1.77 eV binding energy at a monolayer of coverage. They also discovered that a minimum work function of 1.70 eV occurred below a monolayer of coverage and at the maximum in the electron emission. These pioneering experiments showed how adsorbed films can affect the fundamental properties of metal surfaces which was an unproven phenomena at the time and needed both experimental and theoretical verification. Both experimentalists and theorists were willing to devote time to this issue because of the way it enhanced the electron-emission properties of surfaces and provided the one of the simplest examples of chemisorption.

The theoretical situation has been studied from first principles by many researchers. A brief review of some their results will be outlined in chapter three of this report. Experimentally, various techniques have been developed to study the electronic structure of chemisorbed atoms and molecules. These techniques range from the more advanced chemical analysis technique of metastable-He de-excitation spectroscopy[5] to the early surface structure oriented field emission studies of Gomer, *et al.*[6] The combined efforts of these studies have yielded several different models to describe the electronic structure of the electropositive adsorbate/metal system but this continued debate does not hide the fact that alkali and alkaline earth coated metal surfaces enhance the performance of many devices. Although, the present investigation was motivated by technological reasons, hopefully, the results of this investigation can contribute to the debate over how the electronic structure of a metal surface is affected by alkali or alkaline earth metal adsorption.

The need for a highly reliable and efficient power source to meet the space power requirements has led to the design of several different advanced thermionic energy converters. The use of cesium as the sole interelectrode vapor is considered standard technology today. The operation of the cesium only device has been well characterized in terms of output limitations as well as fundamental processes occurring in the interelectrode plasma and at the surface of the electrodes. The cesium/electrode (i.e. tungsten) surface has been the subject of numerous surface physics studies to determine the significant surface characteristics which include evaporation rates, work function changes, cesium activation energies and electron emission. Cesium only devices have been shown to have the most stable output performance characteristics but have not always achieved the performance requirements needed for a particular application. Several techniques have been investigated to achieve the additional output requirements. In the present investigation, we will experimentally verify the viability of one such technique. The technique includes the introduction of an additional vapor to the interelectrode space. It is known that the coadsorption of electropositive and electronegative elements on a metal surface will increase the electron emission and offer a greater work function reduction than the adsorption of electropositive elements alone. The adsorption properties of two different electropositive vapors (i.e., alkali and alkaline earth metals) on a metal surface has been much less characterized but studies[7,8,9] have shown an improvement in high temperature characteristics. In light of these facts, we have undertaken a careful investigation into the adsorption and desorption of cesium and barium on model thermionic converter electrode surfaces. In this study, we compare the results obtained for the interaction of cesium, barium, and cesium plus barium on clean W(110), Nb(110) and Mo(110) surfaces.

The output performance of a thermionic converter is directly affected by the work function of the electrode surface and the stability of the electropositive adsorbate at high temperatures, so the purpose of this investigation was to gain an understanding of the various composite Cs/Ba/Me(110) surfaces by studying the work function changes and the thermal stability of cesium and barium. Because the surface structure of the clean and adsorbate covered systems can sometimes affect the adsorption kinetics of a solid surface, a study of the structural properties was also undertaken. The analytical surface techniques used and the surface properties measured by each technique are outlined in Table 1.00. The surface structure, the work function and activation energies of each adsorbate/metal system were studied at the same time to insure accurate and reliable results. The measurements on each of the different adsorbate/metal systems were conducted in the same vacuum chamber under equivalent conditions so that reliable comparisons could be made between properties of each system.

Table 1.00. Surface Characterization Analysis and Techniques.

Surface Property	Analysis Technique
Clean Surface Work Function	Field Emission Retarding Potential (FERP)
Surface Composition and Distribution	Auger Electron Spectroscopy (AES)
Surface Geometric Structure	Low Energy Electron Diffraction(LEED)
Thermal Stability of Surface	Quadrupole Mass Spectrometry (QMS)

a. Clean Surface Characterization Analysis and Techniques

Surface Property	Analysis Technique
Adsorbate Coverage Calibration	AES
Work Function *vs*. Adsorbate Coverage	FERP
Adsorbate Thermal Stability	QMS
Adsorbate Surface Structure	LEED
Cs-Ba Co-Adsorption	AES, FERP, QMS, LEED

b. Adsorbate/Surface Characterization Analysis and Techniques

References

1 I. Langmuir and K. H. Kingdon, Phys. Rev. 21 (1923) 380.

2 J. A. Becker, Phys. Rev. 28 (1926) 341.

3 I. Langmuir and J. B. Taylor, Phys. Rev. 40 (1932) 463.

4 J. B. Taylor and I. Langmuir, Phys. Rev. 44 (1933) 423.

5 B. Woratschek, W. Sesselmann, J. Kuppers, H. Haberland and G. Ertl, Phys. Rev. Letters 55 (1985) 1231.

6 L. Schmidt and R. Gomer, J. of Chem. Phys. 42 (1964) 3573.

7 R. Henne, Thesis, Univ. of Stuttgart, West Germany, 1975.

8 J. Psarouthakis, Surf. Sci. 17 (1969) 321.

9 A. G. Kalandarishvili, Working Medium Sources for Thermionic Power Converters, Energoatomizdat, Moscow, (Los Alamos Translation LN 633-689) (1986) 183-188.

Chapter 2

The Application: Thermionic Energy Conversion

Thermionic energy conversion is a method of converting heat directly into electrical power utilizing thermionic electron emission from metal surfaces. Unlike other more conventional methods of generated electrical power, thermionic energy conversion does not require any moving parts or working fluid other than the emitted electrons to change heat into electricity. The research effort in the area of thermionic energy conversion has gone through many ups and downs in the approximate 90 years since it was identified that electron emission could be utilized as a possible power source. Not only has there been extensive research done on the fundamental physics of thermionic emission from a metal surface but also on the development of high-temperature materials and heat sources for a compact and efficient power source in space. Researchers have developed a relatively thorough understanding of the operation and the limitations of vacuum and cesium only thermionic converters.

In a simple thermionic energy converter, diagrammed in Fig. 2.00, the electrons are emitted by a hot electrode, the emitter, and collected by a cold electrode, the collector, which is at a more positive electrical potential. Some of the heat produced by the evaporating electrons is rejected by the collector, while the remaining part is converted to electrical power through a external electrical load as it returns to the potential of the emitter. The space between the electrodes (interelectrode space) is either evacuated or consists of a suitable vapor or gas.

2.0 Thermionic Energy Converter as a Heat Engine

The operation of a thermionic energy converter is analogous to the thermodynamic heat engine cycle. The thermionic cycle is similar to a modified Rankine (steam engine) cycle that uses electrons as the sole working fluid. The work

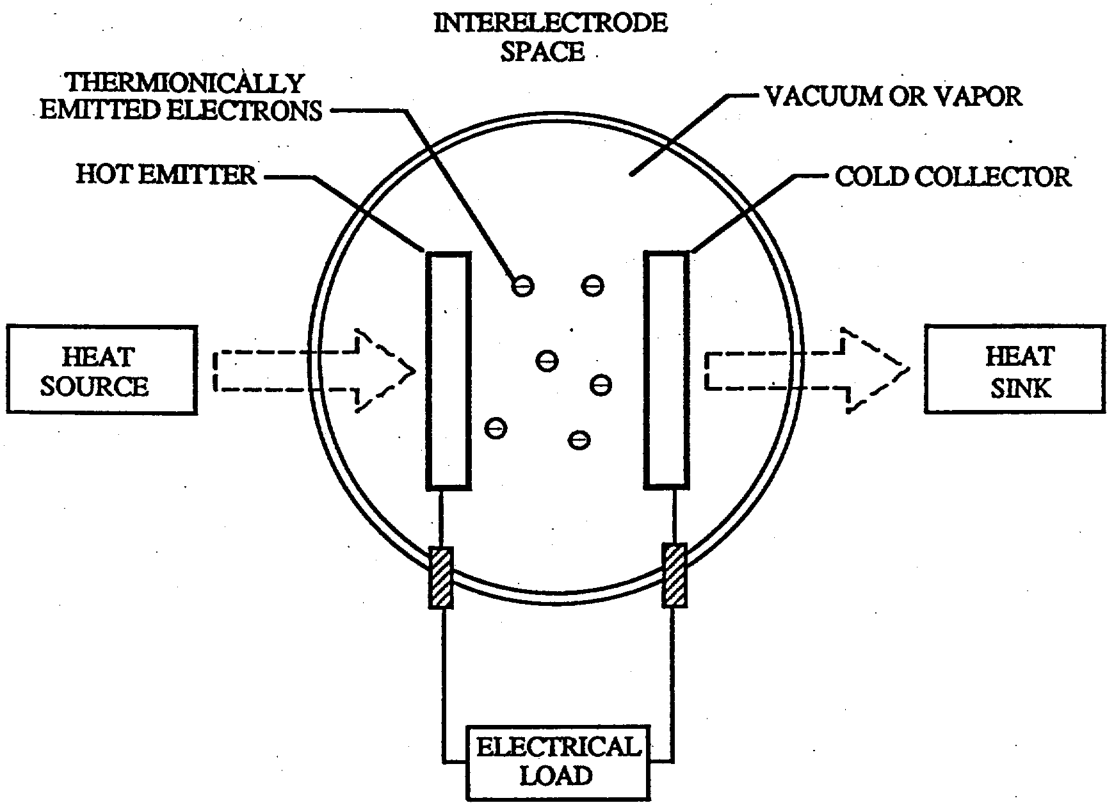

Figure 2.00. Schematic of simple thermionic energy converter.

made possible by conventional heat engines is produced by a process in which the steam molecules have a greater average energy then do the molecules of the liquid by the amount of the heat of vaporization at the temperature of the boiler. In the steam engine, the difference in the heat of condensation and the amount of heat exhausted to evaporate the liquid into steam is converted into mechanical work by the engine and then into electrical energy by a generator. In thermionic energy conversion, the emitter operates as the electron boiler and the collector as a electron condenser in which an electrical potential (pressure) difference is developed to produce electrical work instead of a vapor pressure difference to produce mechanical work. In a thermionic energy converter, the emitted have a potential energy with respect to the emitter fermi level equal to the work function of the emitter (ϕ_e) plus some additional kinetic energy determined by the temperature of the emitter. Passing over to the collector, the electrons have the potential energy corresponding to the work function of the collector (ϕ_c) plus the additional energy associated with the temperature of the collector. When $\phi_c < \phi_e$, the energy of the electrons after condensation is larger than in their original state in the emitter by $\phi_e - \phi_c$. The difference in energy is converted to electrical work by passing the electrons through the external electrical load. If there is a potential difference (ΔV) between the emitter and collector, then the potential energy level in the collector exceeds the potential energy level of the emitter by a smaller amount given by ($\phi_e - \phi_c - \Delta V$). The main feature of a thermionic converter is the fact that the energy gain depends directly on the work functions of the emitter and collector, plus the potential drop inside the converter, and not on the heat of evaporation and condensation as in the steam engine. Thermodynamically, this is an obvious advantage because the electrons in a thermionic converter are emitted at high temperature and used at a high efficiency. The efficiency of an ideal thermionic energy converter at practical power densities is at about 60% of the Carnot efficiency, but the typical present day thermionic converter rarely achieves 25% of the Carnot thermodynamic limit. However, some advanced thermionic converters are being investigated that approach the more ideal converter efficiency limit. From a more practical point of view, the thermionic converter avoids the mechanical work stage by converting heat directly into electricity and therefore has the possibility of providing a simpler, more reliable and more compact power plant.

2.1 The Ideal Thermionic Energy Converter

To better understand the concept of thermionic energy conversion and how to improve the performance of such a device, it is important to define the performance limit of ideal thermionic converter. The motive diagram in fig. 2.01 shows the potential energy of an electron as it moves from the emitter surface to the collector surface[1]. As seen in the diagram, for an electron to reach the collector, it has to first overcome the work function of the emitter (ϕ_e). Next, it must move from the surface of the emitter into the interelectrode space and then surmount the potential barrier equal to the collector work function (ϕ_c). In the ideal thermionic converter, the electron does not incur any losses in transit and an energy barrier V + ϕ_c must be overcome if the electrode potential energy difference V is greater that the contact potential V_0 (i.e. ϕ_e - ϕ_c), and a barrier ϕ_e must be overcome if V is less than V_0. The output current density of the ideal thermionic converter is given by the Richardson-Dushman equation (note: The Richardson-Dushman equation will be defined in the next chapter).

$$J = AT_e^2 \exp\left(-\frac{\phi_e}{kT_e}\right) \qquad \text{for } V < V_0 \qquad (2.00)$$

$$J = AT_e^2 \exp\left(-\frac{V+\phi_c}{kT_e}\right) \qquad \text{for } V > V_0 \qquad (2.01)$$

where T_e is the emitter temperature, A = 120 A/cm^2-K^2 and *k* is Boltzmann's constant. Equation 2.00 is defined as the saturation current density and is the maximum current the emitter can emit at temperature T_e. In fig. 2.02, the current versus the output voltage is given for the ideal thermionic converter. Clearly, there are two distinct regions of operation which are defined by eqns. 2.00 and 2.01. Two problems with simple picture are immediately apparent. First, typical refractory metals have work functions exceeding 4.0 eV. Polycrystalline tungsten, for example, has a work function of 4.6 eV. Hence, to obtain a current density of 1 A/cm^2 with this material, it would require an operating temperature of 2600 C and even tungsten has a significant evaporation rate at such a temperature. Second, the electron space charge effects would limit the current flow in a vacuum converter to less than a milliampere with an interelectrode space of 10 mils.

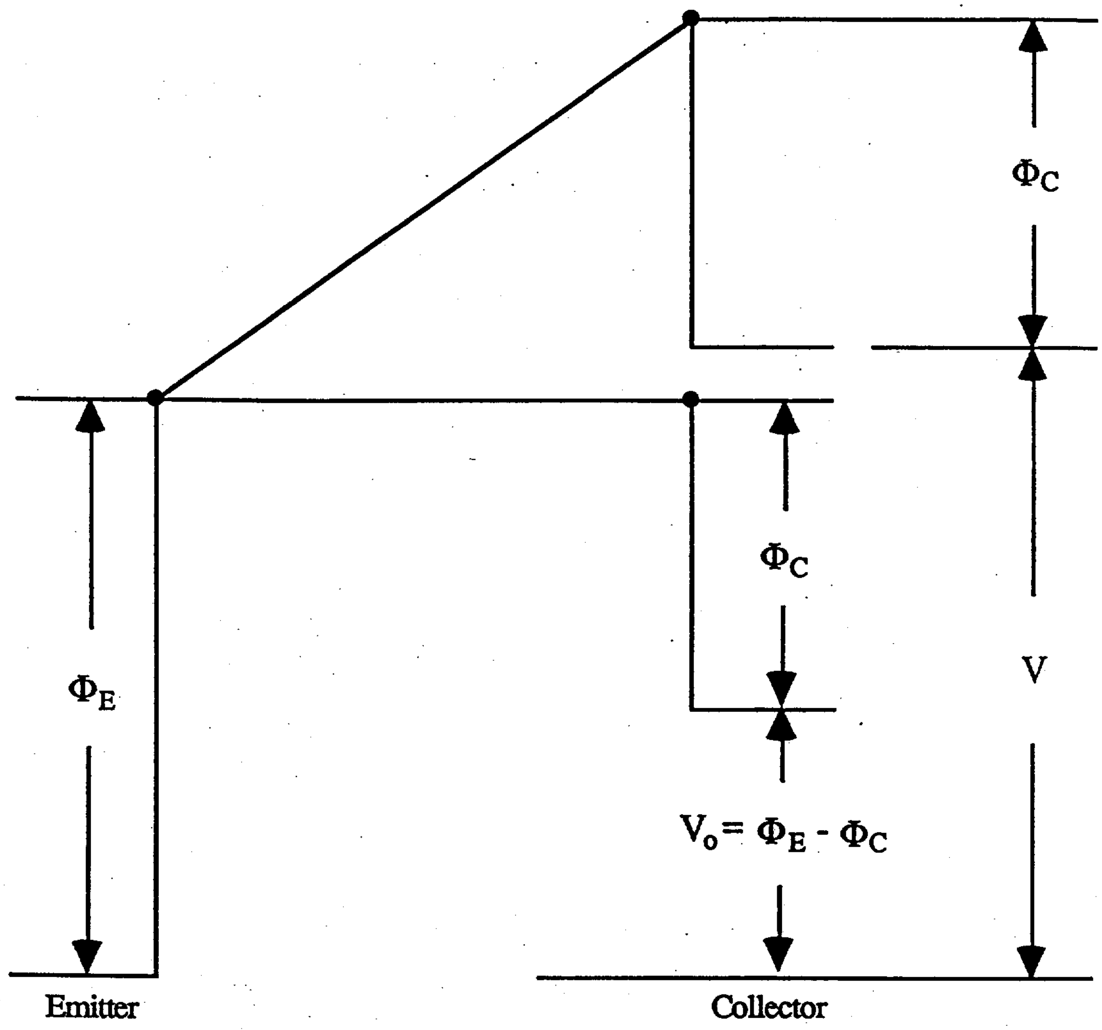

Figure 2.01. Motive diagram for an ideal thermionic converter.

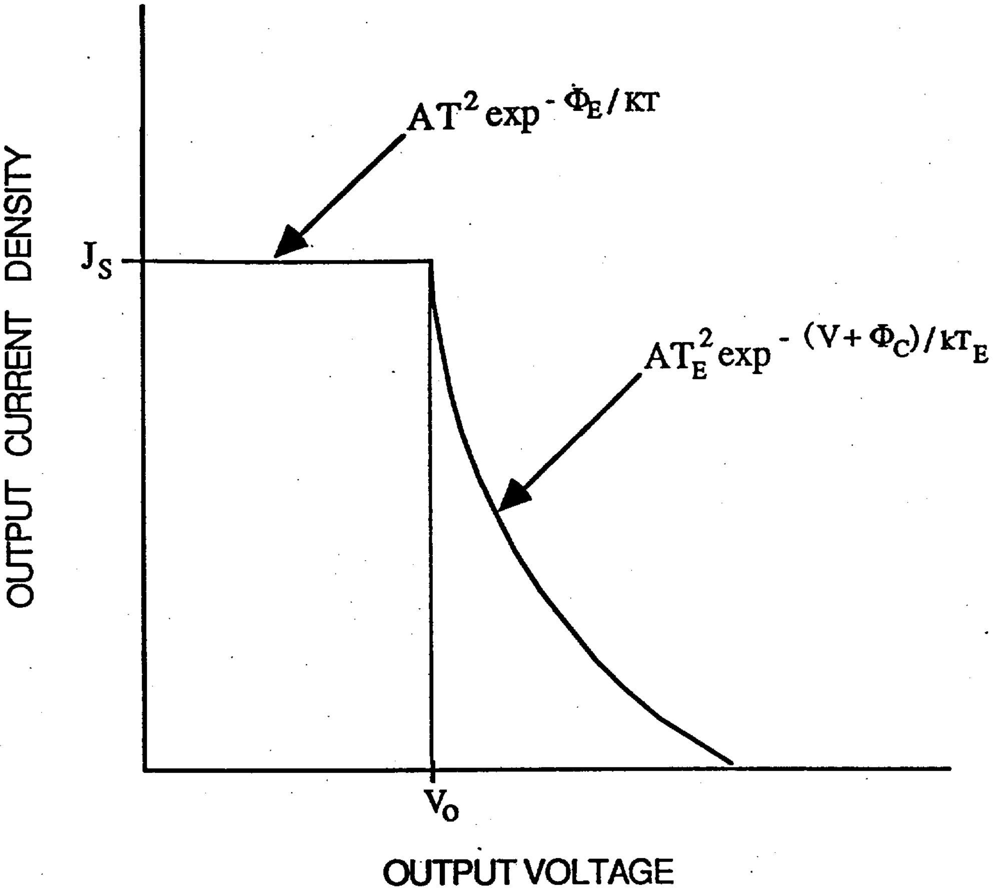

Figure 2.02. Current versus voltage characteristics for an ideal thermionic converter.

2.2 Operating Modes

Thermionic energy conversion is based on the understanding of two processes, the emission processes by which electrons, ions, neutrals and photons are emitted or collected at the surface of the electrodes, and the transport processes which involve the migration and interaction between these particles in the interelectrode space. Thermionic electron emission is essential and inherent to the operation of thermionic converters, as already indicated. Principles of thermodynamics, quantum mechanics, surface physics and physical chemistry are used to describe the mechanisms that affect the emission and evaluate how they depend on the electronic properties of the surface, the materials of the electrode, the structure of the electrode surface and the adsorbates on the surface. Transport processes directly influence the performance of the converter by limiting the flow of the thermionically emitted electrons. Although some transport processes are not directly related to thermionic emission and can be suppressed, the adverse effects of others can severely limit the operation of the converter. The principles of electrostatics, gaseous electronics and plasma physics are used to analyze and understand how to reduce these limitations. The most significant transport process is the negative electrical charge of the electrons that transit the interelectrode space (see fig. 2.00). The flow of electrons creates a negative space charge barrier in the interelectrode space, and the current flow through the thermionic converter is greatly reduced. Unless the space charge effects are suppressed, the efficiency and therefore the output power of the converter will be limited.

A researcher working in the area of thermionic energy conversion is always striving for ways to increase the thermionic electron emission while suppressing losses due to the transport processes, especially the negative space charge. Ever since 1885, when Edison[2] discovered that electric current could be made to flow between two electrodes in a vacuum, while one or both were heated, researchers have been experimentally and theoretically analyzing the thermionic energy converter in search of new ways to improve thermionic electron emission and suppress the associated negative space charge. Several of types thermionic converters have been investigated that have yielded useful power densities under practical operating conditions. The different types of converters are distinguished by the method used to suppress the negative space charge. Table 2.00 lists a number of the most successful thermionic

Table 2.00. Types of Thermionic Converters

Type	Space Charge Neutralization Method
Vacuum:	
Close-space diode	Very small interelectrode space
Vacuum triodes	Focused electron beam magnetically or electrically accelerated
Vapor or Gas-filled:	
Cesium diode	Surface and/or volume ionization
Pulsed diode	Ions produced by applied voltage pulses
Surface ionization triode	Cesium vapor thermally ionized by third electrode
Dual emitter arc triode (plasmatron)	Ions produced by arc from third electrode

converter designs, separated into two broad categories, vacuum thermionic converters and vapor filled thermionic converters. Table 2.00 does not include the variations that could occur between thermionic converter designs within a given type, such as electrode materials and configurations. Also, thermionic converters operated at different current levels, temperatures, interelectrode spacing or other physical dimensions are not considered different types.

Vacuum thermionic converters operate with an interelectrode space that is highly evacuated. The negative space charge is suppressed by either making the space between the emitter and collector small enough to reduce the flow of electrons needed to maintain a certain current density ($d/\lambda < 1$, where d is the distance between the electrodes and λ is the mean free path of the electron) or by adding a third electrode to either electrostatically or magnetically increase the speed of the electrons, and hence, for a given current density, the flow of electrons will be reduced. Although, under experimental conditions, the performance characteristics of vacuum diodes have been favorable, their design is impractical for most applications requiring extended operation.

In vapor-filled thermionic converters, the interelectrode space is filled with a particular electropositive vapor which can be easily ionized. In these converters, the negative space charge effect is partially neutralized by the positive ions created from the ionization of the vapor. The alkali metal cesium has long been used as the interelectrode vapor because it has the lowest ionization potential (3.89 eV) of any stable gas. Other alkali metal (Li, Na, K) and alkaline earth metal (Ba, Sr, Ca) vapors have been experimentally investigated but none have been found that could provide the consistent output characteristics of a cesiated thermionic energy converter. Under the right operating conditions, different combinations of the above alkali and alkaline earth metals have recently shown promise, but at the present time, cesium diodes are the only practical converters.

2.2.a Cesium Thermionic Energy Converter

The application of thermionic energy conversion is still based almost exclusively on cesium thermionic converters operating at high pressure. The properties of the cesium converter are essentially determined by the dual function of the cesium vapor.

In cesium thermionic energy converters the positive cesium ions are emitted either thermionically from the emitter surface or generated by electron-atom collisions in the interelectrode space, or both. Thermionic ion emission occurs when cesium vapor is adsorbed on the surface of the hot emitter and then desorbed into the interelectrode space as positive ions. The mechanics of surface ionization have been studied theoretically and applicable theories have been made to fit certain operating conditions, in particular, at high emitter temperatures and low cesium pressures when it is generally accepted that thermionic ion emission is the dominant ionization process. Ion production by electron impact in the interelectrode space becomes the dominant ionization process as the cesium pressure is increased, but the details describing this situation are not well understood because researchers have not been able to understand the role of other contributing processes, such as thermionic emission, atom excitation and photon ionization.

Cesium adsorption also increases the thermionic emission and the output voltage by lowering the emitter and collector work functions, respectively. The alkali metal cesium performs these two functions quite well, since cesium has the lowest ionization potential of any stable element (3.89 eV) and provides the greatest reduction in the work function of any electropositive element. However, cesium has a relative weak bond with most metal surfaces, so at moderate temperatures cesium will readily desorb. Thus in order to keep the required amount of cesium on the electrode surfaces to maintain the required operating conditions, a high equilibrium pressure of cesium is needed in the interelectrode space. For emitter temperatures of 2000 K or higher required for various advanced thermionic energy converters, the cesium pressure to maintain a suitably low work function could be as high as 10 Torr. The high cesium pressure needed to lower the work function can be an order of magnitude greater than needed for space charge neutralization. A high cesium pressure causes low electrical efficiency due to the high thermal losses in the interelectrode space, thus lowering the output voltage and reducing the current of the device. Later in this section there will be a discussion on possible ways the circumvent this problem.

At practical operating conditions, both processes take place to some extent and losses are incurred when pressure of the cesium vapor is changed in the converter. Figure 2.03a illustrates the motive diagram for a cesiated diode. The diagram shows that the arc drop contains three separate elements: 1) plasma loss, V_p, due to the electron scattering by collisions with cesium atoms, 2) sheath loss, V_s, caused by the double valued potential sheath adjacent to the collector, 3) ionization loss, V_i, associated with the ionization of cesium atoms by electrons. Its performance can no longer be represented by a ideal diode but has to include an added voltage loss term in the ideal diode equation. As shown in fig. 2.03a, the sum of voltage losses, includingthe collector work function, is defined as the barrier index, V_B. Operationally, V_B is defined as the potential difference between the tangent of the measured I-V curve and the tangent to the Boltzmann line (see fig. 2.03b). The Boltzmann line represents the ideal I-V characteristic assuming zero arc drop, zero collector work function and zero collector temperature. The actual converter performance is shown in fig. 2.03b and is given by the following equation,

$$J = AT_e^2 \exp\left(-\frac{V+V_B}{kT_e}\right). \qquad (2.02)$$

The barrier index therefore characterizes the performance of any real thermionic converter relative to parametric performance data of the ideal diode converter, with $V_B = \phi_c$.

The efficiency is defined by the actual power output of the device divided by the total heat supplied to the emitter,

$$\eta = {}^{JV}\!/_{q_E}\,. \qquad (2.03)$$

The power output is a product of the voltage and current, defined by eqn. 2.02, but only about 90% of this power is available at the load due to the voltage drop across the converter's electrical leads. Consequently, the useful output power density of a practical converter is given by

$$P_{Load}(\text{watts}/\text{cm}^2) = JV = (0.9)J\left[kT_e \ln(AT_e^2/J) - V_B\right]. \qquad (2.04)$$

The total heat supplied to the emitter is

$$q_E = q_e + q_r + q_L \qquad (2.05)$$

where q_e is the heat removed by the electron emission and is equal to $J(\phi_e + 2kT_e)$, q_r is the heat removed by thermal radiation and is equal to $\sigma\varepsilon(T_e^4 - T_c^4)$ and q_L is the heat conducted down the emitter lead and is approximately equal to $q_E/10$. The thermionic efficiency is shown in fig. 2.04 as a function of the emitter temperature

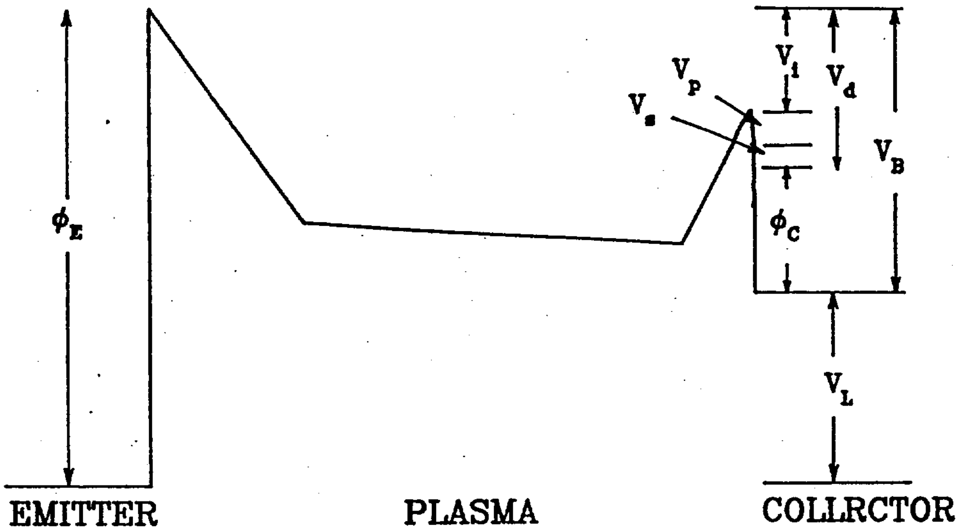

Figure 2.03a. Motive diagram for a cesiated thermionic converter.

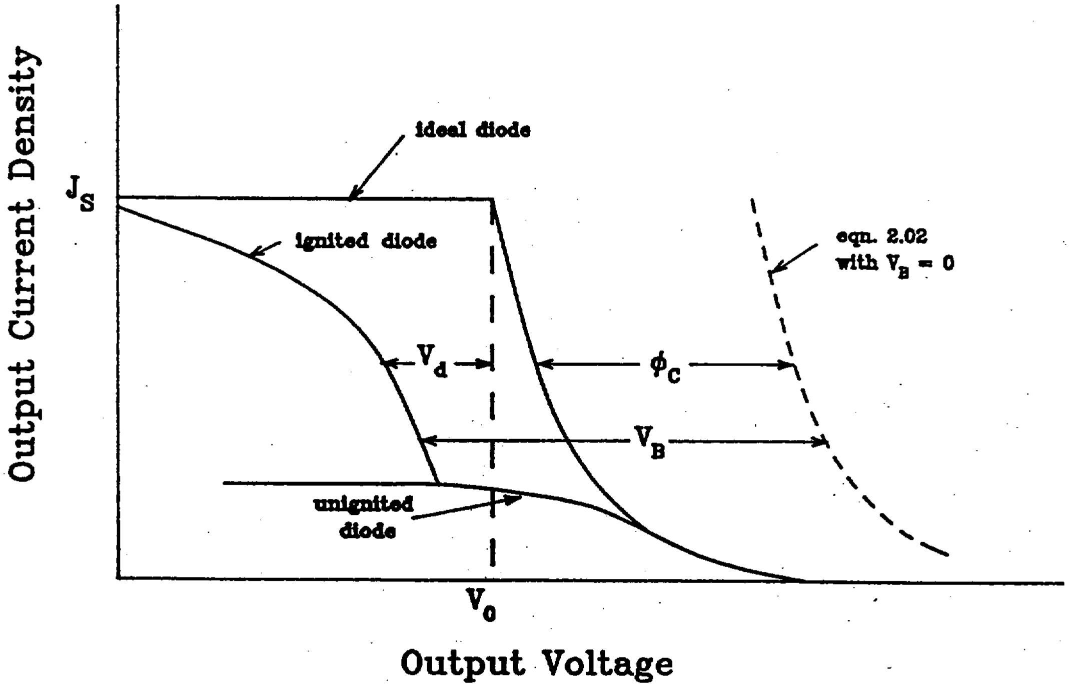

Figure 2.03b. Performance characteristics of a cesiated thermionic converter.

and parametric of the barrier index. To avoid excessively high plasma losses in the interelectrode space, the distance between the electrodes must be reduced to the extent that is difficult to maintain operation and can cause questionable reliability for the converter. It is of great interest to increase the life and reliability of the cesium thermionic converter, especially in light of the advanced space power applications. It is the aim of many researchers to find ways to reduce the cesium pressure and therefore the plasma losses. This would make possible larger interelectrode spacing as well as improvements in efficiency.

2.2.b Cesium/Oxygen Thermionic Energy Converter

The barrier index, as seen in fig. 2.04, characterizes the performance of the thermionic converter, so if the barrier index could be decreased, the thermionic converter could operate at greater efficiency and higher power output at much lower electrode temperature and cesium pressure. One breakthrough method that has allowed acceptable current densities to be maintained at low electrode temperatures and cesium pressures is the introduction of a small partial pressure of oxygen into the interelectrode space. The use of cesium-oxygen vapor in the converter allows the emission current to be increased under practical operating conditions because oxygen increases the cesium adsorption on the emitter surface[3]. Furthermore, the presence of oxygen also results in very low collector work functions at low collector temperatures (low cesium pressures)[4]. The reductions in the arc drop and collector work function have a direct effect on the value of the barrier index and therefore on the output characteristics of the thermionic converter. Figure 2.05[5] illustrates this fact by comparing the output current versus output voltage (J-V curves) for a converter with and without an oxidized collector. The barrier index is reduced by approximately 0.4 eV for the converter with the oxidized collector. Another significant advantage of the lower cesium pressure is that the interelectrode spacing can be increased while maintaining acceptable converter performance. Although the addition of oxygen into the thermionic converter has lead to substantial improvements, the basic properties of the electrodes in the cesium-oxygen vapor along with the maintenance and control of the cesium-oxygen vapor need further research.

2.2.c Cesium/Barium Thermionic Energy Converter

Recently, there has been a rebirth in the idea of using mixed electropositive vapors in thermionic energy converters. Studies have shown that thermionic converters with mixed vapors have some advantages over cesium-only devices for applications requiring high-temperature and efficient operation. These advantages include (1) lower vapor pressures, (2) operation in the unignited mode (limited plasma losses) and (3) increased electrode spacing. The discussion and possible application of this method is the main focus of this investigation. In this method, another electropositive vapor is added to the interelectrode space that has an acceptable low work function, compared with cesium, and also a greater adhesion to the surface of the electrode. Given this scenario, the two vapors will each perform a particular function. The cesium will still be used to neutralize the space charge while the other electropositive vapor will be used to lower the work functions of the emitter and collector. Thus, lower cesium pressures will be needed which should lead to a decrease in plasma losses. This would also allow for greater interelectrode spacing. Barium and other alkaline earth metals, including strontium and calcium, are suitable for the role of reducing the work function at relative high surface temperatures[6,7,8]. Figure 2.06 illustrates that for high collector temperatures, a barium-cesium converter will out perform a cesium-only converter. For space applications, high temperature devices are suitable because excess heat is radiated easily. Besides the fact that alkaline earth metals have lower vapor pressures than cesium and greater binding to the surfaces of the electrode at higher temperatures, they also have another advantage. They have a substantially smaller cross sections for electron collisions compared to the alkalis, so plasma losses are kept to the minimum. The higher emitter temperatures and lower cesium pressures in a dual vapor thermionic converter result in a higher percentage of the ions needed for space charge neutralization being produced by surface ionization, hence, plasma losses should be almost eliminated. A thermionic converter operating in the unignited mode (no high temperature arc needed to produce positive cesium ions) has shown to have improved efficiency over ignited mode devices[6]. Barium vapor, by itself, was investigated in Ref. 6, but because of insufficient ion production, the space charge effects lead to low power densities at

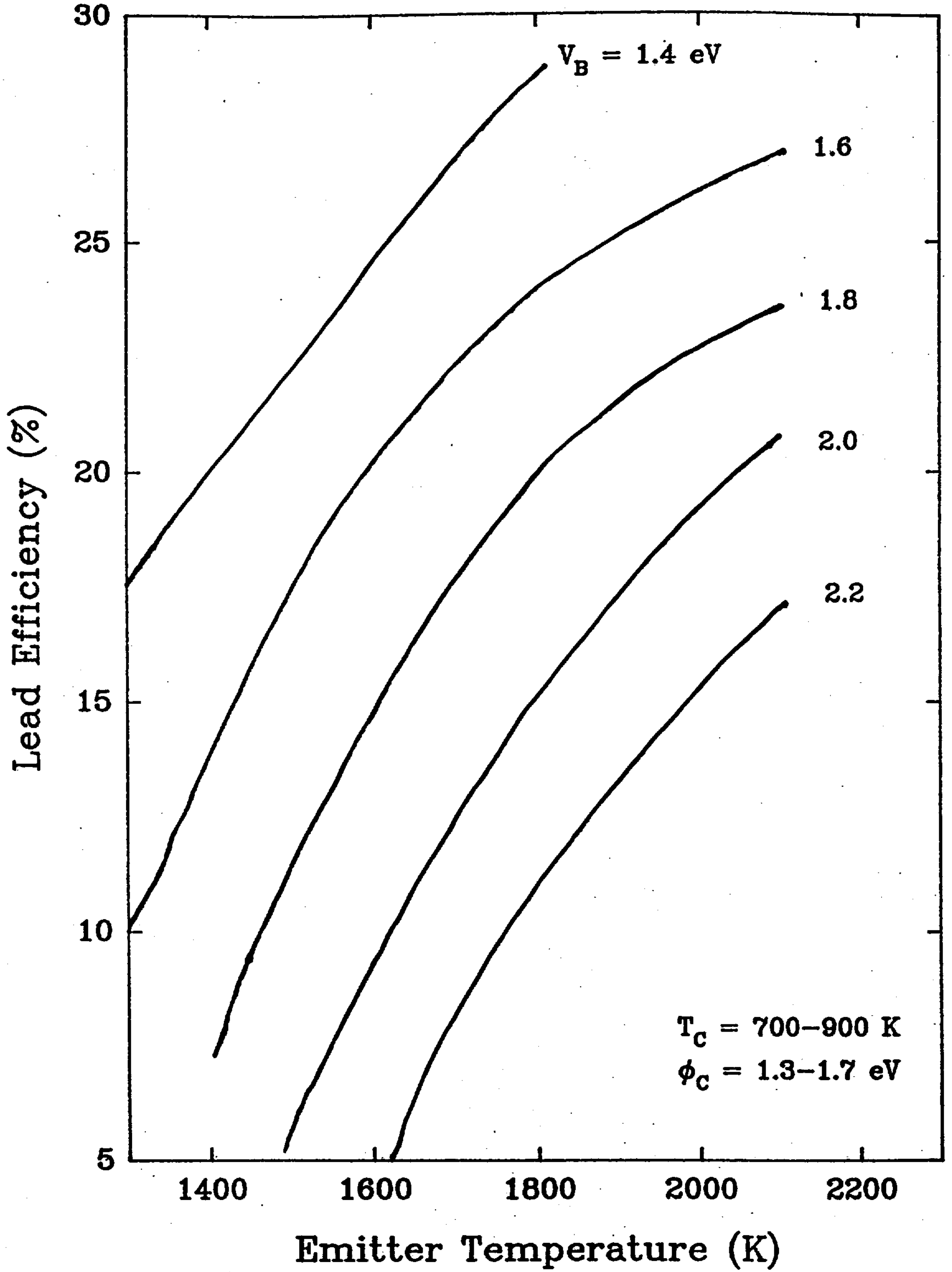

Figure 2.04. Lead efficiency as a function of emitter temperature, parametric in the barrier index.

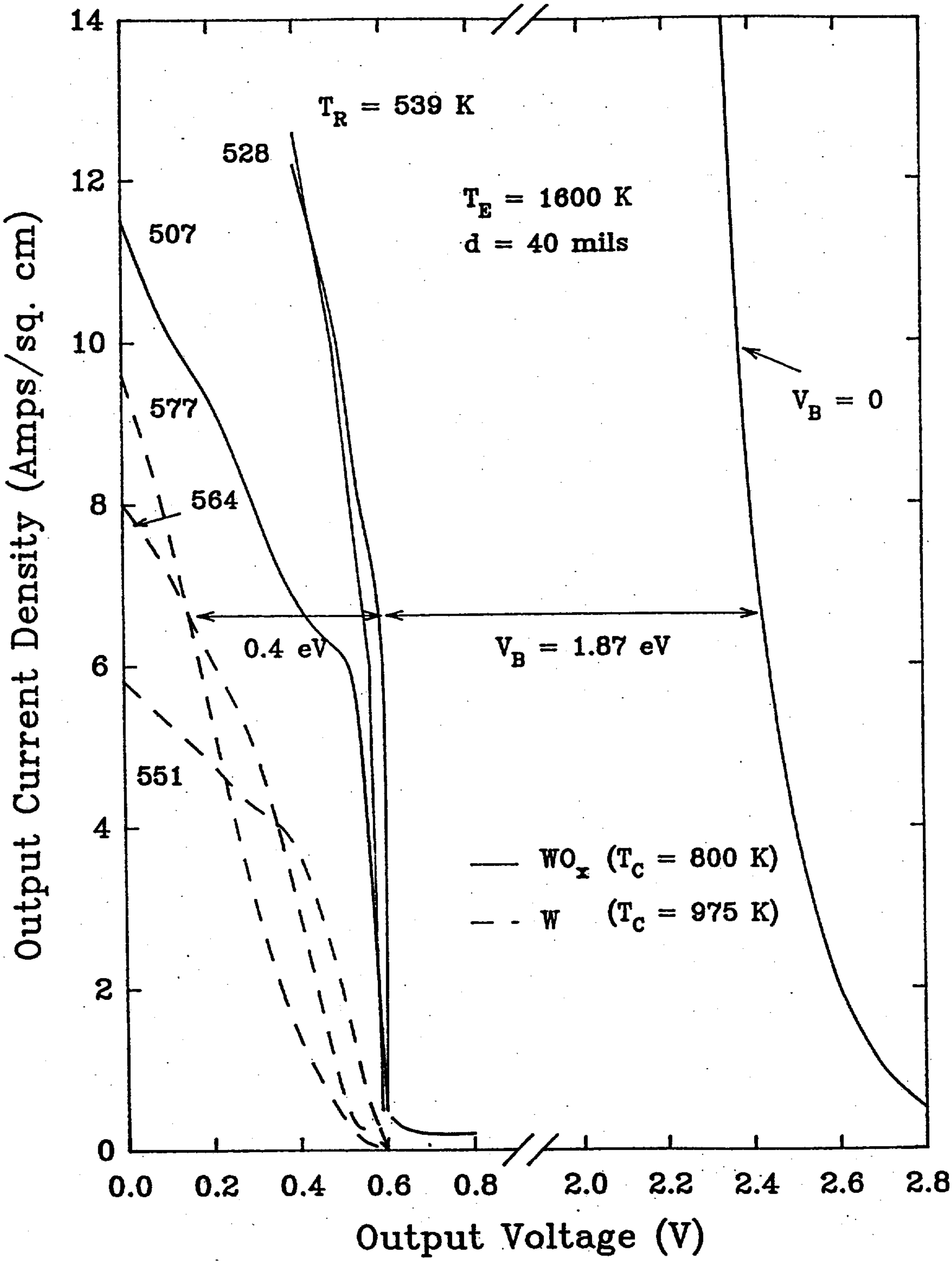

Figure 2.05. Comparison of current versus voltage characteristics of two thermionic converters identical except for an oxide coating on the collector.

practical operating conditions. Therefore, it is highly unlikely that a thermionic converter will operate effectively without cesium.

The use of a second vapor, like barium for example, does not only have advantages. The low vapor pressures of barium require the collector to be operated at relatively high temperatures compared to a cesium-only device. For space power applications this is not a big disadvantage because heat is radiated more efficiently in space at higher temperatures, but for terrestrial applications this becomes a major concern. Also liquid and vaporized barium have strong corrosive effects on many standard converter materials. This problem becomes more severe when oxygen and barium are added to the converter. Barium oxide is very corrosive to many insulator materials. From an applications standpoint, a second reservoir must be built into the system, and since the reservoir temperatures for setting optimum pressure are much different for cesium and barium, migration occurs from the hotter to the colder reservoir. The condensation of barium into the cesium source disturbs the optimum pressure settings of the cesium source. The problem associated with the pressure effect caused by the barium reservoir has not been clearly outlined but several solutions[6,8] have been suggested to circumvent the problem.

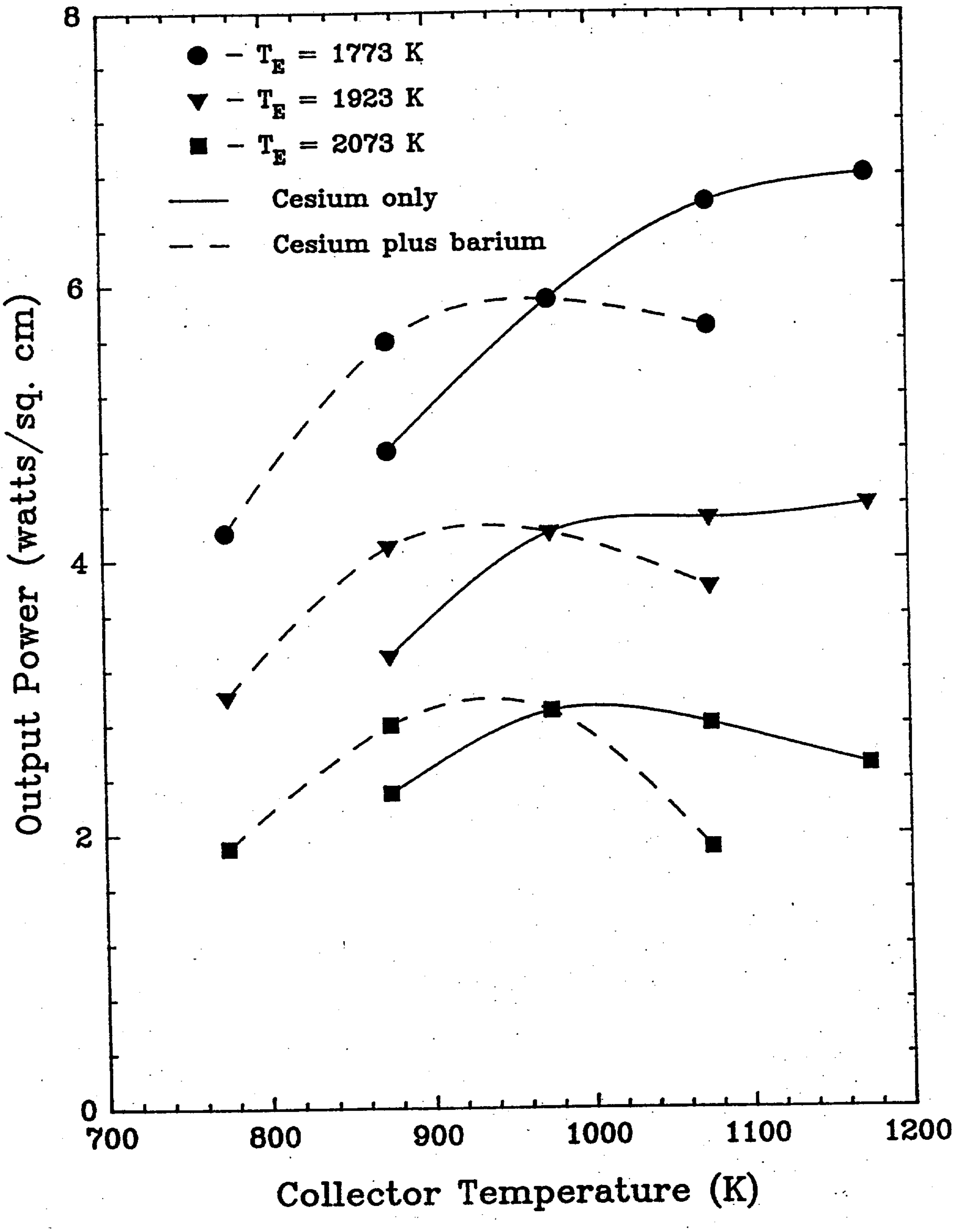

Figure 2.06. Comparison of output power versus collector temperature for cesium and cesium-barium thermionic converters, parametric in emitter temperature. [Ref. 8]

References

1 N. S. Rasor, in: Fundamentals Handbook of Electrical and Computer Engineering, vol. II, (S. S. L. Chang, Ed. New York 1983) 688.

2 W. H. Preece, Proc. Roy. Soc. (London) Ser. A 38 (1885) 219.

3 B. M. Zykov, V. K. Tskhakaya and V. I. Yarygin, Sov. Phys. Tech. Phys 27 (1982) 481.

4 J-L. Desplat, Rasor Associates, Inc., Sunnyvale, CA. (1983), written communication.

5 F. Huffman, Thermo Electron Corp. R & D Center, Waltham, MA. (1988), written communication.

6 R. Henne, Thesis, Univ. of Stuttgart, West Germany, 1975.

7 J. Psarouthakis, Surf. Sci. 17 (1969) 317.

8 A. G. Kalandarishvili, Working Medium Sources for Thermionic Power Converters, Energoatomizdat, Moscow, (Los Alamos Translation LN 633-689) (1986) 183-188.

Chapter 3

Theoretical Considerations at the Electrode Surface

3.0 Adsorption Dynamics

Adsorption is separated into two main categories: physisorption and chemisorption. Physisorption is the weakest form of adsorption to solid surfaces and lacks a true chemical bond between the adsorbate and the substrate. The binding force that exists in this type of interaction is identified as the van der Waals interaction. In our investigation we are not interested in this type of adsorption due to the strong chemical bonds inherent to alkali and alkaline earth metals on metal surfaces. This type of adsorption is better described as chemisorption. In discussing chemisorption, three important quantities need to be understood: (1) the chemisorption energy ΔE, (2) the induced dipole moment μ, and (3) the change in the charge density and how it effects the electronic structure at the interface.

The chemisorption energy ΔE is the energy difference between the energy of separated adsorbate and substrate and energy of the combined adsorbate-substrate system. At $T = 0$ K, ΔE is defined as the work needed to remove the adsorbate from the substrate surface. A simple criterion[1] for chemisorption has been set such that $\Delta E \geq 1$ eV. A comparative example of this criterion between physisorption and chemisorption is $\Delta E = 0.4$ eV for xenon[2] and $\Delta E \cong 3.0$ eV for cesium[3] on W(111), respectively.

The bond formed by chemisorption usually involves some charge transfer either to or from the substrate and the sign and magnitude of the transfer can be determined from the dipole moment, μ of the adsorbate. The dipole length is difficult to measure experimentally, so the Helmholtz equation, $\Delta\phi = 4\pi\mu n$, is used to relate μ to the change in substrate work function, $\Delta\phi$. The change in the substrate work function is easily measured using a variety of techniques. For alkali adsorption on transition metals, $\Delta\phi$ can be as large as 3.5 eV, indicating a large transfer of electronic charge from the adsorbate. On the other hand, the adsorption of oxygen tends to increase the work function of the substrate by a much smaller amount (~1.0 eV), thus indicating a rather small charge transfer to the adsorbate or possibly a smaller adsorbate to substrate dipole length..

The last variable connected with chemisorption is the change in density of states introduced by the adsorption process. The changes in the charge distribution plays a major role in the adsorbate bonding structure and the electronic structure at the interface. The adsorption of alkali and alkaline earth metals on transition metal surfaces is a special type of chemisorption that is characterized by specific interactions and bonding mechanisms. To understand these interactions, we need to realize the general theoretical arguments concerning chemisorption at clean metal surfaces.

3.0.a Alkali and Alkaline Earth Metal Adsorption

Alkali and alkaline earth metals are electropositive elements with weakly bound valence electrons, and when adsorbed on the surfaces of transition metals, such as tungsten and molybdenum, they cause a drastic change the of electronic structure. When these metals are adsorbed on the transition metal surface, the valence s-electrons interact with the upper states of the valence band (i.e. *d*-states) of the substrate. The interaction both broadens and shifts the energy of the s-state in such a way that the adsorbed species becomes partially ionic. The interaction of these states gives rise to a surface dipole layer at the interface of the adsorbate and substrate opposite to that of the natural surface dipole barrier. The changes in electronic structure of the substrate's surface have interesting effects on the work function, electron emission and adsorption properties. The enhancement of the surface properties by this phenomenon has led to advances in many technological applications, such as field emission, vacuum technology, catalysis and thermionic energy conversion. The vast amount of information obtained, both theoretically and experimentally, on the properties of films on surfaces of metals has led to some definite conclusions but not without much debate.

The vast amount of experimental data stimulated a variety of theoretical models to describe the adsorption of alkali and alkaline earth metals on metal surfaces. After discovering the effects cesium could have on the work function and emission characteristics of tungsten, Langmuir[4] proposed his own model. Since the ionization potential of cesium is lower than the work function of the metal substrate, the cesium was adsorbed as an ion giving one electron to the surface. The Cs^+ ion formed a dipole with its negative image charge which reduced the work function of the metal surface. He explained the characteristic work function curve found for alkali metals as the interaction between the dipoles, which reduced the effective dipole moment per adatom. Thus, the work function goes through a minimum and increases for higher coverages. He also noted that the model explains the relationship between binding energy and increasing coverage. The decrease in the binding energy is a due to the interaction between the ion and its image. Langmuir further suggested that cesium will desorb from the surface as an ion if the work function of the surface is higher than the ionization potential of cesium (3.89 eV), so at high temperatures (low coverages) cesium will desorb only as ions.

Experimental measurements of alkali and alkaline earth metals on both polycrystalline[5,6] and monocrystalline surfaces[7,8,9] have shown inadequacies in the classical theory. First, studies have shown that the bond between the adsorbed adatom and the metal substrate is usually not completely ionic[5]. Second, covalent bonding should not be neglected. Third, the classical theory does not always fit the work function curves for coverages approaching a monolayer[4,9]. The simple image charge and field depolarization given in the classical representation is an oversimplified view. It does not account for the overlapping of the of the electron orbitals known to be important at relatively high coverages. Finally, there are large differences in the dipole moment and activation energy for adatoms adsorbed on metal surfaces of different crystallographic orientation.[8,9,10] New theoretical models were needed to remedy these inadequacies.

Gurney[11] criticized this simple model proposed by Langmuir and thought this behavior could only be understood in terms of quantum mechanics. He recognized that although the ionization potentials of calcium, strontium and barium were greater than the work function of tungsten, they behaved in the same way as the alkali metals with much lower ionization potentials. In Gurney's simple quantum mechanical model, it is shown that the initially discrete valence n*s* (n = 2,...,6) levels of an free alkali atom gradually broaden as it is brought near the surface and its valence level resonance is found close to the Fermi level of the substrate. The change in work function and consequently the dipole moment depends on occupation of this broadened valence band with respect to the substrate Fermi level. The increase in the alkali metal coverage causes an interaction between atoms on the surface which leads to a lowering of energy of the broadened level and to a decrease of the dipole moment per adatom. The depolarization of adatoms as a function of coverage causes the minimum in the work function versus coverage curve. Schmidt and Gomer[9] examined the fact that the adatom/metal bond will be ionic, polar-metallic or metallic depending on whether the broadened and shifted valence level of the adatom was above, at the same level as or below the Fermi level of the substrate. The task of producing a rigorous treatment of the alkali-metal adsorption system quantum mechanically has proven to be a very difficult task.

Gadzuk[12] extended Gurney's idea of the adatom being in a virtual impurity state and treated the interaction of the metal and the adatom through perturbation theory (Fig. 3.00a). In the illustration, *s* is the distance of the ion core from the surface, and *E* is the position of the *n*s level relative to the Fermi level of the metal substrate. The presence of the alkali or alkaline earth ion core in the surface region perturbs the metal and alters the electron-metal interaction. This is most easily seen in the classical picture shown in Fig. 3.00b. To describe the adatom-metal interaction, Gadzuk, considered a solution of the Schrodinger equation with the total Hamitonian

$$H_{tot} = H_M + H_a + H_{int}, \qquad (3.00)$$

in which H_M describes the unperturbed metal, H_a the unperturbed atom and H_{int} the coupling of the atom with the metal. He discussed each Hamiltonian as it related to the significance of virtual bound electron states at the surface deriving from the n*s* states of the adatom. The metal substrate is assumed to be a free-electron like and hydrogen-like wave functions, $\psi_{n,s}$ are used for the unperturbed atom. Gadzuk reduced eqn. 3.00 to a single electron Hamiltonian of the form

$$H = \frac{-h^2}{2m}\nabla^2 - \frac{e^2}{4d_1} + \frac{e^2}{R} - \frac{e^2}{r} \qquad (3.01)$$

where the first term is the kinetic energy operator, the second term is the image potential of the electron in the presence of the metal, the third is the repulsive potential between the electrons and the final term is the attractive potential between the electron and ion. The distances d_1, R and r are defined in Fig. 3.00b. The interactions in the single Hamiltonian may be split into a two separate equations describing the unperturbed Hamiltonian plus a perturbation. Since

$$H_a = \frac{-h^2}{2m}\nabla^2 - \frac{e^2}{r} \qquad (3.02)$$

eqn. 3.00 can be rewritten as

$$H = H_a + H'_{a-m}, \qquad (3.03)$$

where

$$H'_{a-m} = -\frac{e^2}{4d_1} + \frac{e^2}{R}. \qquad (3.04)$$

Equation 3.03 describes a n*s* alkali electron which is perturbed by the potential H'_{a-m} When the metal and the adatom are separated by infinite distances the metal is characterized by its work function ϕ and adatom by its *ns* valence level with ionization potential V_i. As the adatom approaches the surface of the metal, mixing of the outer bands occurs and the eigenstate broadens and shifts in energy. The virtual state associated with the adatom ion core has a width Γ and is shifted by ΔE. The first order energy shift due to the interaction of the adatom with the metal is given by

$$\Delta E = \frac{\langle \psi_{n,s} | H'_{a-m} | \psi_{n,s} \rangle}{\langle \psi_{n,s} | \psi_{n,s} \rangle}, \qquad (3.05)$$

and the bandwidth of the alkali adatom electronic level is the product of h and the transition frequency for an electron in the resonant atom-metal state which is given by the Golden Rule[13]

$$\Gamma(x) \approx 2\pi \sum_{\text{deg}} \rho_K |T_{i,f}|^2 \qquad (3.06)$$

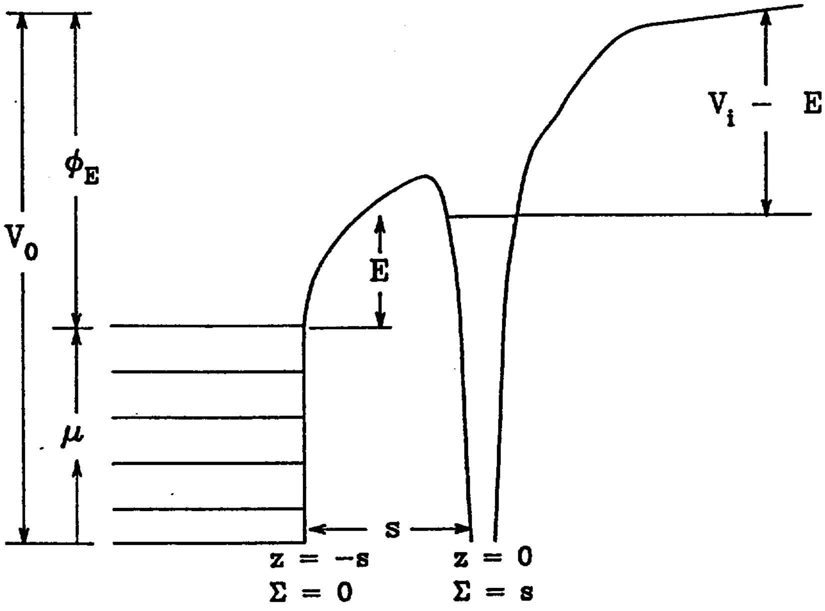

Figure 3.00a. Model for the atom-metal interaction.

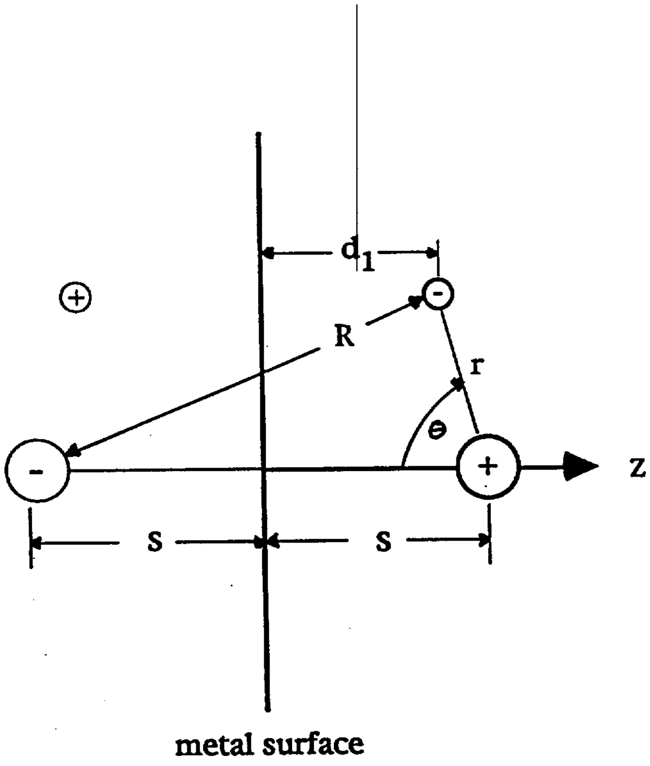

Figure 3.00b. Classic picture of the atom and its image charge induced in the metal.

where ρ_K is the density of states in the metal, $|T_{i,f}|$ is the transition matrix[13] and the summation is over degeneracies of the metal state. It has been shown that an element of the transition matrix may be approximated by

$$T_{i,f} \equiv \left\langle \psi_{n,s} \middle| H'_{m-a} \middle| u_i \right\rangle \qquad (3.07)$$

where u_i is the single-electron wave function and

$$H'_{m-a} = \frac{e^2}{R}. \qquad (3.08)$$

The shift and the natural broadening of the originally discrete *n*s valence level was found to be ~0.3 eV and ≤1.0 eV, respectively. It was noted that the positioning and broadening relative to the conduction band of the metal suggested that ionic bonds were formed between the adsorbate and substrate. This conclusion is discussed by showing the types of bonds allowed between alkali adsorbates and metals and the dipole layer formed.

The wave functions corresponding to two different energies are shown in Fig. 3.01. The waveform ψ_m is for an electron with energy not falling within the range of the broadened and shifted atomic state. This is a sinusoidal wave function inside the metal and a decaying exponential outside the metal with a slight increase in amplitude at the ion core. The second wave function ψ_a, is that which describes an electron with energy falling within the range of the broadened virtual state. This wave function resembles the atomic wave function in the atomic core with considerable amplitude. At the interface, the true wave function is a combination of the overlapping unperturbed atom and the metal wave functions. We also note the position of the ionization potential, V_i of the adatom with respect to the work function of the substrate, ϕ (V_i and ϕ were defined in Fig. 3.00a). The charge state of the adatom depends upon the occupation of the various allowed states. If any of the electrons of the metal and one electron of the adatom are in states similar to ψ_a, then there would be a huge population in the region of the adatom and the broadened virtual state would fall below the Fermi level of the metal (see Fig. 3.02a). The bond in this case would be classified as metallic ($V_i > \phi$) and there would be no charge on the adatom ion core. In this case, the ionization potential would be much greater than the work function of the substrate. The next allowed state is when the broadened level partially

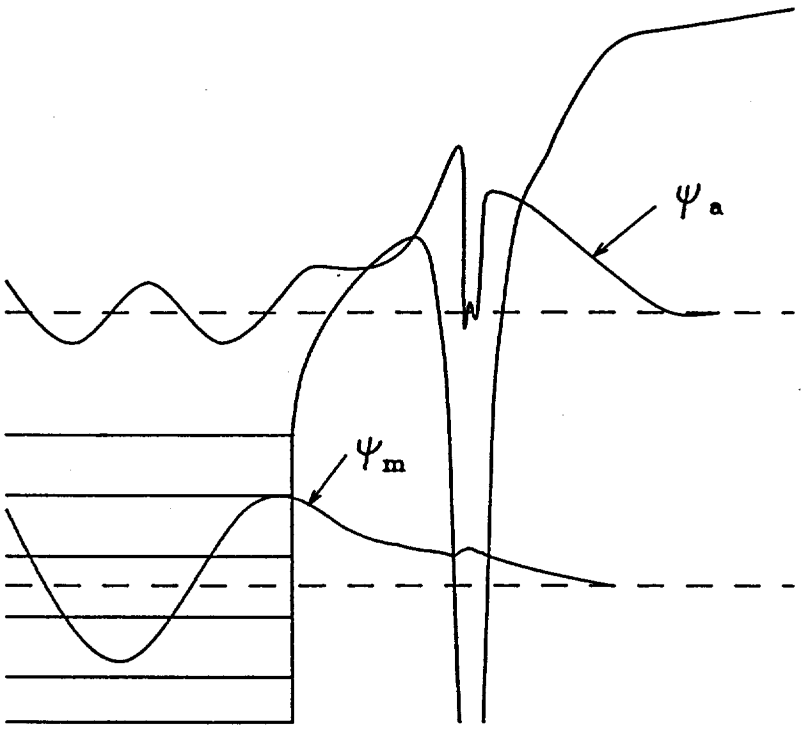

Figure 3.01. Wavefunctions of the electrons. ψ_m is the wavefunction for an electron not within the energy broadened band. ψ_a is a possible wavefunction for an electron in the band.

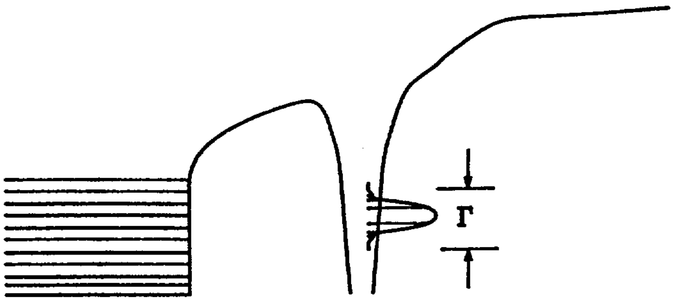

Figure 3.02a. Position for broadened band required for metallic bond

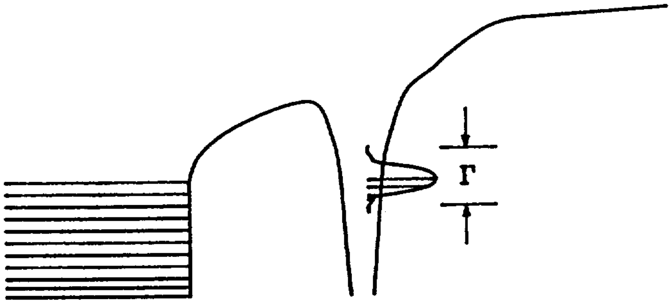

Figure 3.02b. Position for broadened band required for partially metallic-partially ionic bond.

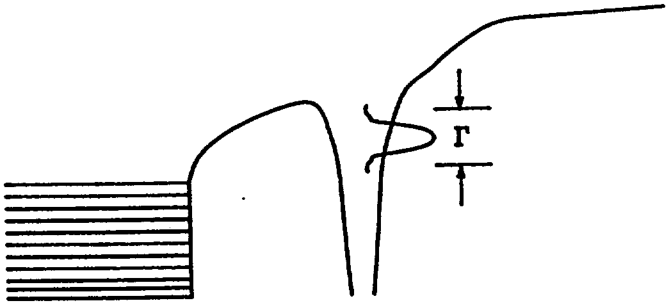

Figure 3.02c. Position for the broadened band required for ionic bond.

overlaps the Fermi level (see Fig. 3.02b). In this state most of the n + 1 electrons are in a state corresponding to the wave function, ψ_m and only partial charge neutralization occurs in the adatom ion core. The bond is classified as partially ionic-partially metallic ($V_i \approx \phi$). The other state occurs when all the occupied electron states are of the form ψ_m and there is no neutralization of the ion core (see Fig. 3.02c). This state is a purely ionic bond between the adatom and the metal and the broadened level is totally above the Fermi level ($\phi > V_i$). Gadzuk justified the ionic bond picture for alkalis from the value of dipole moments for the various allowed states, and he determined that the polar metallic bonds did not provide a sufficient dipole moment for the work function changes that occur from the adsorption of alkalis on metals. The transfer of charge from the atom into the metal is needed to form a strong enough surface dipole.

Although these basic models, in different variations, have been used extensively to approximate the interaction of alkali and alkaline earth metals on transition and other metal surfaces, they haven't completely satisfied the whole scientific community. Recently, several new models have been constructed to resolve the inadequacies found in the basic models described above. It was found that the local approximation to the density-functional theory gave a consistently accurate and realistic description of the electronic structure and energetics of the adsorbate-metal system. One of the most accurate and efficient theoretical and computational approaches to these systems is the linearized-augmented-plane-wave (LAPW) method[14]. It has been demonstrated that this single layer model provides a promising approach to the treatment of the electronic structure of clean surfaces and surfaces with overlayers[15]. Wimmer, *et al.*[16] presented the full-potential-linearized-augmented-plane-wave (FLAPW) method for thin films to eliminate the shape approximations made for the density and potential due to the reduced symmetry and reduced coordination number of atoms at the surface. The local density functional one-particle equations were solved fully self-consistently for FLAPW method. The FLAPW method was illustrated by studying the nature and mechanism of the bonding of cesium on W(100) in the high coverage limit in order to better understand the lowering of the work function and to explain the role of the tungsten surface and resonance states in the adsorption process. The analysis was performed on three thin film slabs: (1) a five layer slab of tungsten, (2) an unsupported cesium monolayer and (3) cesium in a *c*(2×2) structure on both sides of the five layer slab for three different cesium-tungsten separations (2.60, 2.75, and 2.90 angstroms). In this investigation the cesium was found to form a polarized-metallic rather than ionic overlayer. The cesium valançe electrons (6*s*) were found to be polarized toward the tungsten surface which leads to a charge increase at the cesium-tungsten interface and a decrease in charge on the vacuum side of the overlayer. The polarization of the cesium overlayer results in a lowering of the work function and a decrease in the activation energy. The cesium-induced changes in charge density and surface dipole are mostly confined to the region outside the tungsten surface. Although the results of this investigation differ in some aspects from the classic charge transfer theory, the model does introduce some interesting conclusions that have been experimentally verified. Photoemission[17] was used to assess the nature of the interaction between the surface atoms of W(110) and the adsorbates sodium, potassium and cesium for coverages up to 1 monolayer. A study of the shifts in structure of the outermost *p* shell of the adatom and the 4*f* surface atom core level concludes that there is little or no charge transfer from the adatom to the tungsten surface, even at low coverages.

A recent article by Benesh and King[18] criticizes the argument that core level shifting, or the lack of core shifting, of surface substrate atoms induced by adsorption be attributed solely to charge transfer between adsorbate and substrate atoms. An analysis of core level shifts induced by the altering of the coordination of the tungsten atoms by cesium and oxygen indicate that factors such as final state relaxation and environmental effects may be as substantial as those incurred by charge transfer. They concluded that the shifts to higher or lower binding energy due to alkali metal adsorption originate from the cancellation of the environmental shift by charge transfer and final state relaxation shifts together. The authors noted that a recent model using a self-consistent Green's function calculation of an isolated sodium adatom on Al(100)[19] clearly demonstrates that a partially ionized description of the bond is appropriate.

3.1 Work Function

3.1.a General Definition

The characterization of the work function is probably the single most important surface measurement for applications depending on electron emission. The work function represents the potential barrier that occurs at the vacuum/surface interface and is simply defined as the amount of work needed to remove an electron from the metal at 0 K. Due to the variation in structure and composition of surfaces, the work function is directly influenced by the properties of the surface atoms and of the periodicity of the bulk. Any change in the physical makeup of the surface, such as adsorption or surface reconstruction, can be seen in the effect it has on the work function.

The thermodynamic state of an electron in a clean metal can be described by the change in the Helmholtz free energy[20]. The Helmholtz potential is defined as F = U - TS, where U is the energy of the system, T is the temperature and S is the entropy. In the case of a solid with fixed volume and temperature, the change in the Helmholtz potential is known as the electrochemical potential, $\bar{\mu}$ and is given by

$$\bar{\mu} = \left(\frac{\partial F}{\partial n}\right)_{T,v} \tag{3.09}$$

which requires that $(\partial S/\partial n)_{T,v} \rightarrow 0$ as $T \rightarrow 0$. The requirements on equation 3.09 are equivalent to defining the electrochemical potential as the work done to bring an electron from infinity and adding it isothermally to the metal. The work function of the metal, ϕ, can then be defined in electron-volts as

$$\phi = W - \frac{\bar{\mu}}{e} \tag{3.10}$$

where W is the kinetic energy of an electron deep inside the metal would have to overcome to escape into the vacuum. If the chemical potential, μ is defined as the difference in kinetic energy between the electrons at the bottom of the conduction band and the electrochemical potential, then eqn. 3.10 can be rewritten in electron-volts as

$$\phi = \chi - \frac{\mu}{e} \tag{3.11}$$

where χ is the surface potential and is defined as the difference in kinetic energy of an electron inside and outside the metal surface. The chemical potential is dependent on the bulk properties and temperature of the metal while the surface potential depends on the properties of the surface and varies with different crystallographic orientations. Hence, changes in the surface potential, for example by adsorption, can be readily seen in changes in the work function.

In the case of adsorption, a change in work function of the metal occurs due to the modification of the dipole layer at the surface of the metal. The initial dipole moment, M arises from the asymmetric distribution of electrons at the surface compared to the symmetry of the bulk and is oriented normal to the surface. The adsorption of an additional layer of charges either reduces or increases M depending on the charge of the adsorbate and results in changes in the surface potential. The change in the work function of the surface is equal to the change in surface potential if σ is defined as the number of dipoles per unit area and can be given by

$$\Delta\phi = \Delta\chi = \pm 4\pi\sigma\mu_e \tag{3.12}$$

where μ_e is the effective dipole moment of the charged layer and is equal to the product of the charge of the adsorbate and the distance between the charged layers. If the coverage is given as $\theta = \sigma/\sigma_0$ then eqn. 3.12 can be rewritten as a function coverage,

$$\Delta\phi = \pm 4\pi\theta\sigma_0\mu_e\,, \tag{3.13}$$

where σ_0 is the number of adsorption sites.

Equations 3.12 and 3.13 have been used extensively to relate experimentally measured work function changes to the physical changes in the electronic structure of a metal surface in terms of bonding mechanisms. The accurate prediction of change in work function due to adsorption and calculation of work functions given crystallographic orientations from first principles have yielded poor results, so several analytical models have been developed to predict the work functions of metal surfaces.

3.1.b Jellium Model

One of the more popular models devised to deal with the electronic properties of simple metal surfaces is known as the "jellium" model. In simple metals the conduction electrons are scattered only weakly from the screened ion core pseudopotentials, hence the jellium model can approximate this situation by replacing the discrete ion cores with a uniform, positive background charge density equal to the average ion charge distribution given by,

$$n_M^+(\mathbf{r}) = \begin{cases} n_M, & x \leq 0 \\ 0, & x < 0 \end{cases}, \tag{3.14}$$

where n_M is related to the effective radius of the valence electrons by $4\pi r_s^3/3 = 1/n_M$.

Lang[21] described the electronic structure of the metal surface solving the jellium model fully and self-consistently based on the theory of an inhomogeneous electron gas developed by Honhenberg, Kohn and Sham[22,23]. In Ref. 22 and 23, it is shown that the total electronic ground state energy for the many-electron system in an external potential $v(\mathbf{r})$ can be written in the following form:

$$E_v[n] = \int v(r)n(r)dr + \frac{1}{2}\iint \frac{n(\mathbf{r})n(\mathbf{r}')}{|\mathbf{r}-\mathbf{r}'|}d\mathbf{r}d\mathbf{r}' + T_s[n] + E_{xc}[n], \tag{3.15}$$

where the first term is the ion-electron interaction, the second term is the average electrostatic potential energy of the electrons and $T_s[n]$ is the kinetic energy of the non-interacting inhomogeneous electron gas in its ground state with charge density $n(\mathbf{r})$. The correlation-exchange term, $E_{xc}[n]$, represents all of the quantum mechanics of the many-body problem. By writing the total ground state energy in this form, the effective potential can be defined as

$$v_{eff}[n;\mathbf{r}] = v(\mathbf{r}) + \int \frac{n(\mathbf{r}')}{|\mathbf{r}-\mathbf{r}'|}dr + v_{xc}[n;\mathbf{r}], \tag{3.16}$$

where $v_{xc}[n;\mathbf{r}] \equiv \dfrac{\delta E_{xc}[n]}{\delta n(\mathbf{r})}$. The practical implementation of the this problem requires a good approximation of this quantity. The local density approximation (LDA) has been found to successfully approximate correlation-exchange potential. The advantage of this formulation is that the exact density distribution for a system with *N* interacting electrons can now be found for the equation

$$-\frac{1}{2}\nabla^2\psi_i(r) + v_{eff}(\mathbf{r})\psi_i(\mathbf{r}) = \varepsilon_i\psi_i(\mathbf{r}) \tag{3.17}$$

where $n(\mathbf{r}) = \sum_{i=1}^{N} \left|\psi_i(\mathbf{r})\right|^2$ and ψ_i are the N lowest lying orthonormal solutions. Using the above results, the energy of the system, $E_v[n]$, can now be found from eqn. 3.15, given

$$T_s[n] = \sum_{i=1}^{N} \varepsilon_i - \int v_{eff}[n;\mathbf{r}]n(\mathbf{r})d\mathbf{r}. \tag{3.18}$$

In the presence of the surface the above formulation changes due to the formation of a finite potential barrier at the surface defined in terms of the work function, ϕ. The work function is simply defined as the difference in potential energy between an electron just outside the surface of the metal and one deep inside the bulk (Fig. 3.03). The electrostatic potential energy difference of an electron between x = +∞ and x = -∞ defined as $\Delta\phi$, is given by Poisson's equation

$$\Delta\phi \equiv \phi(+\infty) - \phi(-\infty) = 4\pi \int_{-\infty}^{\infty} x\left[n(x) - n_M^+(x)\right], \tag{3.19}$$

and the chemical potential, μ, defined as the ground state energy difference of the n+1 and n electrons is given by $\mu = \phi(-\infty) + \bar{\mu}$ where $\bar{\mu}$ is the intrinsic chemical potential of the metal. From its definition, $\bar{\mu}$, is given by

$$\bar{\mu} = \frac{1}{2}\kappa_F^2 + \left(\frac{\delta E_{xc}[n]}{\delta n}\right) \equiv \frac{1}{2}k_F^2 + \mu_{xc}(n_M) \tag{3.20}$$

where κ_F is the Fermi momentum of a electron gas of density n_M and $\mu_{xc}(n)$ is the exchange-correlation part of the uniform gas of density n. If the exchange-correlation energy per particle is denoted by $\varepsilon_{xc}(n)$, then

$$\mu_{xc}(n) = \frac{d}{dn}\left[n\varepsilon_{xc}(n)\right]. \tag{3.21}$$

Now, the work function can be defined as the potential energy change due to the difference across the dipole layer minus the exchange-correlation potential and the kinetic energy at κ_F

$$\Phi_\mu = \Delta\phi - \bar{\mu}. \tag{3.22}$$

The model is made more realistic by taking into account the effect of each metal ion on the conduction band electrons and is represented by a pseudopotential. Lang[24] refers to this as the ion-lattice model in which the effect of each metal ion on the conduction electrons is represented by a pseudopotential. The replacement

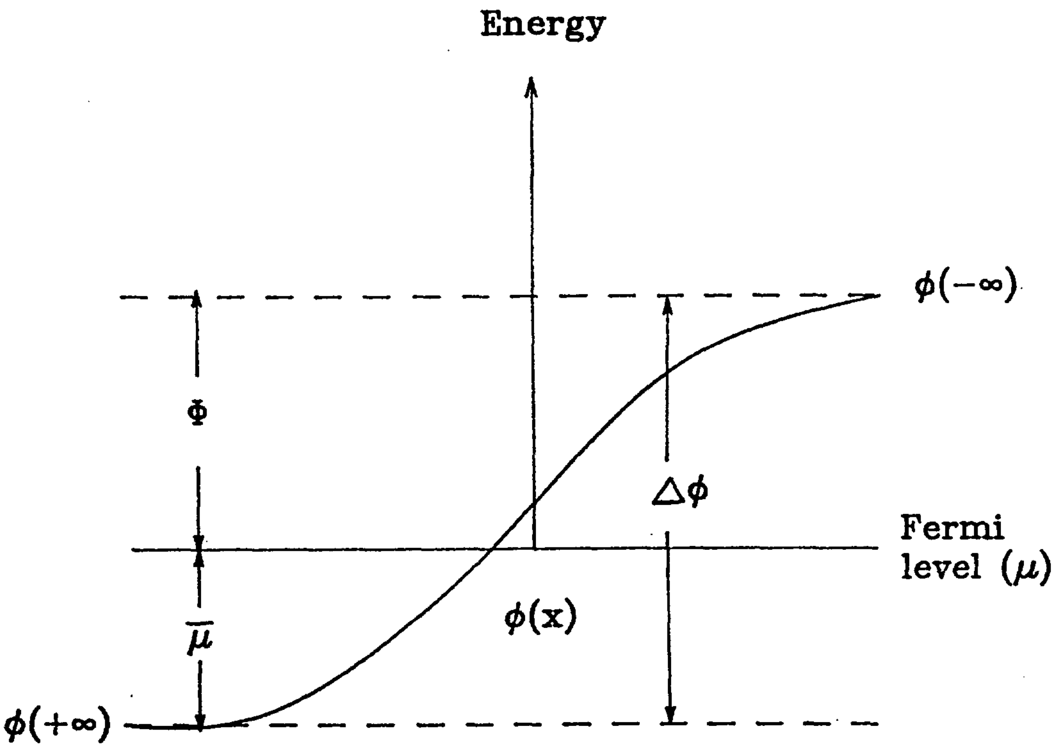

Figure 3.03. The various energies relevant to the study of the work function of a metal.

pseudopotentials are represented by small perturbations, $\delta v(\mathbf{r})$, and are solved by standard perturbation theory to yield small changes in the work function,

$$\delta\Phi = \int \delta v(\mathbf{r}) n_s(\mathbf{r}) d\mathbf{r}\,. \qquad (3.23)$$

The surface charge density $n_\sigma(\mathbf{r})$ is calculated for the uniform background model with one electron removed from the metal. The electron deficiency is localized near the surface and causes a small finite field outside the surface. Thus, $n_\sigma(\mathbf{r})$ corresponds to the difference in the densities for a neutral metal with a vanishing field outside and a metal with a small surface charge and finite field outside. Equation 3.22 is rewritten to account for these small changes and now represents a more accurate work function measurement,

$$\Phi = \Phi_\mu + \delta\Phi\,. \qquad (3.24)$$

The general features of this approach are given in Fig. 3.04. The model does include the anisotropies that occur for the work function of different crystal faces. The lowest work function was found on the least densely packed surface which is the (110) for fcc and (111) for the bcc crystal surface. This agrees well with the theory presented by Smoluchowski[25] and with experimental results. Lang used the above formulation to compute the theoretical work functions for simple metals and a few noble metals. The results in Fig. 3.04 agree reasonably well with experimental values for the simple metals but are 15-30% low for the noble metals, hence, the method is satisfactory for simple metals but is less appropriate for metal surfaces with higher electron densities and work functions such as transition metals. The method may not be suitable for all surfaces but it has been found useful for understanding the fundamental aspects of metal surface electronic structure.

Lang[26] extended the jellium model to describe the work function change induced by the adsorption of alkali metals by applying a self-consistent quantum-mechanical analysis of the model to a metallic substrate-adsorbate system. In this model the ionic charge of the adsorbate layer is replaced by a homogeneous positive slab of thickness d and density $n_A^+(\theta)$ adjoining the substrate background. The total positive background for the adsorption model is

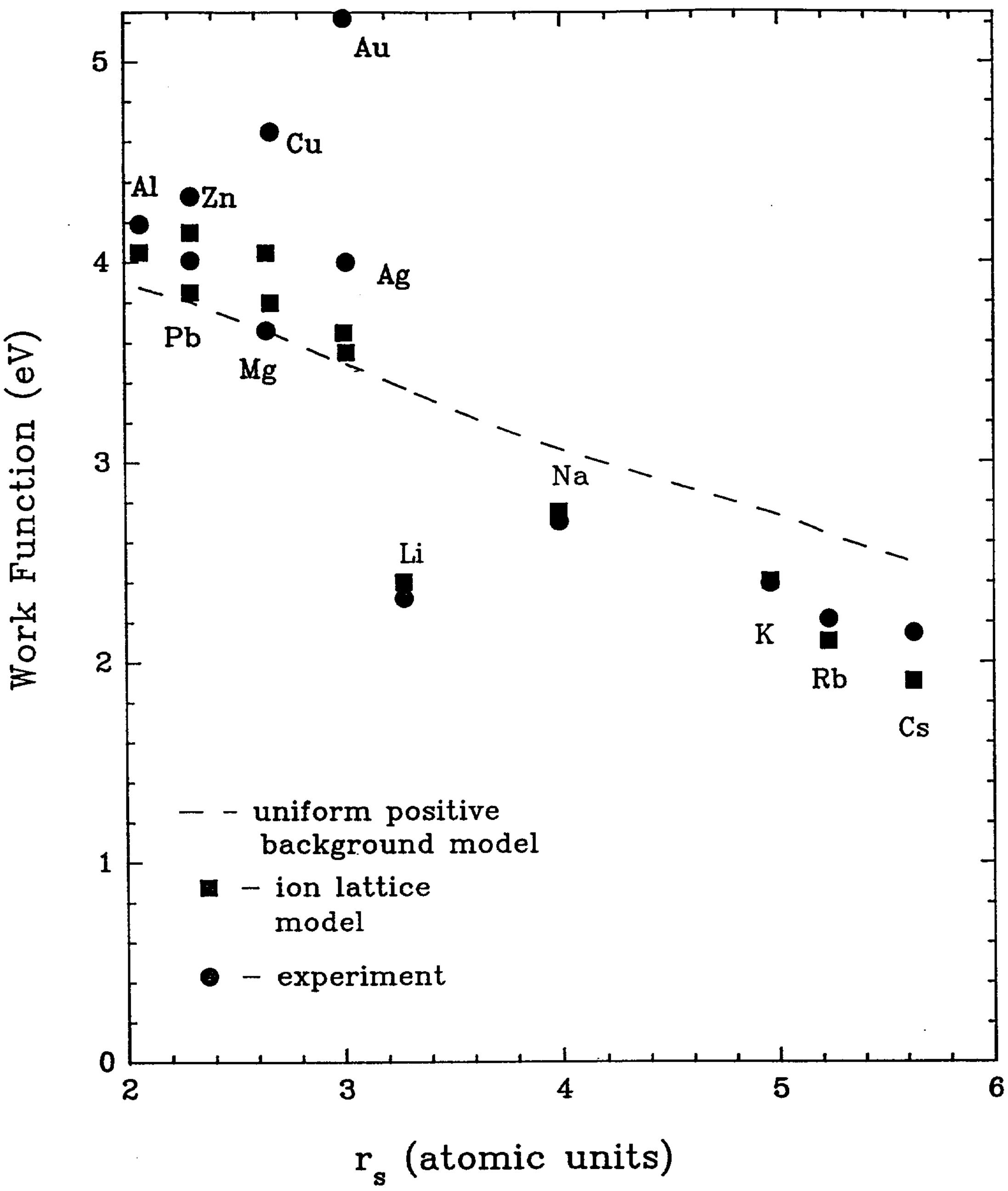

Figure 3.04. Comparison of theoretical values of the work function with the results of experiments on polycrystalline samples. [Ref. 24]

$$n_A^+(x,\theta) = \begin{cases} n_M^+ & , \quad x \le 0 \\ n_A^+(\theta) = \theta n_A & , \quad 0 < x \le d \\ 0 & , \quad x > d \end{cases} \qquad (3.25)$$

where θ is the coverage of the adsorbate on the metal surface ($\theta = 1$ for a monolayer), n_A the bulk density of the adsorbate and x the distance from the center of the adatom to the substrate surface. Since the alkalis are monovalent, $N = d(\theta n_A)$, where N is the number of adatoms per unit area. Changes in N could be represented by changes in either n_A or d, or both. In this model, d is fixed for each adatom and n_A is allowed to change. For high coverages, the d value is set equal to the spacing of the most densely packed lattice plane in the bulk adsorbate and closer to the ionic diameter of the adsorbate at low coverages. The electron density was computed self-consistently with and without an adsorbate layer as shown in Fig. 3.05 and value of the work function versus N was calculated for $d = d_{Cs}$ and $d = d_{Na}$ as shown in Fig. 3.06. The curves show a work function versus coverage curve characteristic of alkali and alkaline earth metals. In order to verify the results of this theory, Fig. 3.06 also contains the work function versus adatom concentration for cesium on Nb(110). Although the results can not be compared directly, the curves shown in Fig. 3.06 do suggest the uniform background model is somewhat representative of alkali adsorption on metal surface. It is suggested by this model that in the coverage region below the minimum work function the adlayer is not fully metallic and some charge transfer takes place. After the minimum work function, a transition takes place in which the adlayer becomes more metallic in nature and develops properties similar to those of bulk adsorbate material. The model is inappropriate for low coverages, but can be used for coverages high enough for the adatom wave functions to appreciably overlap with each other, although it has shown that reasonable results are still obtained at low coverages for the work function due to adsorption. The model is also not meant for transition metal substrates, but does give a reasonable approximation for the work function versus coverage curve and other adsorbate properties, such as electron densities and dipole moments.

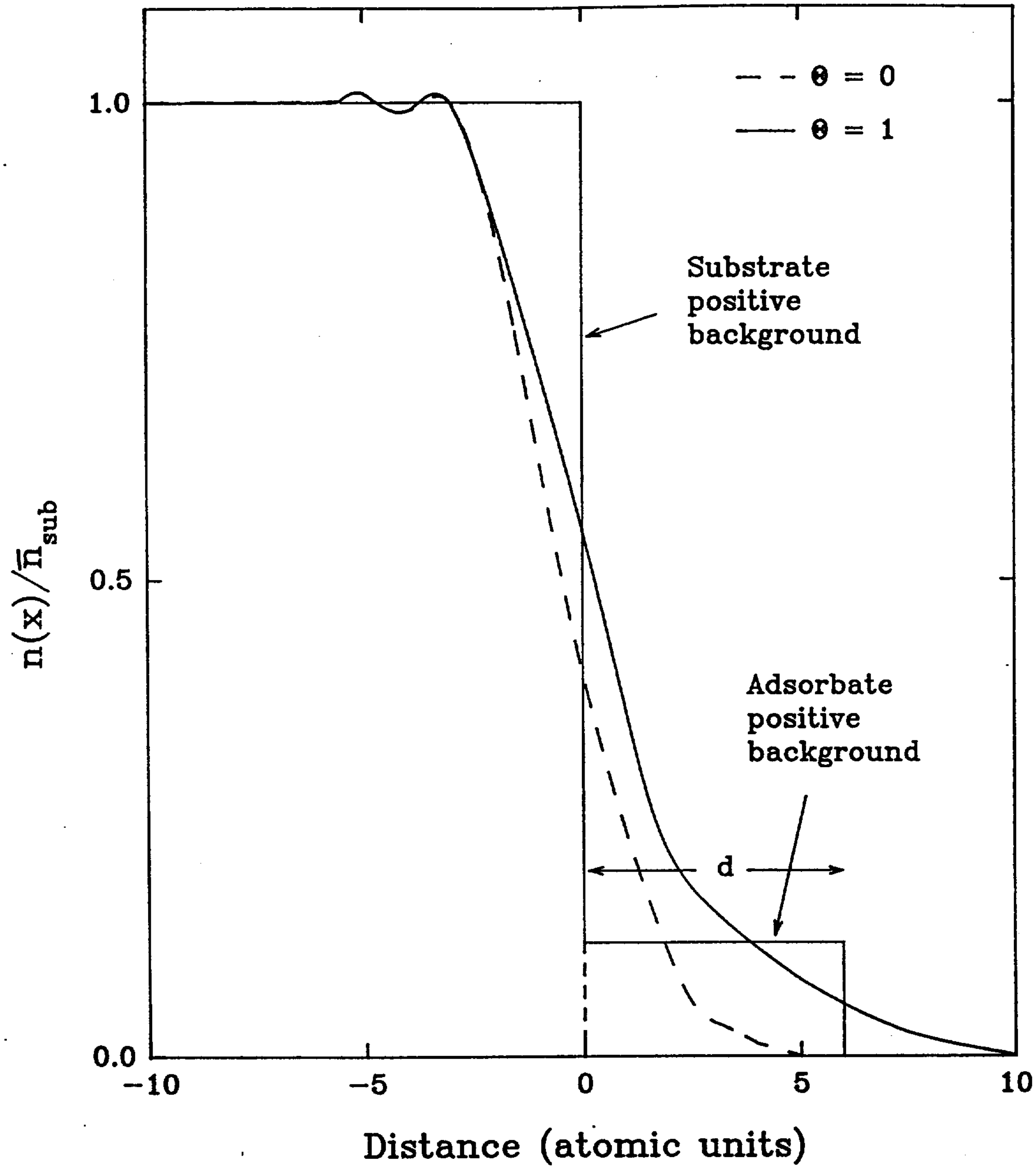

Figure 3.05. Electron density distributions for the uniform background model of alkali adsorption on a high work function metal surface.

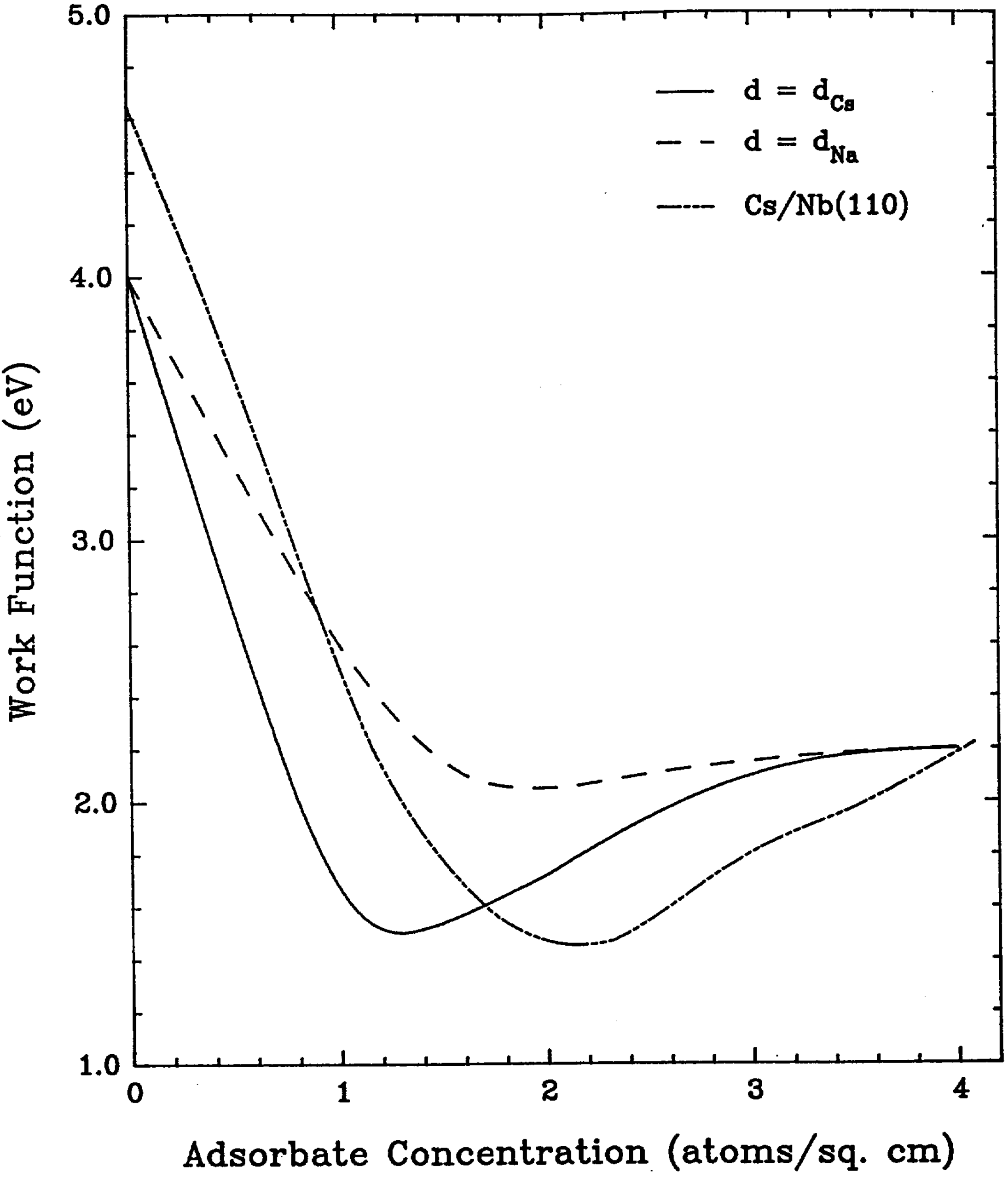

Figure 3.06. Calculated work function curves for Na and Cs on the uniform background model compared to the actual work function curve measured for Cs on Nb(110).

3.1.c Steiner-Gyftopoulos Theory

Steiner and Gyftopoulos[27] (SG) proposed an empirical correlation for the work function of pure uniform surfaces of various metals of different crystallographic orientation. To justify this correlation, the metal is interpreted approximately as a collection of individual perturbed atoms which are thermodynamically equal to the whole metal. Accordingly, the value of the chemical potential of each atom must be the same as the chemical potential of the metal. The work function of a metal is equal to the negative of the chemical potential with respect to the points just outside the surface, and therefore the work function must be equal to the negative of the chemical potential of an atom on the surface. The work function is identified as the negative of the chemical potential of the surface atom or the "electronegativity" of this atom.

The electronegativity of an atom can be expressed in terms of the energy state of the electrons in its valence orbitals. If the energy state is neutral, the valence orbital energy is zero, if ionized, the energy is eI, and if doubly ionized, the energy is -eI, where I and A are the ionization potential and electron affinity of the orbital, respectively. The atom energy can be represented in terms of the valence electrons and characterized by the fractional charge, q in that orbital. The energy of the orbital can be approximated by the second order equation[28]

$$E(q) = \frac{I+A}{2}q + \frac{I+A}{2e}q^2. \qquad (3.26)$$

The orbital electronegativity represents the energy per valence electron when the charge of the orbital is q and is defined by the relation

$$x(q) = \frac{dE(q)}{dq} = \frac{I+A}{2} + \frac{I+A}{e}q \qquad (3.27)$$

In other words, the electronegativity is the work required to remove a valence electron without altering the energy state of the atom. From the works of Gordy[29] and Pritchard and Skinner,[30] SG proposed that the electronegativity can be computed from the extension of the atoms of a surface to the correlation derived for molecules. In Ref. 27 , the electronegativity of a neutral atom in a molecule is approximated by the relation

$$x(0) = 0.98\left(\frac{v+1}{r}\right) + 1.57 \text{ eV} \qquad (3.28)$$

where v is the number of electrons per atom which participate in bonding and r is the effective radius (in angstroms) of the atom in the bonded state. SG assumed that eqn. 3.27 would apply to the atoms on a surface of a metal and used the following relation to predict the bare work function:

$$\phi = x(0) = 0.98\left(\frac{v_s + 1}{r_m}\right) + 1.57 \text{ eV} \qquad (3.29)$$

where v_s is the surface valence which is equal to the number of electrons per surface atom to participate in bonding and r_m is the effective size of the surface atom in angstroms. The results of this model are consistent with other models and yield work functions reasonably close to experimental values, and like the jellium model the close-packed surfaces give the highest work functions.

The model devised by SG was extended to bi-metal adsorption systems[31]. The extension of this model was based on the assumption that each substrate atom in a bi-metal adsorption system was characterized by a neutral electronegativity that was different from that of a pure metal surface. In their discussion, SG proposed that the bonds formed between the adsorbate and substrate atoms are chemical in nature. The assumption suggests that the bonds arise from the pairing of valence electrons of atoms on the surface. They further characterize that bond as being both purely covalent (pairing of valence electrons between neighboring adsorbate atoms) and partially ionic and partially covalent (pairing of valence electrons between the adsorbate and substrate atoms). The adsorbate-adsorbate interaction leads to an overlap charge, Q, while the adsorbate-substrate bond leads to a charge transfer, F, along with some overlap charge, Q_1. The perturbed neutral electronegativity of the substrate atoms was taken as a linear function of the charge transfer and the overlap charge. The overlap charge was assumed to be proportional to a Morse function[32] similar to that used to describe the binding energy of like atoms in molecules or solids. The amount of charge transfer was computed so that the adsorbate-substrate bond energy was maximum. The revised model leads to a direct relationship for the work function and the desorption energy versus adsorbate coverage.

In an earlier discussion, the work function of the bare metal surface was taken as the electronegativity of the valence electrons of the surface atoms. The bi-metal work function can also be described by the electronegativity of the substrate atoms, but now it is perturbed by the adsorbate atoms. These perturbations are introduced by the substrate-adsorbate and the adsorbate-adsorbate interactions. The adsorbate-substrate interactions result in the formation of a dipole layer at the surface proportional to the charge transfer, F. The dipole layer introduces some potential onto the electronegativity of the surface atoms. The overlap charge, Q_1, associated with the substrate-adsorbate interaction does not introduce any perturbation because covalent bonding between atoms does not effect the relative electronegativity of the bonding atoms[28]. The overlap charge associated with the adsorbate-adsorbate interaction, does however give rise to a potential (proportional to Q) which effects the electronegativity of the surface atoms. Hence, the work function of the bi-metal system is the sum of the two perturbations, proportional to Q and F, and the electronegativity of the surface atoms given by the following equation

$$\phi = \phi_s + cQ + bF \tag{3.30}$$

where ϕ_s is the work function of the bare surface and c and b are proportionality constants. When there is zero coverage the factors cQ and bF are equal to zero and eqn. 3.30 satisfies the boundary condition $\theta = 0$, $\phi = \phi_s$. It is also required that at a monolayer of adsorbate coverage $\phi = \phi_f$, where ϕ_f is the bare work function of the adsorbate.

The perturbation cQ was found to be equal to the following equation

$$cQ = -(\phi_s - \phi_f)M, \tag{3.31}$$

where M is the Morse function[32] that is assumed to be proportional to the overlap charge Q. The Morse function is given by the following relation

$$M = 2\exp[-a(d - d_0)] - \exp[-2a(d - d_0)], \tag{3.32}$$

where a is a constant of the adatoms and d and d_0 are the average distance between adatoms at coverages θ and at a monolayer, respectively. For a square array of adatoms, d can be expressed in terms of d_0 and θ by the relationship

$$d = d_0\theta^{-1/2}. \tag{3.33}$$

Now eqn. 3.32 can be rewritten as

$$M = 2\exp\left[-ad_0\left(1 - \theta^{-1/2}\right)\right] - \exp\left[-2ad_0\left(1 - \theta^{-1/2}\right)\right] \tag{3.34}$$

with $\theta = 0$, M= 0 and at $\theta = 1$, M = 1. The constant a is not known for most adsorbates on bare metal surfaces but because d_0 approaches the interatomic separation of the bulk adsorbate at $\theta = 1$, plots of M versus θ yield an average value of $ad_0 = 2.97$. However, the work function is not sensitive to this value because of the compensating effects of the Morse function on both of the perturbations cQ and bF.

The solution to the perturbation bF is somewhat more involved and will only be outlined in this paper. The complete solution can be found in the Ref. 31. The charge transfer results in a surface dipole layer with the following electrostatic potential

$$bF = -2\pi\sigma_f\theta\mu\,, \qquad (3.35)$$

where σ_f is the number of adsorbate atoms per unit area at a monolayer of coverage and μ is the effective dipole moment per adatom. For a specific geometrical arrangement of the adsorbate on the substrate, μ is given by the following relation

$$\mu = \frac{Fv_f R\cos\beta}{\left(1+\alpha/R^3\right)\left(1+9\alpha\sigma_f^{3/2}\theta^{3/2}\right)}\,, \qquad (3.36)$$

where F is the amount of charge transferred per bonding electron of the adatom, v_f is the number of bonding electrons per adatom, R is the sum of the atomic radii of the substrate atom and an adatom, α is the polarizability of the substrate-adsorbate bond and

$$\cos\beta = \left[1 - \frac{1}{2\sigma_s R^2}\right]^{1/2} \qquad (3.37)$$

for a square array of substrate atoms. The cosβ can be computed for each type of substrate orientation. The two factors in the denominator of eqn. 3.36 are the self-depolarization[33] and the dipole-dipole depolarization[34], respectively. The quantity v_f equals one for alkali metals and equals one-half the metallic valence for other metals. The polarizability is the sum of the polarizabilities of the adsorbate and the substrate, where $\sigma_i = nr_i^3$ for i = s or f . The subscripts s and f represent the atomic radii associated with the substrate and adsorbate and n is the coefficient representing the effect of the electronic shell structure. For alkali metals n =1 and for alkaline earth metals n = 1.65.

Using the above definitions eqn. 3.35 can now be rewritten to yield the coefficient b as follows

$$b = \frac{0.905 \times 10^{-6} \nu_f \sigma_f \theta R \cos\beta}{\left(1+\alpha / R^3\right)\left(1+9\alpha\sigma_f^{3/2}\theta^{3/2}\right)} \text{ eV/electron,} \tag{3.38}$$

where R is in cm, α is in cm^3 and σ_f is in $atoms/cm^2$.

The amount of charge transferred between the adsorbate and the substrate is computed so that the corresponding bond energy is maximized with respect to F. The bond energy is considered the sum of the ionic and covalent contributions and approximated by the following relation[35]

$$\begin{aligned} D = D_0\left(1-F^2/e^2\right)^{1/2} + {kF^2}\!\Big/\!{R} + \left(\frac{I_s+A_s}{2} + cQ - \frac{I_f+A_f}{2}\right)F \\ - \left(\frac{I_s-A_s}{2} + \frac{I_f-A_f}{2e}\right)F^2, \end{aligned} \tag{3.39}$$

where D_0 is the energy of the purely covalent bond, I_i and A_i (for i = s or f) are defined earlier, k is a coefficient less than or equal to one and e is the charge of the electron. The first term is the covalent bonding term associated with the overlapping of the bonding orbitals. The second term is due to the electrostatic potential between the charged adsorbate and substrate atoms. The third and forth terms account for the energy variations associated with charge transfer between bonding orbitals. The charge transfer is simply the integral solutions of orbital energy at some charge, which is equal to the electronegativity of the adsorbate and substrate, from -F to zero and from F to zero. The energy is maximized with respect to F when dD/dF = 0 and given by

$$F\!\Big/\!e = \frac{(\phi_s - \phi_f)(1-M)}{\left(D_0\!\Big/\!e\right)\left(1-F^2\!\Big/\!e^2\right)^{-1/2} + D_1} \tag{3.40}$$

using the eqn. 3.31 and the relations

$$\phi_s = \frac{I_s+A_s}{2}, \quad \phi_f = \frac{I_f+A_f}{2} \tag{3.41}$$

and

$$D_1 = I_s - A_s + I_f - A_f - 2ke\!\Big/\!R\,. \tag{3.42}$$

The energy, D_0, of a single purely covalent bond is found using equation

$$D_0 = \left(\lambda_f \lambda_s\right)^{1/2} S_{fs}\!\Big/\!V_f\,, \tag{3.43}$$

where S_{fs} is the angular strength of the adsorbate and substrate valence electrons and λ_s and λ_s are the heats of sublimation for the adsorbate and substrate, respectively. Equation 3.40 could be solved for F as a function of θ if the value of D_1 is known for the particular bi-metal system. The parametet D_1 is of the order of 1.0 eV and can be estimated several ways. First, D_1 can simply be adjusted to fit the ϕ versus θ experimental data curve. Secondly, D_1 can be estimated by assuming the coefficient k is equal to unity and using the following equations

$$I_s - A_s = c_1\phi_s, \quad I_f - A_f = c_1\phi_f \quad \text{and} \quad c_1 = 1.3 \tag{3.44}$$

This method usually yields a good initial estimate but there is no physical significance assigned to this method. The value of c_1 may have to be adjusted by as much as ±10% to improve the agreement between theoretical and experimental data curves. Finally, D_1 could be determined if the energy band structures of the adsorbate and substrate are known, provided k is equal to 0.5. From the above methods for determining D_1, it should be noted that D_1 is a adjustable parameter that can effect how the theoretical ϕ versus θ curve compares to the actual experimental data. Figures 3.07 and 3.08 show how the SG formalization compares to experiment for the adsorbates and substrates used in this investigation. Both figures show that both theory and experiment agree fairly well.

3.2 Thermionic Emission

If the temperature in a metal is raised, the kinetic energy of some of the electrons is increased. If the temperature is high enough electrons may even have a enough kinetic energy normal to the surface to surmount the work function barrier and escape. The emission thermally excited electrons is known as thermionic emission. This section defines the saturation electron current density characteristic of a pure uniform surface of an emitter in a steady state. Steady state conditions are such that the electrons in the metal are in mutual stable equilibrium with the electrons outside the metal and that outside the metal the perfect gas approximation is valid.

In equilibrium, the electrons of a metal follow the Fermi-Dirac statistics and occupy a wide range of energy states with a probability of occupancy given by

$$f(\varepsilon) = \left\{ \exp\left[\frac{\varepsilon - \mu}{kT}\right] + 1 \right\}^{-1} \tag{3.45}$$

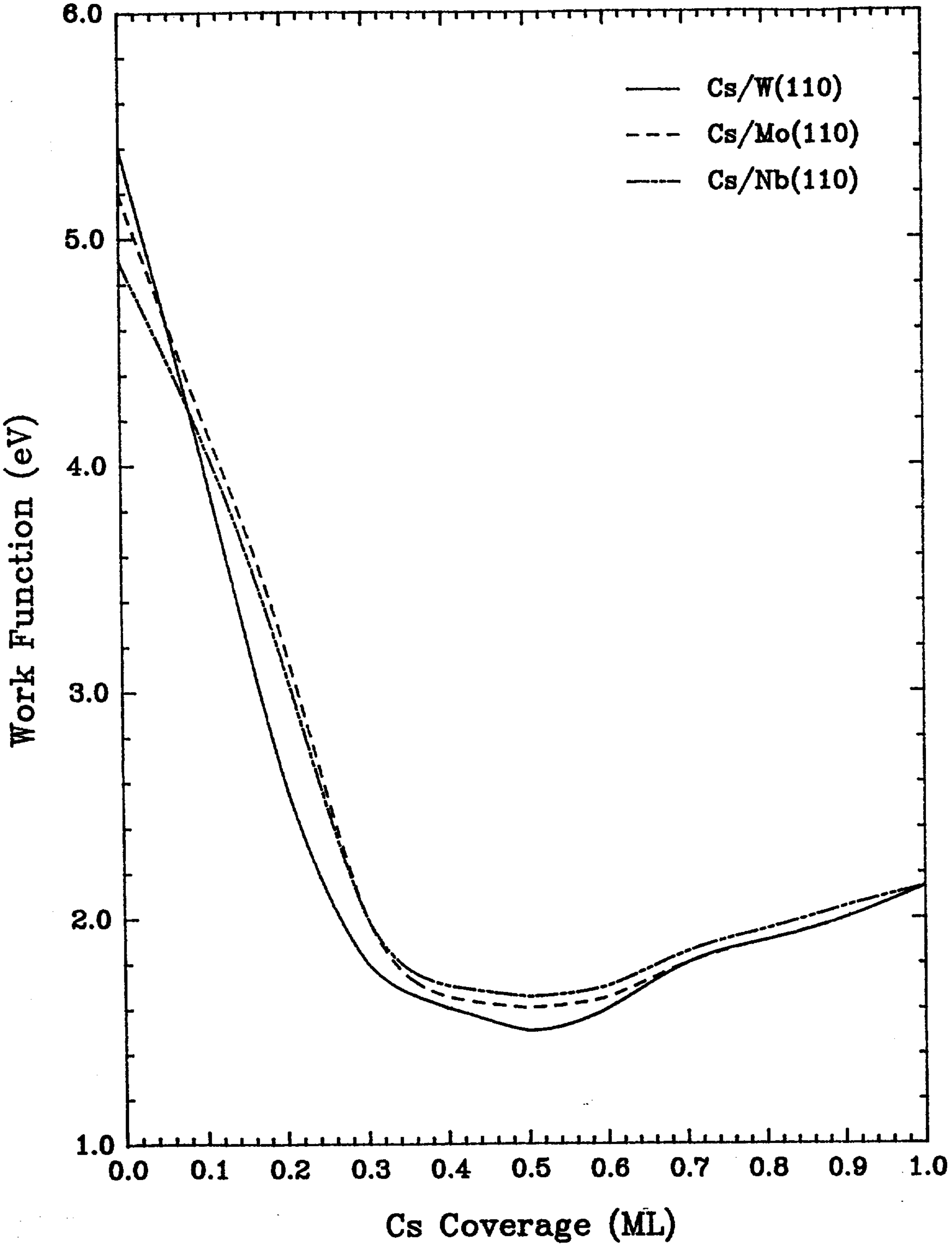

Figure 3.07. SG theoretical work function versus cesium coverage.

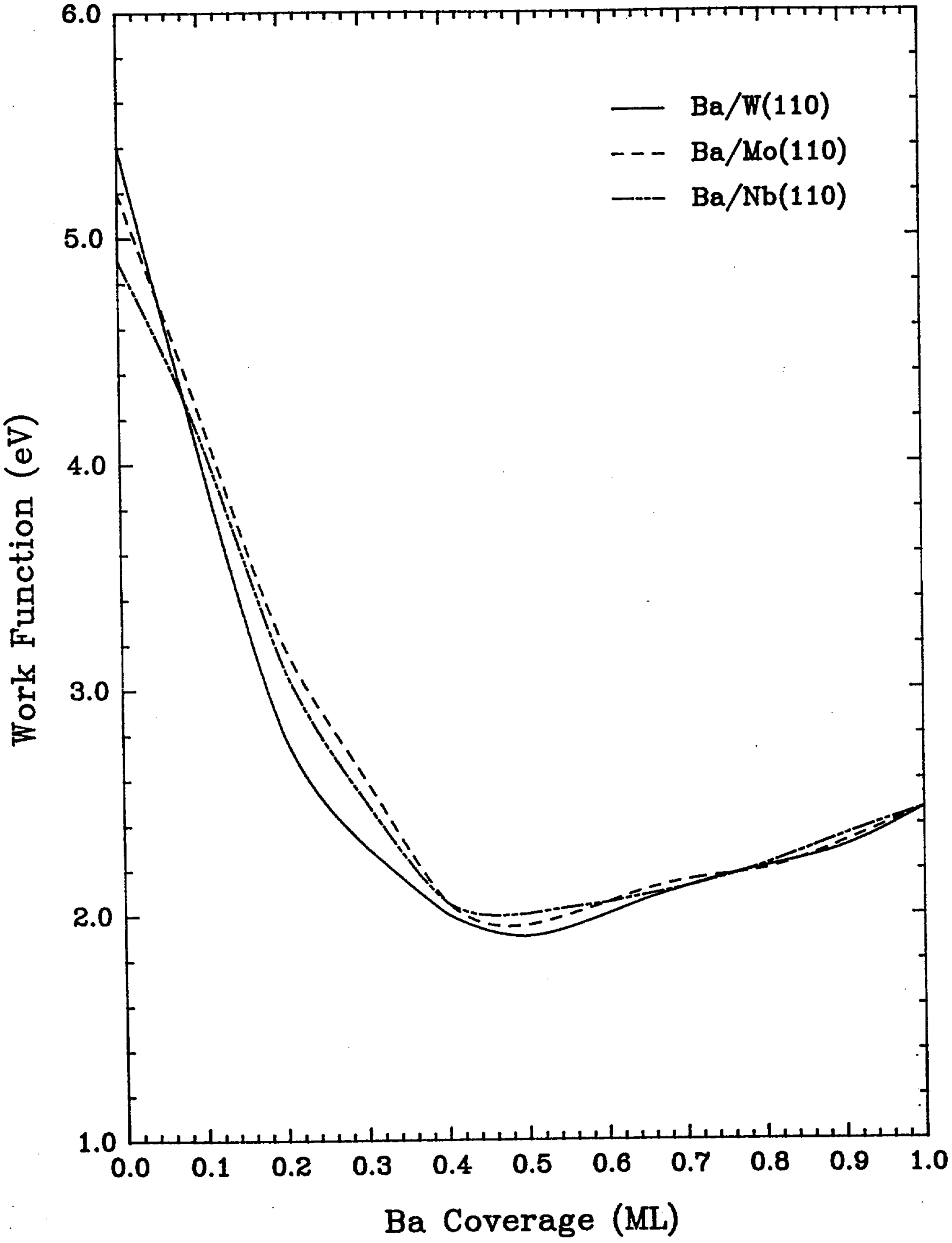

Figure 3.08. SG theoretical work function versus barium coverage.

where μ the chemical potential or Fermi energy, ε_F, of the metal. Figure 3.07 shows how the distribution function varies with temperature. At T = 0 K, all the states for which $\varepsilon \leq \mu$ will be filled and all the states in which $\varepsilon > \mu$ will be empty. When the temperature is above 0 K, the states with $\varepsilon > \mu$ will have a finite probability of occupancy and the sharp boundary between the occupied and vacant states fades. However, the electron gas in the metal remains degenerate even at high temperatures, in other words, most of the electrons are in states in which $(\varepsilon - \mu)/kT < 0$ and $f(\varepsilon)$ is close unity. It can also be shown using eqn. 3.45 that the Fermi level shifts slightly lower as temperature rises. For the electrons with energy $(\varepsilon - \mu) >> kT$, the number one in eqn. 3.44 can be dropped and eqn. 3.45 becomes the Maxwell-Boltzmann distribution,

$$f(\varepsilon) = \exp\left[\frac{\mu - \varepsilon}{kT}\right]. \qquad (3.46)$$

Figure 3.03 shows that for all metals the Fermi level lies below the zero energy vacuum level by an amount of energy equal to the work function. This means that the electrons emerging from the metal must overcome a potential barrier and only the electrons with a sufficient velocity component perpendicular to the surface can escape.

To find the thermionic emission current from a metal into the vacuum, it is necessary to calculate the flux of electrons incident on the surface from with in the bulk having sufficient enough energy to overcome the potential barrier. This can be found from the following summation

$$j = \sum_{i}^{\varepsilon_i > V_0} e v_i f(\varepsilon_i)(1 - r_i) \qquad (3.47)$$

where r_i is the quantum-mechanical electron reflection coefficient for the surface barrier and v_i is the velocity component perpendicular to the surface. Calculating the thermionic emission using eqn. 3.47 is difficult because the electron velocities and the density of states near the surface are not always known. Also, collisions between the fast electrons and the enormous number of slow electrons in the metal alters the one electron approximation. However, if the metal-vacuum interface is in thermodynamic equilibrium, the electrons in the metal and vacuum should have the same temperature

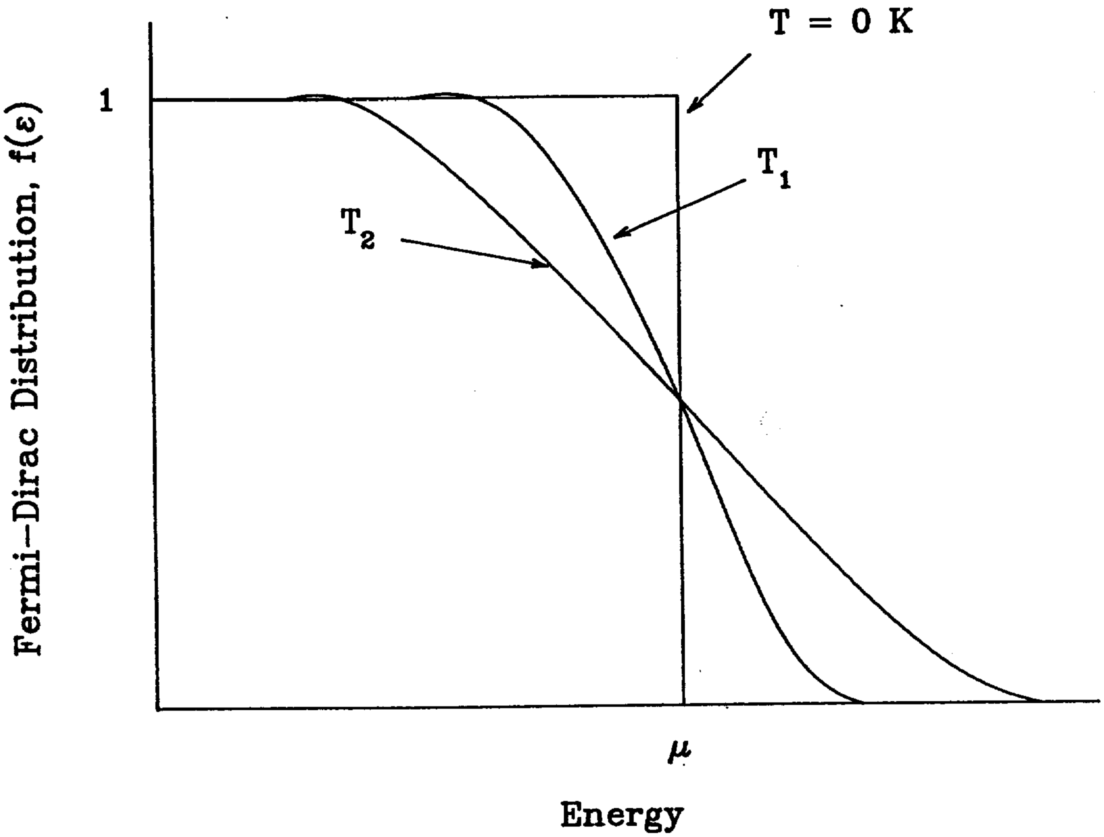

Figure 3.09. Fermi-Dirac distributions for different temperatures (T1 < T2). μ represents the Fermi level.

and chemical potential. Now, rather than calculating the current from the metal into the vacuum, the current from the vacuum to the metal is calculated by

$$j = e\int_{V_0}^{\infty} f(\varepsilon)d\varepsilon \,. \qquad (3.48)$$

Since only the electrons incident normal to the surface are of interest, the solution to eqn. 3.48 is found by substituting eqn. 3.47 into eqn. 3.48 and setting $\varepsilon_n = (mv_n)^2/2m$. Finally, eqn. 3.48 can be rewritten as

$$j = \frac{2em^3}{h^3}\left[1 - r(v_n)\right] \cdot \exp(\mu / kT) \int_{V_0=0}^{\infty} v_n \exp\left[-(mv_n^2)/2kT\right] dv_n \qquad (3.49)$$

where the factor $2(m/h)^3$ is the number of quantum-mechanical states per unit volume. Integration of eqn. 3.49 yields the well known Richardson-Dushman equation

$$j_s = AT^2(1-\bar{r})\exp\left[\frac{-\phi}{kT}\right] \qquad (3.50)$$

where $\phi = -\mu$, and $A = 4\pi emk^2/h^2 = 120.4$ amp/(cm^2-deg^2). The factor $1 - \bar{r}$ is the average reflection coefficient for the barrier in the vicinity of the emitter surface. In general, the reflection coefficient for metal surfaces is much smaller than unity and can be neglected in eqn. 3.50. In the context of eqn. 3.50, the electron saturation current density depends primarily on the value of the work function and, to a lesser degree, on the small value of the average reflection coefficient. Accordingly, the calculation of the saturation current density is equivalent to determining the work function and the reflection coefficient, so an accurate measurement of the work function is needed because small errors in the work function result in large errors in the saturation current density.

References

1 D. O. Hayward and B. M. W. Trapnell, Chemisorption, (Butterworths, London 1964).

2 J. T. Yates and N. E. Ericsson, Surf. Sci. 44 (1974) 489.

3 V. K. Medvedev and A. I. Yakivchuk, Sov. Phys. Solid State 17 (1975) 7.

4 I. Langmuir, Phys Rev 43 (1933) 224.

5 L. D. Schmidt and R. Gomer, J. Chem. Phys. 42 (1965) 3573.

6 V. M. Gavrilyuk and V. K. Medvedev, Sov. Phys.-Solid State 8 (1966) 1439.

7 A. G. Fedorus and A. G. Naumovets, Surf. Sci. 21 (1970) 426.

8 L. W. Swanson and R. W. Strayer, J. Chem. Phys. 48 (1968) 2421.

9 L. D. Schmidt and R. Gomer, J. Chem. Phys. 45 (1966) 1605.

10 V. M. Gavrilyuk, A. G. Naumovets, and A. G. Fedorus, Sov. Phys.-JETP 24 (1966) 899.

11 R. W. Gurney, Phys. Rev. 47 (1935) 479.

12 J. W. Gadzuk, Surf. Sci. 6 (1967) 133.

13 J. W. Gadzuk, Surf. Sci. 6 (1966) 159.

14 O. K. Andersen, Phys. Rev. B 12 (1975) 3060.

15 D. S. Wang. A. J. Freeman and H. Krakauer, Phys. Rev. B 26 (1982) 1340.

16 E. Wimmer, H. Krakauer, M. Wienert and A. J Freeman, Phys. Rev. B 24 (1984) 864.

17 D. M. Riffe, G. K. Wertheim and P. H. Citrin, Phys. Rev. Lett. 64 (1990) 571.

18 G. A. Benesh and D. A. King, Chem. Phys. Lett. 191 (1992) 315.

19 M. Scheffler, Ch. Droste, A. Fleszar, F. Maca, G. Wachutka and B. Barzel, Physica B, 143 (1971) 172.

20 G. A. Haas and R. E. Thomas, in: Techniques of Metals Research, (Interscience Publishers, 1972) chapter 2.

21 N. D. Lang and W. Kohn, Phys. Rev. B 1 (1970) 4555.

22 P. Hohenberg and W. Kohn, Phys. Rev. B 136 (1964) 864.

23 W. Kohn and L. J. Sham, Phys. Rev. A 140 (1961) 1133.

24 N. D. Lang and W. Kohn, Phys. Rev. B 3 (1971) 1215..

25 R. Smoluchowski, Phys. Rev. **60** (1941) 661.

26 N. D. Lang, Phys. Rev. B 4 (1971) 4234.

27 D. Steiner and E. P. Gyftopoulos, in: Proc. of the 27th Conf. on Phys. Electronics, Cambridge Mass. (1967) 160.

28 J. Hinze, M. A. Whitehead and H. H. Jaffe, Journal of Am. Chem. Soc. 85 (1963) 148.

29 W. E. Gordy Phys. Rev. 69 (1946) 604.

30 H. O. Pritchard and H. A. Skinner, Chem. Rev. 55 (1955) 745.

31 E. P. Gyftopoulos and D. Stiener, in: Proc. of the 27th Conf. on Phys. Electronics, Cambridge Mass. (1967) 169.

32 J. C. Slater, Introduction to Chemical Physics, (McGraw-Hill, New York, New York 1963).

33 E. S. Rittner, Journal of Chem. Phys. 10 (1951) 1030.

34 J. Topping, Proc. Roy. Soc. (London) A114 (1927) 67.

35 R. Ferreira, Journal of Phys. Chem. 68 (1964) 2240.

Chapter 4

Experimental Methods

4.0 Sources, Samples and System

All the experiments in this investigation were conducted in a bakeable stainless steel ultrahigh vacuum (UHV) chamber which contains the various analytical instruments and vapor sources which are illustrated in Fig. 4.00. The UHV environment was achieved with a series of different pumps and a bakeout procedure. When the chamber was opened to repair one of the analytical devices, replace a source or change a sample, the chamber was always back filled with dry nitrogen to reduce contamination. After the system was opened and repairs were made, the chamber was pumped down to ~1×10^{-6} with a roughing pump and turbo pump combination. The chamber was then wrapped in aluminum foil and baked into the ion pumps and turbo pump at ~220 C for 10-15 hours. After baking, the aluminum foil was removed and the chamber was allowed to cool. Next, the turbo pump was disconnected and the sublimation pumps, ion gauge and sample were outgassed. After the bakeout procedure, the chamber was left alone until the pressure dropped into the 10^{-10} Torr range which usually took 12 to 24 hours. Once the sample was completely outgassed, a background pressure of 3×10^{-10} Torr could be maintained which helped limit sample contamination. The pressure did rise to ~4×10^{-9} Torr during thermal desorption mass spectrometry (TDS) measurements and flash cleaning.

Four surface analytical techniques were used in this investigation, and they are Auger Electron Spectroscopy (AES), Quadrupole Mass Spectrometry (QMS), Low Energy Electron Diffraction (LEED) and Field Emission Retarding Potential (FERP) work function measurement. These four techniques allowed us to both qualitatively and quantitatively analyze the surface of the various adsorbate-metal systems under

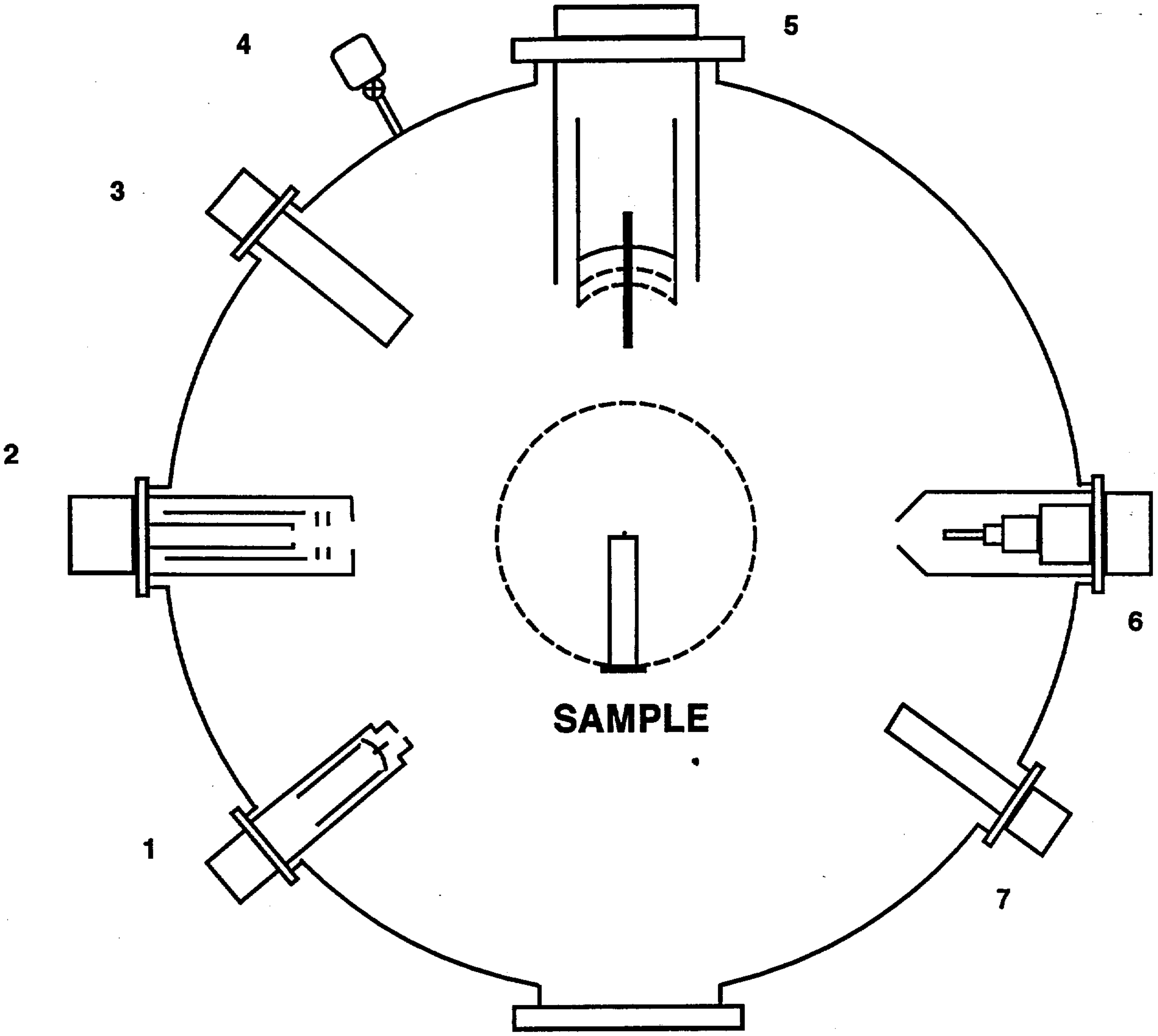

Figure 4.00. Schematic of vacuum chamber. (1) Field emission retarding potential (FERP) gun. (2) Quadruple mass spectrometer (QMS). (3) Cesium source. (4) Oxygen supply. (5) Low energy electron diffraction (LEED) optics. (6) Auger electron spectroscopy (AES) optics (7) Barium source.

investigation. Two Fluke 8840 A/D converters along with an ICS model 4831 power supply programmer were used to input the data from the Auger, FERP and mass spectrometer to a 386 computer, which was used to plot and analyze the data. Simple C and assembly language programs were written to control these devices and format the data. The LEED data were photographed with a Olympus OM-2 camera using various speeds of film, exposure times and f-stops, depending on the brightness of the LEED pattern.

Maintaining a clean source of adsorbate is one of the most important concerns when studying the adsorption alkali and alkaline earth metals. Alkali and alkaline earth metals are extremely reactive elements, so limiting source contamination becomes a major undertaking. Figure 4.01 shows the two different types of getters used for the barium and cesium sources. The cesium source was a SAES cesium getter consisting of a nickel boat filled with cesium-chromate compound that when heated produces a constant flux of elemental cesium. This type of source is convenient since it can be exposed to air without being contaminated. The barium source was constructed of iron clad getter wire filled with elemental barium. As seen in Fig. 4.01, the iron clad getter wire was bent into a small loop and notched with a small file. Again by heating the wire, a constant flux of pure elemental barium was produced. Exposure of the small notched opening to air did not seem to affect the operation of the source. It will be shown later in the discussion of AES, that after a typical outgassing procedure, the two sources produce pure adsorbate with only a small percentage of oxygen contamination. The coverage calibration of the two sources will also be discussed in the AES section of this chapter. Oxygen gas was introduced to the system through a bakeable Varian leak valve at 2×10^{-8} Torr, so one Langmuir ($1 \text{ L} = 1 \times 10^{-6}$ Torr-sec) of coverage was reached after 50 seconds of exposure.

Three different single crystal transition metal substrates were used in this investigation: tungsten, molybdenum and niobium. The samples were introduced into the system using a UHV manipulator that could move the samples in x, y, and z directions and also rotate 360 degrees. The samples were attached to the manipulator with hand-crafted sample holders illustrated in Fig. 4.02. All three of these substrates have body-centered cubic (bcc) crystal structure and were oriented exposing the (110)

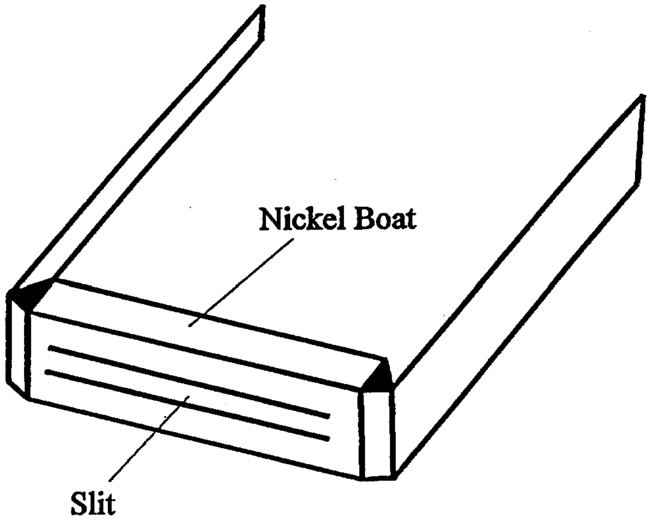

(a)

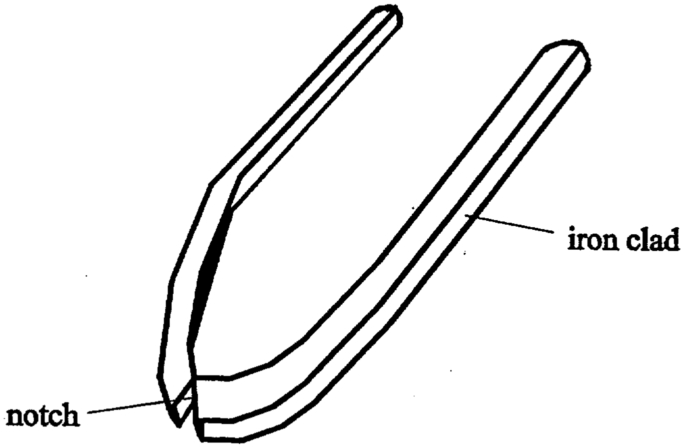

(b)

Figure 4.01. Schematic of the two types of getters used for the cesium and barium sources. (a) Cesium SAES getter. (b) Iron-clad barium filled getter wire.

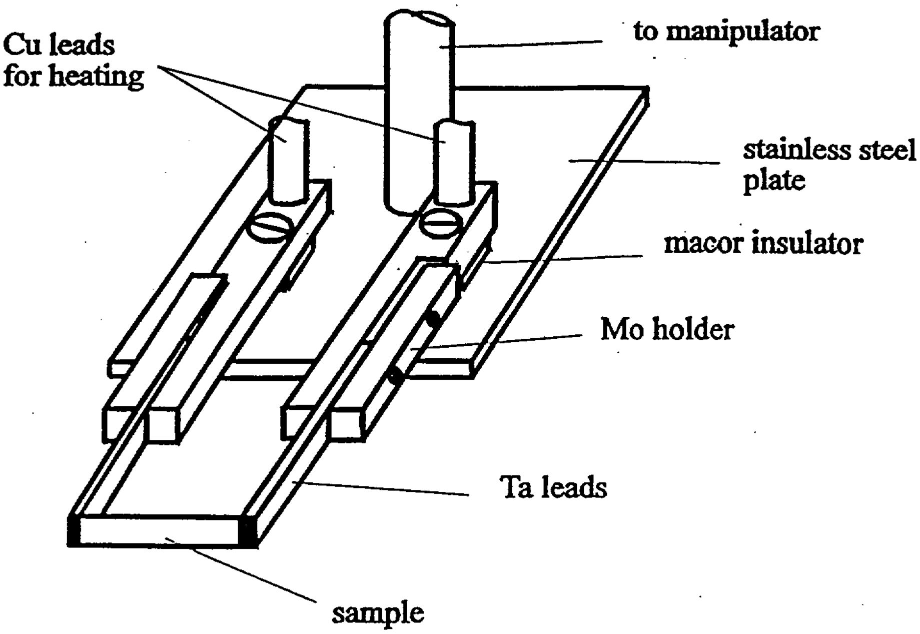

Figure 4.02a. Sample holder for the W(110) and Mo(110) single crystal (0.25 × 4.0 × 15.0 mm) ribbons.

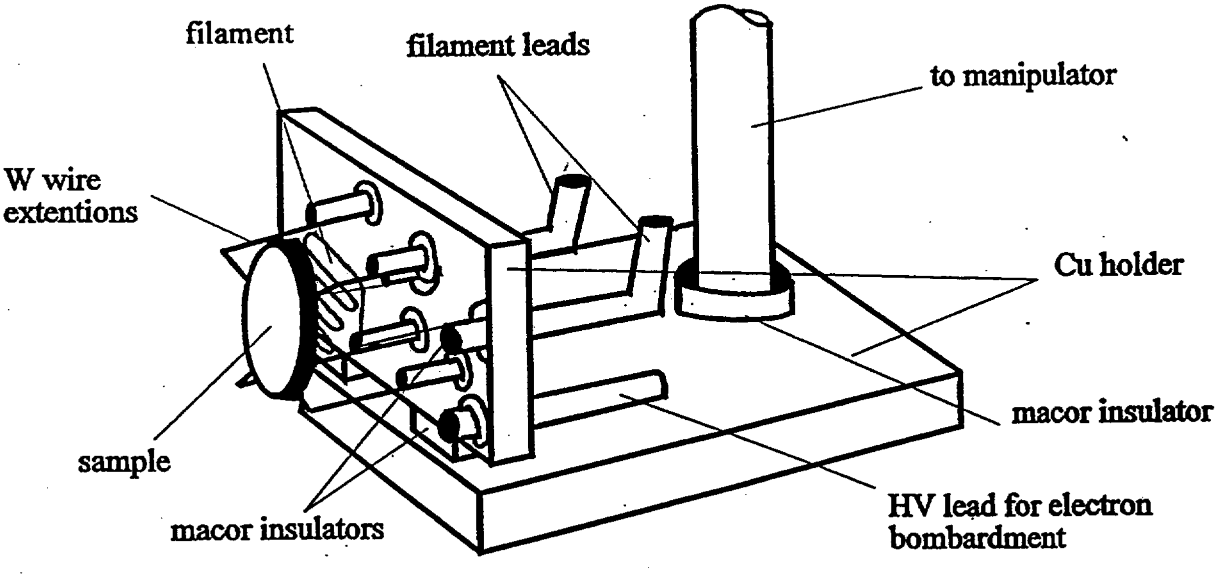

Figure 4.02b. Sample holder for the Nb(110) single crystal disk (10.0 mm diameter and 1.5 mm thick).

crystal plane. The (110) crystal plane was chosen for a variety of reasons. The (110) face is the most densely packed and atomically smooth surface for bcc materials, and consequently the most stable. Stability of the substrate surface, under many different conditions, is important in a fundamental study of adsorbate-metal interactions. The elimination of surface reconstruction and phase transitions of the substrate surface allows for a more complete and understandable investigation. The (110) crystal plane also has the highest bare work function for the above mentioned substrates. From the earlier discussion involving work function change versus alkali and alkaline earth metal adsorption, the strong negative dipole moment of the clean (110) surface would induce a big change in the work function of the substrate with adsorption. It has been shown experimentally[1,2,3] and theoretically[4,5] that the higher the bare work function of the substrate the greater the change in work function which will occur with adsorption of alkali and alkaline earth metals. The tungsten and molybdenum (110) single crystals were 0.25 × 4.0 × 15.0 mm ribbons and could be resistively heated to 2400 K. The Nb(110) sample was in the form of a disk 10.0 mm in diameter and 1.5 mm thick which was cut from an electron beam zone refined single crystal. The surface was mechanically polished and oriented within 2° of the (110) plane. Crystal heating was provided by electron bombardment. The samples were cleaned by heating them in oxygen at various temperatures depending on material (1100 K for tungsten), followed by flashings to ≥2100 K. The substrate temperatures were measured by viewing the sample through a pyrex window using an optical pyrometer. The correction factors for the pyrex window and the spectral emissivity were introduced into the measurement. The substrate temperatures could also be monitored by a tungsten-rhenium thermocouple (W-5% Re and W-26% Re) welded to the back side of the crystal surface. The thermocouple temperature readings were calibrated to fit the pyrometer temperature readings for each sample.

In a typical experimental run , the clean sample was exposed to a constant flux of cesium or barium or both for a series of short time intervals. Each source was calibrated for a particular dose rate. For example, the Ba source was calibrated for approximately 0.1 monolayer per 2.0 minute dose on the Nb(110) sample. After each exposure an AES spectrum was recorded and then either a work function, LEED or a thermal desorption measurement was taken.

4.1 Field Emission Retarding Potential (FERP) Work Function Method

A complete understanding of the work function and work function changes due to adsorption is of fundamental importance when studying surfaces and surface interactions. Knowledge of the work function is of particular importance for applications involving electron emission. Inadequacies in both experimental and theoretical work function measurement techniques along with imperfect samples have lead to a disagreement among accepted work function values, but advances in vacuum technology and fabrication of pure materials with specific crystal orientation have provided standardized work function results for clean surfaces. Bare surface work functions and changes in work function can be measured by a variety of techniques: thermionic, photo-electric, contact potential difference and field emission. Each method has its own advantages and limitations depending on the application and experimental apparatus used in the investigation. The field emission retarding potential (FERP) method for measuring the true work function circumvents most, if not all, the limitations and difficulties of other methods. The FERP method does however have some requirements of its own that need to be satisfied. Two of the most critical parameters are that the vacuum must be at least 1×10^{-9} Torr and the sample has to be kept at or near room temperature. The FERP technique for measuring work functions was introduced by Henderson[6] and was theoretically and experimentally examined for both polycrystalline and single crystal materials by Holscher[7] and Strayer[8], *et al.*, respectively.

4.1.a. General Theory

The FERP technique utilizes the concept of the Sommerfeld free electron model which gives the differential emitted current from a field emitter between the energies ε and $d\varepsilon + \varepsilon$, where ε is the energy of an electron relative to the Fermi level, as

$$\frac{dI}{d\varepsilon} = \frac{I_o e^{\varepsilon/d}}{d(1+e^{\varepsilon/pd})}, \tag{4.00}$$

where p = kT/d is a dimensionless parameter. The value of d, in eV, is given by

$$d = \frac{heF}{2(2m\phi_e)^{1/2}\,t(y)} = \frac{0.976F}{\phi_e^{1/2}t(y)}, \tag{4.01}$$

where F, in volts/angstroms, is the electric field and ϕ_e, in eV, is the emitter work function. The maximum emitter current I_0 in eqn. 4.00 is given by the Sommerfeld based Fowler-Nordheim equation

$$I_0 = \frac{e^3F^2A_0}{8\pi h\phi_e[t(y)]^2}\exp\left[-4(2mf_e^3)^{1/2}v(y)/3heF\right]$$

$$= \frac{1.5\times10^{10}F^2A_0}{\phi_e[t(y)]^2}\exp\left[-0.683\phi_e^{3/2}v(y)/F\right], \qquad (4.02)$$

where A_0 is the surface area of the emitter from which the collected current originates. The terms t(y) and v(y) are slowly varying image corrections terms based on the function $y = e^3F^{1/2} / \phi_e$[9].

The potential energy diagram shown in Fig. 4.03 describes the main features of the FERP method. The sharp emitter tip is held at a high electrostatic potential so that the electrons occupying energy levels at or near the Fermi level can tunnel through the barrier. After passing through a set of focusing lenses and an accelerating anode grid, the electrons are retarded in the region between the anode and the collector. If the collector (i.e. sample) and the emitter are connected electrically, the Fermi levels of the of the two metals are at the same energy level. The Fermi level (ε_F) is defined as the top most filled energy level in an a metal at 0 K. The emitted electrons can only reach the sample with work function ϕ_c if their total energy meets the condition

$$E > \phi_c + \varepsilon_F - V_c, \qquad (4.03)$$

where V_c is the emitter-to-collector bias potential. If V_c is increased, then all the electrons with energy greater than $\varepsilon = \phi_c - V_c$, will be collected at T = 0 K. Since at 0 K no electrons occupy energy levels above the Fermi level, the condition $V_c = \phi_c$ represents the current cutoff. The total collected current, I_c at some specific value of ε is given by

$$I_c = \frac{I_0}{d}\int_{\varepsilon}^{0} e^{\varepsilon/d}d\varepsilon = I_0\left(1 - e^{\varepsilon/d}\right). \qquad (4.04)$$

Since only the electrons with energy $\varepsilon = \phi_c - V_c$ can be collected, eqn. 4.04 can be rewritten in working form as

$$\ln\left(\frac{I_0-I_c}{I_0}\right)=\frac{\phi_c-V_c}{d}. \tag{4.05}$$

From the plot $\ln(I_0 - I_c)/I_0$ versus V_c, the values of ϕ_c and d can be obtained from the intercept and the slope respectively. Equations 4.04 and 4.05 are valid only when T = 0 K, and reflection losses are neglected. At emitter temperatures above 0 K, the plot of $\ln(I_0 - I_c)/I_0$ versus V_c varies from linearity due to the Boltzmann distribution of electrons above ε_F. It has been experimentally verified in Ref. 8 that at $T \leq 300$ K there is only a small variance from linearity due to this effect.

4.1.b. Experimental Method

In this investigation a slightly different method of obtaining the work function of the collector was used. Equation 4.00 may be differentiated with respect to ε in order to obtain the difference in energy between the peak of the electron energy distribution and the Fermi level, denoted ε_p, and given by

$$\varepsilon_p = kT\ln\left[\frac{kT}{d-kT}\right]. \tag{4.06}$$

The theoretical value of ε_p, which is equal to $\phi_c - V_p$, may be obtained from a plot of eqn. 4.06 for several different values of d, as shown in Fig. 4.04. The experimental value of V_p may be obtained from the position of maximum on the energy axis of the differential current-voltage or total energy distribution (TED) curve. The difference in energy between the 10% and 90% points on the leading edge of the TED curve was chosen as the parameter to characterize the resolution of the FERP analyzer since the leading edge suffers the most distortion due to the analyzer transmission function[10]. An accurate position of V_p, at room temperature, could only be obtained if the minimum voltage difference between 10% and 90% of the leading edge for a given TED curve was approximately equal to the theoretical value of 100 mV. The value of ε_p is usually found to be ≈30 mV and the work function of the collector, ϕ_c, can now be found to within 1% accuracy[8]. The 10-90% voltage difference of ≈160 mV was achieved in this investigation. The difference between the experimental and theoretical 10-90% of the TED curves was probably caused by not being able to achieve the proper alignment between the gun and sample or optimal analyzer focusing. The value of ε_p was taken to be 40 mV instead of 30 mV. It will be shown

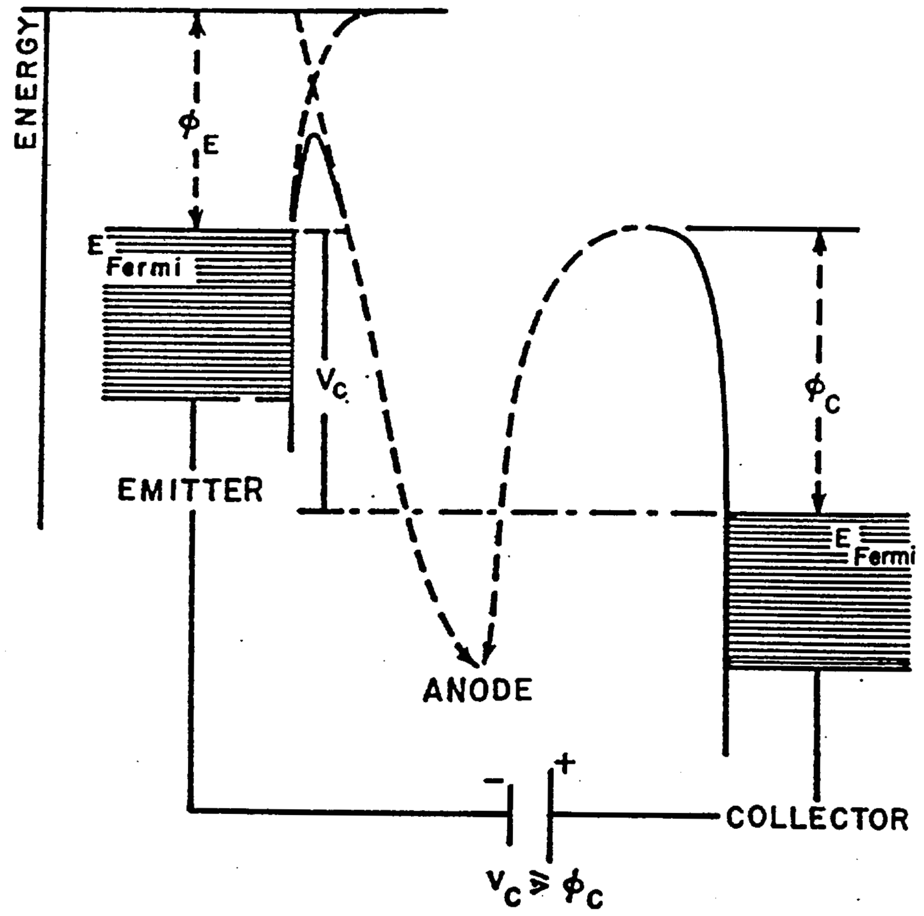

Figure 4.03 Potential energy diagram for the field emission retarding potential (FERP) method of determining surface work function. A bias voltage is applied to the collector in such a way that only the electrons from the Fermi level of the emitter are collected, at which point, the bias voltage is equal to the collector work function.

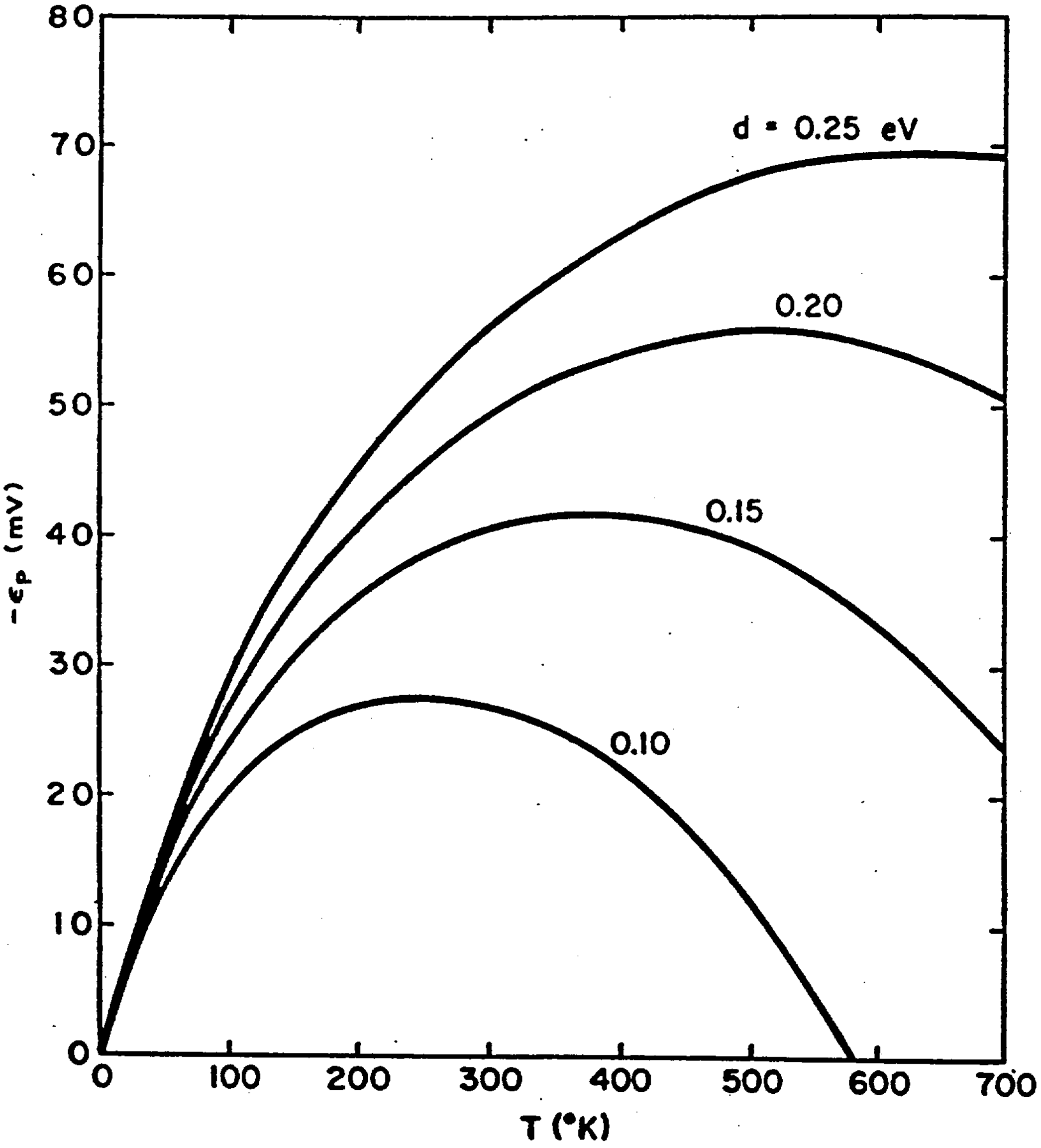

Figure 4.04. Energy distribution peak position, ϵ_p as a function of temperature, T, and distribution parameter, d.

that the difference does not create a big error in the results. The differential method of determining ϕ_c yields accurate results since it is less affected by reflection, and the only errors in ϕ_c are the accuracy of ε_p due to the uncertainty in d and the uncertainty in the exact position of V_p.

4.1.c Experimental Apparatus and Procedure.

The FERP method was an appropriate method to use for this investigation because the measured collector work function is unaffected by contamination of the emitter due to adsorbates and therefore provides absolute work function values. The FERP gun and associated power supply were prototypes provided by FEI Company. The focusing system consisting of an anode, lens and a 250 line/in decelerating mesh screen. The emitters used in this study were <111> oriented tungsten wire. A previous study[11] has shown that field emitted electrons from this orientation of tungsten exhibit TED curves corresponding to the Sommerfeld free electron model. Furthermore, the (111) crystal plane of tungsten has a low work function (4.4 eV) and consequently provides the highest beam transmission values. A total emission current of 0.5 to 1.0 μA was used. A collected current of 2.0 to 6.0 nA was focused by adjusting the lens and screen voltages to maximize the slope of the leading edge of the TED curve. Optimal focusing depended not only on the lens and screen voltages but also on the position of the sample and the sample surface. Optimal focusing was obtained through trial and error by adjusting all three parameters after every couple of work function measurements. The differential $I_c(V_c)$ or TED curve was acquired by inputting the preamplified collected current into a PAR 122 lock-in amplifier. The lock-in amplifier provided a tip modulation of 1000 hz at 30 mV peak-to-peak. The magnitude of this modulated signal was then proportional to dI_c/dV_c and could be plotted on a X-Y recorder or a computer as a function of V_c.

4.2 Auger Electron Spectroscopy (AES)

The identification of atoms by core level spectroscopies is based on the values of the binding energies of the electrons. With Auger electron spectroscopy (AES), the energy of the emergent electron is determined by the differences in binding energies associated with the de-excitation of an atom as it rearranges its electron shells and emits electrons (Auger electrons) with characteristic energies related to the material under investigation. The Auger electrons are generally analyzed in a device known as a cylindrical mirror electron energy analyzer or simply a CMA. The CMA is adjusted to pass only a narrow range of electron kinetic energies. As the analyzer is swept over the range of interest, the n(E) versus E distribution is obtained. More commonly, to improve the signal-to-noise ratio, a small ac modulation is superimposed on the sweep voltage and inputted in to a lock-in amplifier to obtain the derivative of the detected signal, dn(E)/dE versus E. The Auger spectrum contains three kinds of information.

The positions of the peaks along the energy axis allows a qualitative determination to be made about what is present on the sample surface, by comparing the spectra to reference spectra[12]. The peak to peak height of the derivative mode is directly proportional to the atomic concentration of the species in the near-surface region of the sample and can be used, with the appropriate corrections for relative transition intensities and chemical effects, to provide quantitative information about surface concentrations. Information on the chemical state of the atom can also be obtained from the Auger spectra. This information derives from the peaks involving transitions of valence electron states, as these states have energies that are most affected by chemical state changes. For completeness, an additional common use of AES will be mentioned although it was not used in this investigation. Auger electron spectroscopy can be used to determine the variation of composition with depth in thin films. The material of the thin film may be remove by bombarding the surface with ions, typically Ar^+, by a process called sputtering. As the surface is etched away, Auger spectra are taken repeatedly to determine the way in which concentrations of the various elements change with depth. This is done by plotting the peak-to-peak height of each element as a function of the bombarding time, which is directly proportional to the depth below the original surface.

Auger electron spectroscopy is one of the most useful surface elemental chemical analysis techniques. In this investigation, AES was used to monitor the near surface both quantitatively and qualitatively. It was important to know what was on the surface and how much, especially in our controlled metal adsorption study. Both the presence and amount of contaminant and adsorbate needed to be monitored so that useful predictions could be made about their interactions and particularly how they affected the adsorbate-metal interactions. Auger electron spectroscopy was used for both adsorbate coverage calibration and contamination monitoring for each adsorbate-metal system.

4.2.a General Theory

Auger electron spectroscopy determines composition of the surface by measuring the energy distribution of electrons emitted during irradiation with a beam of energetic electrons. A primary electron beam generally has an energy of 3000 - 5000 eV and probes a depth of ~10-15 angstroms depending on the escape depth of the electrons. The energetic electrons have sufficient energy to penetrate deeply into the solid, well beyond the escape region for characteristic energy electrons. The electrons that undergo inelastic collisions and loss energy leave the surface of the solid at lower energy and make up the background signal peak. Only those electrons close to the surface can escape with no energy loss. Hence, these are the electrons that create energy peaks characteristic of the solid. Auger electron spectroscopy can be used to detect surface atoms present in concentrations of a few percent.

Auger electron spectroscopy is a three electron process which can be characterized by two main events, excitation and de-excitation. The two event process giving rise to Auger electrons is illustrated in Fig. 4.05a. The Auger process begins with the excitation of an atom, in this case by electron impact, in which an electron is removed from a stable core level state. The core level states are the allowed electronic states of the solid which are derived from the atomic orbitals of the atoms that make up the solid. They are sharply defined in energy and are localized around a particular ion core. These excitations can also be caused by adsorption of a photon or by ion impact. Once the atom is excited, it can relax by one of two ways (see Fig. 4.05b and 4.05c). One alternative is for the electron from a less tightly bound state to drop to the empty core level, with a photon being emitted to carry away the difference in energy between the two levels. In the example shown in Fig. 4.05b, the energy difference would be E_K - E_{L2}. In the other alternative relaxation process, the Auger process involves the dropping of an electron from a less tightly bound level with the

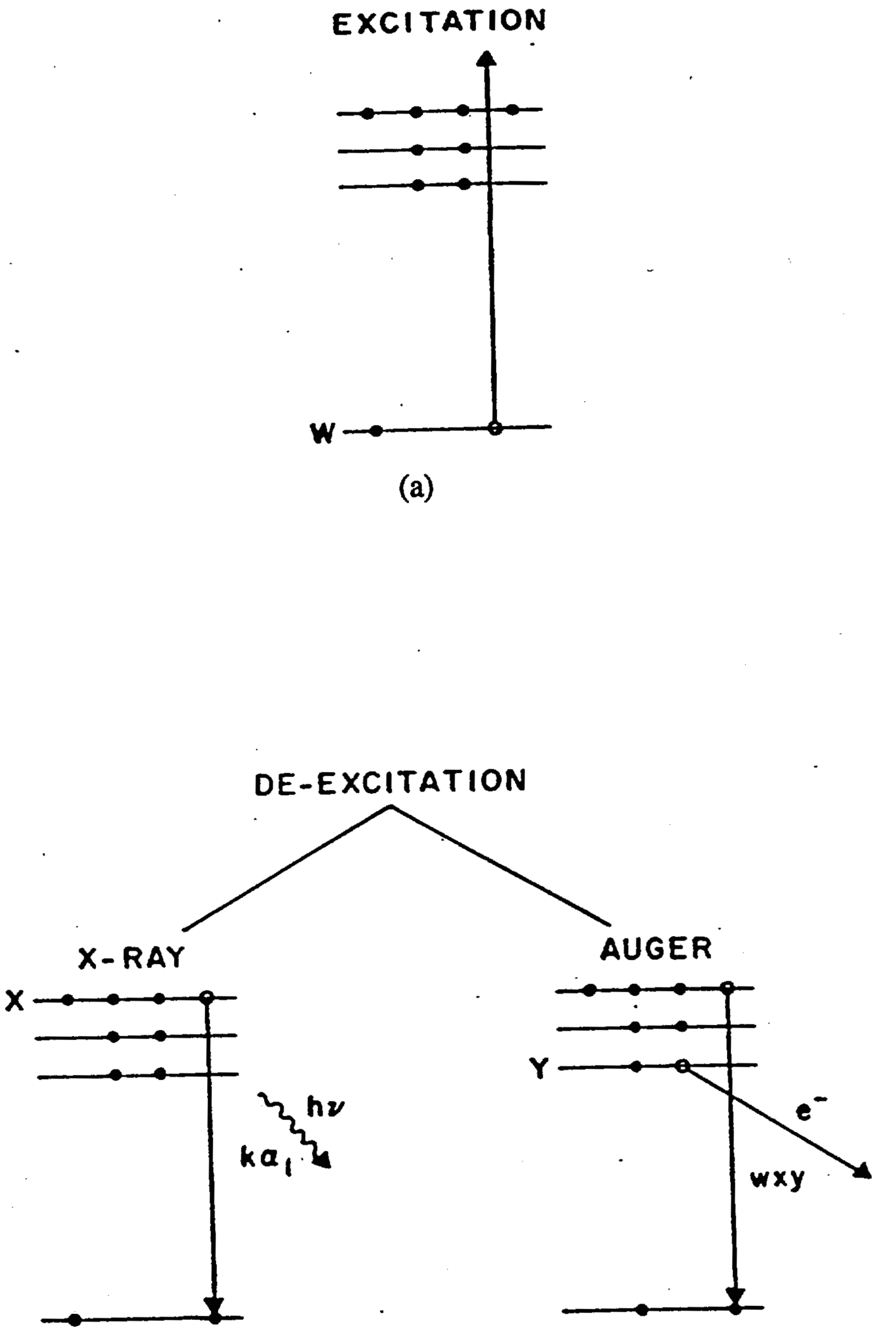

(a)

(b)

(c)

Figure 4.05. The three electron Auger process characterized by the two main events: de-excitation and excitation.

excess energy being carried off by the emission of a second electron from another less tightly bound level. The kinetic energy of the emitted electron is given, for the example shown, by

$$E_{KLL} = E_K - E_{L2} - E_{L3} - e\phi \qquad (4.07)$$

where ϕ is the work function of the surface. The Auger process shown in Fig. 4.05c is described by the nomenclature KL_2L_3. In this example, a hole in the 1*s* (K) level was created by the initial electron impact (excitation). The vacancy is then simultaneously filled by the outer L_2 shell electron and the excess energy is then given to the L_3 electron (Auger electron) which is ejected from the atom. Auger electron spectroscopy is a radiationless process in which the atom is left in a final state with two vacancies or holes. The KL_2L_3 Auger process described above would leave the vacancies in the 2*p* shell and would be indicated KL_2L_3 ($2s^22p^4$). Since electron-electron interactions are the strongest between electrons whose orbital are closest together, the strongest Auger electron transitions are of the type KLL, LMM or MNN. As it turns out, oxygen is the only element characterized in this investigation that doesn't have a principle MNN Auger electron transition. The principal MNN Auger electron energy peaks for the three substrates and the two adsorbates and the principle KLL Auger electron energy peak for oxygen are listed in Table 4.00.

4.2.b Experimental Apparatus and Procedure

The CMA has a internal electron gun that was focused to a point on the sample at the focal point of the CMA. Electrons ejected from the sample pass through an aperture and then into the electron multiplier. The pass energy is proportional to the potential applied to the outer cylinder, and the range of the energy of the transmitted electrons is determined by the resolution. The resolution is typically 0.2-0.5%. A Physical Electronics Industries (PHI) CMA model 10-155 with an internal electron gun was used in this research. A heated 5 mil rhenium wire electron source was controlled with a PHI model 11-110 electron gun controller and provided the desired emission current of 20 μA at a beam energy of 3 or 5 keV. The Auger system controller was a PHI model 11-500A.

The output of the electron multiplier, given as *n*(E), is plotted versus the pass energy, E, but in practice, Auger spectra are usually given in the derivative mode

Table 4.00. Principle Auger Transitions and Sensitivities.[12]

Element	Transition and Peak Energy	Sensitivity at 3 keV
Tungsten	MNN : 1736 eV	0.05
Molybdenum	MNN : 186 eV	0.34
Niobium	MNN : 167 eV	0.27
Barium	MNN : 584 eV	0.13
Cesium	MNN : 563 eV	0.17
Oxygen	KLL : 503 eV	0.50

because of the small signal and huge background signal in the *n*(E) mode. The differentiation of the signal from a CMA is done electronically by superimposing a small ac voltage on the outer cylinder voltage and synchronously detecting the in-phase signal from the electron multiplier with a PAR model 122 lock-in amplifier. The output of the lock-in amplifier is then plotted on an X-Y recorder or recorded by the computer where the y-axis is proportional to dn(E)/dE and the x-axis is the kinetic energy of the Auger electrons.

4.2.c Qualitative Analysis

As mentioned earlier, one of the main uses of AES is a qualitative determination of what is present on the surface of the sample under investigation. The identification of the peaks of the different elements in the Auger spectrum was accomplished by using the CMA to determine the element in question and then by matching the recorded Auger spectrum to the reference spectra of Ref. 12. All of the metals and adsorbates used in this investigation have relative low principal Auger energy peaks and are easily discernible from the 3 keV Auger spectra. The principal Auger peaks for barium (584 eV) and cesium (563 eV) are fairly close in energy so good resolution is needed when both metals are present on the surface.

Both cesium and barium are very reactive elements so monitoring of contamination from background gas and adsorbate sources was important. It has been seen by others that small amounts of gases, such as oxygen[13,14] and hydrogen[15], adsorbed on the surface of single crystal transition metal surfaces can greatly affect the behavior of cesium and barium. In order to make the data reproducible, the sample was cleaned before each data run and examined with the AES. Auger electron spectroscopy was also used during and after data runs to monitor the contamination from the sources and the various analytical techniques.

4.2.d Chemical Effects

Auger electron spectroscopy also can determine the chemical environment of the atom on or near the surface of the metal substrate. Chemical shifts in electronic structure of an atom are evident in AES spectra as shifts in the Auger peak energy or peak shape. These shifts reflect the changes in the valence shell electrons which affect the atomic potential and the binding energy of the core level electrons. Chemical shifts originate from the concept that the inner shell electrons feel an alteration in energy due to a change in the valence shell electrons' contribution to the outer shell electrons' chemical bonding. Depending on the type of bond present, the outer shell electrons can be drawn away from or towards the nucleus. Changes in electronegativity of the surface atoms due to the alterations in the valence electrons or charge transfer either increase or decrease the atomic potential and binding energy of the core level electrons. The one electron process of X-ray photonelectron spectroscopy is better suited for studying the chemistry of the surface as the photoelectron peaks are sharper and chemical effects are more easily seen than in corresponding Auger peaks. The ionic/metallic bonds produced by alkali and alkaline earth metals adsorbed on transition metal surfaces introduce subtle changes in the peak shape of the lower energy Auger peaks involving the valence electrons. Although a complete study to understand the effects of these changes was not performed, they will be discussed as they relate to other results.

4.2.e Quantitative Analysis

It is especially important in any analytical technique to be able to relate the observed peak intensities to the actual composition of the metal surface. Quantitative analysis in AES is somewhat difficult due to the fact that the signal from the element is strongly dependent not only on the average concentration but also on how it is distributed over the entire surface. The sensitivity of AES to electrons from the outer surface layers is greater than those originating from subsurface layers because of elastic scattering. Thus, in order to make an accurate measurement of the concentration some assumptions need to be made about the composition of the surface and near surface layers. It is usually acceptable to assume that the composition in the near surface region is homogeneous. A study of both the qualitative and chemical effects of the surface should help verify this assumption.

A simple way to approximate the atomic concentration of an element is to compare the intensity of the Auger signal from a given sample to that of a pure standard recorded under identical conditions. The atomic concentration C_A for an element A may be given by

$$C_A = \frac{I_A / I_{A'}}{\sum_j I_j / I_{j'}}, \qquad (4.08)$$

where I_A and $I_{A'}$ are the intensity of the measured Auger signal and the standard Auger signal respectively. The summation in the denominator is the intensity ratios of all the other elements present on the surface on the sample. The Auger peak intensities were measured from the peak-to-peak height of the differential Auger spectrum. The more sophisticated peak area measurements and peak resolution techniques used in XPS could also be employed on Auger peaks if chemical effects and peak shifts make peak-to-peak measurements impractical. Equation 4.08 is a good estimate of the composition but it ignores some of the matrix effects that may lead to a error in the results. An improved analysis may be used that includes a set of matrix correction factors that allow for atomic density, electron back scattering and changes in escape depth.

In this investigation a modified version of eqn. 4.08 was used to find the atomic concentration of the adsorbates on the surface of the substrate. The relative sensitivity factors shown in Table 4.00 for a primary electron beam of 3 keV were introduced and eqn. 4.08 is now given by

$$C_A = \frac{I_A / S_A}{\sum_j I_j / S_j}, \qquad (4.09)$$

where S_A is the relative sensitivity of the element A and S_j's are the relative sensitivities of the other elements present on the surface. The relative sensitivities include the atomic densities of the elements present thus the matrix effects are somewhat diminished, but there are still some inherent problems with this method such as changes in surface topography and chemical effects on peaks shapes. The clean single crystal samples used in this investigation tend to reduce the errors caused from surface roughness and allow relative concentrations to be obtained from the reproducible data runs.

4.3 Thermal Desorption Mass Spectrometry (TDS)

In the chapter 3, the effect of the adsorption of alkali and alkaline earth metals on the electronic structure of transition metal surfaces was discussed in terms of chemisorption. The technique of thermal desorption mass spectrometry (TDS) was developed as a way to study chemisorption and other surface chemical reactions. After diagnosing what was present on the surface of the substrate (AES) and determining the structure of the adlayer (LEED), it was important to understand how strongly the adatoms were bound to the surface. It was meaningful to find out how the strength of these bonds change by varying coverage, temperature and adlayer structure. Studies of this sort provide practical information on the overall rates of surface processes at the molecular level and on the macroscopic variables influencing these rates, however, as in most time dependent processes obtaining experimental accuracy and theoretical understanding can be difficult. Efforts to overcome these difficulties can lead to a more complete understanding of properties of adsorbates like the desorption activation energy and the electronic coupling to the surface. When analyzing thermal desorption data of alkali and alkaline earth metal, surface processes such as diffusion and the repulsive interaction between adatoms have to be expected.

4.3.a General Theory

The rate of desorption from a surface for the Polanyi-Wigner model of desorption may be written in the form

$$R_d(t) = -\frac{dN}{dt} = \nu_m N^m \exp(-E_m / RT), \tag{4.10}$$

where m is the reaction order for the desorption, ν_m is the frequency factor, E_m is the desorption activation energy, N^m is the number of adatoms per cm^2 in state m and R is Boltzmann's constant (8.617×10^{-5} eV/K). The coverage dependency of the reaction is contained in the N-term and the temperature dependency of the reaction in the exponential term. The Polanyi-Wigner equation relies on the basic concept that the coverage term is produced by a number of adatoms in transition towards a surface reaction step, the pre-exponential is equal to the frequency of attempts of the system to move in the direction of the reaction and the exponential term represents the number of attempts with sufficient energy to achieve the reaction. The reaction order of the step depends on whether the adatoms desorb individually or recombine before desorbing. The reaction is said to be first order ($m = 1$) if the desorption of independent single particles occurs throughout the coverage range. The pre-exponential in this case would simply be the number of attempts to leave the surface or the frequency of vibration of the adatom. If the adatoms recombine and desorb as a diatomic molecule then the reaction is considered to be second order (m = 2). Now ν_m and E_m are coverage dependent and governed by the interactions between the adatoms. In a given coverage range, it is possible to have first order desorption that is dependent on coverage. The basis for this statement will be discussed in a later in this section.

The method most often used to determine the parameters (E_m and ν_m) governing eqn. 4.10 is temperature programmed desorption. The basic idea of this method is to continuously heat the substrate and follow the rate of desorption as a function of temperature. The rate could be determined by the temperature and the amount of adsorbate left on the substrate after a previous desorption. It will show a maximum at the point where the increase due to the temperature rise is equal to the diminished coverage. The method has become popular for several reasons: 1) different adsorption states can be determined rapidly by correlating the maximum desorption rate with a distinct adsorption state, 2) an integration of the desorption rates could be used to determine the relative coverage and 3) approximate values of m, E_m and with in limits ν_m can be found in just a few measurements. The temperature programmed desorption method does have its limitations. It is often not possible to determine whether a certain desorption peak corresponds directly with a distinct adsorption state or from product of a desorption species produced from a surface reaction at lower temperature. The second limitation is that the method samples over a wide range of temperature and with a continuously changing temperature, so if there is a reaction that is dependent on the temperature, the only reaction products observed are those produced at lower temperature.

The temperature programmed method is used in this investigation with a linear temperature rise with time

$$T = T_0 + \beta t . \qquad (4.11)$$

The substitution of eqn. 4.11 into eqn. 4.10 leads to the following expression

$$R_d(t) = -\frac{dN}{dt} = \nu_m N^m(t) \exp\left[-E_m / R(T_0 + \beta t)\right] \qquad (4.12)$$

which is equal to

$$-\frac{dN}{dT}=\left(n_m N^m / \beta\right)\exp\left[-E_m / RT\right]. \tag{4.13}$$

If E and ν are considered independent of coverage, then the temperature T_p at which the rate curve is maximum, can be obtained from eqn. 4.13. It can be found that

$$-\frac{E_1}{RT_p^2}=\left(\nu_1 / \beta\right)\exp\left[-E_1 / RT_p\right] \qquad \text{for } m=1 \tag{4.14}$$

and

$$-\frac{E_2}{RT_p^2}=\left(2N_p\nu_2 / \beta\right)\exp\left[-E_2 / RT_p\right] \qquad \text{for } m=2 \tag{4.15}$$

where N_p is the coverage at the rate maximum and $2N_p \sim N_0$ for $m = 2$.

The resulting desorption rate curve obtained from the temperature programmed desorption method could be analyzed by eqns. 4.14 or 4.15. Equation 4.14 shows that for first order desorption with constant E and ν_1, the peak is asymmetric about T_p (T_p is independent of initial coverage for linear-programming). Redhead[16] goes on to show the relationship between E and T_p is almost linear and for $10^{13} < \nu_1 < 10^{8}$ (K^{-1}) is given to ±1.5% by

$$\frac{E_1}{RT_p}=\ln\left(\nu_1 T_p / \beta\right)-3.64. \tag{4.16}$$

To evaluate E using eqn. 4.16 for one T_p-value only, a value for ν_1 must be assumed. The value used most often is $\nu_1 = 10^{13}$ sec^{-1}. The real value of E and ν_1 could be determined from the desorption spectra taken for different heating rates, but in order to obtain acceptable accuracy, β must be varied by two powers of ten or more, which is usually impossible. The accuracy is limited for small β due to wall and re-adsorption effects and for large β there is poor resolution of multiple peaks. The variation of β is important to make sure redistribution does not occur during heating.

In the second order case, it can be seen form eqn. 4.15 that T_p now depends on the coverage. The initial coverage N_0 is found from the area under the desorption curve and the $\log[N_0(T_p)^2]$ plotted versus $1/T_p$ yields a straight line with slope of E_2/R. The value of ν_2 is then found by the substitution back into eqn. 4.15. The first order reaction with fixed activation energy of desorption gives rise to a peak that does not change in temperature with changing coverage. If the temperature of the peak decreases with increasing coverage then the reaction is considered second order or first order with activation energy dependent on coverage. The two cases can be distinguished by plotting $\log[N_0(T_p)^2]$ versus $1/T_p$. The second order reaction will produce a straight line with a slope E_2/R and the first order reaction will produce a line parallel to the y-axis. Second order reactions are also symmetric about T_p.

4.3.b Experimental Apparatus and Procedure

An EAI QUAD 210 quadrupole mass spectrometer (QMA) was used to monitor the desorbing species from each of the samples used in this investigation. The quadrupole mass spectrometer consists of an ionizer, a quadrupole section and an ion detector. The substance to be analyzed is introduced into the ionizer as a gas at low temperature. A small percentage of the gas is then ionized by electron bombardment. The positive ions are then accelerated and focused into the quadrupole section. In the quadrupole section the ions are filtered so that only those within a specific range of energy are allowed to pass through the quadrupole. The quadrupole filter rod assembly consists of four stainless steel rods and acts as an ion selector or mass filter by allowing only ions with a specific mass/energy ratio to traverse the length of the rods. A RF/DC generator supplies both RF and DC voltages to filter rod pairs, one pair being at negative potential and the other pair at positive potential. A sawtooth sweep voltage is applied and ions pass through in order of increasing mass number as the voltage is swept from low to high potentials. The RF frequencies used provide mass ranges of 1-50 amu, 10-150 amu and 50-500 amu for the EAI quadrupole mass spectrometer. The ions that pass through the quadrupole section are collected by the ion detector (electron multiplier). The output of the electron multiplier is amplified by a Keithley electrometer and recorded by a computer.

The thermal desorption spectra were obtained by heating the sample linearly in front of the QMA and recording the neutral desorption of 133 amu cesium or 138 amu barium. The QMA can be used to monitor the whole mass range or it can be programmed to continuously (no sweep) monitor certain peaks. In background gas analysis, the sweep output from the electrometer was connected directly to the X-Y recorder so the full spectrum of the system residual gases could be displayed. In neutral cesium or barium TDS, the QMA was programmed with an ICS model 4831 power supply programmer to continuously monitor cesium 133 amu and barium 138 amu peaks. A linear heating rate of 36 - 40 K/sec was used.

4.4 Low Energy Electron Diffraction (LEED)

Next, consider the adlayer structures formed on the substrate's surface in the course of chemisorption. The structures formed by chemisorption give additional information about how the adsorbates affect the surface properties of the substrate. Low energy electron diffraction (LEED) was the analytical technique used to monitor the structures formed on the surface. Low energy electron diffraction patterns are obtained by subjecting the surface of a metal to a mono-energetic beam of electrons at energies between 30 and 200 eV. At these low energies, the electrons are elastically and inelastically scattered within the first couple of atomic layers, therefore, it is a good surface structure monitor. As the incident beam collides with the surface, the elastically back-scattered electrons are observed and reflect the periodicity of the atoms on the surface. If the wavelength of the incident beam is precise and the surface is considered to be infinitely periodic, then the elastically diffracted electrons are all in phase and give rise to a diffraction pattern or LEED pattern. The LEED pattern is obtained using a set of retarding grids to reflect the unwanted inelastically scattered electrons and let pass the elastically scattered electrons. The elastically scattered electrons are accelerated to cause fluorescence when they collide with a phosphor screen. The diffraction pattern is viewed from behind the sample and can be photographed for further analysis.

Several aspects need to be considered when studying the structures formed by chemisorption, namely, long-range periodicity, transformations in the adsorbed layer and positions of adsorbate and substrate atoms. Most LEED studies show that chemisorbed layers form ordered adlayers. Additionally, many systems show that more than one adlayer arrangement can take place, depending on coverage and temperature. Changes in coverage or temperature can cause additional order or the disappearance of order due to the increase or decrease in the lateral interaction energy. Periodic structures imply that the interaction energy between adjacent surface sites is repulsive in nature. The repulsive interaction can be accounted for by the dipole-dipole interaction or the weakening of the bonding at adjacent sites due to the bond energy required by the chemisorptive bond. It has been observed, however, that ordered structures occur at low coverages which implies that there is some net attractive force between adatoms at second or distant neighbors.

Chemisorptive structures observed show periodicities that are related to the surface unit mesh. This relationship is in most cases relatively simple, such as 2×2 or 2×1. In some other cases, especially at high coverages, more complex orientations are observed. When observing an adlayer structure it is important to consider the equilibrium adatom positions on the surface. On a given crystal face there are several possible binding sites which involve one or more substrate atoms. Chemisorption bonds usually have strong directional preferences, but the energetically favorable position is not always the position that provides the most nearest neighbors. The 3-fold site of the bcc(110) substrates used in this investigation is the most energetically favorable geometry for monatomic adsorbates. Information on atomic positions can be obtained by analyzing the spot intensity versus voltage curves, but that was not done in this study.

4.4.a General Theory

The elastic interaction of low energy electrons with the surface is confined to a finite thickness of the surface, so the penetration of the electrons into deeper layers can be neglected. The surface is then treated as a two-dimensional lattice with periodicity equal to that of the atoms of the surface region and is given a unit cell with the basis vectors $\mathbf{a}_1$ and $\mathbf{a}_2$. A plane wave incident on an atom or atoms within the unit cell will be scattered in all directions, but if the atoms are periodic in nature then the interference between the waves scattered from neighboring unit cells will be restricted in the direction in which all scattered waves will be in phase. In order for this situation to occur, the scattered waves must differ only by an intergral number of wavelengths, λ. An illustration of this effect is shown in Fig. 4.06 for a one dimensional lattice with incident plane wave at angle γ_0 and an emergent plane wave at angle γ_n The in phase condition is met by all integers *n* which satisfy the condition

$$a(\sin\gamma_n - \sin\gamma_o) = \lambda n \qquad (4.17)$$

where a is the lattice separation distance and λ is given in angstroms by

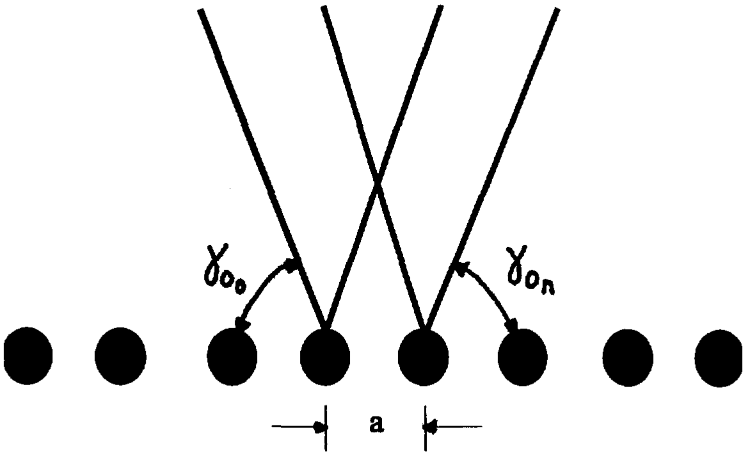

Figure 4.06. Illustration of the scattering of inphase waves incident on a one dimensional lattice. The incident plane wave at angle γ_{0_0} and the emergent plane wave at angle γ_{0_n} satisfy the inphase condition, $a(\sin\gamma_{0_n} - \sin\gamma_{0_0}) = \lambda n$.

$$\lambda = \sqrt{150.4 / E(eV)} \,. \tag{4.18}$$

Equation 4.17 is commonly known as the Laüe condition. If, as is usually the case, LEED experiments are performed with normal incidence of the primary electrons ($\gamma_o = 0$), then equation 4.17 can be written as

$$\sin \gamma_n = \frac{n}{a}\sqrt{150.4 / E(eV)} \,. \tag{4.19}$$

Equation 4.19 says that any particular beam of electrons will be diffracted for the first time (n = 1 and $\gamma = 90°$) with energy E(eV) = $150.4/a^2$. A decrease in the electron energy (larger unit cell) leads to a diffraction maximum closer to the surface normal while an increase in the electron energy would move the diffraction maximum towards total reflection. The analysis of LEED patterns gives a complete description of the directions of the diffracted electrons and the value of a, therefore the geometry of the unit cell is known. However, the arrangement of atoms in the unit cell cannot be determined by this method since that information can only be determined from the intensity of the diffraction spots on the screen.

The impinging primary beam of electrons is given by $\mathbf{s}_0$ and the interference maxima is given by a set of vectors $\mathbf{s}_n$, which is given in vector form as

$$\mathbf{a} \cdot (\mathbf{s} - \mathbf{s}_0) = n\lambda \,. \tag{4.20}$$

If $\Delta\mathbf{s} = (\mathbf{s} - \mathbf{s}_0)$, then it is seen that the diffracted beams are given by $\Delta\mathbf{s}$ and are found as intergral multiples of $\lambda/|\mathbf{a}_i|$. This introduces the reciprocal of the real space lattice vector. The reciprocal lattice vectors are defined as $\mathbf{a}_1^* = 1/\mathbf{a}_1$ and $\mathbf{a}_2^* = 1/\mathbf{a}_2$ for two dimensions and must obey the equations

$$\mathbf{a}_i \bullet \mathbf{a}_j^* = \delta_{ij} \tag{4.21}$$

where (i, j = 1, 2). The Kronecker symbol is defined so that $\delta_{ij} = 0$ if $i \neq j$ and $\delta_{ij} = 1$ if i = j which indicates $\mathbf{a}_1^* \perp \mathbf{a}_2$ and $\mathbf{a}_2^* \perp \mathbf{a}_1$. There is also a simple relationship between the angles which subtend the basis vectors of the real and reciprocal lattice. If the angle between $\mathbf{a}_1$ and $\mathbf{a}_2$ is given as α, and $\mathbf{a}_1^* \perp \mathbf{a}_2$, then the angle between $\mathbf{a}_1$and $\mathbf{a}_1^*$ is $\pi/2 - \alpha$. From equation 4.21, $\mathbf{a}_1 \bullet \mathbf{a}_1^* = 1$ and by the definition of the dot product $1 = |\mathbf{a}_1| \bullet |\mathbf{a}_1^*| \bullet \cos[(\pi/2) - \alpha]$ so that

$$|\mathbf{a}_1| = \frac{1}{|\mathbf{a}_1^*| \bullet \sin\alpha} \,. \tag{4.22}$$

The same relationship can be made between $\mathbf{a}_2$ and $\mathbf{a}_2^*$. The angle between the reciprocal vectors, $\mathbf{a}_1^*$ and $\mathbf{a}_2^*$, can be defined as $\alpha^* = \alpha + 2(\pi/2 - \alpha) = (\pi - \alpha)$ which means that

$$\sin\alpha^* = \sin\alpha . \tag{4.23}$$

These relationships are illustrated in Fig. 4.07.

Any vectors relating any two reciprocal lattice points must take the form

$$g_{hk} = h\mathbf{a}_1^* + k\mathbf{a}_2^* \tag{4.24}$$

where h and k are integers. A LEED pattern is seen if the diffracted electrons from a two dimensional lattice satisfy the Laúe conditions

$$\mathbf{a}_1 \bullet (\Delta s) = h\lambda \tag{4.25}$$

and

$$\mathbf{a}_2 \bullet (\Delta s) = k\lambda \tag{4.26}$$

which can be solved any time

$$\Delta s = \lambda(h\mathbf{a}_1^* + k\mathbf{a}_2^*) = \lambda g_{hk} . \tag{4.27}$$

The above argument shows that there is a correspondence between the observed diffraction pattern and the reciprocal lattice of the surface.

If $\mathbf{a}_3^*$ in a three dimensional crystal is allowed to go to infinity, then the two dimensional situation is approached with continuous lines or rods in the third dimension aligned perpendicular to the real space plane. This situation is seen in eqn. 4.27 where the change in beam vectors upon diffraction is given by the spacing between reciprocal lattice vectors about some origin ($\mathbf{a}_1^* = \mathbf{a}_2^* = 0$) in reciprocal space. If the incident beam is represented by a vector of length λ and is elastically scattered, it must have wavelength $1/\lambda$ in reciprocal space. A simple graphical method known as the Ewald construction is often used to visualize the diffracted beams, but is not very practical for interpreting diffraction patterns. Shown in Fig. 4.08 is an Ewald sphere in one dimension. The Ewald sphere is constructed with a radius of $1/\lambda$ and it center at point at $-1/\lambda \bullet s_0$ from the origin of the reciprocal lattice. All points where the sphere intersects the lattice rods determine the direction s of the diffracted beams. In the one dimensional case, this statement can be verified quickly since

$$\frac{1}{\lambda} \bullet \sin\gamma = \frac{1}{\lambda} \bullet \sin\gamma_0 + h_1 \bullet \frac{1}{a} \tag{4.28}$$

or

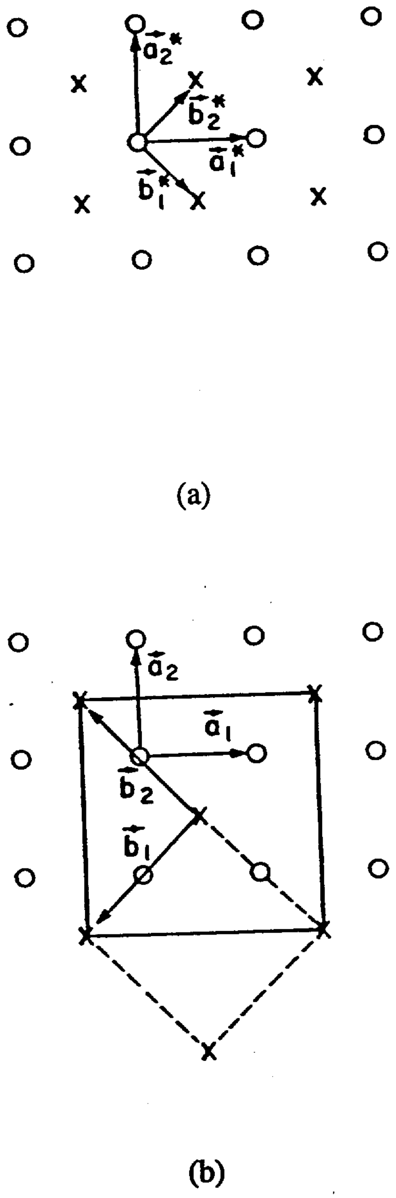

Figure 4.07. Schematic of the relationship between the lattice vectors and the reciprocal lattice vectors of asimple 2-D LEED diffraction pattern. (a) LEED pattern (reciprocal lattice), (b) Real lattice. (o - substrate atoms, x - adsorbate atoms)

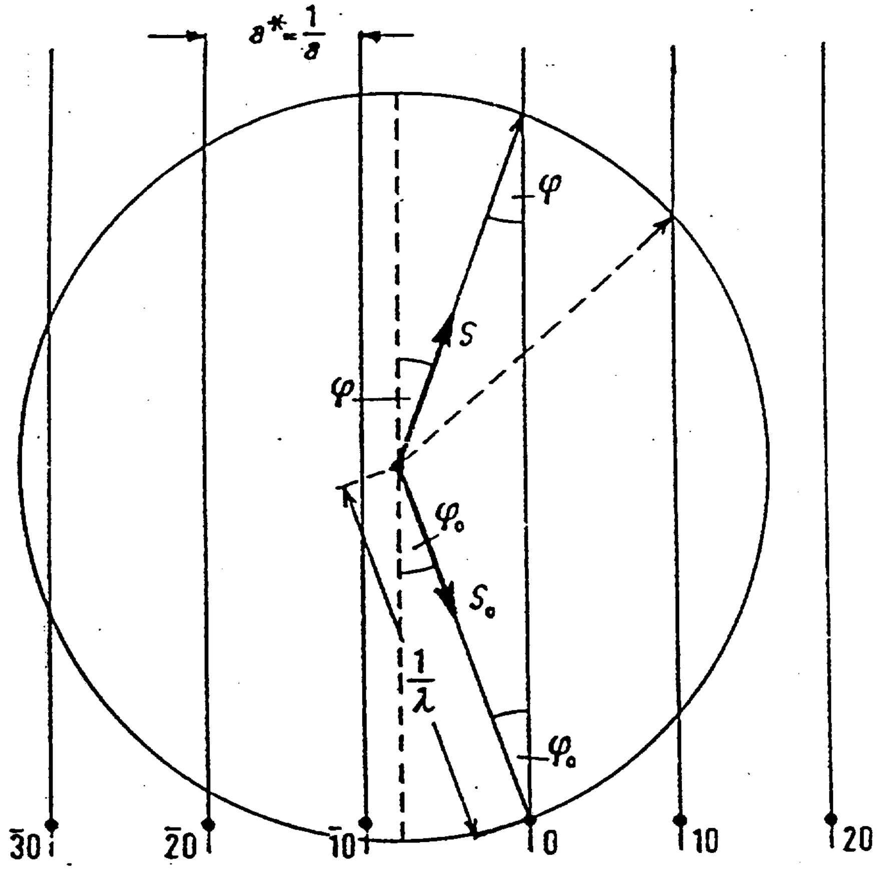

Figure 4.08. The Ewald construction for a one dimensional lattice.

$$a(\sin\gamma - \sin\gamma_0) = h_1\lambda\,. \qquad (4.29)$$

Decreasing the wavelength of the incident beam (or increasing the electron energy) leads to an increase in the radius of the Ewald sphere, which means that more diffraction spots will appear and move towards the specular beam with increasing energy. One result of this is that the rods are cut at different positions along their length, and consequently the diffracted intensity will be a function of the electron energy.

4.4.b Experimental Apparatus and Procedure

In this investigation, a typical "display type" LEED system from Varian was used. The basic configuration of the system is shown in Fig. 4.09. The system used an electron gun which produces the incident electron beam. The beam voltage was varied from 50 to 200 eV, and the beam current was set a 25 μA. The system also consisted of three of transparent hemispherical grids and a phosphor screen held at high potential. The sample was held perpendicular to the electron beam at the center of curvature of the grids. The innermost grid was maintained at sample potential (ground) to provide a field free flight path for the diffracted electrons. The middle grid was held at a negative potential whose magnitude was slightly smaller than the incident beam energy and reflected all but the elastically scattered electrons. The third grid was grounded and served to further help the retarding grid in cutting off the inelastically scattered electrons by shielding it from the phosphor screen. The elastically scattered electrons were accelerated towards onto a phosphor screen which was held at a few kilovolts potential. The screen would exhibit the diffraction spots where maximum interference occurred. The diffraction pattern was observed through a window in the vacuum chamber and could be photographed with a camera.

In a study of the adsorption of alkali and alkaline earth metals on clean and oxygenated surfaces, it is important understand and interpret overlayer structures. LEED studies can provide information on symmetry a well as determine the absolute position of the surface and near surface atoms relative to each other. In this study, we did not do the necessary analysis on the diffraction spot intensities to determine adatom positions, but we were interested in determining the geometry of the overlayer structure from the diffraction pattern. A unique way has been developed to determine

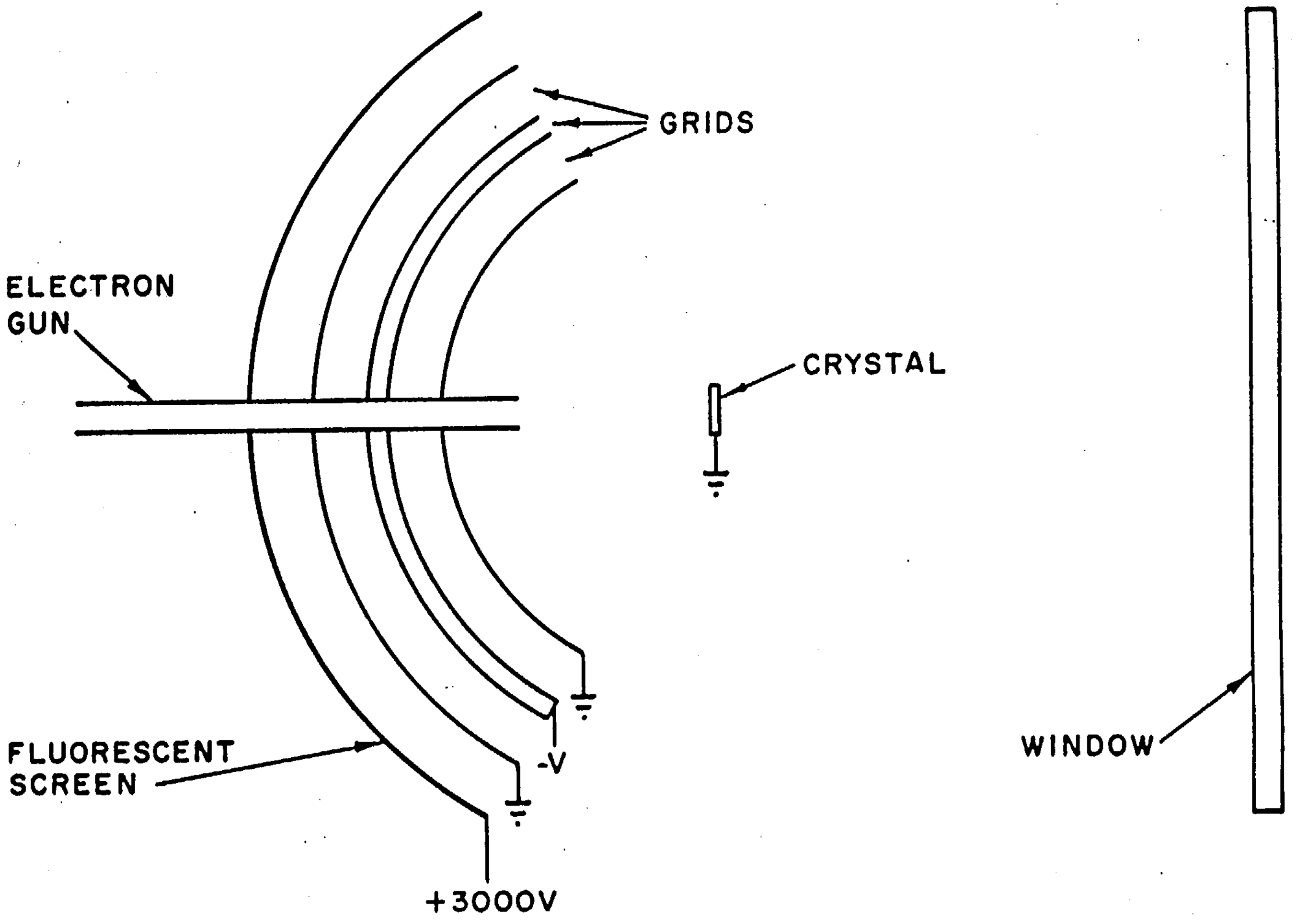

Figure 4.09. The basic design of the LEED optics used in this investigation.

what the real lattice looks like compared to the observed diffraction pattern (reciprocal lattice). An overlayer structure with basis vectors ($\mathbf{b}_1$,$\mathbf{b}_2$) and the substrate structure with basis vectors ($\mathbf{a}_1$, $\mathbf{a}_2$) are related to each other by the matrix equation

$$\mathbf{b} = \mathrm{M} \cdot \mathbf{a} \text{ or } \mathbf{b}_1 = m_{11}\mathbf{a}_1 + m_1\mathbf{a}_2 \tag{4.30}$$

$$\mathbf{b}_2 = m_{21}\mathbf{a}_1 + m_{22}\mathbf{a}_2. \tag{4.31}$$

A similar correlation occurs between the reciprocal lattice $\mathbf{b}^*$ and $\mathbf{a}^*$:

$$\mathbf{b}_1^* = m_{11}^*\mathbf{a}_1^* + m_{12}^*\mathbf{a}_2^* \tag{4.32}$$

$$\mathbf{b}_1^* = m_{21}^*\mathbf{a}_1^* + m_{22}^*\mathbf{a}_2^*. \tag{4.33}$$

The m_{ij}^*'s may be obtained from the inspection of the diffraction pattern while the m_{ij}'s are evaluated using the following relationship. It can be shown that M* is the inverse transpose matrix of M, so that $\mathrm{M}^* = \mathrm{M}_\mathrm{T}^{-1}$ and $\mathrm{M} = \mathrm{M}_\mathrm{T}^{*-1}$ or

$$\begin{pmatrix} m_{11} & m_{12} \\ m_{21} & m_{22} \end{pmatrix} = \frac{1}{\det\mathrm{M}^*}\begin{pmatrix} m_{22}^* & -m_{21}^* \\ -m_{12}^* & m_{11}^* \end{pmatrix} \tag{4.34}$$

where

$$\det\mathrm{M}^* = m_{11}^* \bullet m_{22}^* + m_{21}^* \bullet m_{12}^*. \tag{4.35}$$

References

1 E. V. Klimenko and A. G. Naumovets, Sov. Phys. Tech. Phys. 24 (1979) 710.

2 V. M. Gavrilyuk, Yu. S. Vedula, A. G. Naumovets and A. G. Fedorus, Fiz. Tverd. Tela 9 (1966) 881.

3 L. W. Swanson and R. W. Strayer, J. Chem. Phys. 48 (1968) 2421.

4 L. D. Lang, Phys. Rev. B 4 (1968) 4234.

5 E. P. Gyftopoulos and J. D. Levine, J. Appl. Phys. 33 (1965) 67.

6 J. E. Henderson and R. K. Dahlstrom, Phys. Rev. A 34 (1934) 764.

7 A. A. Holscher, Surf. Sci. 4 (1966) 89.

8 R. W. Strayer, W. Mackie and L. W. Swanson, Surf. Sci. 34 (1973) 225.

9 R. H. Good and E. W. Müller, Handbuch der Physik, Vol. 21, ed. S. Flugge (Springer-Verlag, Berlin 1956).

10 R. D. Young and C. E. Kuyatt, Rev. Sci. Instr. 39 (1967) 1477.

11 L. W. Swanson and L. C. Crouser, Phys. Rev. 163 (1967) 622.

12 L. E. Davis, N. C. MacDonald, P. W. Palmberg, G. E. Raich and R. E. Weber, Handbook of Auger Electron Spectroscopy, (Eden Praire, Minn.: Physical Electronics Doiv. of Perkin-Elmer Corp., 1976).

13 Yu. S. Vedula, A. T. Loburets and A. G. Naumovets, Sov. Phys. JETP 50 (1979) 391.

14 B. M. Zykov and V. K. Tskhakaya, Sov. Phys. Tech. Phys. 25 (1980) 1035.

15 C. A. Papageorgopoulus, (Dept. of Physics, University of Ioanina. Ioanina, Greece), written communication.

16 P. A. Redhead, Vacuum 12 (1962(203.

The Chapter 5

Results

In this chapter, we present the results of the adsorption and desorption of cesium, barium and cesium plus barium on the refractory metal substrates W(110), Mo(110), and Nb(100). We will present the coverage calibration, work function, desorption energy and surface structure data for each adsorbate separately, hence, cesium on the three substrates, barium on the three substrates and then cesium plus barium on the three substrates.

5.0 Surface Analysis of Clean W(110), Mo(110) and Nb(110)

Before investigating the interaction of alkali and alkaline earth metal vapor on clean metal surfaces, it is useful to look at the substrate metal surface itself. It was imperative in this investigation to maintain consistent substrate surface conditions. Any changes in surface structure due to surface relaxation and surface point defects can affect the bonding sites and bonding energy of the surface atoms and cause inconsistencies to occur in our results. These effects will become evident when we discuss our desorption results. The energetics of a surface of a metal can be affected by the amount of defects or dislocations present, so it is important to both understand and limit their effect when studying the fundamental surface properties of adsorbate-metal systems. We must also maintain the correct crystal orientation. The clean surface and adsorbate/metal surface properties are much different for different crystal planes of a given material. The (110) plane was chosen because it represented the ideal smooth close-packed bcc surface with the highest bare work function of the crystal planes for three substrates: tungsten, molybdenum and niobium.

5.0.a Work Function

Before each experimental data run, the substrate was cleaned by the procedure described in section 4.0, and an Auger spectra was taken to monitor cleanliness of the substrate upon adsorption. The tungsten and molybdenum samples were cleaned so that the Auger spectra revealed only trace (< 2%) amounts of oxygen and carbon. The niobium substrate, however, always contained a small concentration of oxygen. When the Nb(110) sample was introduced into the chamber, it was found to have a native oxide layer on its surface. After extended heating and many flash cleanings above 2200 K, AES showed the Nb(110) sample had only a small percentage of oxygen (2%-4%) present within the Auger detection depth (~10 angstroms). It has been observed by others that the Nb(110) surface has a strong affinity for oxygen and is difficult to remove all the oxygen even after heavy Ar^+ sputtering[1,2], so a small oxygen concentration was always present throughout the investigation. We considered the niobium sample clean if the oxygen concentration was under 4% given by eqn. 4.9.

The work function values of clean W(110), Mo(110) and Nb(110) found using the FERP method are given in Table 5.00 along with a comparison with other values. The work function values are obtained using eqn. 4.06 and the FERP curves shown in figs. 5.00, 5.01 and 5.02. The work functions presented here for clean W(110) and Mo(110) agree well. The work function found for clean Nb(110) is ~0.12 eV too low compared to the values found in the literature. The error can be explained several different ways. The first source of error could be the difference in the method of measuring the work function. The FERP method measures the absolute work function of a closely monitored surface at room temperature and cannot be directly compared to the thermionic emission method or contact potential difference method. The second source of error may be the amount of sample contamination or sample roughness. Studies dealing with oxidation phases of Nb(110)[3] have shown that small amounts of oxygen ($0 < \theta \leq 1/3$) produce a reduction of as much as 0.5 eV in the work function of the clean Nb(110) surface. The reduction in work function is a consequence of the loosening of the Nb(110) surface due to the diffusion of oxygen into the surface layers of the crystal. The close-packed Nb(110) surface with a high bare work function now has the looser structure of the NbO(110) surface, so

Table 5.00. Work functions of clean W(110), Mo(110) and Nb(110)

Material	Work Function (eV)	Method
W(110)	5.38	FERP
	5.34[4]	TE
	5.24[5]	FERP
Mo(110)	5.07	FERP
	5.00[4]	TE
	4.95[6]	PE
Nb(110)	4.62	FERP
	4.87[7]	TE
	4.80[8]	TE

TE - Thermionic emission
PE - Photoelectric

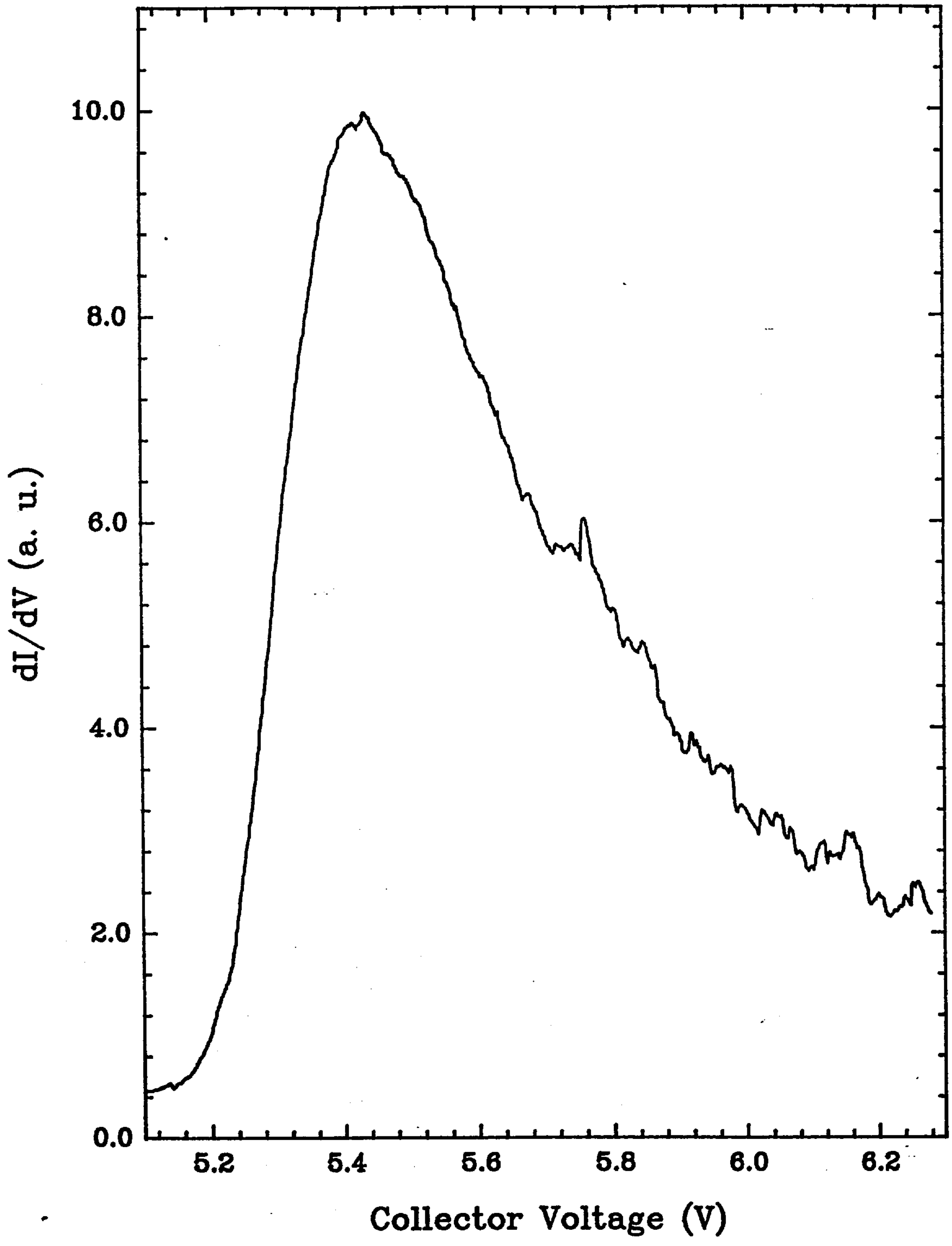

Figure 5.00. Total energy distribution curve for W(110).

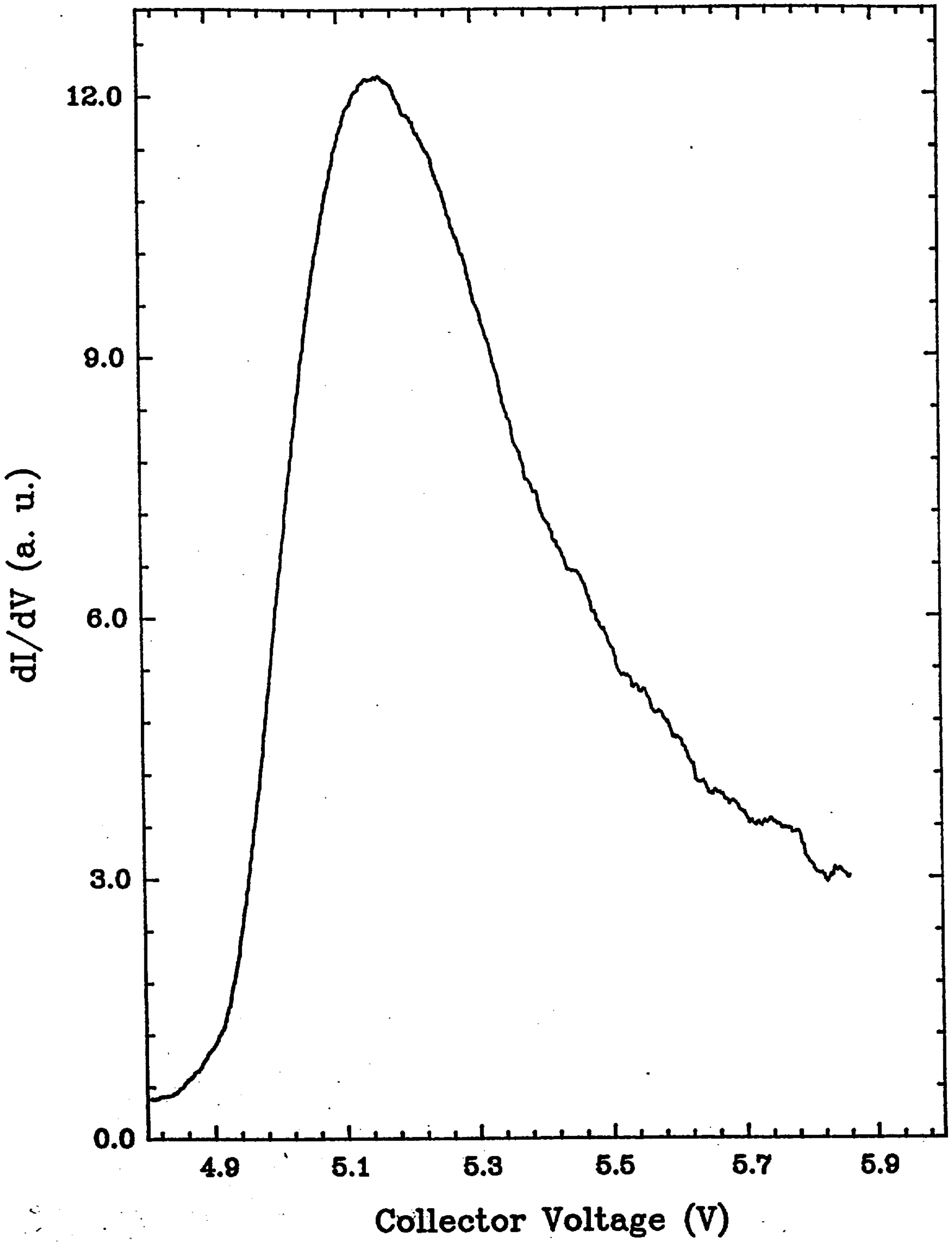

Figure 5.01. Total energy distribution curve for Mo(110).

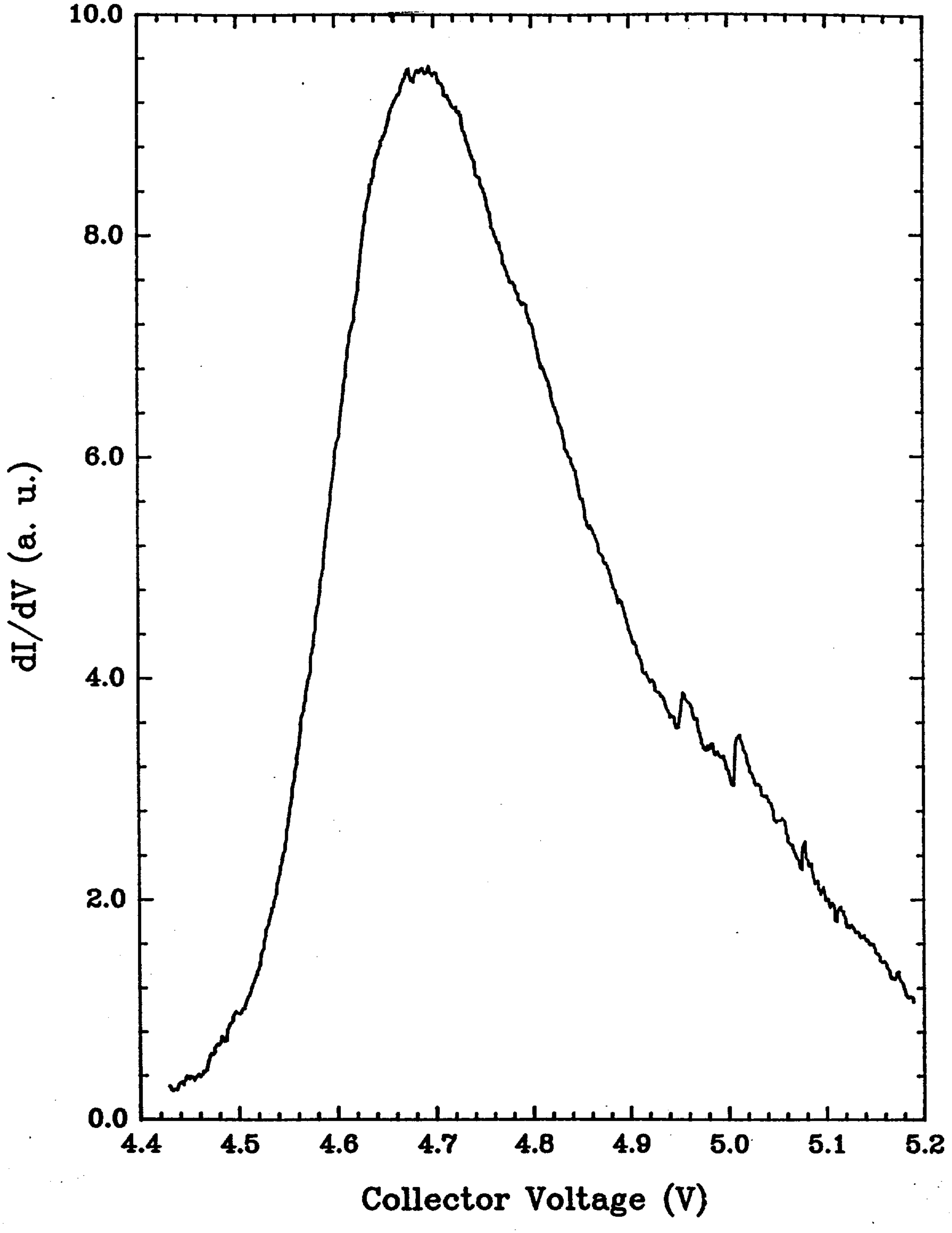

Figure 5.02. Total energy distribution curve for Nb(110).

comparing the work function of the Nb(110) surface is difficult unless the sample cleaning procedure and amount of contamination are known.

5.0.b Surface Structure

Both LEED and Laúe studies were done on the clean surfaces of the substrates used in this investigation. A Laúe diffraction pattern of each of the substrates was taken after the substrate was removed from the vacuum chamber to verify the crystal orientation. All three of the substrates were within ±2° of the (110) plane. Low energy electron diffraction measurements were taken throughout the investigation to monitor the structure of the surface of the clean substrates. A bright hexagonal pattern characteristic of a clean (110) plane of a bcc surface was always present.

5.1 Coverage Calibration for the Various Adsorbate/Metal Surfaces

The determination of the coverage of the adsorbates on the various substrates was central to this investigation. All data was based on how the surface properties of the different substrates changed with adsorbate coverage. We wanted to be able to determine what coverages yielded the minimum work function with the highest activation energies of desorption and how these values differed from substrate to substrate. Auger electron spectroscopy provided a simply and reliable way of calibrating the coverages of the barium and cesium on W(110), Mo(110) and Nb(110). The method has been widely used for a variety of adsorbate/substrate systems[9,10] and has yielded consistent results. For the three substrates used in this investigation, the coverage behavior of cesium and barium was very similar through the first monolayer. The Auger peak amplitude of the two adsorbates increased linearly through each monolayer versus adsorption time while the Auger peak amplitude of the substrate was attenuated linearly versus adsorption time. The thermal desorption and the work function measurements were used to substantiate the breakpoints in the Auger peak-to-peak heights (APPH) curves for cesium and barium on the substrate surfaces. By comparing the results of the three methods, we can determine the validity of the AES coverage calibration results.

The coverage calibration of adsorbed alkali metal or alkaline earth elements has not always been straightforward. The use of AES[11] along with other surface analysis techniques now enables the identification of monolayer coverages more routinely. In this investigation the determination of the adsorbate coverage on the various substrates was accomplished by measuring the normalized APPH, using eqn. 4.09, after each adsorbate deposition. Both the adsorbate and the substrate Auger peaks were monitored and then plotted versus the adsorbate dose time. Assuming a constant sticking coefficient, at least for the first monolayer, the Auger signals of the adsorbate and substrate will vary linearly with time through each monolayer. The change in linearity is due to the difference in the number of Auger electrons detected from the two layers and the possibility of the change in sticking coefficient of the adsorbate on the two different layers. The initial change in the slope or breakpoint in the APPH versus adsorbate dose time spectra identifies the point of monolayer coverage. A monolayer of adsorbate coverage is defined in this investigation as a close-packed layer of adsorbate one atom thick. The breakpoint for cesium adsorption on the metal surfaces was much more identifiable compared to the barium adsorption. The stronger electropositive nature of the cesium atoms and the high mobility of the cesium atoms at room temperature makes it difficult for cesium to form much more than a monolayer. It will be seen from the cesium APPH spectra, that the cesium concentration varies linearly until it reaches a saturation value at a certain dose time. Barium, on the other hand, can form a layer several monolayers thick at room temperature and leads to more subtle breakpoints in the APPH spectra.

The substrates were placed in front of the sources so that an even coverage would be deposited over the entire surface. The calibration was done by exposing the substrate to either the barium or cesium source for exactly 10.0 minutes. Auger peak data was taken at various spots over the entire substrate surface. The normalized adsorbate APPH were compared from the various spots, and the sample was adjusted until the adsorbate Auger peaks were all the same height.

5.1.a Cs/W(110), Cs/Mo(110) and Cs/Nb(110)

Figure 5.03 shows the plot of the normalized cesium 560 eV APPH and the normalized tungsten 169 eV APPH against the cesium deposition time on the W(110) surface. The tungsten signal is attenuated and the cesium signal increases as the cesium is being deposited on the surface. A breakpoint in the normalized cesium 560

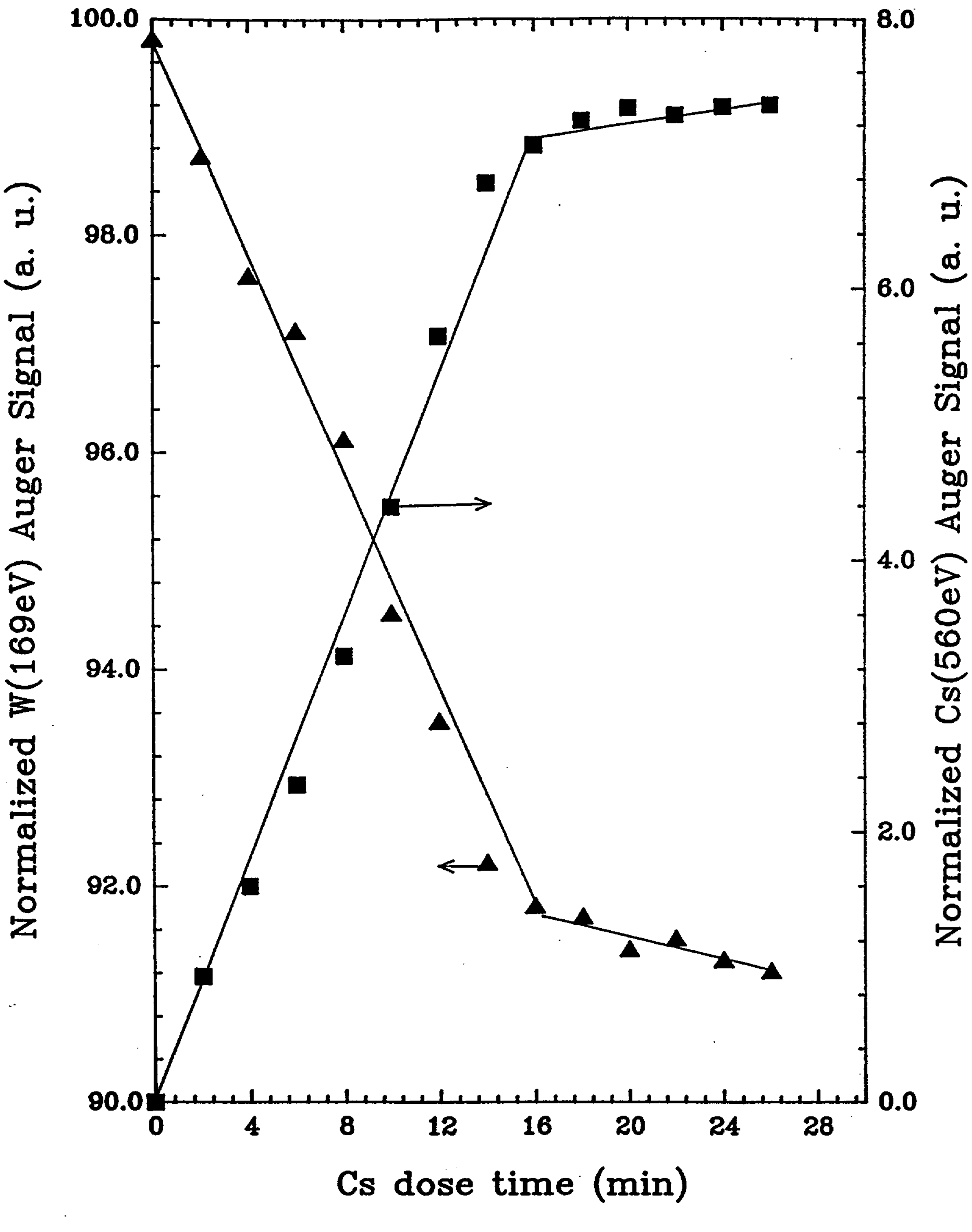

Figure 5.03. Normalized cesium 560 eV APPH and the normalized tungsten 169 eV APPH versus cesium dose time.

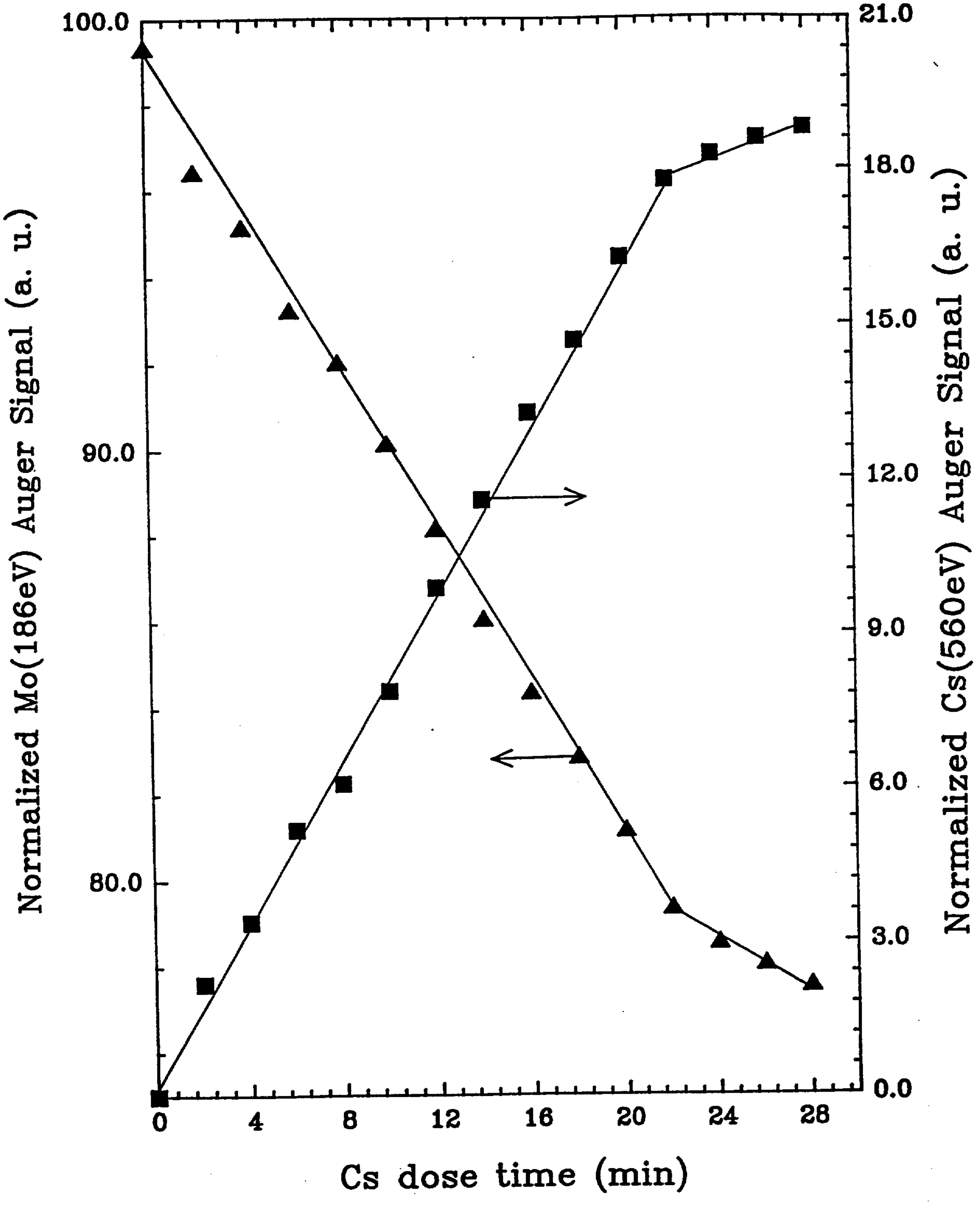

Figure 5.04. Normalized cesium 560 eV APPH and the normalized molybenum 186 eV APPH versus cesium dose time.

eV Auger signal and tungsten 169 eV Auger signal versus cesium dose time occurs after approximately 18.0 minutes. The break in the Auger signal indicates a completion of the first monolayer.

Figure 5.04 shows the plot of the normalized cesium 560 eV APPH and the normalized molybdenum 186 eV APPH against the cesium deposition time on the Mo(110) surface. The plot looks very similar to that of the Cs/W(110) surface. The breakpoint in the normalized cesium 560 eV Auger signal and the molybdenum 186 eV Auger signal versus cesium dose time occurs after approximately 22.0 minutes. The W(110) and the Mo(110) substrates had the same physical dimensions, so we were able to use the same sample holder and x, y and z sample manipulator positions for each substrate. Assuming constant sticking coefficients for both cesium and barium on W(110) and Mo(110) and that our sources continued to operate consistently, we can directly compare the uptake of the adsorbates on the two substrates. The AES coverage results suggest that it takes 18% longer to reach a monolayer coverage on the Mo(110) for a constant adsorption rate of cesium. We will later compare the differences in cesium dose time between the two substrates from the work function and thermal desorption results presented.

Figure 5.05 shows the plot of the normalized cesium 560 eV APPH and the normalized niobium 167 eV APPH against the cesium deposition time on the Nb(110) surface. Again, we have a similar growth of the cesium Auger signal and the attenuation of the substrate Auger signal. The breakpoints in the normalized cesium 560 eV Auger signal and the normalized niobium 167 eV Auger signal versus cesium dose time occur at approximately 16.0 minutes. The breakpoint versus cesium dose time can not be compared with the other substrates due to the difference in substrate configuration and position relative to the source.

5.1.b Ba/W(110), Ba/Mo(110) and Ba/Nb(110)

Figure 5.06 shows a plot of the normalized barium 73 eV APPH and the normalized tungsten 169 eV APPH against the barium deposition time on the W(110) surface. We also monitored the barium MNN 560 eV Auger peak but found that the low energy Auger transition peak gave us better signal to noise ratio for our particular experimental setup and allowed lower electron beam current densities to be used,

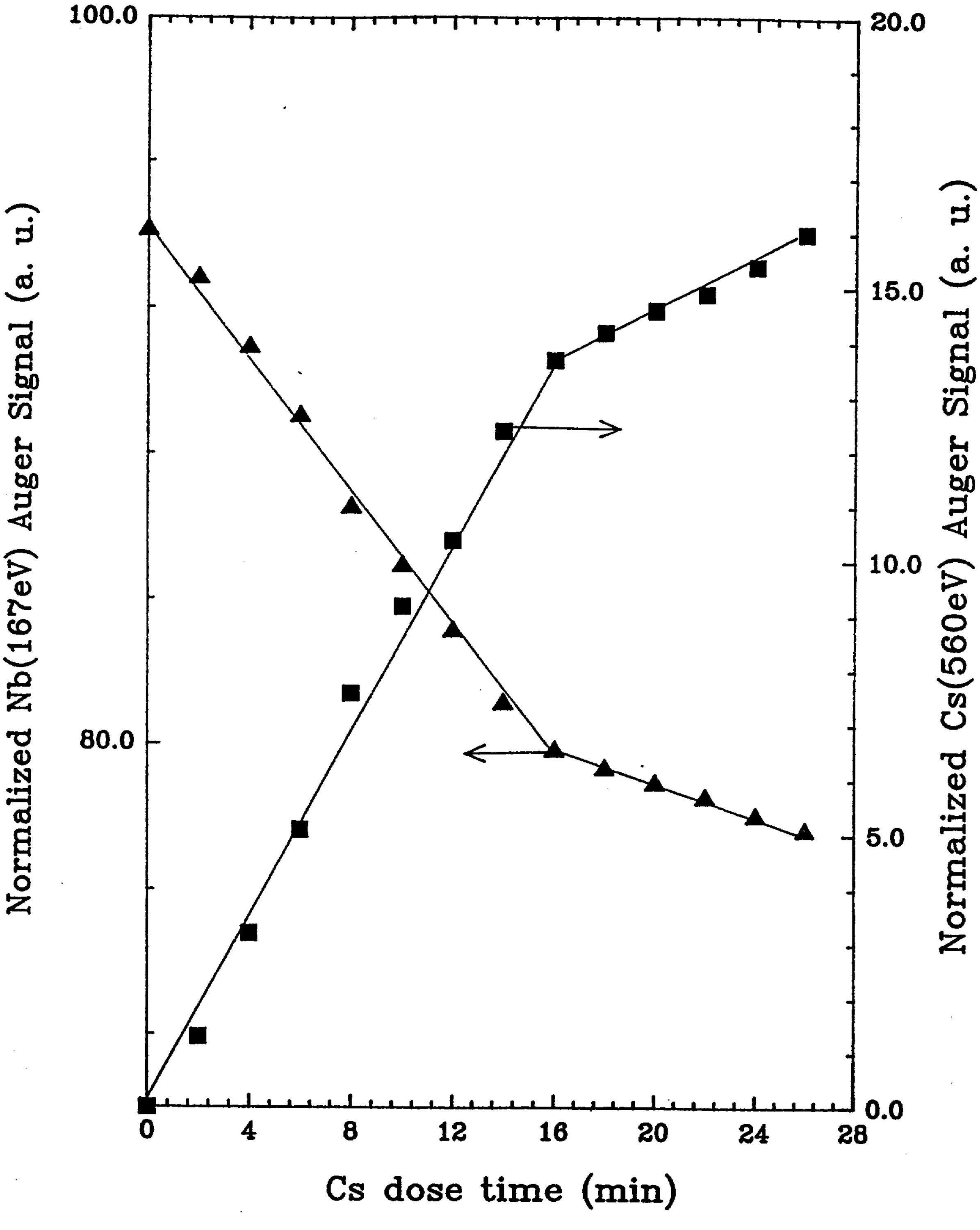

Figure 5.05. Normalized cesium 560 eV APPH and the normalized niobium 167 eV APPH versus cesium dose time.

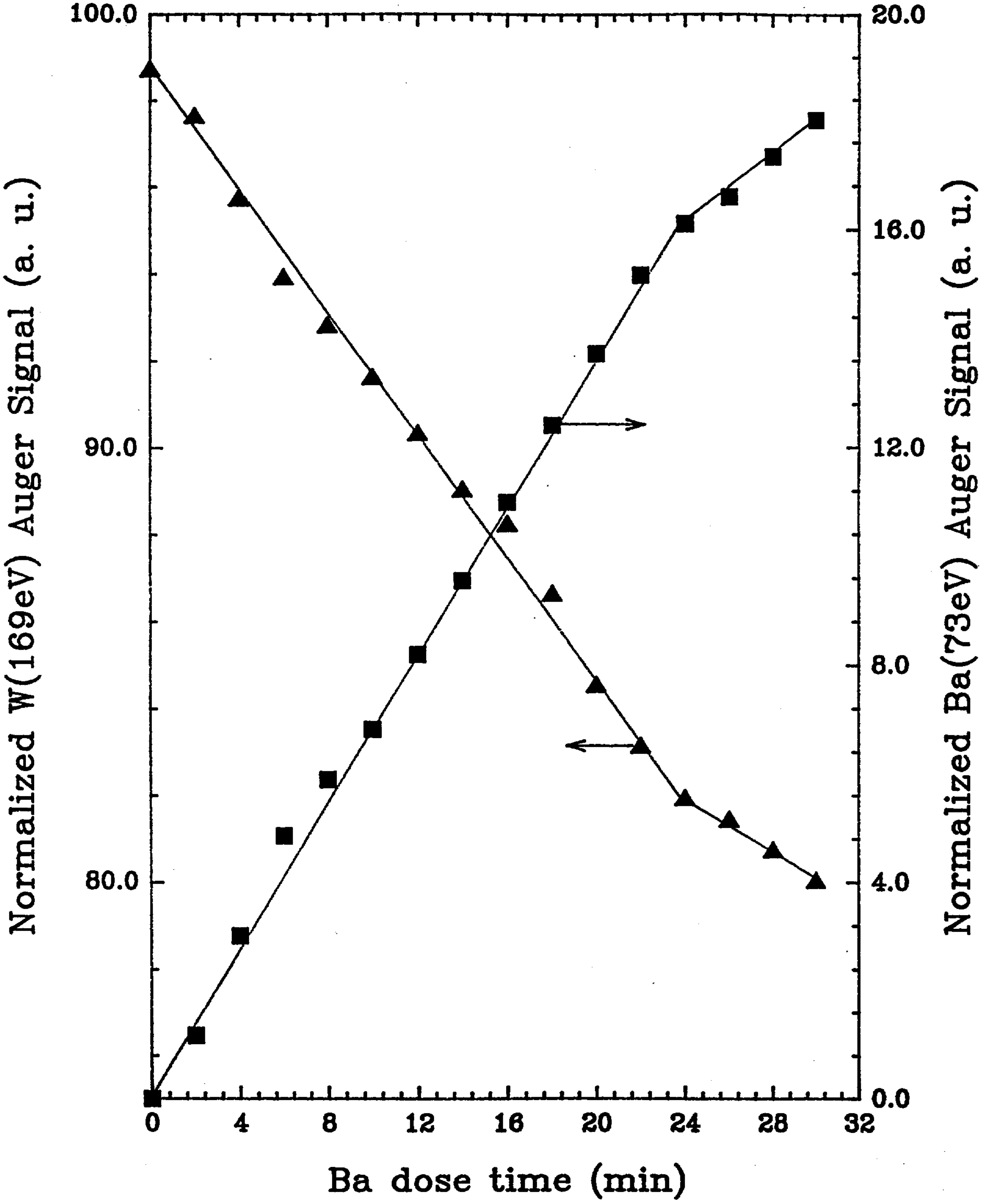

Figure 5.06. Normalized barium 73 eV APPH and the normalized tungsten 169 eV APPH versus barium dose time.

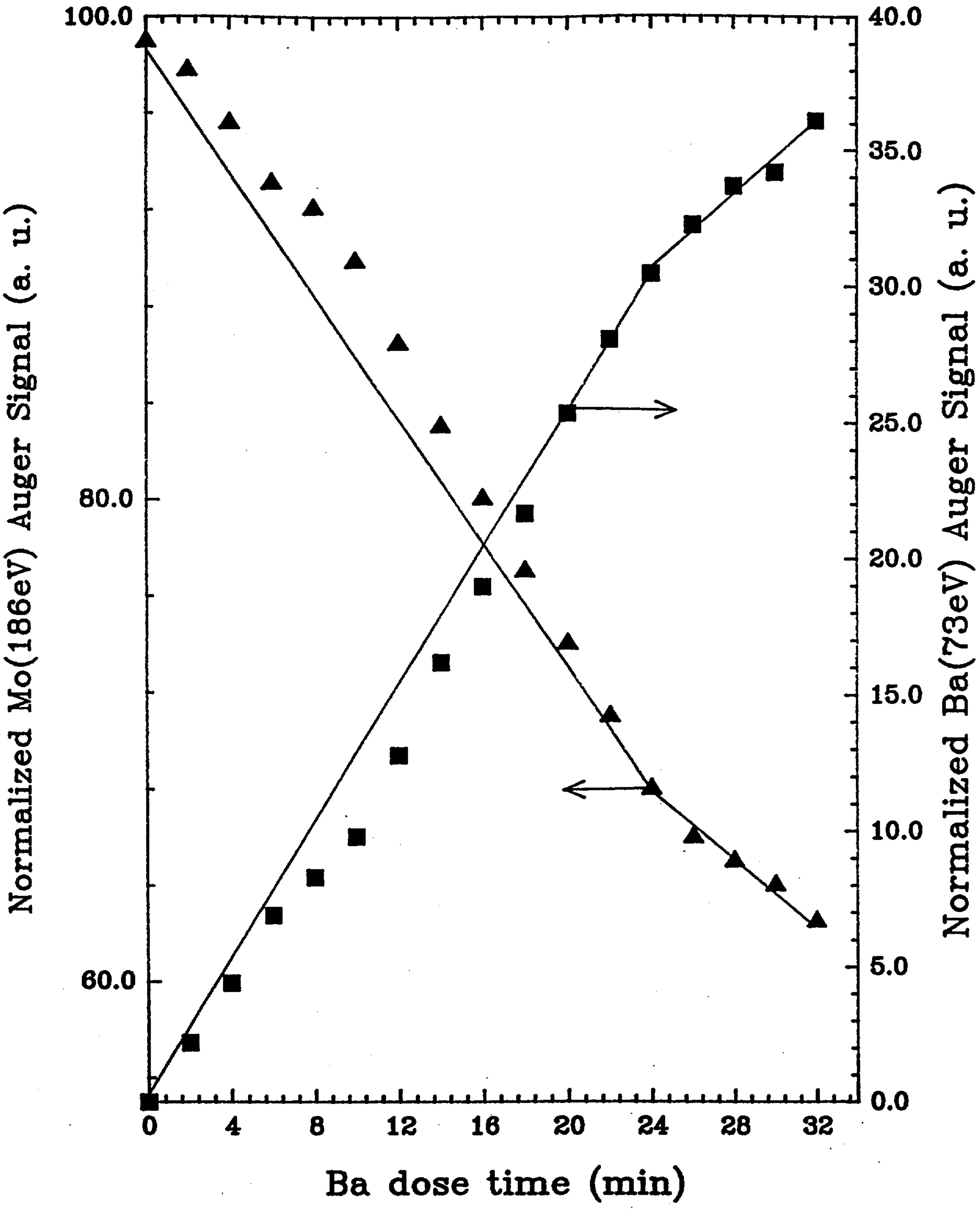

Figure 5.07. Normalized barium 73 eV APPH and the normalized molybdenum 186 eV APPH versus barium dose time.

hence minimizing substrate damage. The 73 eV electrons have a low mean free path compared to the 560 eV electrons, so as the barium adlayer approaches a monolayer , a change in adlayer thickness will be more prominent in the 73 eV APPH. The breakpoint in the normalized barium 73 eV APPH versus barium dose time occurs after approximately 24.0 minutes.

Figure 5.07 shows a plot of the normalized barium 73 eV APPH and the normalized molybdenum 186 eV APPH against the barium deposition time on the Mo(110) surface. The breakpoint in the normalized barium 73 eV APPH versus barium dose time occurs after approximately 24.0 minutes. Following the assumptions made in the previous section about the W(110) and the Mo(110), we can conclude that the adherence of barium is the same for both substrates. Again, we will try justify this assumption in a later discussion.

Figure 5.08 shows a plot of the normalized barium 73 eV APPH and the normalized niobium 167 eV APPH against the barium deposition time on the Nb(110) surface. The breakpoint in the normalized barium 73 eV APPH versus barium dose time occurs after approximately 22.0 minutes.

5.2 Work Function Change for the Various Adsorbate/Metal Surfaces

The effect of adsorption of alkali and alkaline earth metals on the work functions of transition metals was discussed theoretically in detail in chapter 3. It will be seen that the alkali metal cesium has a much greater effect in reducing the work function than does the alkaline earth metal barium for all three of the substrates used in this investigation. The reason for this is that cesium is the most electropositive element and forms an ionic bond with a very positive outward surface dipole layer. However, the work function change due to either cesium or barium behaves in much the same manner. There is an initial drop in the work function versus adsorbate dose time to a minimum value and then a rise to a local maximum as the adsorbate coverage approaches a monolayer. The height of the local maximum usually corresponds to the approximate value of the bare work function of the pure adsorbate. This particular behavior does not only occur on transition metal surfaces but also on simple metal surfaces, refractory metal carbides and borides and semiconductors.

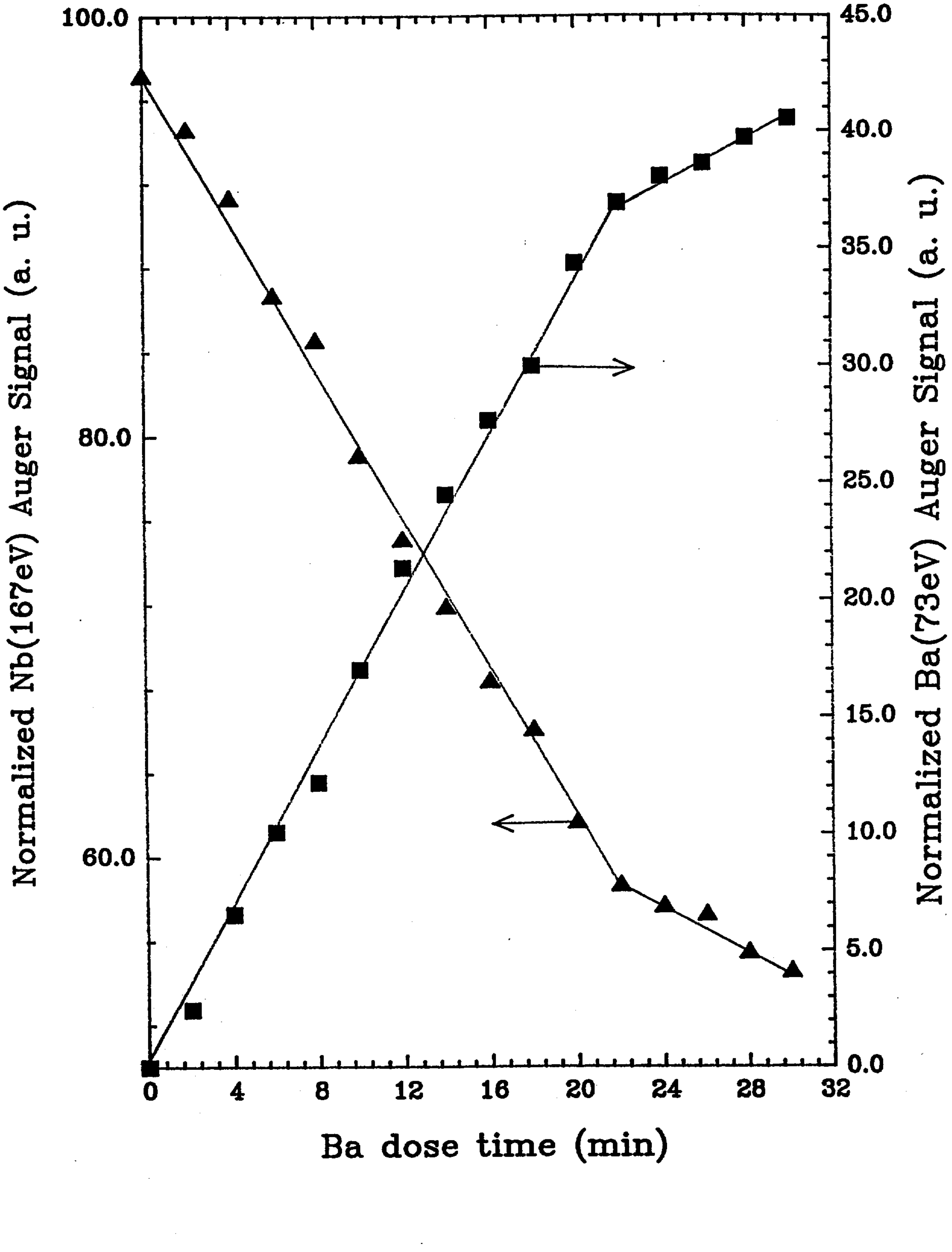

Figure 5.08. Normalized barium 73 eV APPH and the normalized niobium 167 eV APPH versus barium dose time.

5.2.a Cs/W(110), Cs/Mo(110) and Cs/Nb(110)

The work function change of the W(110) surface versus cesium dose time is shown in Fig. 5.09. The change in work function curve is characteristic of alkali metal adsorption onto refractory metal surfaces. As cesium is deposited on the W(110) surface, the work function decreases from its initial value of 5.37 eV to a minimum value of 1.55 eV after ~10.0 minutes, and then rises again to a local maximum of 2.18 eV after 18.0 minutes or a "saturated" cesium coverage. The minimum value of 1.55 eV is in good agreement with previous studies[12,13] of the work function change of W(110) due to the adsorption of cesium. The slight differences in work function minimum found in these two experiments could result from either the physical conditions of W(110) surface before cesium deposition or from the difference in the work function measurement techniques used in each experiment. The minimum work occurred at approximately the same coverage for the three separate experiments: 0.56 monolayers (ML) for this investigation, ~0.60 for Ref. 12 and 0.64 for Ref. 13.

The work function change of the Mo(110) surface versus cesium dose time is shown in Fig. 5.10. The work function change versus cesium deposition curve for Mo(110) is very similar to that shown for W(110) in Fig. 5.09. As cesium is deposited onto the Mo(110) surface, the work function decreases from its initial value of 5.07 eV to a minimum value of 1.50 eV after ~12.0 minutes, and then rises again to a local maximum of 2.20 eV after 22.0 minutes or a saturated cesium coverage.

The work function change of the Nb(110) surface versus cesium dose time is shown in Fig. 5.11. This curve is again very similar to that shown for W(110) and Mo(110). As cesium is deposited on the Nb(110) surface, the work function decreases from its initial value of 4.62 eV to a minimum value of 1.47 eV after ~8.0 minutes, and then rises again to a local maximum of 2.40 eV after 16.0 minutes or cesium saturation. From the work function change versus cesium deposition curve, we can observe the effect the small concentration of oxygen on the surface and in the bulk of the Nb(110) substrate has on the work function of the Cs/Nb(110) surface. The oxygen causes a minimum work function value that is less than expected and a relatively high work function value at the cesium saturation coverage. It also results in achieving the minimum work function at lower cesium coverage than on the

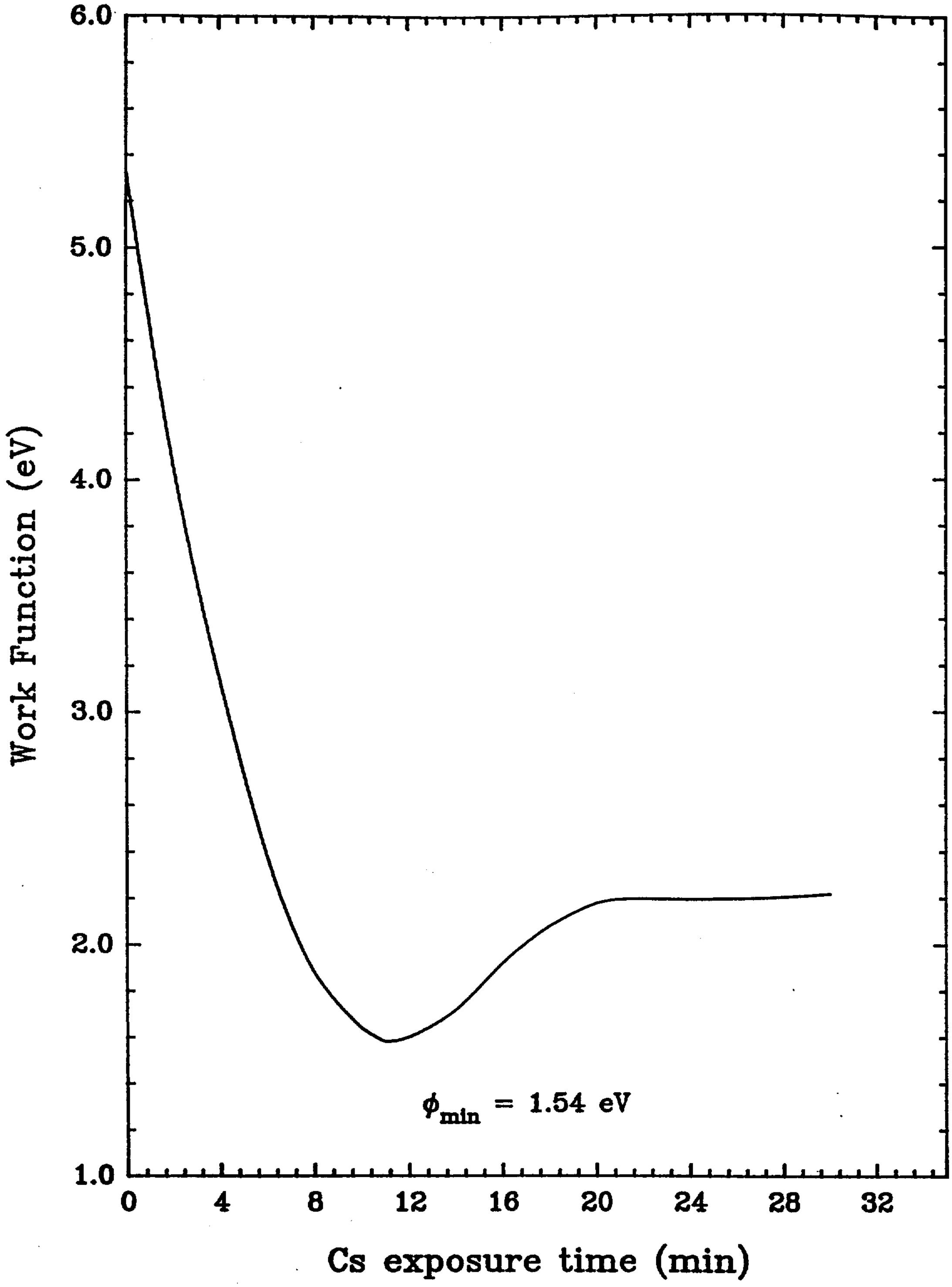

Figure 5.09. Work function change for the W(110) surface versus cesium dose time.

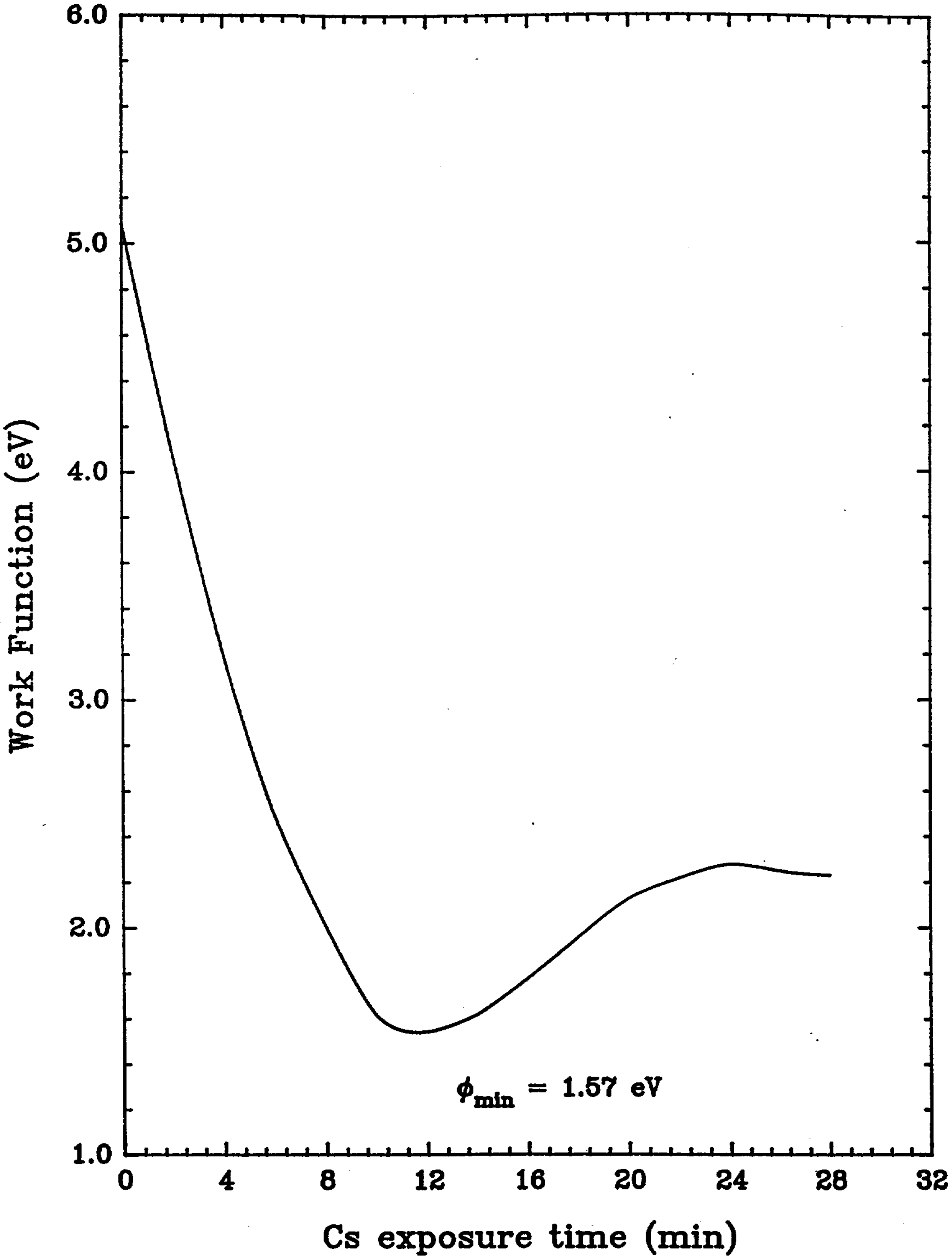

Figure 5.10. Work function change for the Mo(110) surface versus cesium dose time.

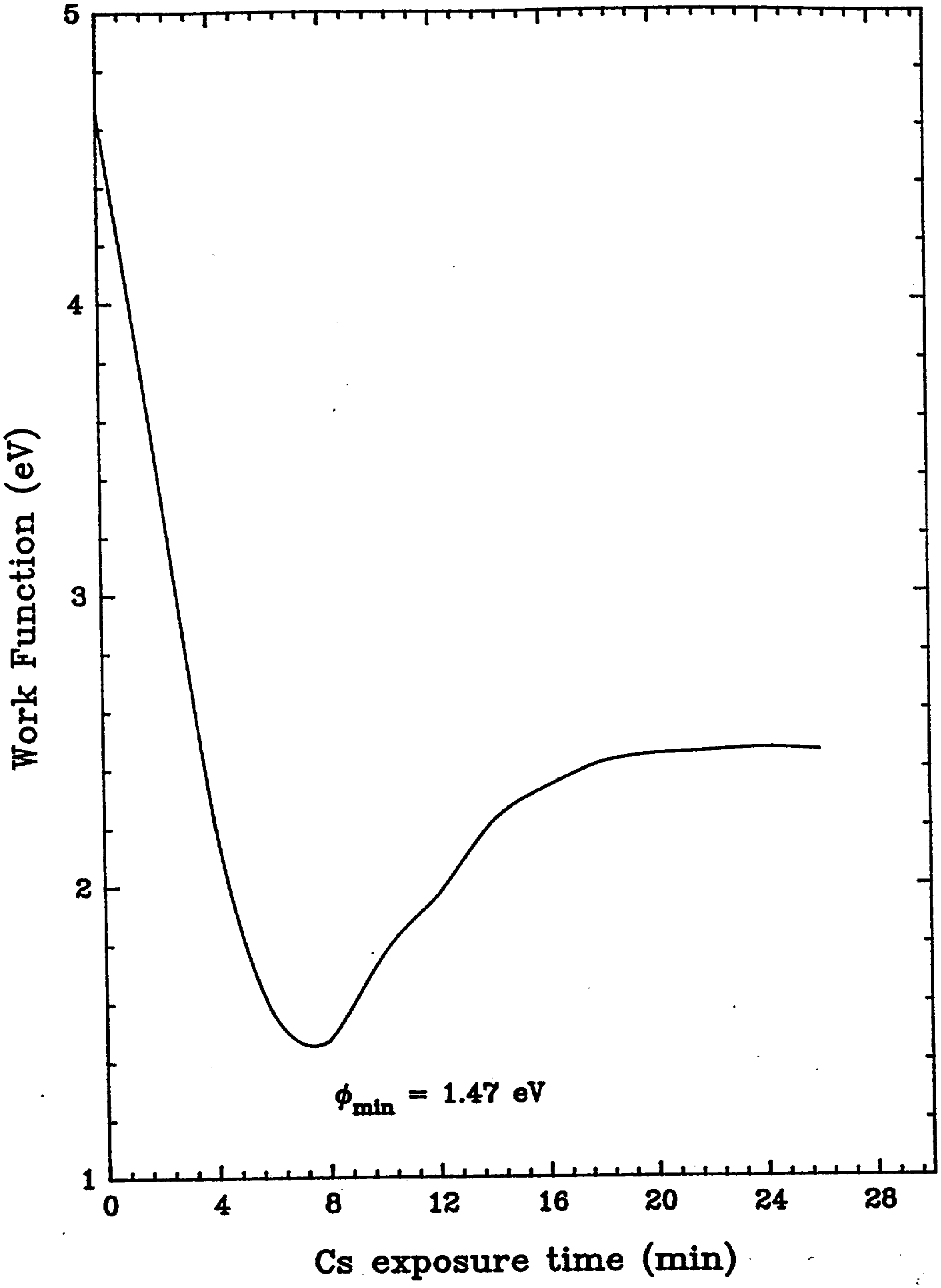

Figure 5.11. Work function change for the Nb(110) surface versus cesium dose time.

W(110) or the Mo(110) surfaces. The minimum work function for the Nb(110) surface occurred at 0.5 ML of cesium coverage compared to 0.55 ML for the Cs/Mo(110) surface and 0.56 ML for the Cs/W(110) surface.

5.2.b Ba/W(110), Ba/Mo(110) and Ba/Nb(110)

The work function change for the W(110) surface versus barium dose time is shown in Fig. 5.12. The work function change due to barium deposition is similar to that of cesium on the W(110) surface. We have initial drop in the work function to a minimum value after 12.0 minutes of deposition and then a rise to a local maximum after we reach an approximate monolayer of coverage. The one big difference between barium and cesium adsorption is the value of the minimum work function. The W(110) surface only reaches a minimum work function of only 2.21 eV with barium exposure compared to a 1.55 eV work function minimum due to cesium exposure. Our minimum work function value is ~0.15 eV greater than the value found in the literature[14,15]. One other difference is that the minimum work function value is obtained at less of a barium coverage. The minimum occurs at ~0.5 monolayers of barium compared to 0.56 monolayers of cesium. It was also found from the work function change versus barium coverage curve that the structure of the adlayers of barium have some effect on the work function. The slight slope changes in the initial drop of the work function to the minimum have been correlated to changes in the adlayer structure[5]. These effects are more apparent on the Mo(110) surface.

The work function change for the Mo(110) surface versus barium dose time is shown in Fig. 5.13. Again, we observe a initial drop in the work function to a minimum value of 2.20 eV and then a rise to a local maximum after we reach a monolayer of barium. The minimum work function value due to the adsorption of the alkaline earth metal barium is again approximately 0.65 eV above the minimum value found for the Cs/Mo(110) surface. The effect the adlayer structure changes have on the work function are seen more easily in the work function change versus barium exposure curve of the Mo(110) surface. There is a definite change in the slope of the curve after about 4.0 to 5.0 minutes. The interpretation of these breakpoints in terms of changes in the adlayer structure will be discussed in a later section. The work

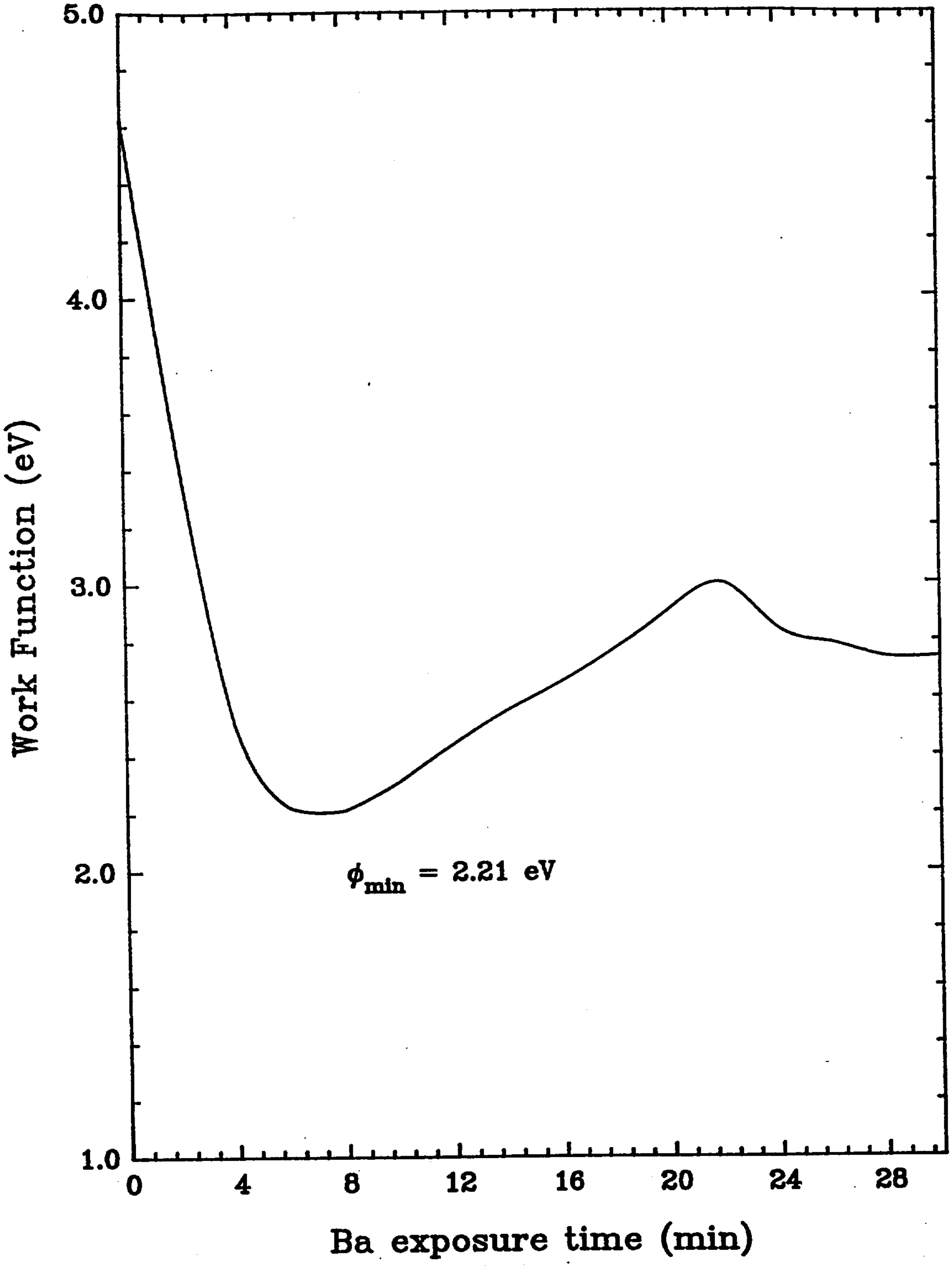

Figure 5.12. Work function change for the W(110) surface versus barium dose time.

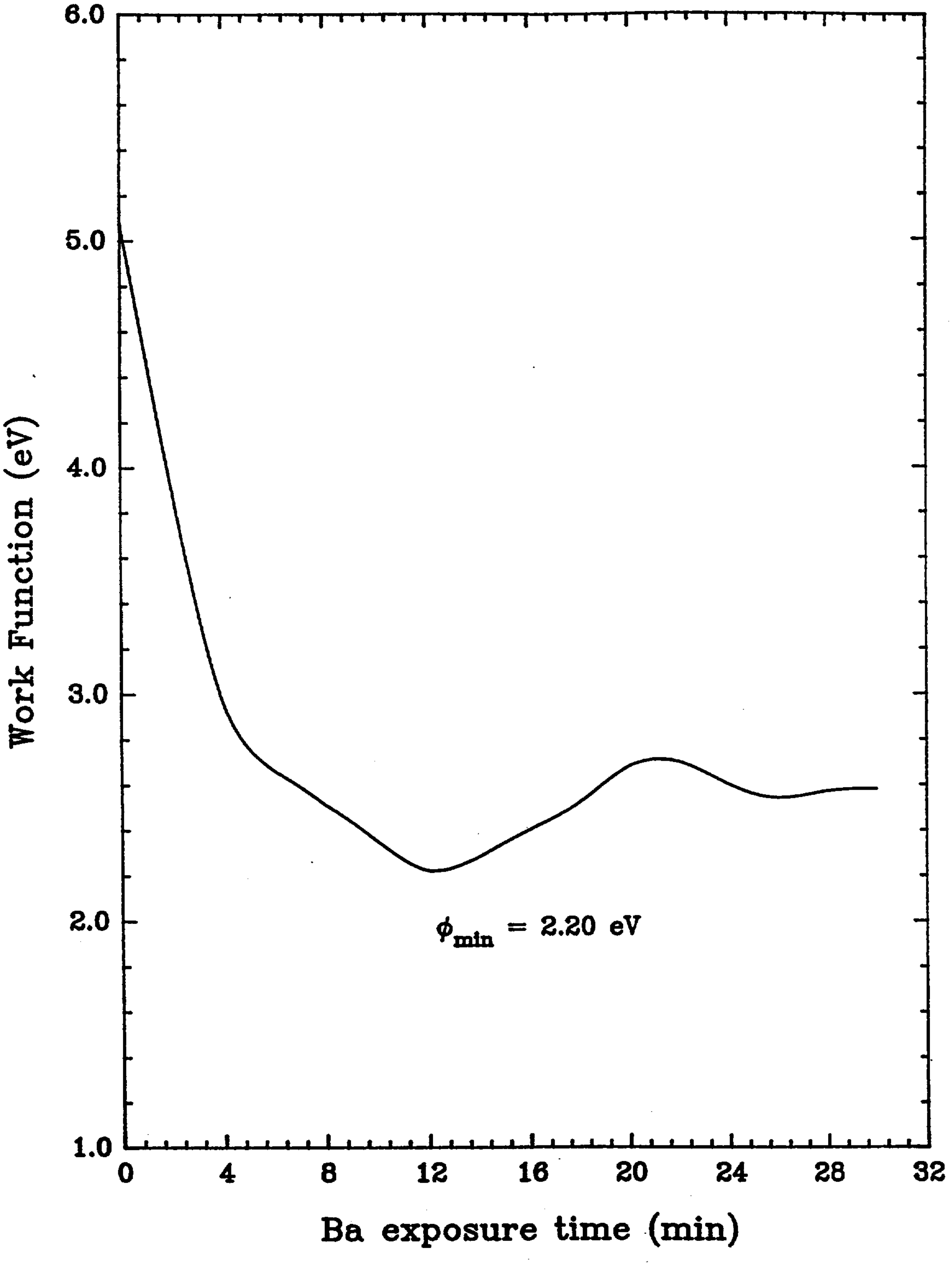

Figure 5.13. Work function change for the Mo(110) surface versus barium dose time.

function change for the Nb(110) surface versus barium dose time is shown in Fig. 5.14. The adsorption of barium on the Nb(110) surface results in a characteristic work function change curve but has a greater initial slope compared to the Ba/W(110) and the Mo(110) surfaces, even though the minimum work function value of 2.21 eV is approximately the same for all the surfaces. The minimum work function for the Nb(110) surface is reached after 0.4 monolayers of barium compared to 0.5 monolayers for both the W(110) surface and Mo(110) surface. The difference is again attributed to the small concentration of oxygen on the surface of the Nb(110) and the structural changes caused by the oxygen in the bulk of the niobium.

5.2.c Cs-Ba/W(110), Cs-Ba/Mo(110) and Cs-Ba/Nb(110)

The experiments involving the co-adsorption of cesium and barium on W(110), Mo(110) or Nb(110) consisted of preparing an adsorbed layer of barium at a particular coverage, and then adsorbing cesium at fixed rate for two minute intervals. Figures 5.15, 5.16 and 5.17 give the results of the work function change versus cesium dose time onto the preadsorbed barium layers on the surface of W(110), Mo(110) and Nb(110), respectively. For all three surfaces, the figures show that the minimum work function increases with a greater barium pre-coverage and the amount of cesium required to reach the minimum value decreases. It can also be seen on all three substrates that cesium adsorption has little effect on the work function for pre-absorbed layers of barium of greater than 0.5 monolayers. The work function simply decreases to the value (2.15 eV) that characterizes a monolayer of cesium on a clean surface. The work function results shown here are almost identical to those Konoplev[14] and co-workers measured for cesium and barium co-adsorption on W(110).

5.3 Thermal Desorption from the Adsorbate/Metal Surfaces

Next, we want to give the results of the thermal stability studies of the cesium and barium adatoms on the W(110), Mo(110) and Nb(110) surfaces. From these studies, we find how the activation energies of desorption of neutral cesium and barium adatoms vary with coverage. The thermal desorption spectra presented for the three surfaces show that as the cesium coverage increases the high energy (low coverage)

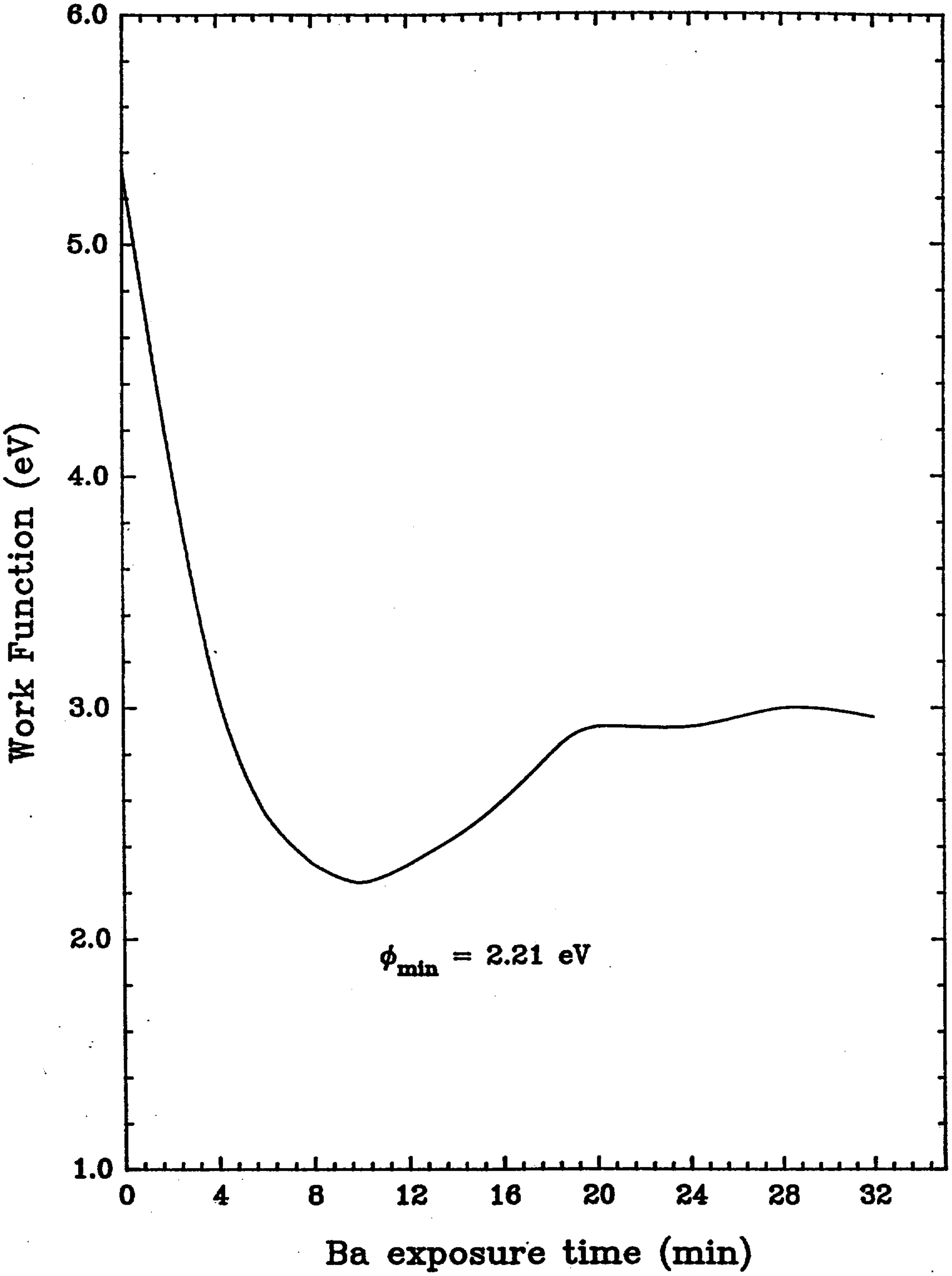

Figure 5.14. Work function change for the Nb(110) surface versus barium dose time.

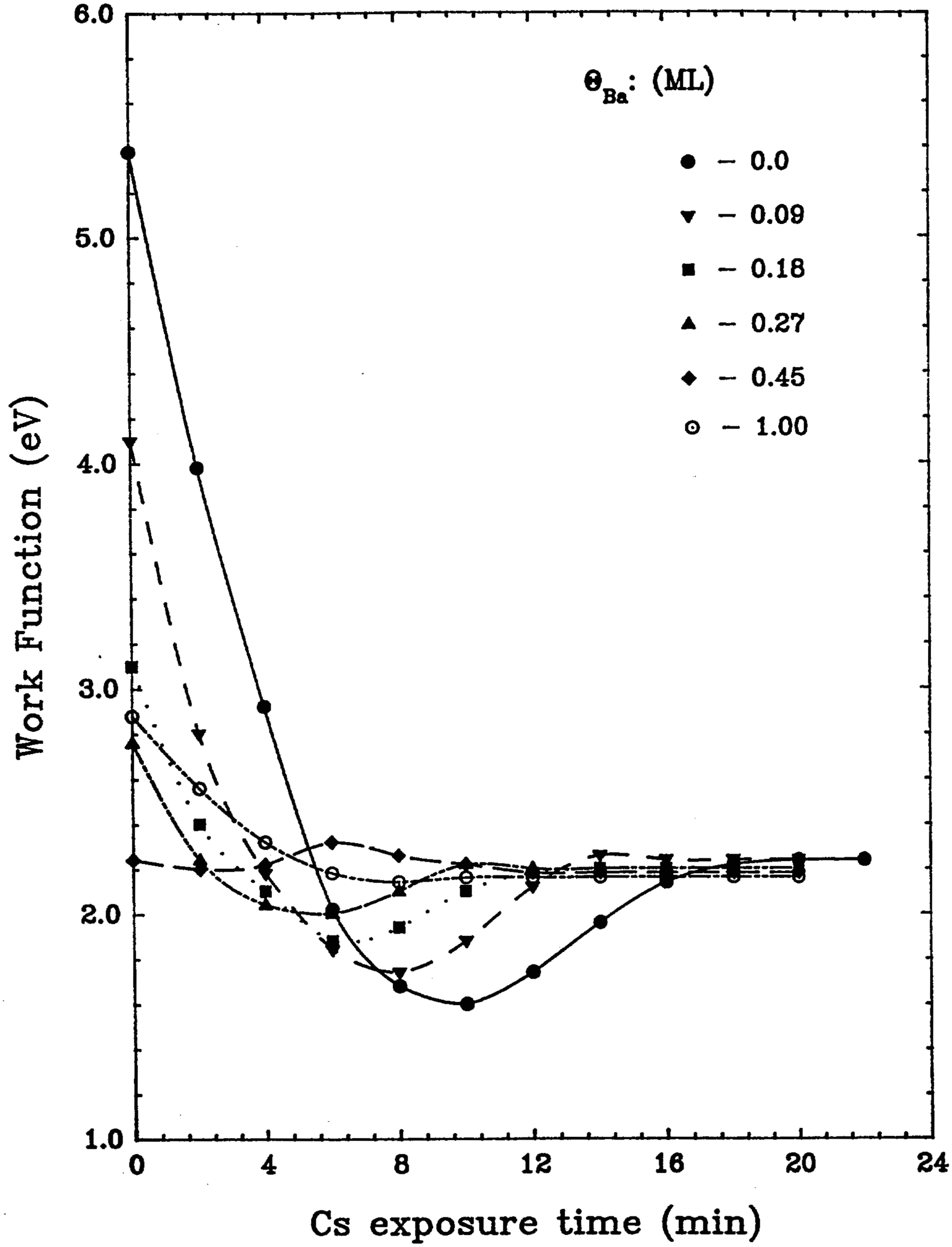

Figure 5.15. Work function change for the W(110) surface versus cesium dose time with various initial coverages of barium.

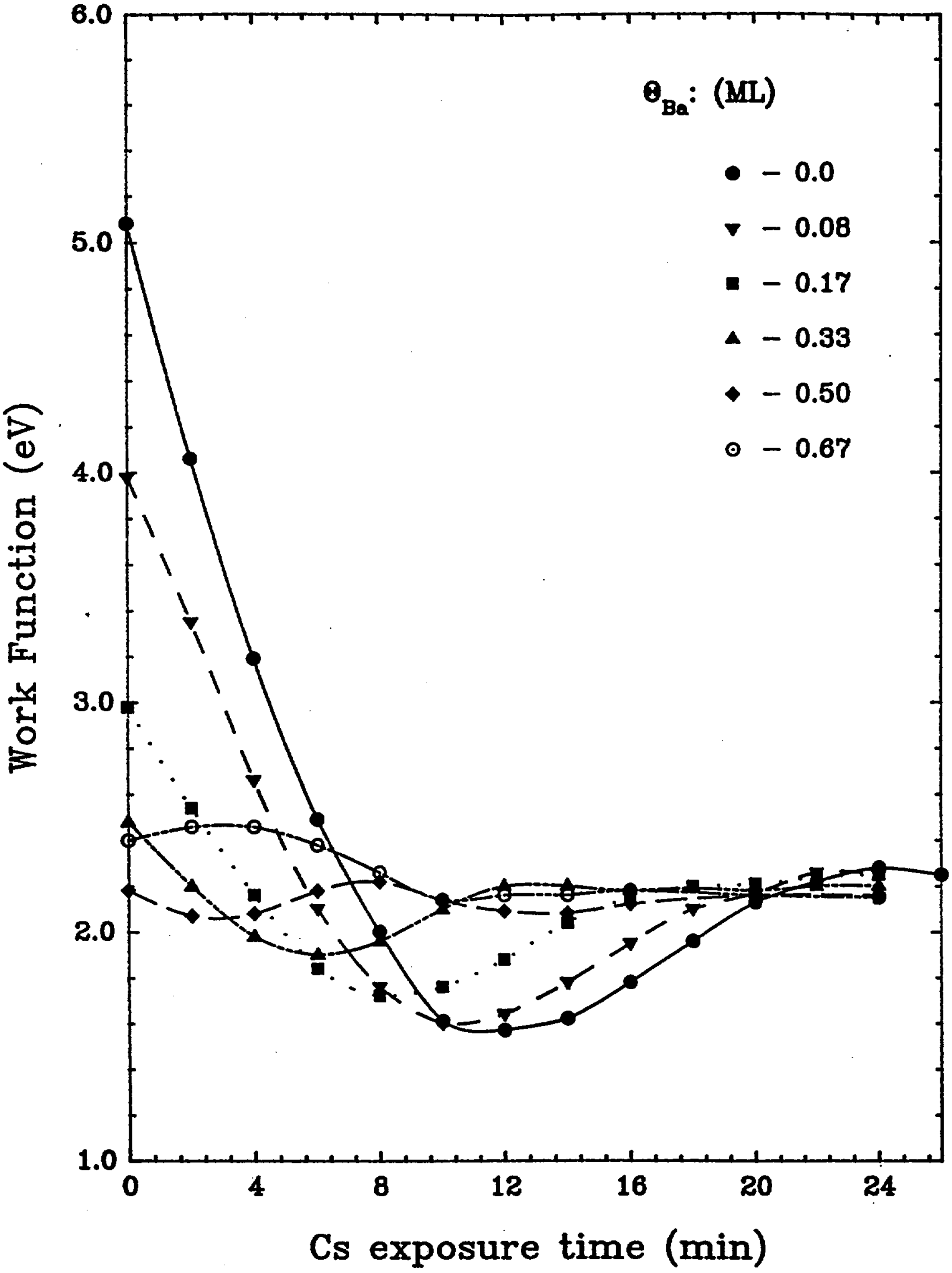

Figure 5.16. Work function change for the Mo(110) surface versus cesium dose time with various initial coverages of barium.

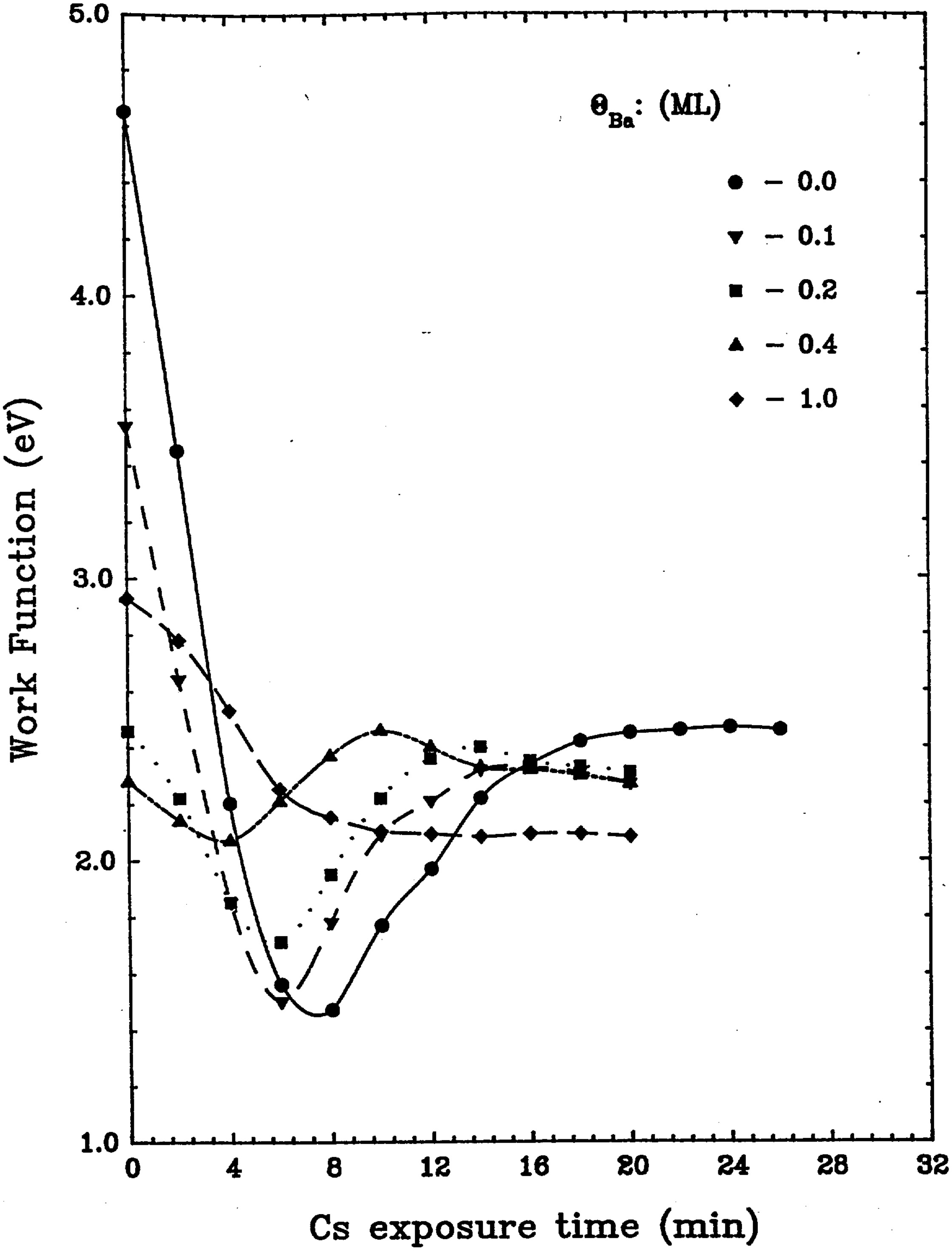

Figure 5.17. Work function change for the Nb(110) surface versus cesium dose time with various initial coverages of barium.

desorption peak shifts to lower temperature. A shift in the activation energy with coverage implies that the activation energy of cesium is dependent on the coverage. The thermal desorption spectra of the three surfaces show that barium acts in a similar manner, but the high energy desorption peak only shifts slightly as the coverage increases. The slight shift in the barium activation energy shows that the it is only weakly dependent on the coverage. Nevertheless, the activation energies were calculated using first order desorption kinetics using eqn. 4.16, with the pre-exponential factor assumed to be $\nu_1 = 10^{13}$ sec^{-1}. The substrates were heated linearly ($T = T_0 + \beta t$) with a β between 35 and 40 K/sec. The heating rate was limited by the physical dimensions of our substrates and the power supplies used. It was assumed that the second layer of adsorbate would also follow first order desorption kinetics since the surface had not yet attained bulk properties of the adsorbate.

5.3.a Cesium from W(110), Mo(110) and Nb(110)

Thermal desorption spectra for cesium from the W(110) surface are shown in Fig. 5.18. The thermal desorption spectrum shows that cesium has four distinct binding states with temperatures of 400 K, 520 K, 720 K and 1200 K and activation energies of 3.08 eV, 1.77 eV, 1.30 eV and 0.96 eV, respectively. The four states correspond to cesium coverages of 0.1 ML, 0.4 ML, 1.0 ML and 1.2 ML. The highest temperature peak represents the cesium-substrate bond with little cesium-cesium adatom interaction taking place. As the coverage increases, the strength of the positive cesium dipole layer is weakened by the repulsive interaction of the cesium adatoms. The peak occurring at the lowest temperature (or highest cesium coverage) corresponds to the onset of the second monolayer of cesium, but at room temperature, as seen in Fig. 5.03, a stable second monolayer of cesium is unable to grow on a clean refractory metal surface. The activation energy of this peak is close to the sublimation energy of bulk cesium. As the coverage approached a monolayer, the activation energy approached a value of 1.30 eV.

Thermal desorption spectra for cesium from the Mo(110) surface are shown in Fig. 5.19. We found three binding states for cesium on the Mo(110) surface. They occur at temperatures of 575 K, 720 K and 1110 K with corresponding activation energies of 2.85 eV, 1.77 eV and 1.43 eV. The three binding states occur at cesium

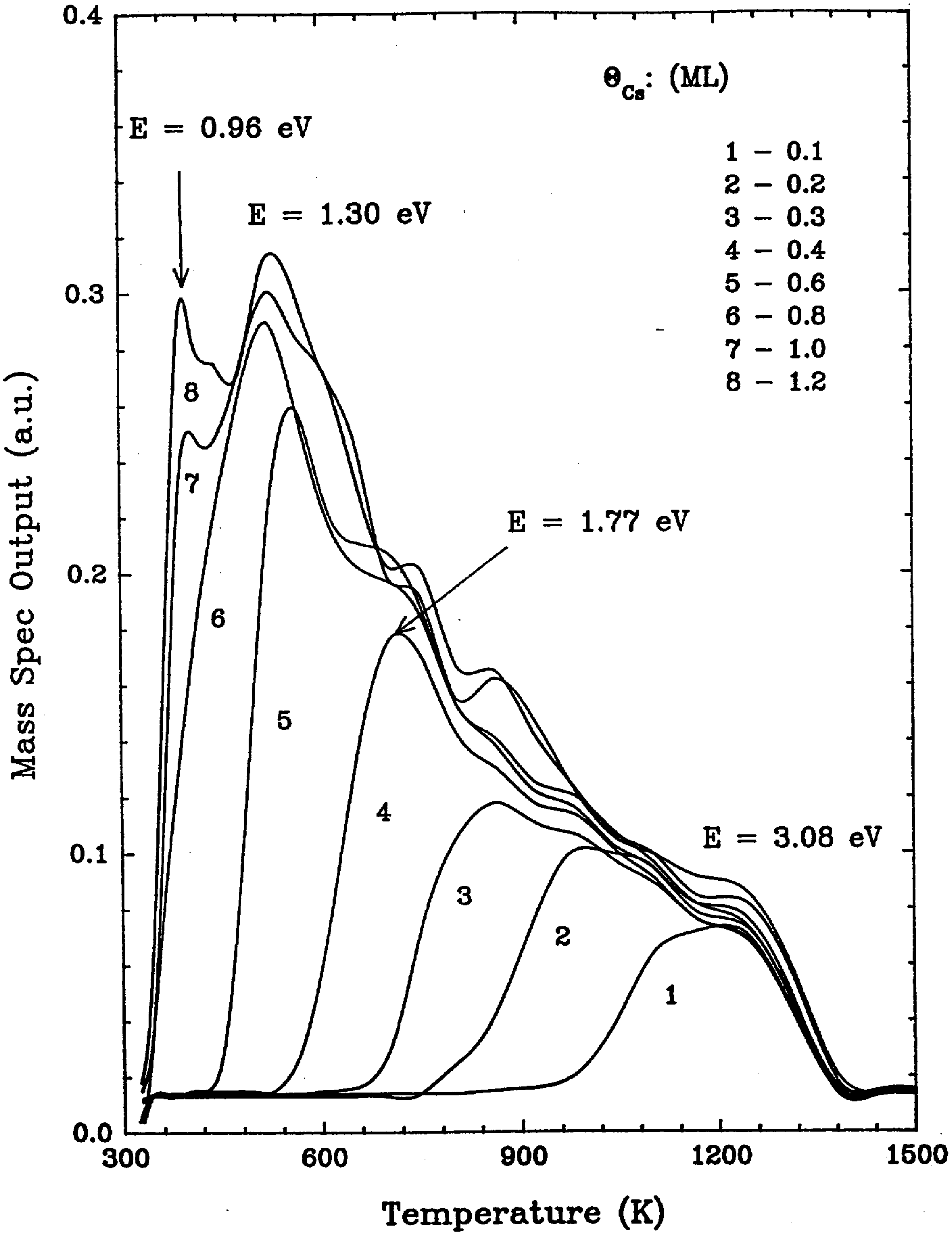

Figure 5.18. Thermal desorption spectra for cesium from the W(110) surface.

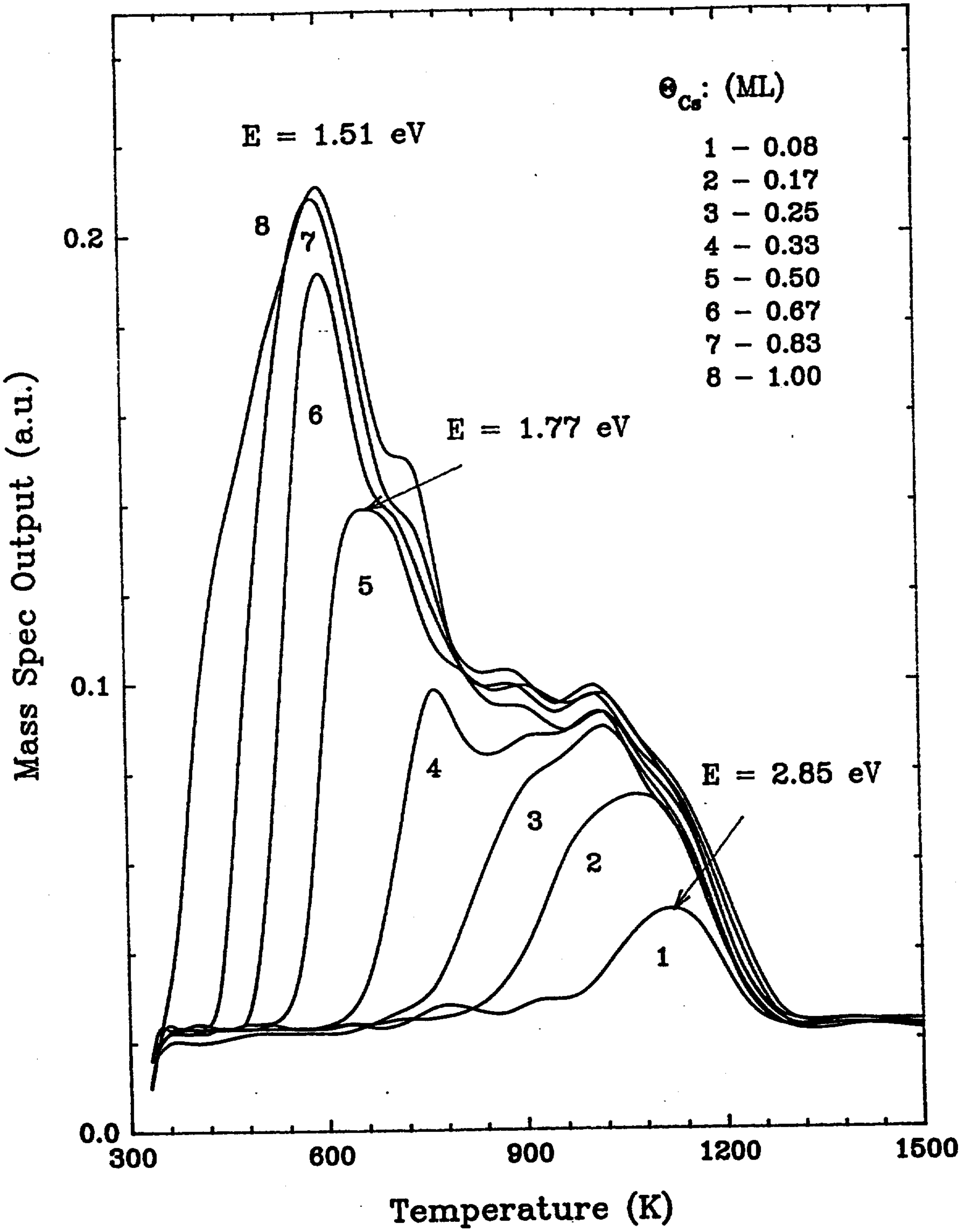

Figure 5.19. Thermal desorption spectra for cesium from the Mo(110) surface.

coverages of 0.1 ML, 0.5 ML and 1.0 ML. The near zero activation energy (low coverage) for cesium on Mo(110) is approximately 0.25 eV less than the near zero activation energy found for the Cs/W(110) surface, but the activation energy at the onset of a monolayer of coverage is 0.10 eV greater than for the Cs/W(110) surface.

Thermal desorption spectra for cesium from the Nb(110) surface are shown in Fig. 5.20. Like the thermal desorption spectra of the Cs/W(110) surface, we find four binding states for cesium on the Nb(110) surface. They occur at temperatures of 410 K, 530 K, 710 K and 950 K. The four binding states correspond to cesium coverages of 0.13 ML, 0.50 ML, 1.00 ML and 1.25 ML. The near zero activation energy of cesium is substantially lower on the Nb(110) surface than on the other two surfaces. This is connected to the fact that the initial work function of the Nb(110) surface is so low and the dipole moment of cesium is weak. The low temperature desorption peak occurs from the onset of second layer of cesium.

5.3.b Barium from W(110), Mo(110) and Nb(110)

The thermal desorption spectra of barium from the W(110), Mo(110) and Nb(110) surfaces do not show distinct binding states, but indicate a continuous decrease in the activation energy to a monolayer of coverage. Figures 5.21, 5.22 and 5.23 show the thermal desorption spectrums for barium from the three substrates. On each surface, the barium forms three distinct desorption peaks with the highest activation energy corresponding to the lowest barium coverage. For near zero coverage, the activation energy for barium desorption was 4.35 eV for W(110), 3.86 for Mo(110) and 3.72 for Nb(110). The highest activation energy represents the amount of energy needed to remove the last barium adatom from the surface of the substrate. The thermal desorption of barium from the three substrate behaves like cesium in that it forms a stronger bond with W(110) and the weakest bond with Nb(110). The activation energy decreases with increasing barium coverage up to a monolayer of coverage, where activation energies of 3.40 eV, 3.13 eV and 2.98 eV were observed for W(110), Mo(110) and Nb(110), respectively. The third desorption peak seen in the thermal desorption spectra begins to appear after the completion of a monolayer of barium and corresponds to desorption from a barium-barium bond such as would occur in bulk barium.

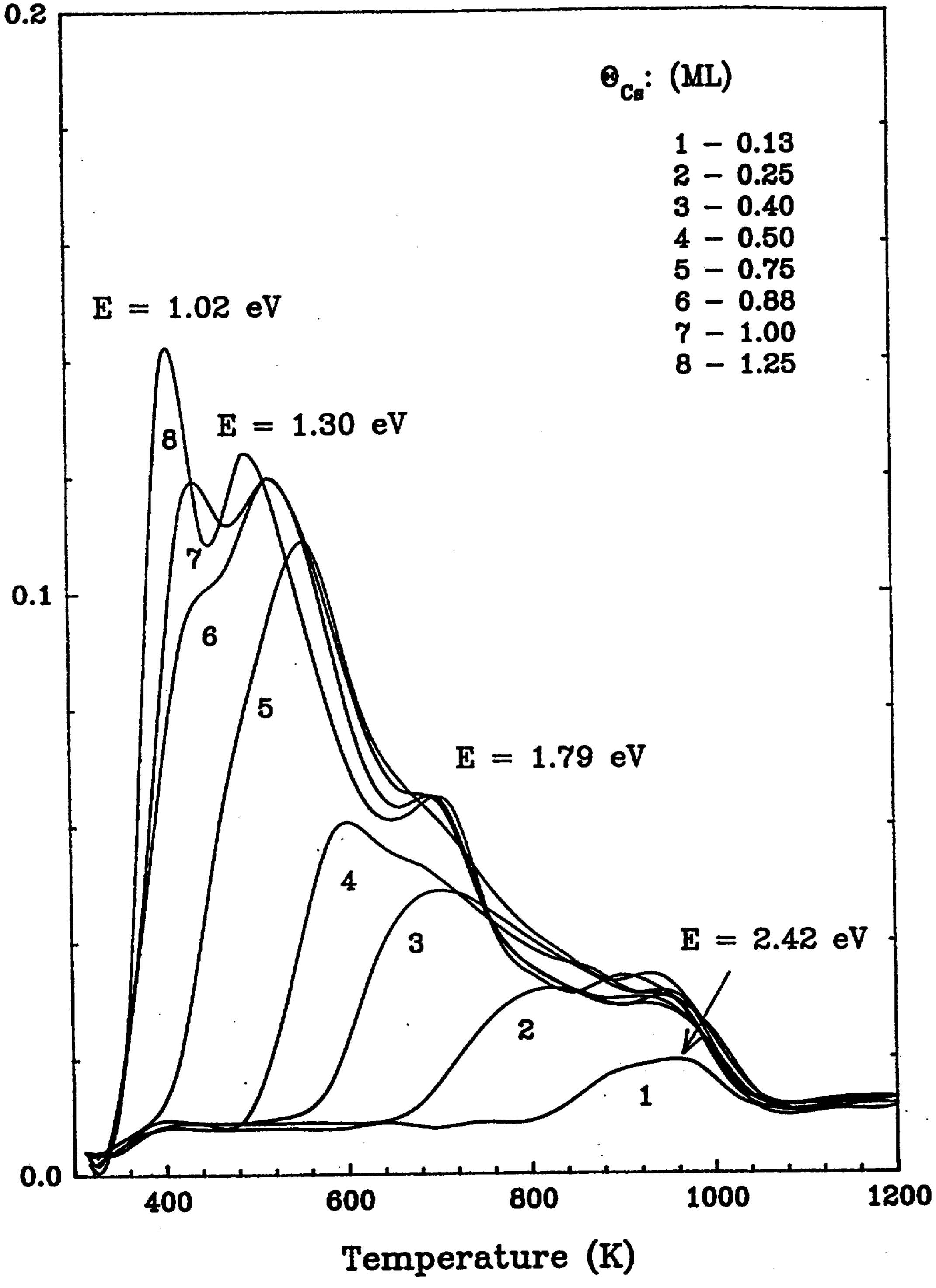

Figure 5.20. Thermal desorption spectra for cesium from the Nb(110) surface.

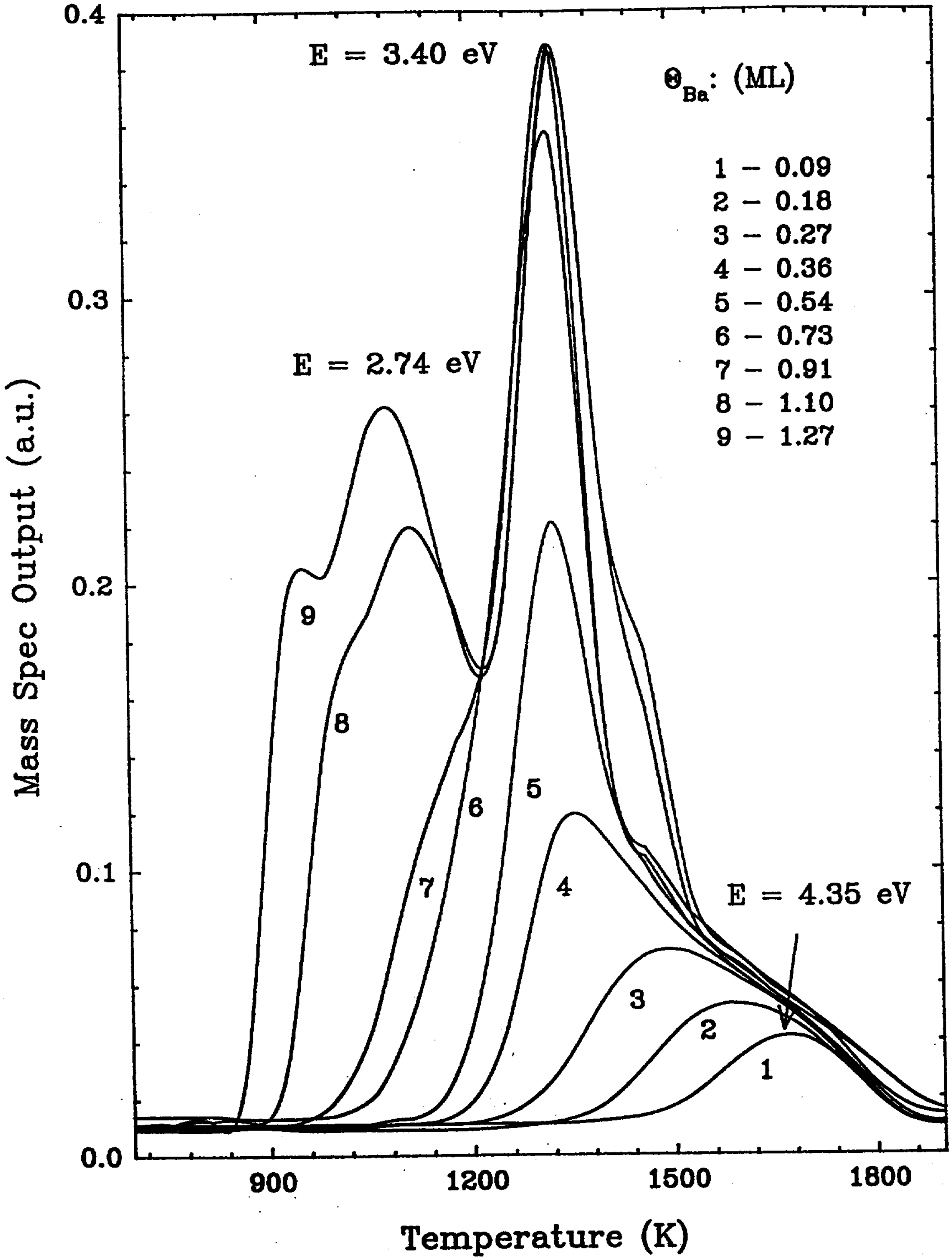

Figure 5.21. Thermal desorption spectra for barium from the W(110) surface.

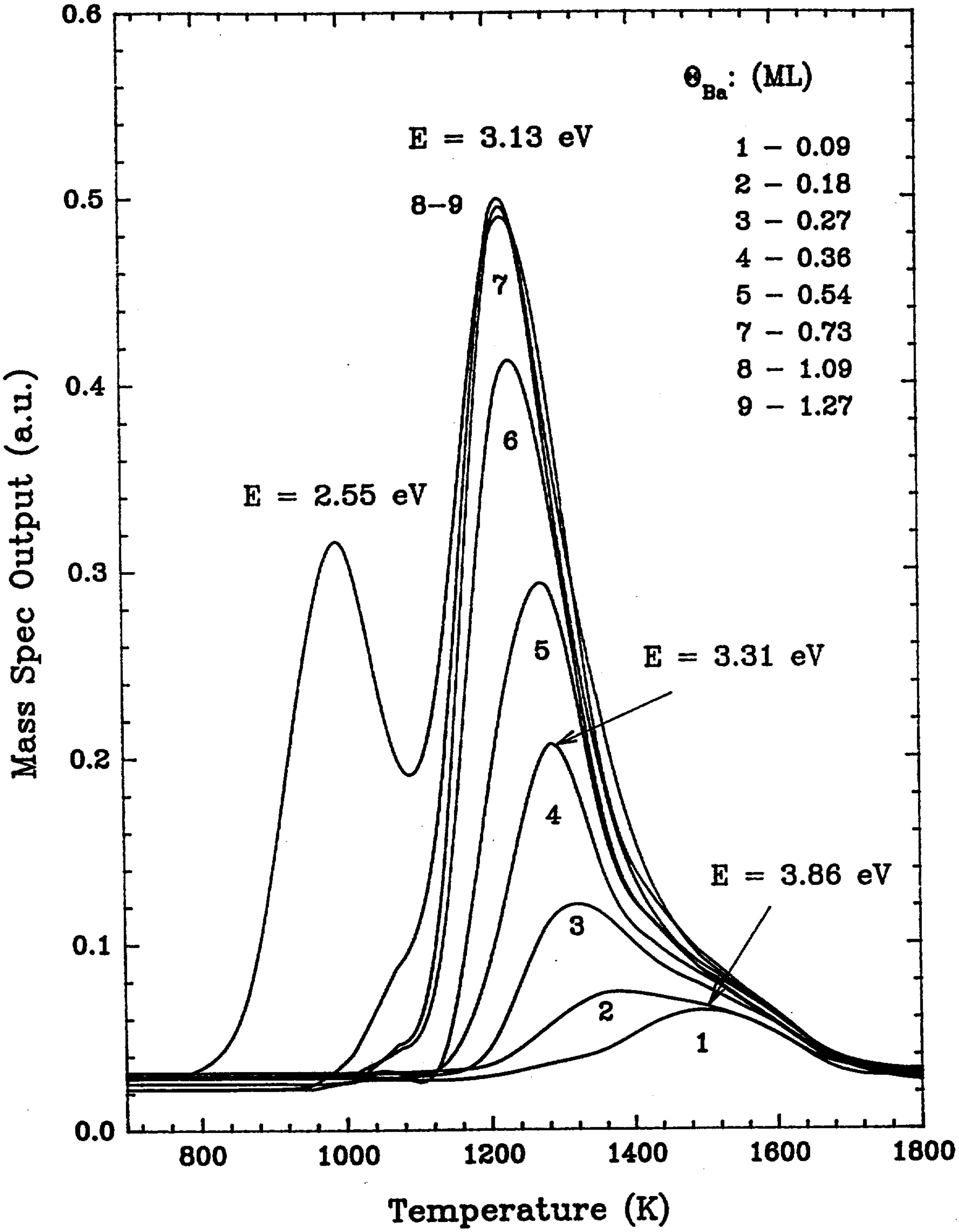

Figure 5.22. Thermal desorption spectra for barium from the Mo(110) surface.

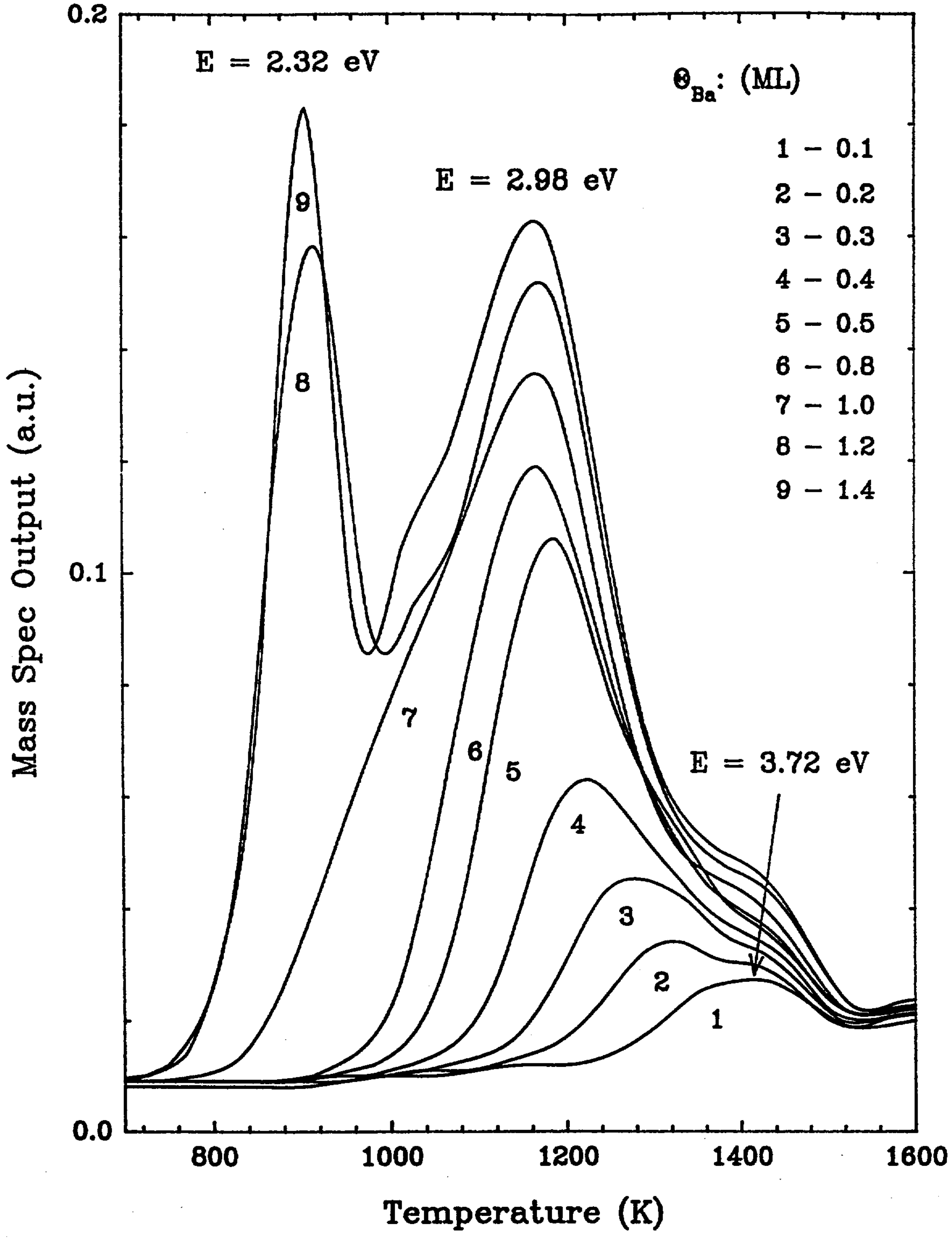

Figure 5.23. Thermal desorption spectra for barium from the Nb(110) surface.

5.3.c Cesium from the W(110), Mo(110) and Nb(110) with Various Amounts of Pre-Adsorbed Barium

The most apparent property of barium and cesium is that they desorb separately from a mixed layer and at significantly different temperatures. The temperature difference between the binding states of cesium and barium on all three of the surfaces allows for the adsorption and desorption of cesium without altering the barium adlayer. The adsorbed layers were prepared in the same manner as discussed earlier in the work function results. Even though the barium layer is unaltered after the desorption of cesium from the mixed adlayers, the substrate was flashed clean before each run and a new layer of barium was adsorbed. By cleaning the substrate between data runs, we were able to limit surface contamination during the desorption process and to insure consistent results. The desorption behavior of cesium from the various barium/substrate surfaces was very similar. As the coverage of pre-adsorbed barium increased, the activation energy of the cesium decreased. When the pre-adsorbed barium coverage becomes greater than 0.5 ML, as in the case of the work function for mixed vapor systems, the desorption behavior of the cesium resembles that of cesium from a clean metal surface.

Figures 5.24 - 5.29 show a set of thermal desorption spectra for different fixed amounts of cesium desorbed from W(110) with pre-adsorbed barium coverages of 0.00, 0.09, 0.18, 0.27, 0.36, 0.54 and 0.73 ML. The activation energies for desorption of cesium for the various combinations of mixed adsorbates are given in the figures and summarized in Table 5.01.

Figures 5.30 - 5.35 show a set of thermal desorption spectra for different fixed amounts of cesium desorbed from Mo(110) with pre-adsorbed barium coverages of 0.08, 0.17, 0.25, 0.33, 0.50, and 0.67 ML. The activation energies for desorption of cesium from the various Ba/Mo(110) surfaces are given in the figures and summarized in Table 5.02.

Figures 5.36 - 5.40 show a set of thermal desorption spectra for different fixed amounts of cesium desorbed from Nb(110) with pre-adsorbed barium coverages of 0.00, 0.10, 0.20, 0.40, and 0.60 ML. The activation energies for desorption of cesium from the various Ba/Nb(110) surfaces are given in the figures and summarized in Table 5.03.

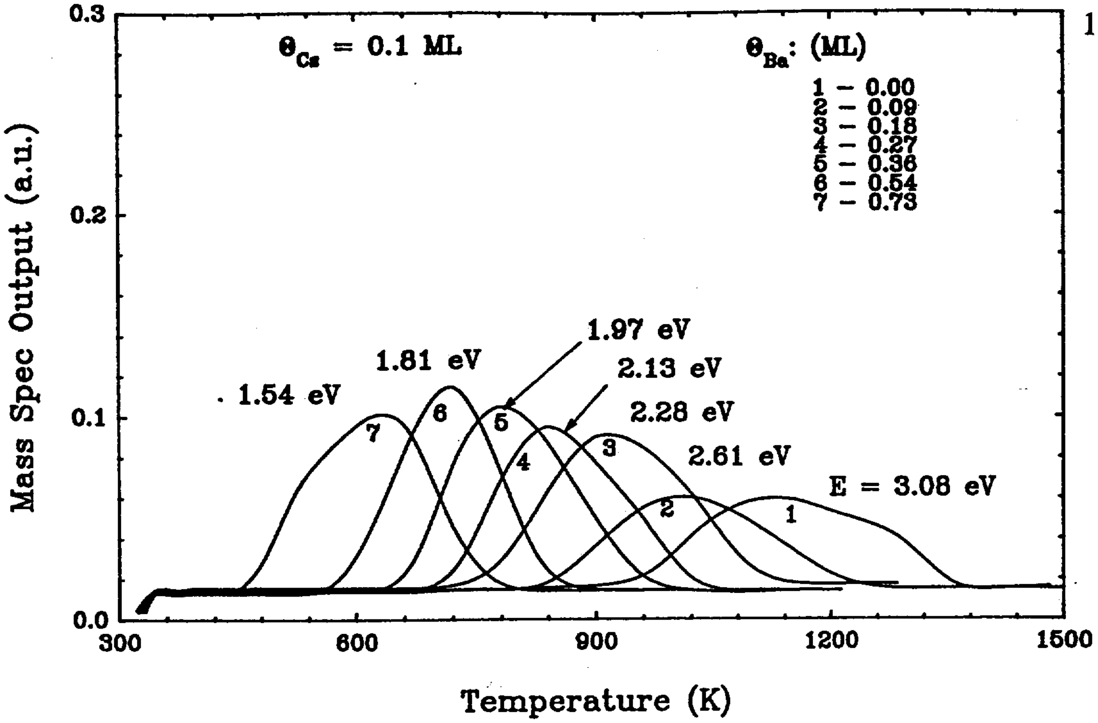

Figure 5.24. Thermal desorption spectra for 0.1 ML of cesium from the W(110) surface with various initial coverages of barium.

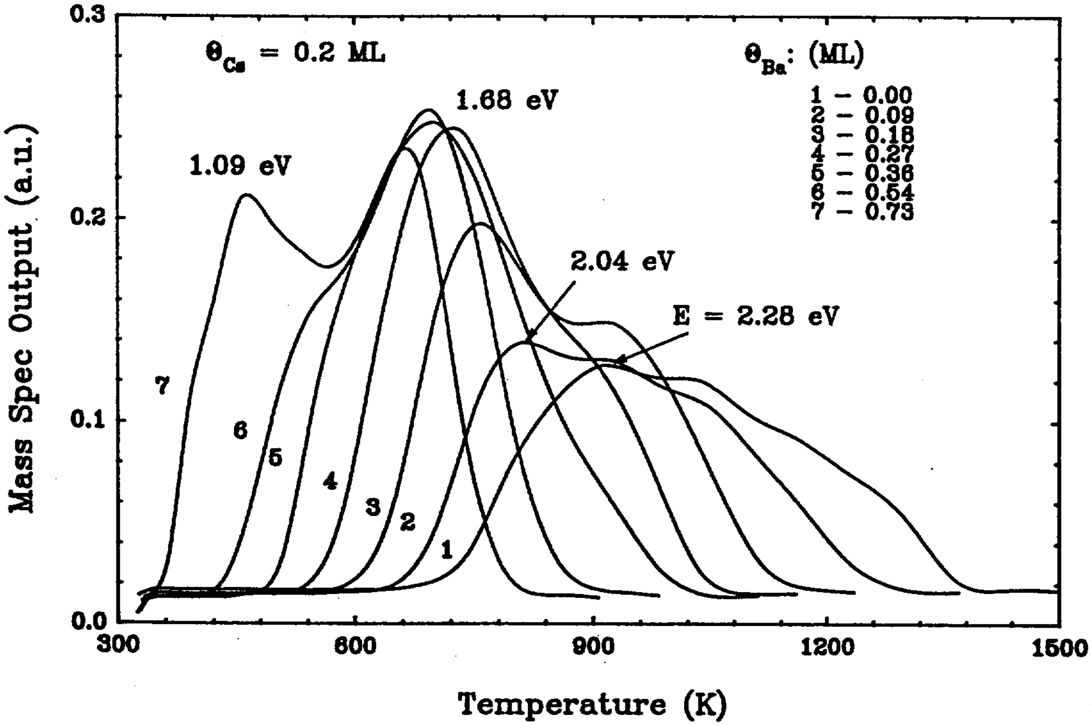

Figure 5.25. Thermal desorption spectra for 0.2 ML of cesium from the W(110) surface with various initial coverages of barium.

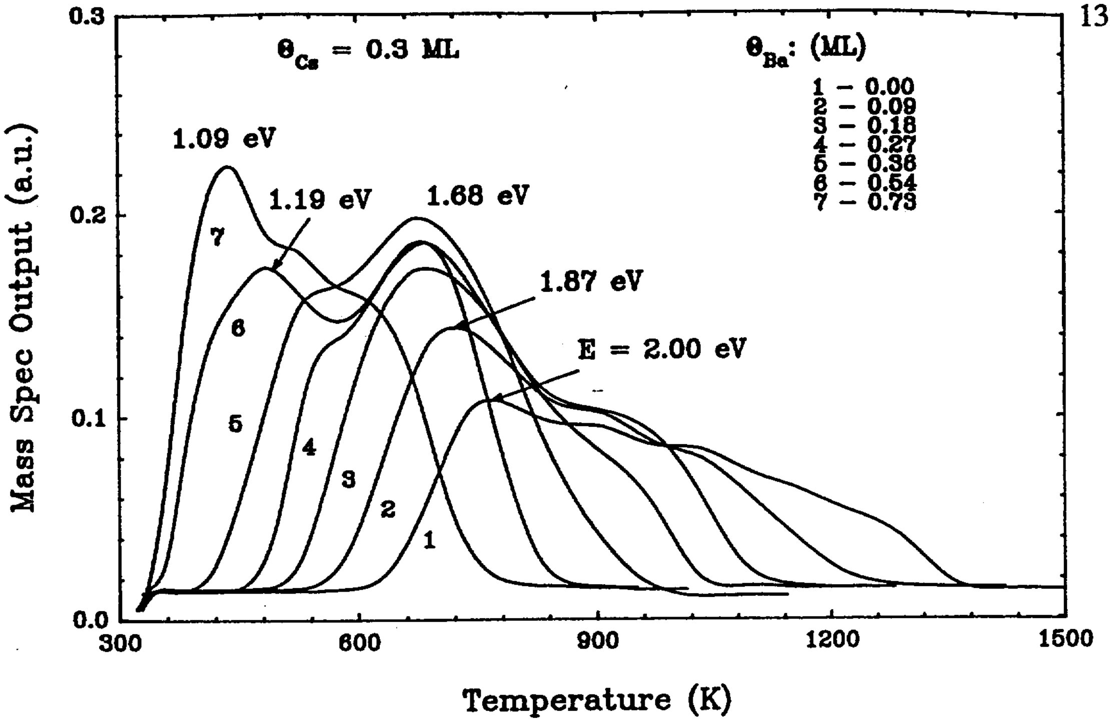

Figure 5.26. Thermal desorption spectra for 0.3 ML of cesium from the W(110) surface with various initial coverages of barium.

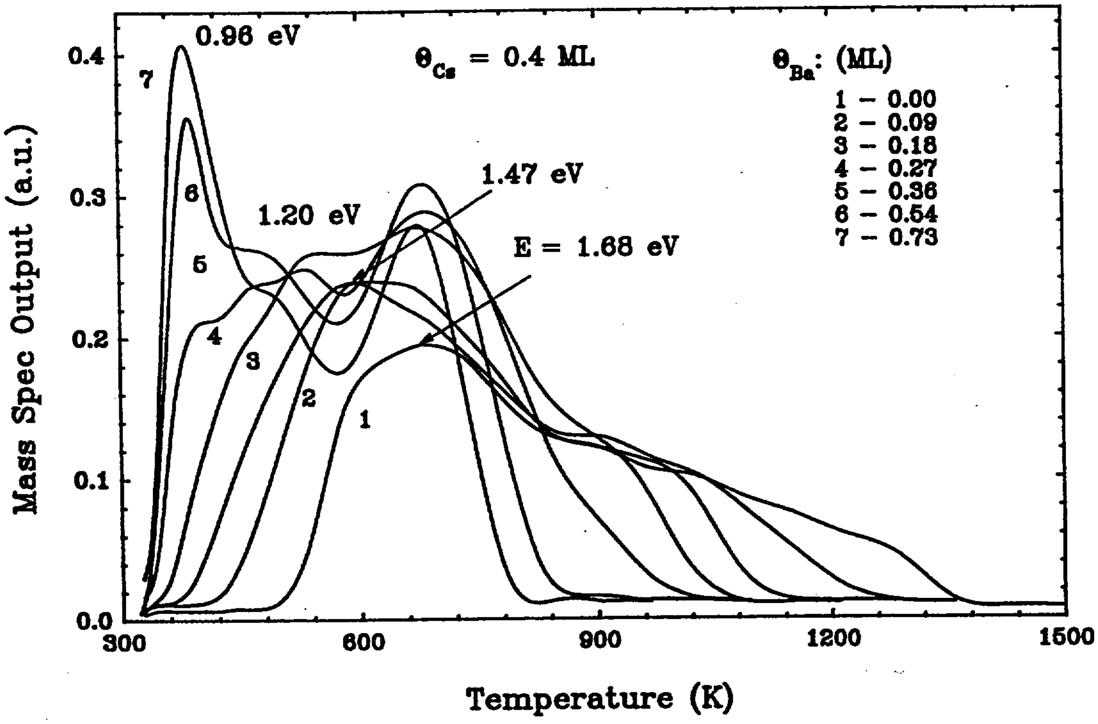

Figure 5.27. Thermal desorption spectra for 0.4 ML of cesium from the W(110) surface with various initial coverages of barium.

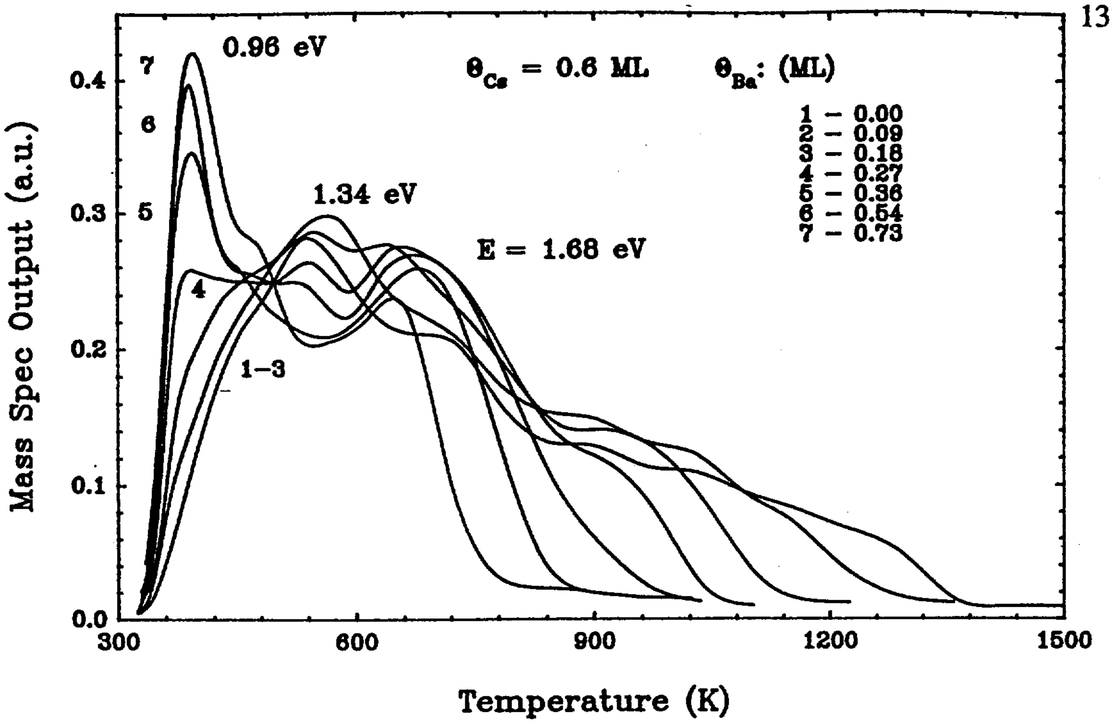

Figure 5.28. Thermal desorption spectra for 0.6 ML of cesium from the W(110) surface with various initial coverages of barium.

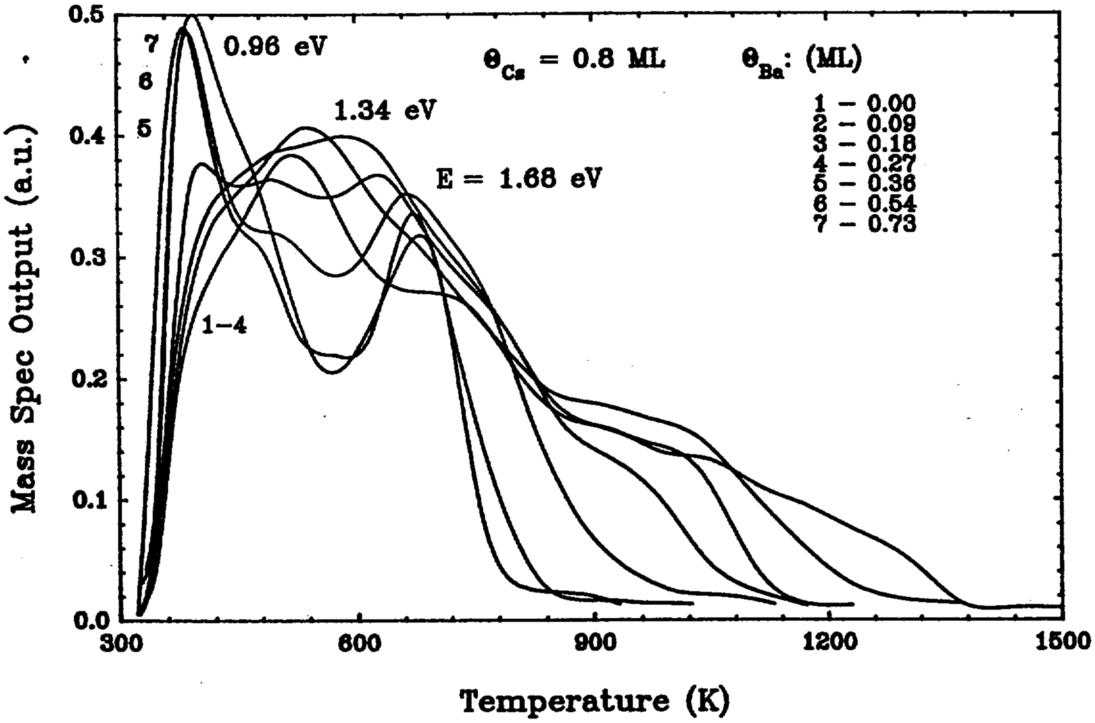

Figure 5.29. Thermal desorption spectra for 0.8 ML of cesium from the W(110) surface with various initial coverages of barium.

Barium Coverage, ML

Cesium Coverage, ML

Θ → ↓	0.00	0.09	0.18	0.27	0.36	0.54	0.73
0.10	3.08 eV	2.61 eV	2.28 eV	2.13 eV	1.97 eV	1.81 eV	1.54 eV
0.20	2.28 eV	2.04 eV	1.87 eV	1.71 eV	1.68 eV	1.68 eV	1.09 eV
0.30	2.00 eV	1.87 eV	1.68 eV	1.68 eV	1.38 eV	1.19 eV	1.09 eV
0.40	1.68 eV	1.48 eV	1.48 eV	1.42 eV	1.42 eV	0.96 eV	0.96 eV
0.60	1.34 eV	1.42 eV	1.34 eV	0.96 eV	0.96 eV	0.96 eV	0.96 eV
0.80	1.34 eV	1.32 eV	1.34 eV	0.96 eV	0.96 eV	0.96 eV	0.96 eV

Θ = 1.0 monolayer = 1.0 ML

Table 5.01 Activation energy of desorption for cesium from W(110) for various initial coverages of barium.

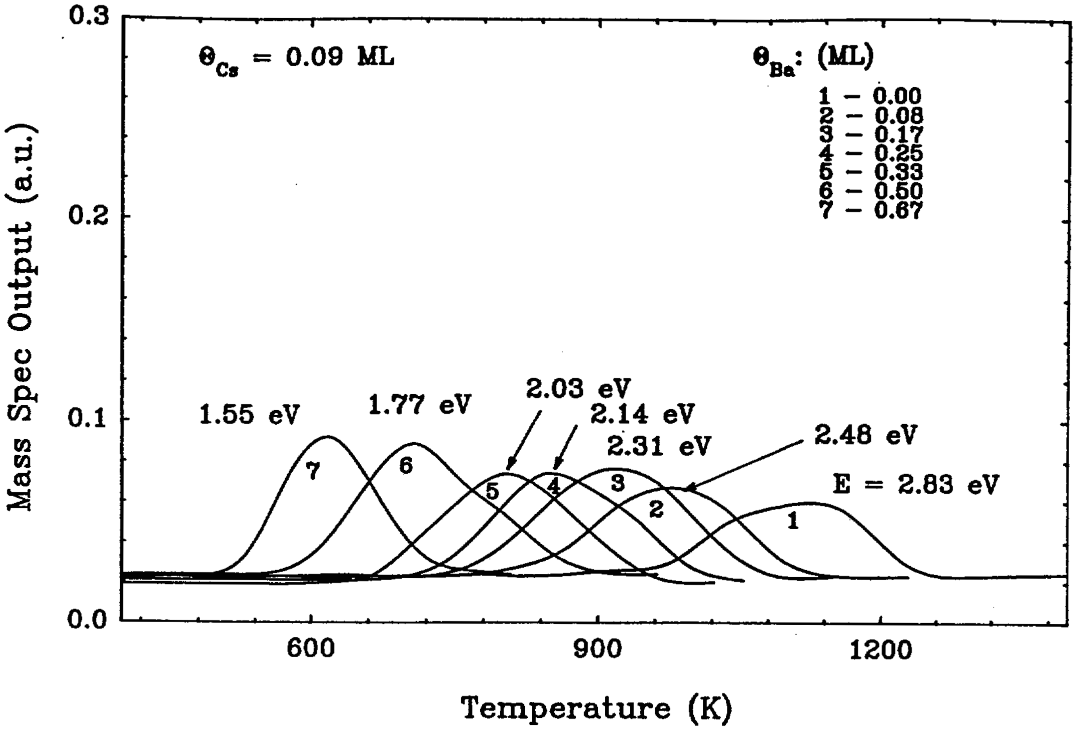

Figure 5.30. Thermal desorption spectra for 0.08 ML of cesium from the Mo(110) surface with various initial coverages of barium.

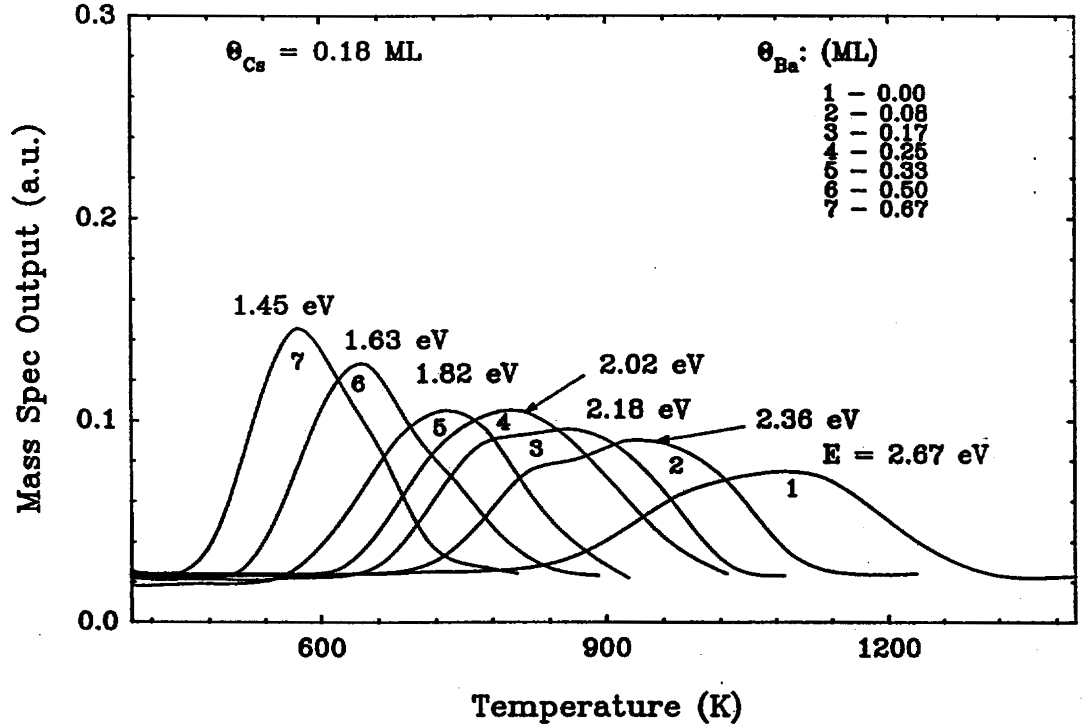

Figure 5.31. Thermal desorption spectra for 0.18 ML of cesium from the Mo(110) surface with various initial coverages of barium.

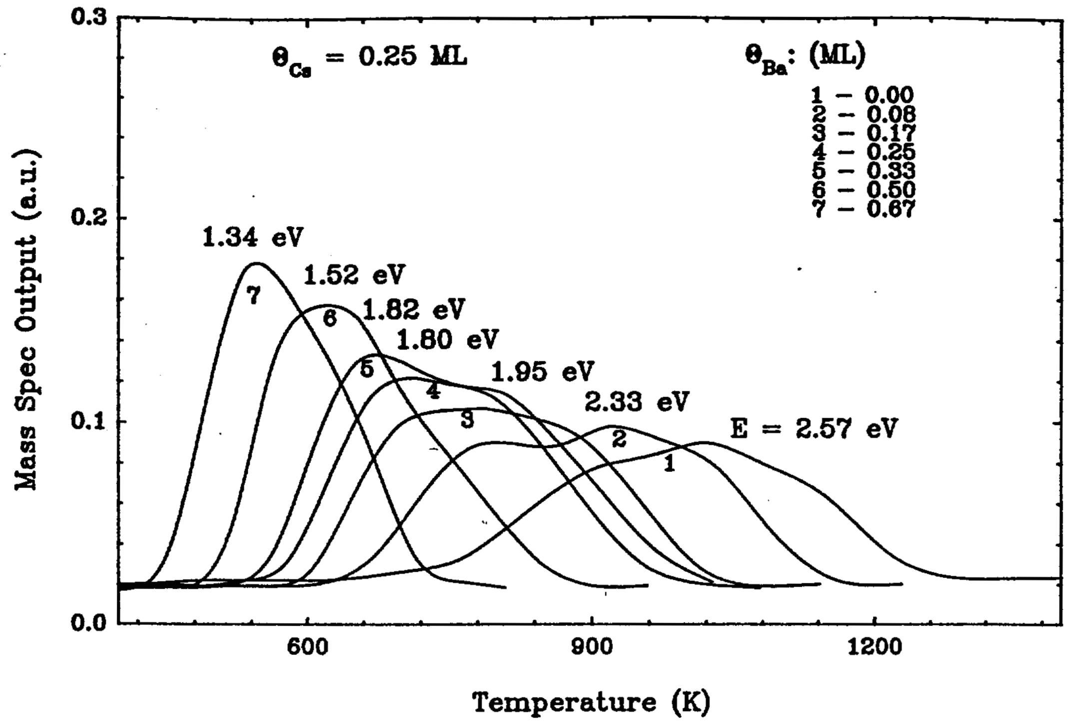

Figure 5.32. Thermal desorption spectra for 0.25 ML of cesium from the Mo(110) surface with various initial coverages of barium.

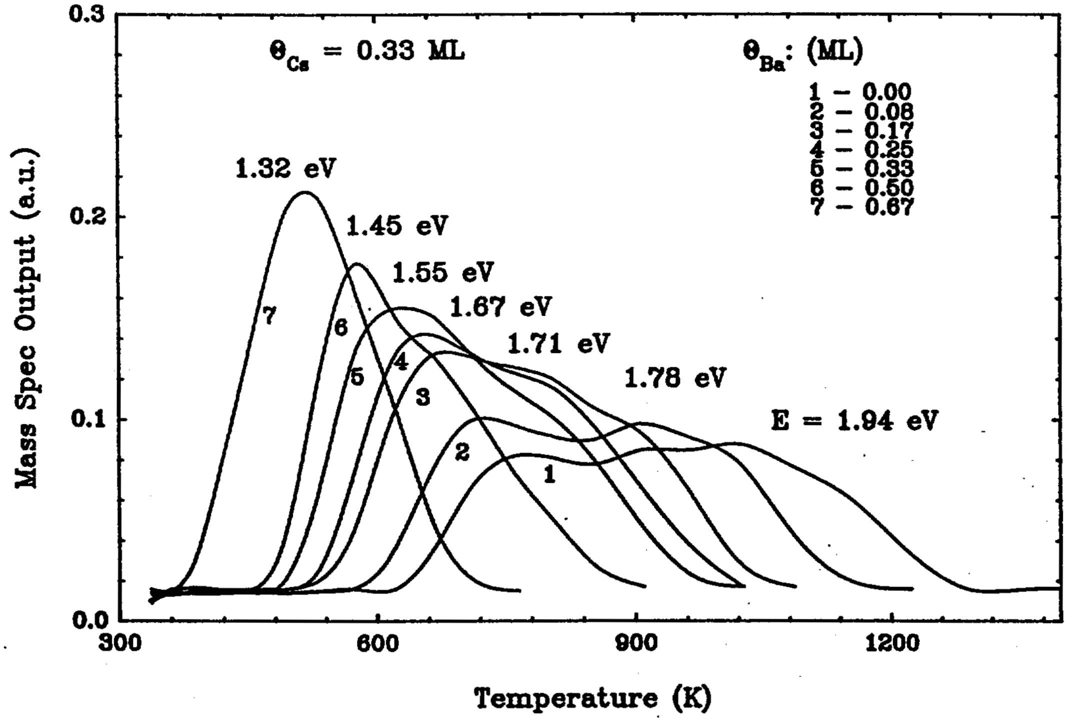

Figure 5.33. Thermal desorption spectra for 0.33 ML of cesium from the Mo(110) surface with various initial coverages of barium.

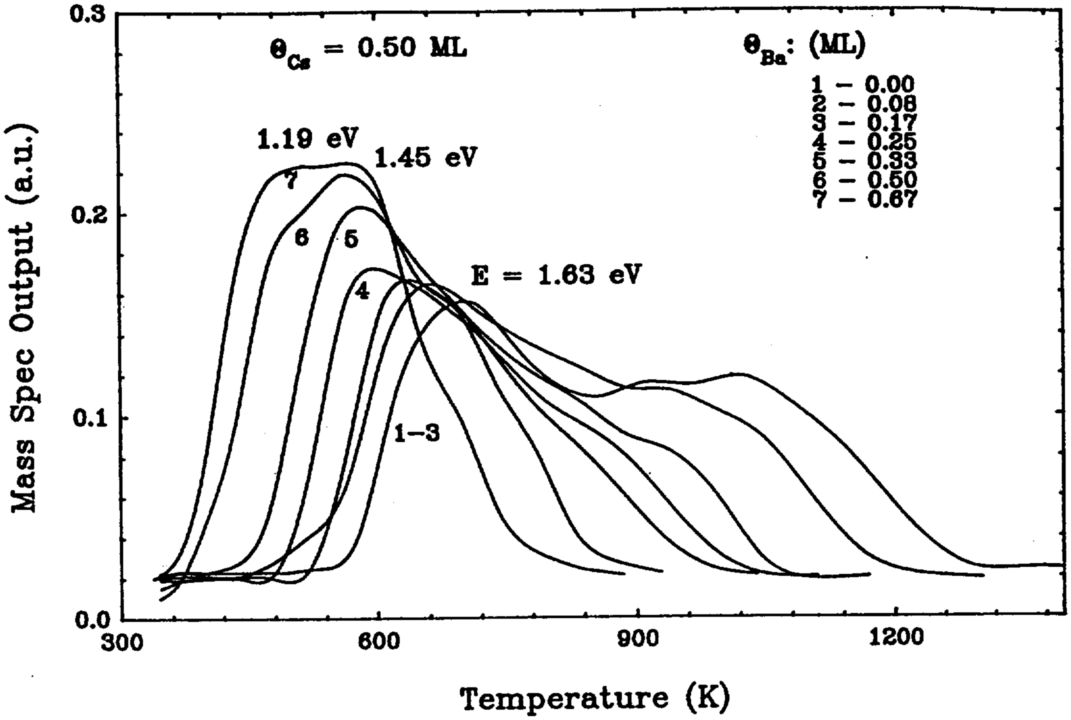

Figure 5.34. Thermal desorption spectra for 0.50 ML of cesium from the Mo(110) surface with various initial coverages of barium.

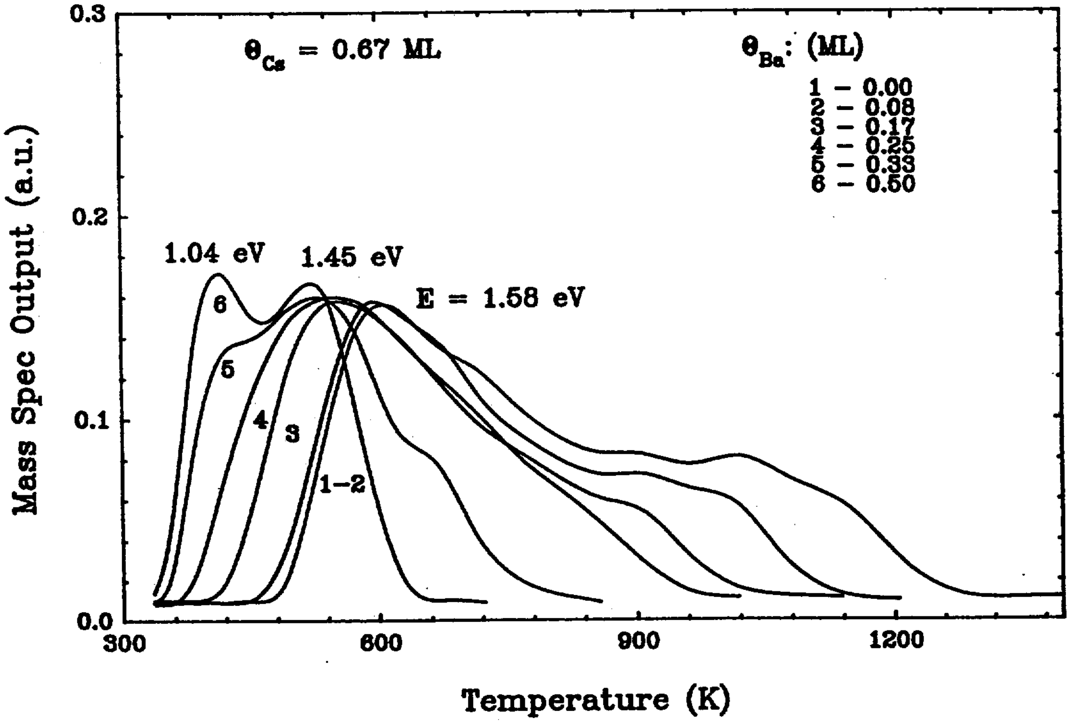

Figure 5.35. Thermal desorption spectra for 0.67 ML of cesium from the Mo(110) surface with various initial coverages of barium.

Cesium Coverage, ML	Barium Coverage, ML						
Θ → ↓	0.00	0.08	0.17	0.25	0.33	0.50	0.67
0.08	2.83 eV	2.48 eV	2.31 eV	2.14 eV	2.08 eV	1.77 eV	1.55 eV
0.17	2.67 eV	2.36 eV	1.18 eV	2.02 eV	1.82 eV	1.63 eV	1.45 eV
0.25	2.57 eV	2.33 eV	1.95 eV	1.90 eV	1.82 eV	1.52 eV	1.34 eV
0.33	1.94 eV	1.78 eV	1.71 eV	1.67 eV	1.55 eV	0.45 eV	1.32 eV
0.50	1.63 eV	1.58 eV	1.54 eV	1.45 eV	1.45 eV	1.45 eV	1.19 eV
0.67	1.58 eV	1.54 eV	1.45 eV	1.45 eV	1.42 eV	1.40 eV	1.04 eV

Θ = 1.0 monolayer = 1.0 ML

Table 5.02 Activation energy of desorption for cesium from Mo(110) for various initial coverages of barium.

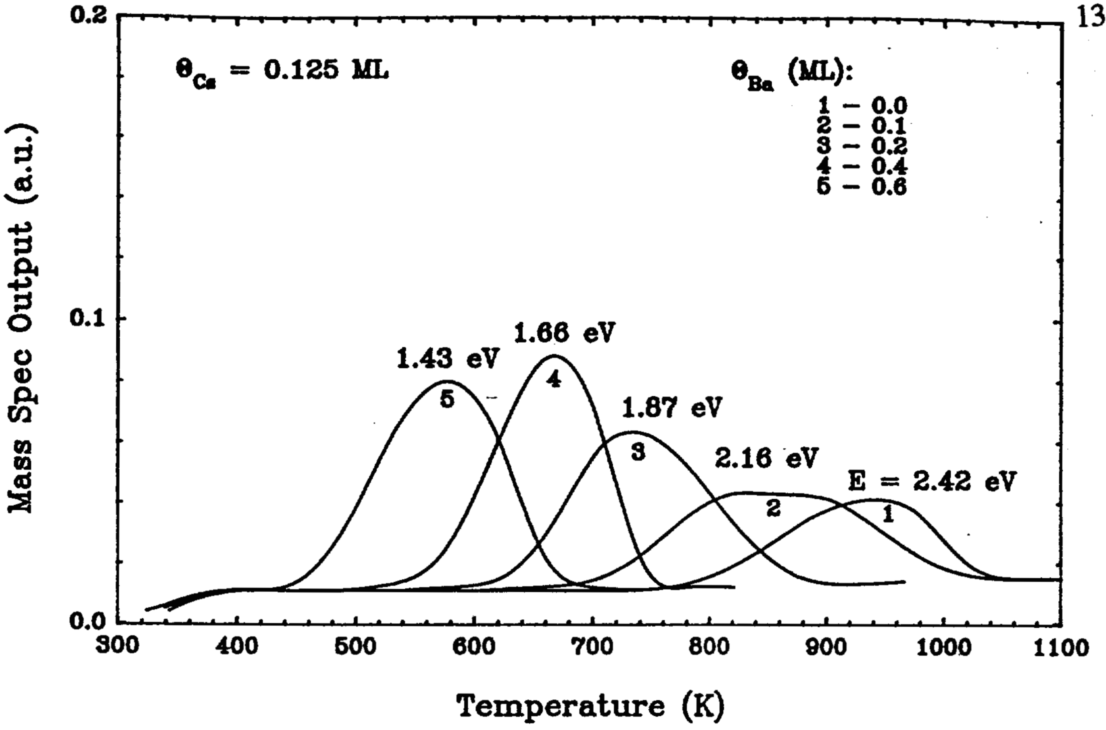

Figure 5.36. Thermal desorption spectra for 0.125 ML of cesium from the Nb(110) surface with various initial coverages of barium.

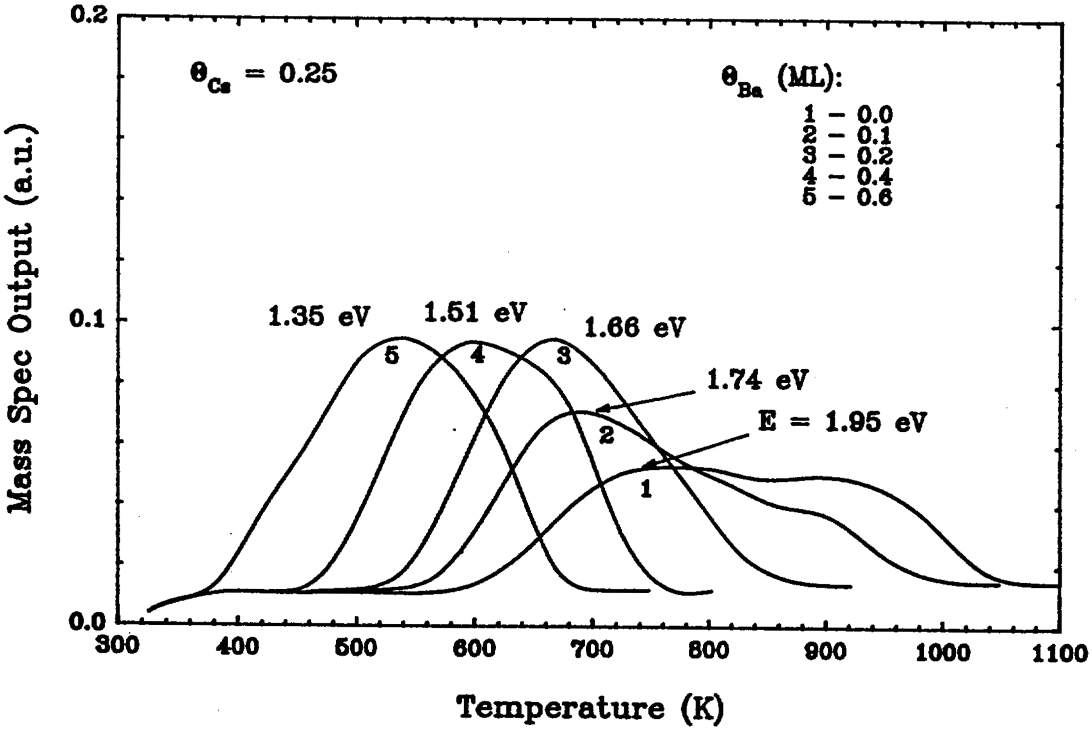

Figure 5.37. Thermal desorption spectra for 0.25 ML of cesium from the Nb(110) surface with various initial coverages of barium.

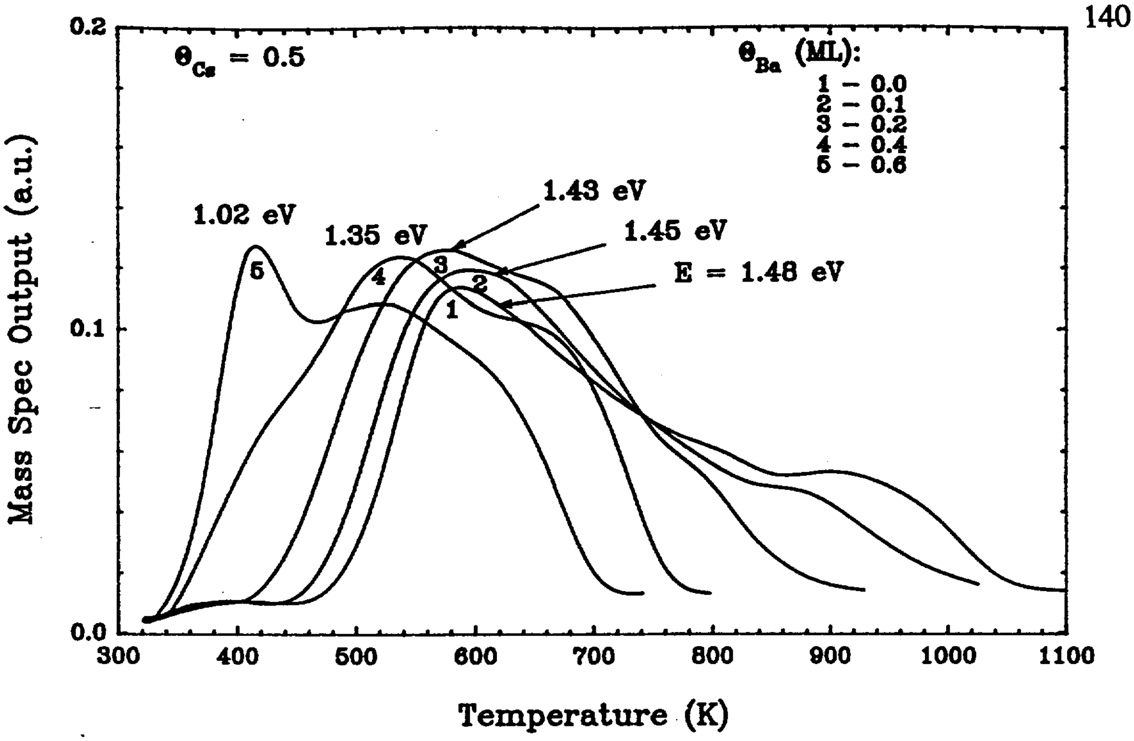

Figure 5.38. Thermal desorption spectra for 0.5 ML of cesium from the Nb(110) surface with various initial coverages of barium.

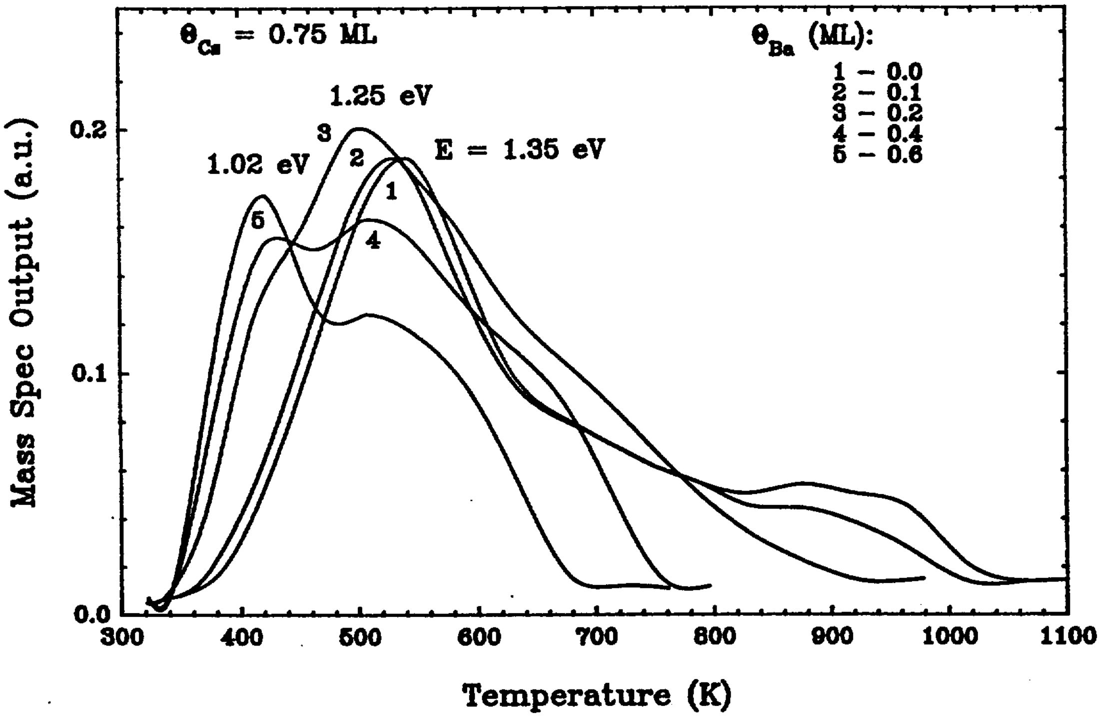

Figure 5.39. Thermal desorption spectra for 0.75 ML of cesium from the Nb(110) surface with various initial coverages of barium.

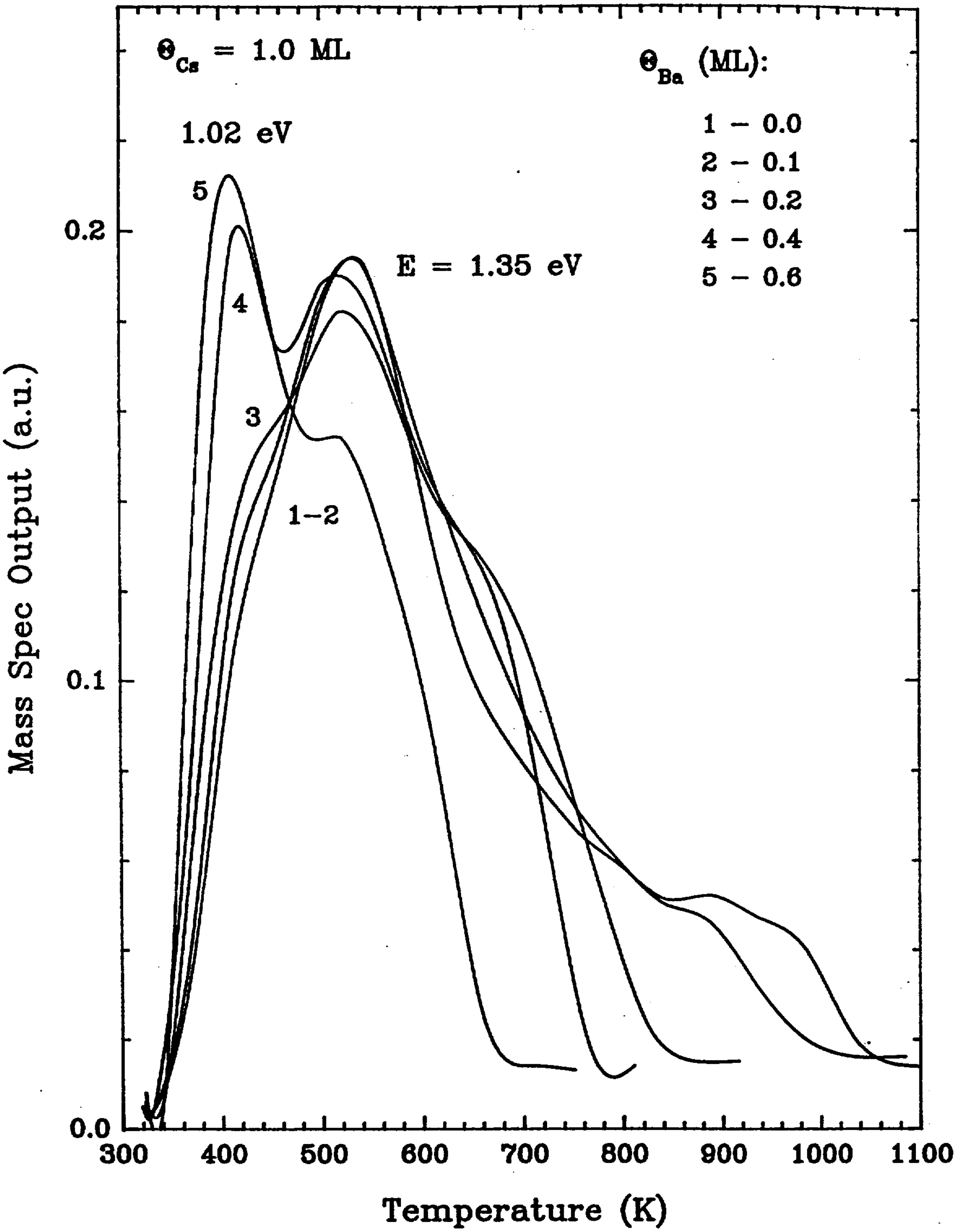

Figure 5.40. Thermal desorption spectra for 1.0 ML of cesium for the Nb(110) surface with various initial coverages of barium.

Barium Coverage, ML

Cesium Coverage, ML

Θ → ↓	0.00	0.10	0.20	0.40	0.60
0.13	2.42 eV	2.16 eV	1.87 eV	1.66 eV	1.43 eV
0.25	1.95 eV	1.74 eV	1.66 eV	1.55 eV	1.35 eV
0.50	1.48 eV	1.45 eV	1.43 eV	1.35 eV	1.02 eV
0.73	1.35 eV	1.33 eV	1.25 eV	1.04 eV	1.02 eV
1.00	1.35 eV	1.33 eV	1.24 eV	1.04 eV	1.02 eV

Θ = 1.0 monolayer = 1.0 ML

Table 5.03 Activation energy of desorption for cesium from Nb(110) for various initial coverages of barium.

5.4 Surface Structures of the Various Adsorbate/Metal Surfaces

The results of previous LEED studies on the surface structure changes occurring from the adsorption of alkali and alkaline earth metals on refractory metal surfaces show the substrate must be cooled for the appearance of any ordered diffraction patterns to be seen at low surface coverages. This is especially true of cesium because of its low desorption energy and high mobility at room temperature. In our experimental apparatus, we were unable to cool our substrates to liquid nitrogen temperatures, so our study of the structural changes of the substrate surface versus adsorbate coverage was limited. Also limiting our LEED study of the surface structure changes was the lack of sensitivity of our LEED optics. I was unable to improve the operation of the LEED optics during this research effort. Therefore, the LEED optics were mainly used to monitor the surface before and after experimental data runs to check for any substrate surface structure changes from adsorption, contamination or surface reconstruction. We will discuss some of the results of other LEED studies done on various alkali and alkaline earth metal adsorption systems to aid our interpretation the effects such metals have on the surface properties of refractory metals.

5.4.a Cs/W(110), Cs/Mo(110) and Cs/Nb(110)

The LEED patterns for the cesium saturated surfaces at room temperature did not change from the clean surfaces except for slight increases in the background intensity. For cesium deposition on W(110) at room temperature (T = 300 K), Fedorus and Naumovets[13] reported that all long range order is lost in all cesium films with coverages less than 0.64 monolayers. At 77 K, the long range order was lost at coverages less than 0.4 monolayers. In Ref. 13, 0.64 monolayers of cesium coverage corresponded to the work function minimum. Desplat[16] found a similar result for cesium adsorption on W(110). He observed ordered LEED patterns for cesium on W(110) at 300 K when the coverage became greater than the coverage corresponding to the minimum work function. The work function and thermal desorption results for cesium on W(110) found in this study were very similar to the two referenced articles, so my LEED results can only be explained by the limitations noted earlier about the

LEED optics and that the cesium may have been deposited at a temperature greater than 300 K.

5.4.b Ba/W(110), Ba/Mo(110) and Ba/Nb(110)

The LEED patterns for barium surfaces did not show any change for barium coverages less than 0.5 monolayers except for an increase in background intensity. For barium coverages between 0.5 and 1.0 monolayers, faint and diffuse rings began to appear around the substrate diffraction spots. With increasing coverage, the rings spread out and become brighter, but no new diffraction spots appeared. The fact that no diffraction spots occurred can also be attributed to the lack of sensitivity of the LEED optics. The resulting diffraction patterns were much easier seen on the Mo(110) and the W(110) surfaces than on the Nb(110).

5.4.c Cesium and Barium on W(110), Mo(110) and Nb(110)

The LEED patterns of the mixed adsorbate surfaces were generally the same as the barium-metal surfaces. No patterns were seen for low coverages, but as the barium coverage increased, the faint diffuse rings appeared around the substrate diffraction spots. However, the diffuse rings formed on the barium-cesium-metal surfaces were less intense than the diffuse rings on the barium-metal surfaces.

References

1 K. H. Rieder, Appl. of Surf. Sci. 4 (1980) 183.

2 T. W. Haas, Surf. Sci. 5 (1966) 345.

3 V. A. Ishchuk, O. V. Kanash, Yu. G. Ptushinskil and A. G. Fedorus, Fiz. Tverd. Tela 23 (1981) 1282.

4 G. N. Shuppe, Izv. Akad. Nauk SSSR, Ser. fiz. 30 (1966) 632.

5 R. W. Strayer, W. Mackie and L. W. Swanson, Surf. Sci. 34 (1973) 225.

6 S. Berge, P. O. Gartland and B. J. Slagsvold, Surf. Sci. 43 (1974) 275.

7 O. D. Protopopov and I. V. Strigushchenko, Sov. Phys.-Solid State 10 (1974) 747.

8 R. P. Leblanc, B. C. Vandrugghe and F.E. Girouard, Can. J. Phys. 52 (1980) 1589.

9 C. Argile and G. E. Rhead, Thin Solid Films 67 (1980) 299.

10 P. R. Davis, Surface Sci. 91 (1975) 385.

11 K. G. Eyink, B. C. Lamartine, W. V. Lampert and T. W. Haas, Appl. of Surf. Sci. 20 (1985) 215.

12 E. V. Klimenko and A. G. Naumovets, Sov. Phys. Tech. Phys. 24 (1979) 710.

13 A. G. Fedorus and A.G. Naumovets, Surf. Sci. 24 (1970) 426.

14 Yu. M. Konoplev, A. G. Naumovets and A. G. Fedorus, Fiz. Tverd. Tela 14, (1972) 326.

15 A. G. Fedorus, A. G. Naunovets and Yu. Vedula, Phys. Stat. Sol. (a) 13 (1972) 445.

16 J.-L. Desplat and C. A. Papageorgopoulos, Surf. Sci. 92 (1980) 97.

The Chapter 6

Discussion

The interaction between electropositive atoms and refractory metal surfaces has been thoroughly studied both experimentally and theoretically. There have been a number of studies done on the adsorption and desorption of alkali metals on single crystal refractory metal surfaces[1,2,3], but alkaline earth metal adsorption has been analyzed in less detail. Fundamental surface studies of the co-adsorption of both alkali and alkaline earth metal vapors on refractory metal surfaces have been limited to just a few investigations[4]. Theoretical and experimental data on the surface structure, work function, activation energy and electronic state of alkali and alkaline earth metals suggest that a great similarity exists in their adsorption properties[5,6,7].

The tungsten surface, whether it be polycrystalline or single crystal, has been one of the most studied refractory metal surfaces in terms alkali and alkaline earth metal adsorption. Because of the many studies done on the tungsten surface, we will use the W(110) surface as the "standard" with which we compare the Mo(110) and Nb(110) surfaces. The Mo(110) should make an interesting comparison since both substrates have the same atomic symmetry and their lattice constants differ by only 0.6%. The strong similarity between the physical dimensions of the W(110) and Mo(110) can also provide information about the effect of the substrate's electronic structure on the adsorption properties.

The Nb(110) surface is the least studied surface of the three surfaces investigated in terms of adsorption and desorption of alkali and alkaline earth metals. I was unable to find any other experimental data for the work function change due to the adsorption of cesium or barium onto the clean Nb(110) surface. Konoplev *et al.*[4] reported a minimum work function of ~2.1 eV for the Ba/Nb(100) surface. The Nb(100) surface does not provide a good comparison because of its atomic structure and low bare work function, but it does give some idea of how alkali and alkaline earth metal adsorption affects the niobium substrate. It would be hard to compare our results with other experimental results because of the initial conditions of the Nb(110) surface. Our initial work function was 0.2 eV low compared to other reported values, and AES showed that our substrate was always contaminated with a small percentage of oxygen. How this oxygen affects the work function due to the adsorption of cesium or barium is not clearly understood from our investigation but our results show that the $NbO_x(110)$ surface properties are similarly to those of W(110) and Mo(110). We observed an unexpected low minimum work function for the Cs/Nb(110) surface at a relatively low adatom concentration compared to the W(110) and Mo(110) surfaces. The low work function values were probably caused by an increase in the sticking coefficient of the cesium atoms and the increased binding energy due to the excess oxygen in the bulk and on the surface of the Nb(110) substrate. What makes this observation confusing is that we did not observe a comparably low minimum work function for barium on the Nb(110) surface, but we did observe the minimum work function value occurring at low barium adatom concentration. The excess oxygen must increase the sticking coefficient of both cesium and barium on the Nb(110) surface, or the loosening of the near surface atomic structure by the oxygen must increase the number available of adsorption sites for the cesium or barium.

Some difficulties arise in comparing our data with the data of previous experimental studies. One difficulty is that most of the experimental work done on the adsorption and desorption of cesium and barium in the area of thermionic emission has been performed by scientists of the former Soviet Union. Interpreting their data can sometimes be challenging because of the interpretation, symbolic representation and translation or lack of translation of many of the articles found in literature. Another difficulty is the lack of information about the conditions of the substrate surface before the adsorption of cesium or barium. The adsorption and desorption of cesium and barium on single crystal surfaces is affected by both the surface structure and contamination. The adsorption properties of different crystal planes of the same material can be very different. For example, small amounts of preadsorbed oxygen can cause decreases in the minimum work function and cause increases in the activation energy for desorption of either cesium or barium[8]. Finally, it is difficult to directly compare the results of different experiments because of the many analytical methods used to obtain the data. We measured the work function absolutely using the FERP technique while many investigators use the Kelvin probe or the thermionic method which rely on a predetermined experimental value for the work function of the substrate. Also investigators use different methods to determine the activation energies of an adsorbed species. In our investigation, Redhead's equation was used for first order desorption assuming $\nu_1 = 10^{13}$ sec^{-1} while others[9] use the equation $N = (\nu n)\exp[q(n)/kT]$ from the theory of rate processes with values of ν ranging from 10^{12} to 10^{14} sec^{-1}. When comparing our data, any differences in methodology will be noted.

6.0 Work Function

The work function versus adsorbate coverage measurements for cesium, barium and cesium plus barium on W(110), Mo(110) and Nb(110) were presented in figs. 5.10 - 5.18. The important data of the work function versus coverage curves are summarized in Table 6.00 and in figs. 6.00 and 6.01. In the table, the clean work function for each substrate is given along with the minimum work function value achieved for each of the adsorbate/metal systems. From the data presented in Table 6.00 and in figs. 6.01 and 6.02, we find that the change in work function of the Cs/Me(110) and Ba/Me(110) surfaces are arranged in the following sequences

$$\text{Cs/Nb(110)} < \text{Cs/Mo(110)} < \text{Cs/W(110)} \qquad (6.00)$$

and

$$\text{Ba/Nb(110)} \sim \text{Ba/Mo(110)} \sim \text{Ba/W(110)}. \qquad (6.01)$$

The work function minimum is the characteristic feature of adsorption of alkali and alkaline earth metals. It was discussed in chapter 2 that the nature of this phenomenon may be interpreted in various ways but there is no doubt about the significance of the change in the adatom's electron state. The results of our investigation show a domination of the repulsive forces at the initial stages of the adsorbate coverage as evident from the strong dipole-dipole interaction between adatoms, meaning a great degree of ionization or polarization of charge. As the coverage increases, the spacing between the adatoms decreases which leads to a possible orbital overlap of their electrons. This induces a considerable change in the

Table 6.00. Minimum work function for the various adsorbate/metal surfaces.

Material	Work Function (eV)	Min. Work Function (eV) Cs	 Ba
W(110)	5.38	1.54	2.21
Mo(110)	5.08	1.50	2.20
Nb(110)	4.62	1.47	2.21

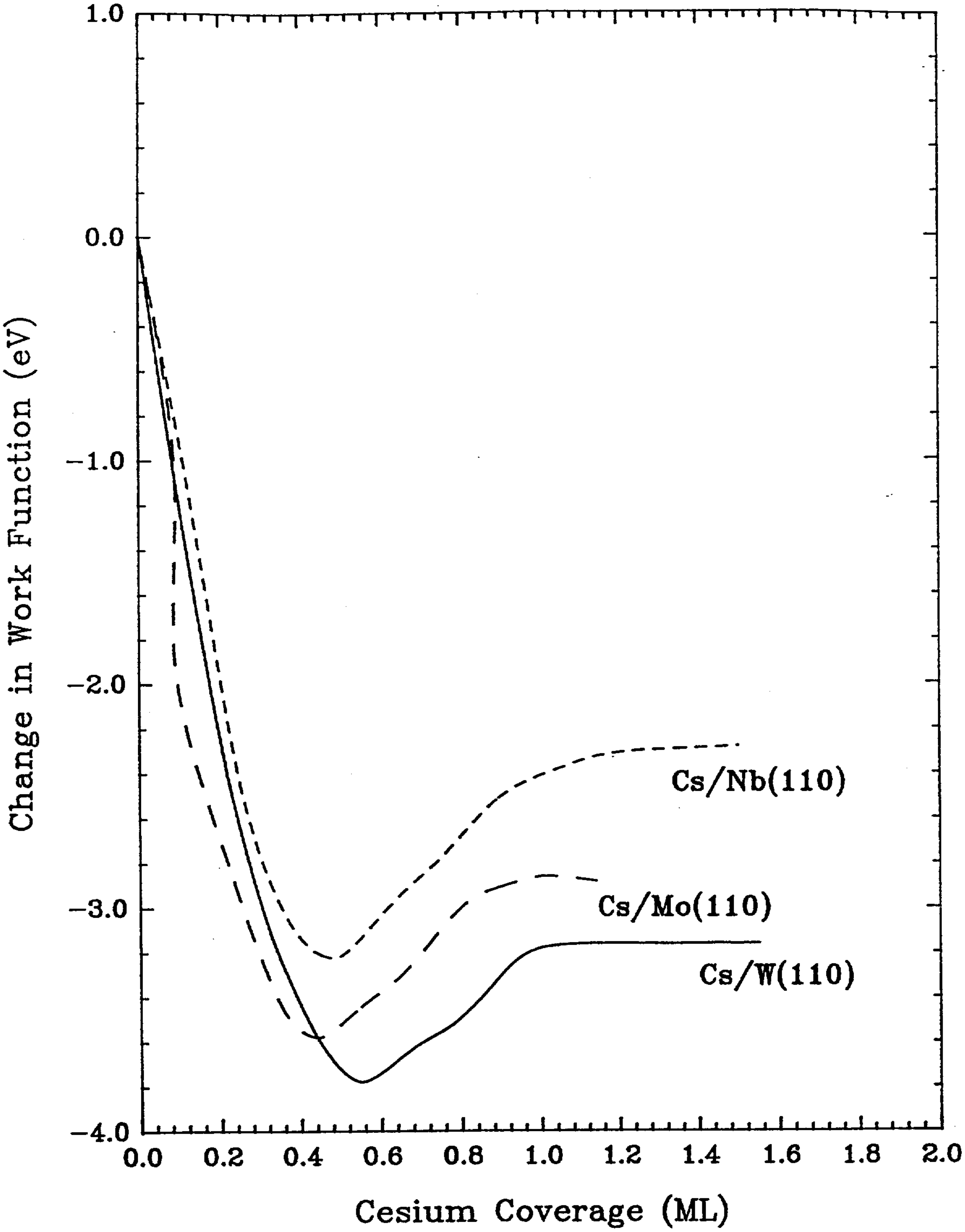

Figure 6.00. Change in work function for the W(110), Mo(110) and Nb(110) surfaces versus cesium coverage.

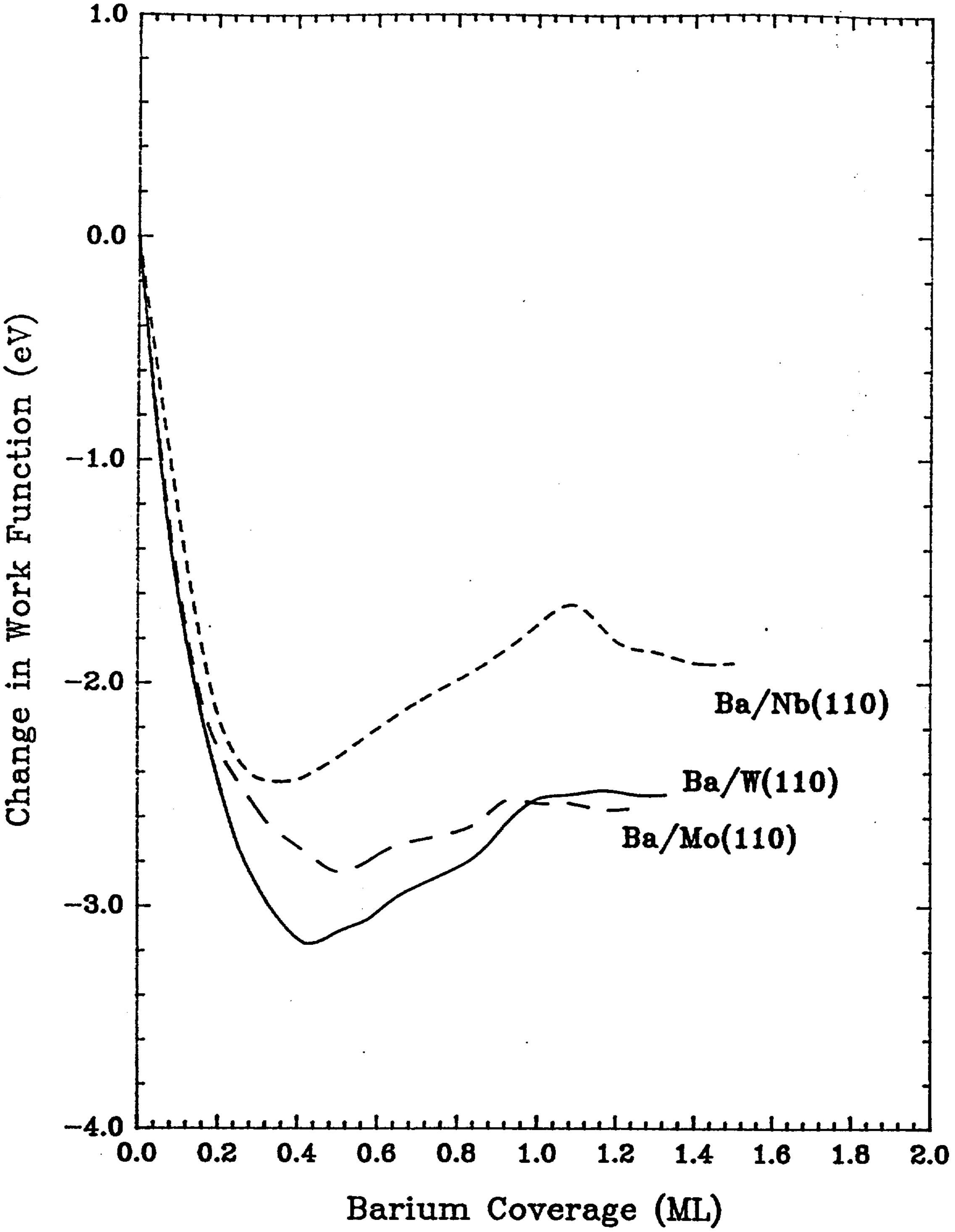

Figure 6.01. Change in work function for the W(110), Mo(110) and Nb(110) surfaces versus barium coverage.

nature of the adsorbate/substrate bond and eventually to metallization of the overlayer[10]. An investigation of the energy loss spectrum of the Ba/W(110) surface gives evidence to this fact. In Ref. 1, it was observed that a low energy peak (3.5 eV) linearly increased in intensity after the minimum work function was reached and decreased at monolayer coverage. The energy loss peak was attributed to a plasma excitation in the adsorbed film, in other words, to the appearance of metallic properties in the film[11,12]. The metallization of the overlayer can also be associated with a decrease in the orbital overlap of the valence electrons between the adatom and the neighboring substrate atoms. This follows with a significant decrease in the covalent bonding between the adatom and the substrate atoms and its influence on the electronic structure of the adlayer film. The polarization in the adatom's electronic state brings about an influence on the work function of the substrate surface. The reduction in the work function in the early stages of adsorption is due to the concentration of totally and partially ionized adatoms. However, as the film metallizes, the surface can be pictured as a pure metal with an increasing surface concentration, having less attraction towards the substrate, which leads to an increase in the work function up to the concentration of a close-packed layer (i.e., monolayer of coverage). If we further increase the coverage past a monolayer, the adatom concentration tends to decrease, and the work function goes through a maximum and then settles to a value corresponding to a several monolayer thick adsorbate layer.

The curves in the figs. 6.01 and 6.02 help to verify the depiction, previously discussed, of how the adsorption of electropositive alkali and alkaline earth metals affect the negative potential barrier (dipole moment) or work function at the surface. In the initial stages of adsorption, the work function reduces noticeably due to the changes in the adatom's electron state as a result of ionization, polarization or metallization which changes the adatom interaction with the neighboring substrate atoms. Cesiation of the substrate surface leads to the polarization of the cesium valence electrons towards the substrate surface leading to an increase of electronic charge in the Cs/Me interface region. This gives rise to a dipole barrier whose effect is opposite to that of the surface dipole. The cesium valance polarization dipole tends to decrease the work function. Wimmer *et al.*[13] noted that the multiple dipoles which reduce the work function are located outside the surface of the substrate, which contradicts the classical dipole picture of the Cs^+ ion and its image charge inside the metal. The changing bonding mechanism causes a decrease in the adatom effective positive charge and a weakening of the adatom-substrate atom interaction. The degree of the covalency of the bond, i.e. the overlap of orbitals and adatom exterior electron shells with the substrate atoms determines the effect the adsorption has on the potential barrier or work function of the surface.

For the Ba/W(110) and Ba/Mo(110) surfaces, Fedorus *et al.*[6] reported minimum work function values of 2.00 eV and 2.10 eV, respectively. These values are as much as 0.2 eV lower than the minimum work function values we reported in this investigation. They used the contact potential difference method to measure the work functions with reference work function values of 5.00 eV for Mo(110) and 5.35 eV for W(110) so some error between the measurements can be accounted for by the different methods used. Bondarenko and Makhov[14] reported a minimum work function value as high as 2.3 eV for barium adsorbed onto clean Mo(110) at 300 K, so there is some discrepancy in the minimum work function value reported in literature. It is very important to know the complete surfaces conditions of the substrate when comparing work function data for alkali and alkaline earth metal adsorption. Contamination and orientation of the substrate can cause significant differences in how the adsorbates affect the work function. Excess oxygen has been found to lower the work function as much as 0.4 eV for the Cs/W(110)[7,8] surface and the Cs/Mo(110)[15] surface.

Thermal desorption studies have shown that divalent barium forms a relative strong site-specific two-electron-bond with the surface, and diffraction studies have proved that it forms a coherent structure over the entire surface at lower coverage. Both these results have been associated with changes in the work function. At low coverages, there is little or no lateral interaction between the barium adatoms, but there is some ionization or polarization occurring and strong interaction with the neighboring substrate atoms. The strong barium/substrate interaction allows the adatoms to form coherent structures on the surface of the metal at room temperature and at low coverages, and certain adlayer structures have been associated with changes in the work function. As the coverage increases, the adlayer of barium is compressed, but because of the large initial separation distances (and strong bond), the lateral interactions (repulsive forces) between the adatoms do not occur until the concentration is relatively high. The lack of interaction between the adatoms allows the barium to interact with the substrate atoms for a longer time and have a greater initial effect on the negative potential barrier of the substrate. With increased coverage, the barium adlayer also loses its short range order with the substrate and the effectiveness of barium in reducing the work function is hindered as the barium adatoms begin to interact and their bonding mechanism changes. The work function and the activation energy versus coverage show that there is less repulsive interaction between the barium adatoms than for cesium adatoms so there is an easier transition from one bonding mechanism to the other for barium. Each transition decreases the effective positive charge of the adatom and the interaction with the neighboring substrate atoms until the surface has the properties of a metal adlayer.

The work function minimum found for the various cesium/metal systems agree quite well with results found in the literature. Desplat *et al.*[8], reported a minimum work function of 1.45 eV which was 0.12 eV less than the value we report. Desplat used the Kelvin probe to measure the work function changes and assumed the work function value of clean W(110) to be 5.3 eV. We measured the clean work function value of W(110) to be 5.38 eV, hence Desplat's value for the minimum work function would be 0.08 eV higher using our value for the clean surface. Fedorus and Naumovets[6] determined the minimum work function of the Cs/W(110) surface using the retarding field method to be ~1.65 eV. A minimum work function value of ~1.5 eV was reported for the Cs/Mo(110) surface[7]. This value was found using the thermionic method with a reference value for Mo(110) of 5.00 eV. We found the clean work function for Mo(110) as 5.08 eV so our minimum work value of 1.50 eV is somewhat lower than their value.

Monovalent cesium has a similar effect on the work function to that of barium but because of differences in the electronic makeup of the two atoms, they yield slightly different results. As already stated, barium has a greater initial effect on the work function but cesium produces the greatest overall reduction in the work function when adsorbed on refractory metal surfaces. For example, figures 6.00 and 6.01 show that cesium reduces the work function of the Mo(110) surface by 3.58 eV compared to a reduction of only 2.85 eV by barium adsorption. The strength of the initial one-electron-bond of cesium is much less than the barium surface bond, but because cesium is the most electropositive element, it eventually has the greatest overall effect on the negative potential barrier at the surface. The strong repulsive forces between cesium adatoms and the polarizibility of the cesium adatoms helps prevent them from being compressed together as the coverage increases and the polarized ionic nature of their bond continues to affect the work function of the substrate. Once the adatoms are compressed together, the electron orbitals of the adatoms are no longer shared only by the substrate but also by the adatoms. Like barium, the sharing of the electrons between the adatoms (the electron density increases in the adlayer) reduces their effective surface dipole moments and their reduction effect on the negative dipole barrier.

The work function change versus adsorbate coverage for the mixed vapor systems yielded more complicated results. There have been a limited number of fundamental surface studies performed on the cesium-barium mixed vapor system. Konoplev *et al.*[4], provided the only other study found concerning the work function change of single crystal refractory metal surfaces due to the adsorption of barium plus cesium. However, there has been several studies done on the adsorption of mixed vapors on polycrystalline substrates[16,17]. It was shown in figs. 5.16 - 5.18 that the minimum values of the work function for the mixed adlayers lie between the minimum work function values of the pure metal adlayers. Also the minimum work functions for the mixed adlayers occurred at lower and lower cesium adatom concentration as the pre-coverage of the barium was increased. At barium coverages that correspond to the minimum work function of the various Ba/Me(110) surfaces, the additional adsorption of cesium has only a slight effect on reducing the work function. Finally, as the pre-coverage of barium approaches a monolayer, the cesium adsorption causes an almost uniform decrease in the work function to a value corresponding to a several monolayer thick cesium layer. The work function results show that the barium adatoms reduce the effective positive charge of the cesium adatoms and hence reduce the effect they have on the negative potential barrier of the substrate. The presence of the strongly bonding barium adatoms creates an electrostatic potential which gradually shifts the cesium adatom valence level downwards with respect to the substrate Fermi level, and thus neutralizes the cesium adatom. When cesium atoms are adsorbed, they do not feel the high negative field of the clean surface and are less likely to become ionized or strongly polarized. A parallel depolarizing mechanism also exists due to the inter-adatom dipole in the field of the barium adatoms[18]. As the barium adatoms are neutralized by their interaction with the substrate atoms with increasing coverage, the work function change of the cesium adsorption resembles that of cesium onto a surface saturated with cesium.

The initial dipole moment per cesium or barium adatom on the three substrates was calculated from the work function change versus adsorbate coverage in figs. 6.00 and 6.01 using the Helmholtz equation

$$\mu_0 = \varepsilon_0 \left.\frac{\Delta\phi}{\Delta n}\right|_{n\to 0} \qquad (6.02)$$

where μ_0, ϕ, and n are coulomb-m, electron-volts, and atoms/m^2, respectively. The permittivity of free space, ε_0 is 8.85×10^{-12} C^2/N-m^2. The results are shown in figs. 6.02 and 6.03 and summarized in Table 6.01. The concentration of adatoms for cesium or barium at a monolayer coverage (n_{sat}) was not measured in this investigation. The values were obtained from the many references within this report. The change in the dipole moment with the increase in coverage is due mainly to the decrease in charge of the adatoms, consequently, it is possible to obtain function quantitative information of the dependence of the charge of the adatoms on the degree of coverage from the measurements of the work function. The coverage for the minimum work function is denoted with a vertical arrow in the dipole moment versus coverage curves. Note that each dipole moment versus coverage curve shows no discontinuity at minimum work coverage which tells us that there is no significant change in the electronic structure at the point of minimum work function. It is important to note that the strength of initial dipole moment follows the general trend of the change in work function for cesium and barium on W(110), Mo(110) and Nb(110) surfaces, as expected by the quantitative models[19,20] given in chapter 3.

The behavior of the work function is also another way to verify a monolayer of adsorbate. It has been determined from previous LEED and work function studies[6] [8] [10] of alkali and alkaline earth metal adsorption that the local maximum in the work function change versus adsorbate dose time curve corresponds to a monolayer of coverage. If we compare the corresponding work function change and the APPH

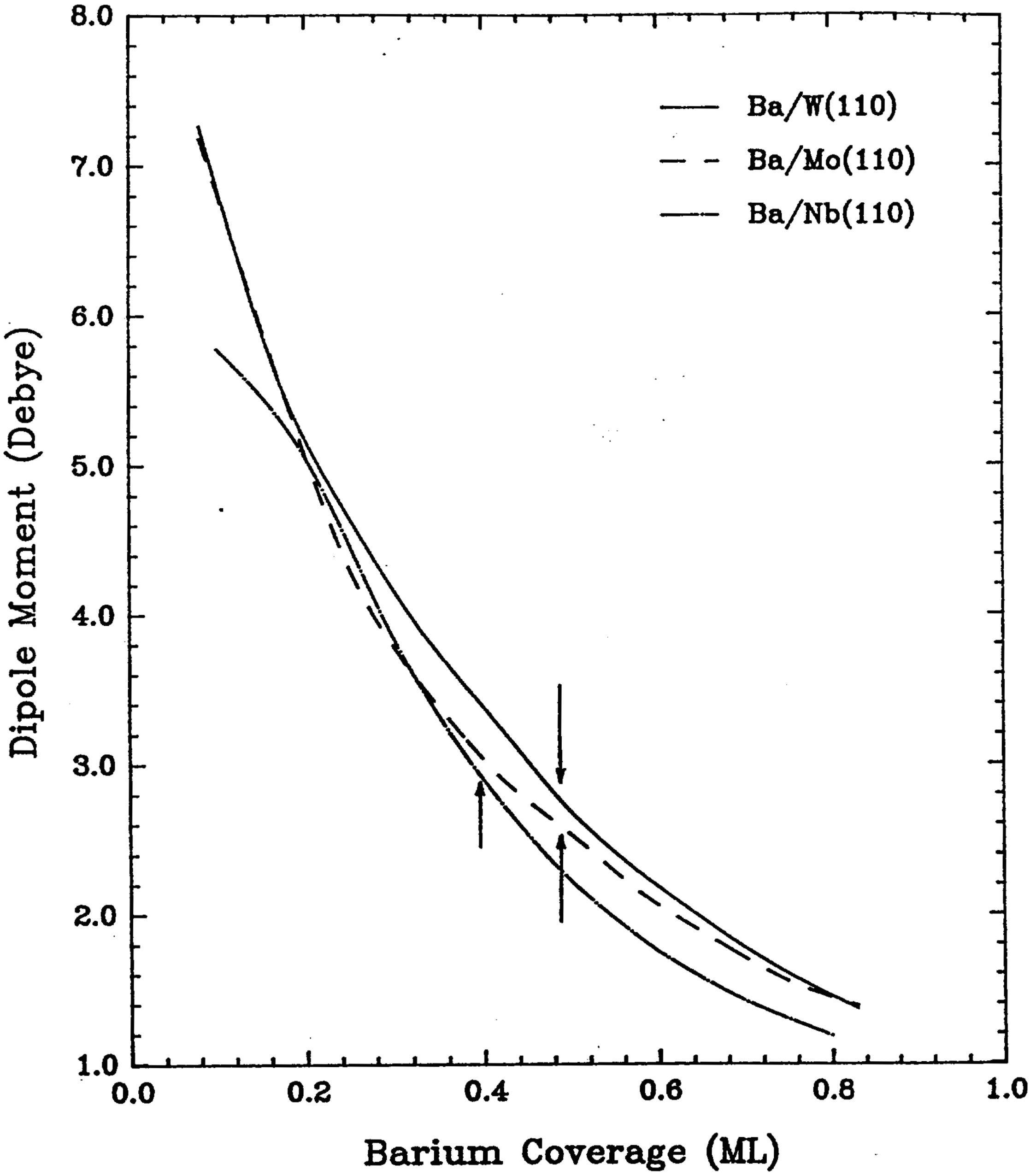

Figure 6.02. Dipole moment versus barium coverage for the W(110), Mo(110) and Nb(110) surfaces.

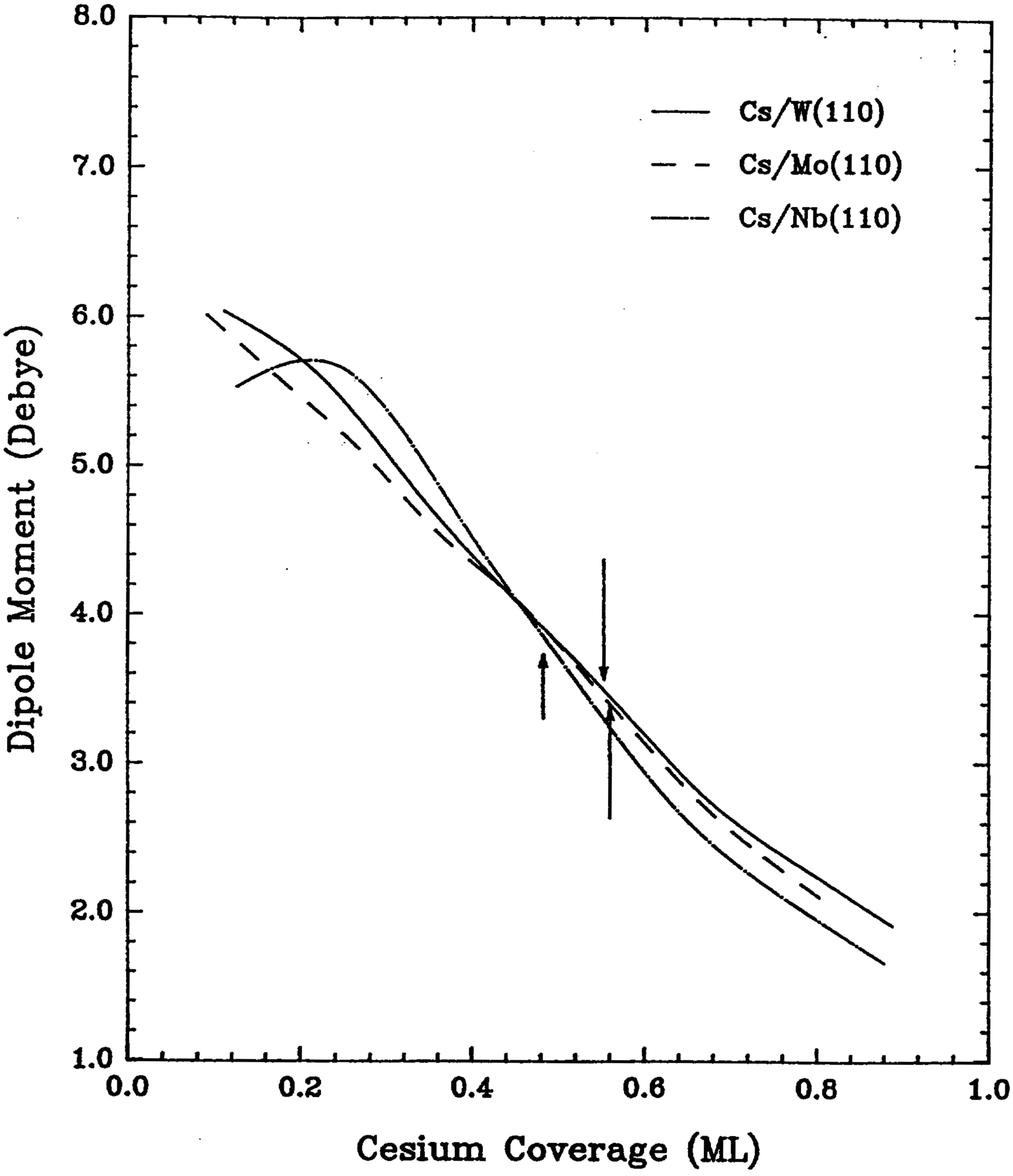

Figure 6.03. Dipole moment versus cesium coverage for the W(110), Mo(110) and Nb(110) surfaces.

Table 6.01. Near zero-coverage dipole moments for the various adsorbate/metal surfaces.

Material	Dipole Moment, μ_0 Cesium	Barium
W(110)	6.02 D	7.26 D
Mo(110)	6.01 D	7.18 D
Nb(110)	5.49 D	5.78 D

change versus adsorption time of either barium or cesium, the monolayer breakpoint in the APPH curve lines up with the rise to the local maximum of the work function change curve[14,21]. An example of this is shown in Fig. 6.04 for cesium on the W(110) surface. In Ref. 18 and 19, the LEED studies verify that adatom concentrations at the local work function maximum yield close-packed adlayer structures. These work function studies and our work function studies show that the work function of the surface at the local maximum is approximately equal to the work function of the pure metal adsorbate. An exception to this is the adsorption of cesium or barium on the Nb(110) surface. In both cases, the work function of the local maximum is a few tenths of an electron-volt higher than for the pure adsorbate metal surface. The high local maximum work function value is again caused by the excess oxygen on the surface and in the bulk of the Nb(110) surface.

6.1 Thermal Desorption

In discussing the results of the thermal desorption of cesium and barium from W(110), Mo(110) and Nb(110), I would first like to verify some of the parameters and assumptions used to determine the activation energy. The frequency factor, ν_1 used in eqn. 4.16 to find the activation energy was assumed to be equal to 10^{13} sec^{-1}. This assumption was made without basis but it turns out to be not such a big assumption. This value has long been accepted as a reasonable value for alkali metal adsorption on metal surfaces and is used by many of the authors referenced within this report. It turns out that if the value of the frequency factor is varied between 10^{12} and 10^{14} sec^{-1}, the error in the activation energy is only 0.2 eV using equation 4.17. In Redhead's paper[22], it is stated that if $10^{13} > \nu_1/\beta > 10^{8}$ (K^{-1}) then the activation energy is given to within ±1.5% by eqn. 4.16. Fedorus *et al.*,[4] reported a value of 2-5 × 10^{12} sec^{-1} for the frequency factor for barium adatoms on the (110) face of tungsten and molybdenum, so our assumption for ν_1 does not introduce any serious error.

Next, we will verify that the desorption of cesium and barium follows coverage dependent first-order reaction kinetics by showing the $\log\sigma_o T_p^2$ versus $1/T_p$ is not a straight line. The initial adatom concentration σ_o, can be found from the area under the desorption curve. Plots of $\log\sigma_o T_p^2$ versus $1/T_p$ for cesium and barium are shown in Figs. 6.05 and 6.06, respectively. If these curves resulted in straight lines, then the

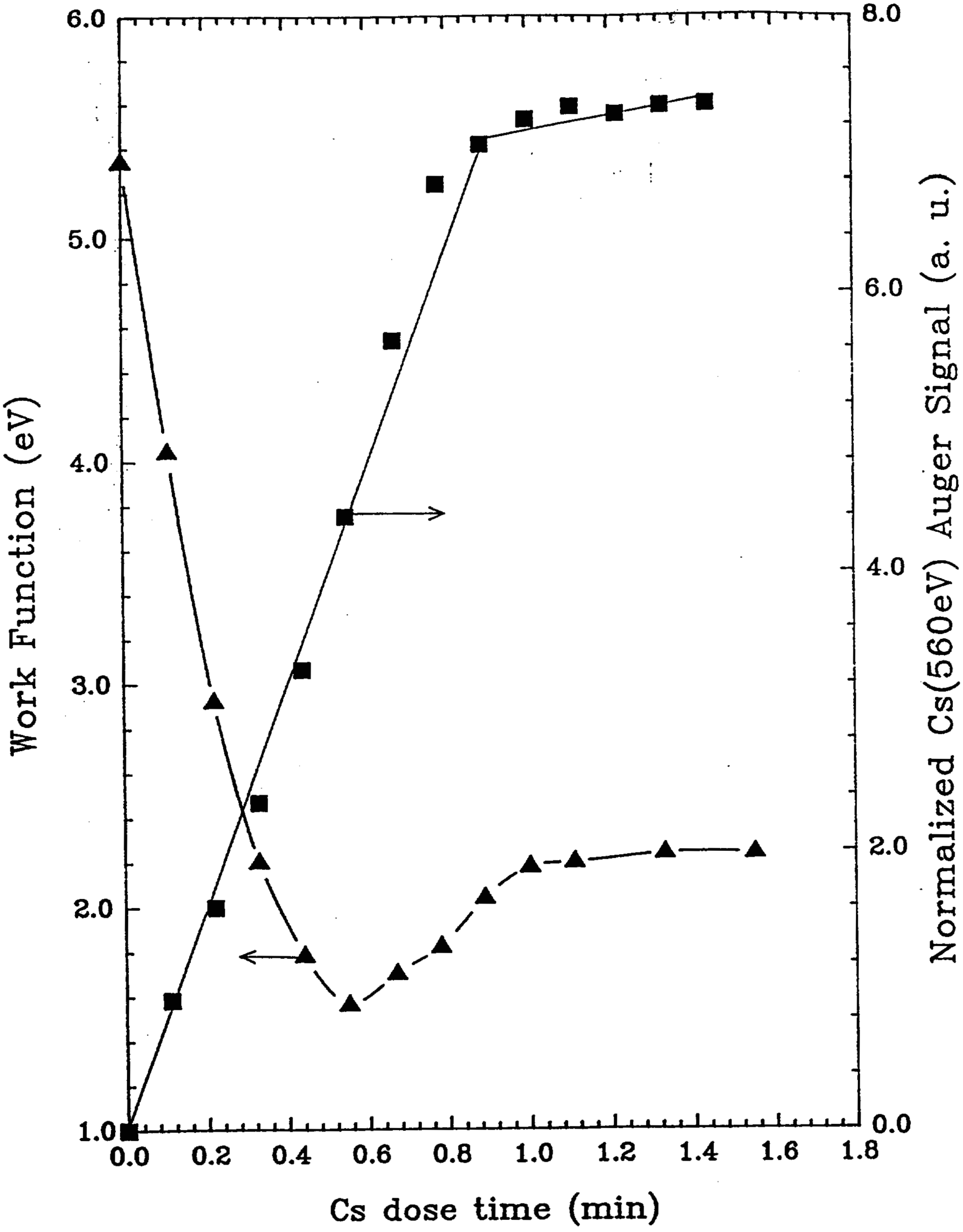

Figure 6.04. Work function change and Cs(506eV) APPH versus cesium dose time. Local maximum of the work function curve was associated with a monolayer of cesium coverage.

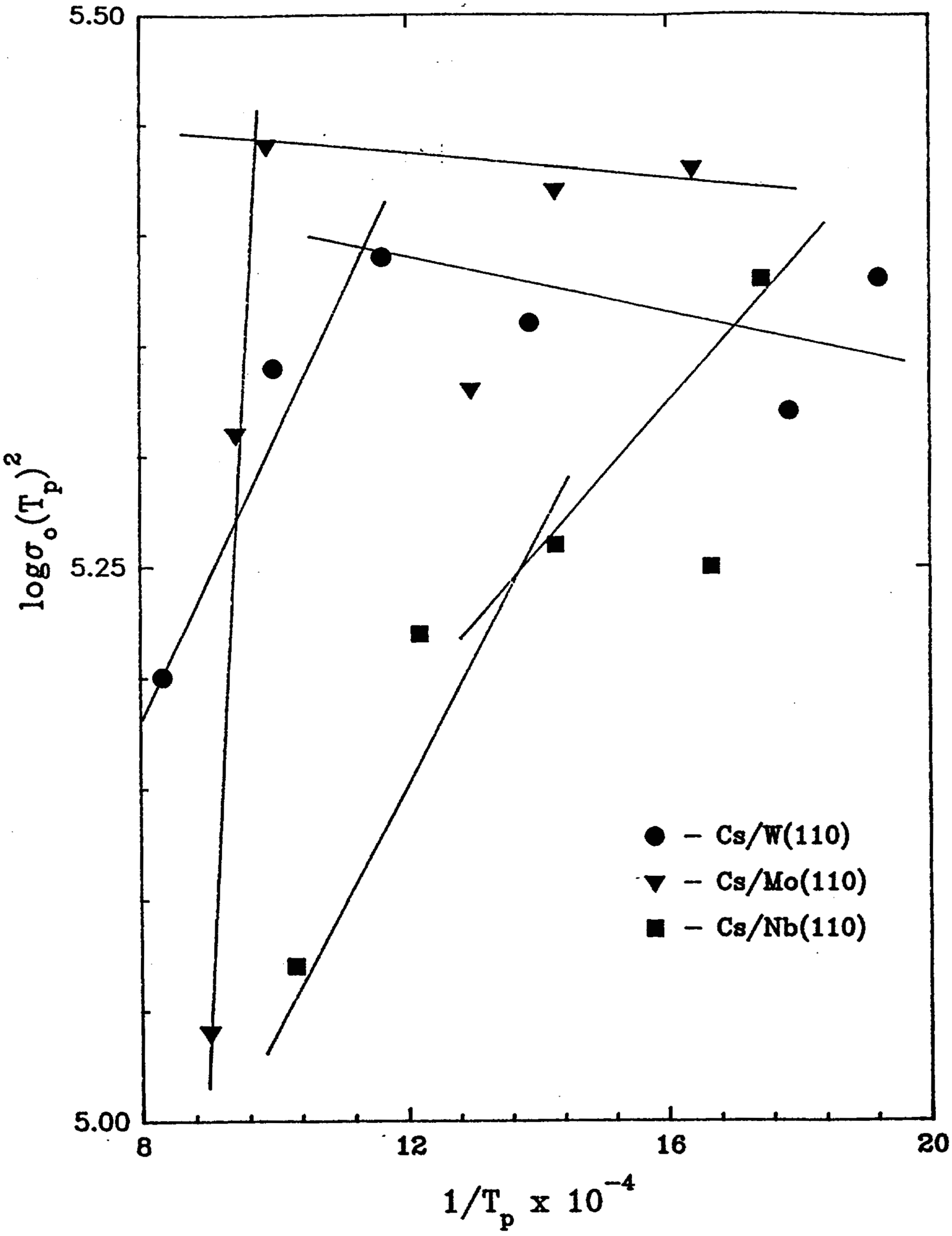

Figure 6.05. Log $\sigma_0 T_p^2$ versus $1/T_p$ for cesium desorption from W(110), Mo(110) and Nb(110).

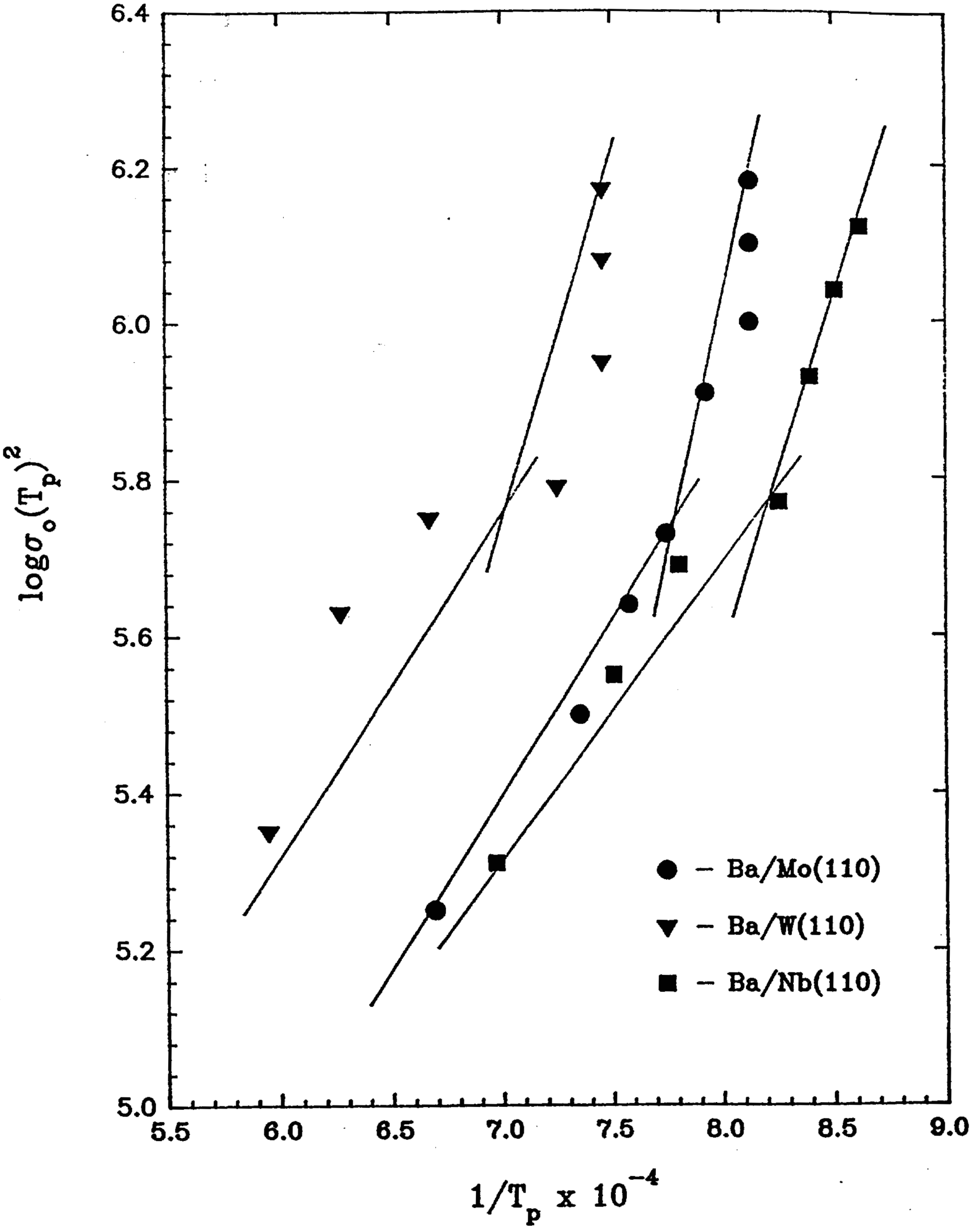

Figure 6.06. Log $\sigma_0 T_p^2$ versus $1/T_p$ for barium desorption from W(110), Mo(110) and Nb(110).

desorption would be considered second-order desorption with fixed activation energy. Since the curves did not result in straight lines, the desorption is considered a first order reaction with the activation energy dependent on coverage. We considered the reaction to be first order only for coverages less than a monolayer. The low temperature peaks observed in the thermal desorption spectra for cesium and barium desorbed from the three substrates should be considered a zeroth order reaction but the activation energy given was found using eqn. 4.16 and $\nu_1 = 10^{13}\ \text{sec}^{-1}$.

The activation energy, E, in the limit of zero coverage, is given in Table 6.02 for cesium and barium on the surfaces of W(110), Mo(110) and Nb(110). Table 6.02 also contains values found in the literature for similar systems. The values of E = ~4.70 eV for Ba/Mo(110) surface and E = ~4.90 eV for the Ba/W(110) surface were observed by Fedorus, *et al.*[6]. These values are somewhat higher than the values listed in Table 6.02 for barium desorbed from W(110) and Mo(110). We believe the higher values found by Fedorus, *et al.* can be attributed to the difference in method used to obtain the activation energy. Fedorus, *et al.* do not present the desorption spectra or the temperatures used to obtain their result so it is difficult to make a direct comparison. On the other hand, values found in the literature for the desorption activation energy for cesium from the W(110) surface agree well with the results presented in Table 6.02. The value of 3.10 eV reported by Desplat can be used as a direct comparison with the value found in this investigation because in both instances the Redhead equation (eqn. 4.16) was used to determine the activation energy. Table 6.02 illustrates the fact that the activation energy for desorption of cesium and barium from the three substrates increase in the sequence

$$E_{Nb(110)} < E_{Mo(110)} < E_{W(110)} \qquad (6.03)$$

and clearly states

$$E_{Cs} << E_{Ba} \qquad (6.04)$$

for all three surfaces. Improvements in the field electron microscopy (FEM) technique allowed Todd and Rhodin[23] a direct assessment of some adsorbate-substrate electronic configurations, as a function of alkali type, by studying the results of the binding energy of a single atom on different crystal faces of tungsten. The results of their experiments and others[24] revealed that the activation energy per

Table 6.02. Near zero-coverage activation energies for cesium and barium from W(110), Mo(110) and Nb(110).

Material	Activation Energy, eV Cesium	Barium
W(110)	3.08	4.35
	3.10[8]	4.90[6]
	3.20[4]	
Mo(110)	2.85	3.85
		4.70[6]
Nb(110)	2.42	3.72

cesium and barium atoms on the different crystallographic planes of tungsten were arranged as follows

$E_{110} > E_{100} > E_{112} > E_{111}$. (6.05)

This relationship was confirmed by the results found on the potassium-tungsten system[25]. Additional collected data from the early works[26] on different adsorbates on tungsten yielded

$E_{Cs} > E_{Rb} > E_{K} > E_{Na}$ (6.06)

and

$E_{Ba} > E_{Sr}$. (6.07)

From Table 6.01, it is seen that the initial dipole moment of both cesium and barium follow the same sequence as eqns. 6.03 and 6.04. The fact that the desorption energy increases with the dipole moment indicates that there is some ionic contribution to the binding energy at low coverages.

The thermal desorption of cesium from the various Ba/Me(110) surfaces provided us with additional information about how the pre-adsorbed barium affects the electronic state of the cesium adatom. The thermal desorption results for the mixed adsorbate surfaces indicate the strong connection between the changes in the desorption energy and the work function. In the discussion of the work function results, it was seen that as the pre-coverage of barium increased the cesium had less and less effect on the work function and the dipole moment. The thermal desorption spectra show that as the barium pre-coverage is increased to a coverage corresponding to a minimum work function, decreases occur in the binding energies of the cesium adatoms. This means that the cesium adatoms are less likely to be ionized by the substrate and are not as strongly polarized compared to cesium adatoms on clean surfaces. Hence, they are less effective in reducing the work function of the surface. It was verified, at low coverages of both cesium and barium, that the thermal desorption results were unchanged when either barium or cesium was deposited first. The strong barium-substrate bond seemed to dominate the adsorbate-metal interaction for the mixed adsorbate system at low coverages. As the pre-coverage of barium was increased past ~0.5 ML on all three substrates, the binding energy of the cesium was reduced to a value corresponding to a monolayer coverage of cesium on a clean surface. These results are analogous to the work function results reported earlier and confirm the fact that as the coverage of electropositive adatoms increase, they have less effect on surface properties of the substrate. By comparing the results for the individual species with the results of the mixed adsorbates, we can say that alkali and alkaline earth metals neutralize the surface properties of the substrate by changes in their bonding mechanism and inter-adatom dipole moment interactions. A qualitative description of these changes based on the theoretical ideas expressed in chapter 3 and the experimental findings of this investigation will be discussed in the next chapter

The results of thermal desorption spectroscopy yielded additional support for the coverage assignments given. Figures 6.07 and 6.08 show the integrated thermal desorption flux of cesium and barium from the various substrates versus adsorption for various times. The linearity of the desorption versus adsorption time implies a constant sticking coefficient, which we assumed to be unity. Therefore, the coverage is directly proportional to adsorption time. The coverage assignments for the various cesium/metal systems are verified by the fact that a low temperature thermal desorption peak arises after approximately the same cesium dose time as the breakpoint in the Auger signal, and the local work function maximum. (The thermal desorption spectrum for the Cs/Mo(110) surface does not show this peak, but there is evidence of a low temperature peak beginning to appear for the desorption of a 1.0 ML cesium coverage.) The activation energy of the low temperature thermal desorption peak approaches the sublimation energy of bulk cesium. The thermal desorption data from the various barium/metal systems showed a similar response. Barium desorbed from the metal substrates with decreasing activation energy as the coverage increased, and furthermore, the barium activation energy decreased to a certain point (temperature) as the barium coverage approached the breakpoint (monolayer coverage) in the corresponding Auger signal. As the coverage was increased, a second lower temperature thermal desorption peak appeared which we conclude comes from barium desorption from barium.

6.2 Surface Structure

A detailed knowledge of the surface structures on the atomic scale formed by adsorption on the substrate surface is necessary for a complete understanding of the system. The effect the adsorption has on the surface structure yields information

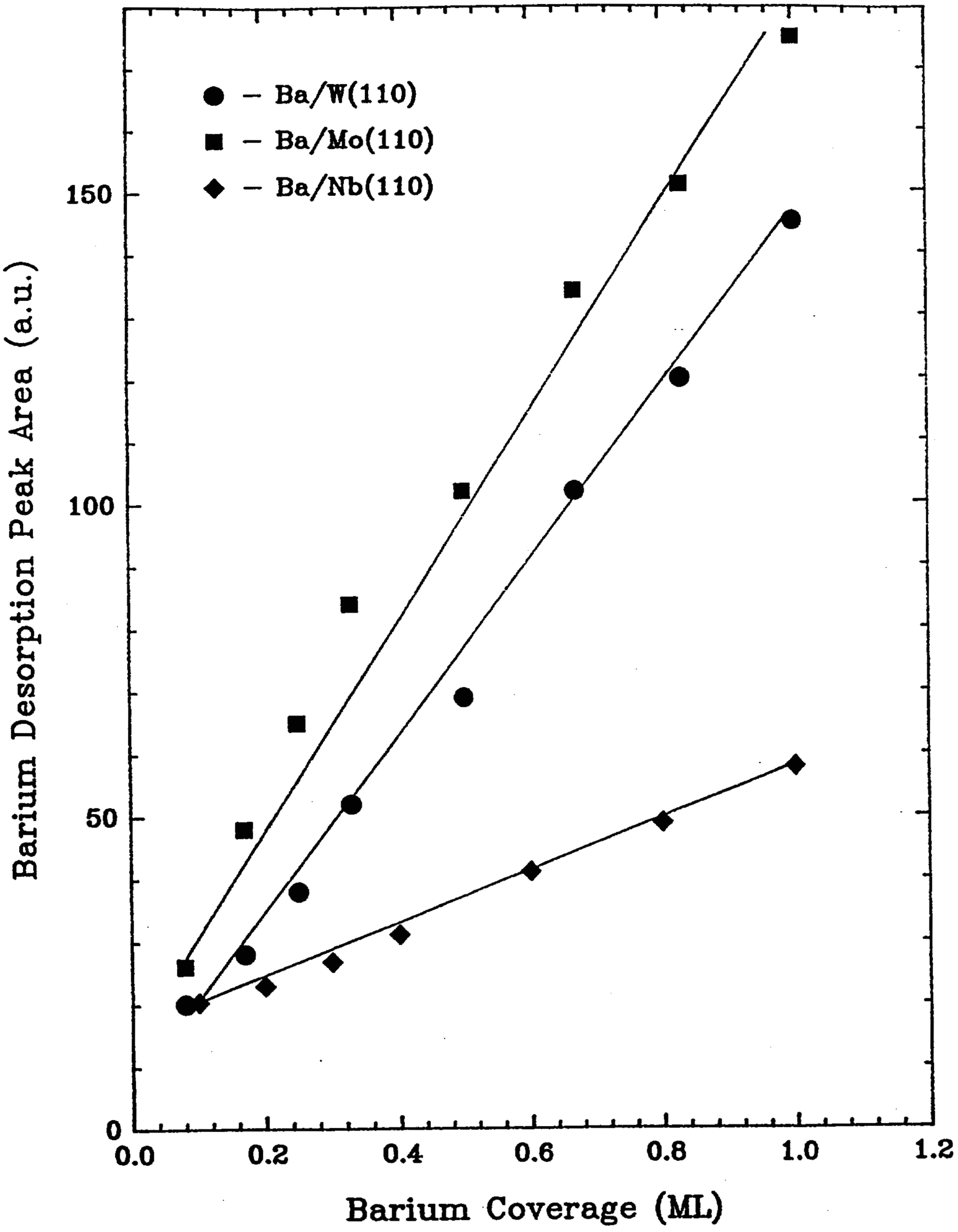

Figure 6.07. Amount of barium thermally desorbed, monitored by the QMS, versus barium coverage.

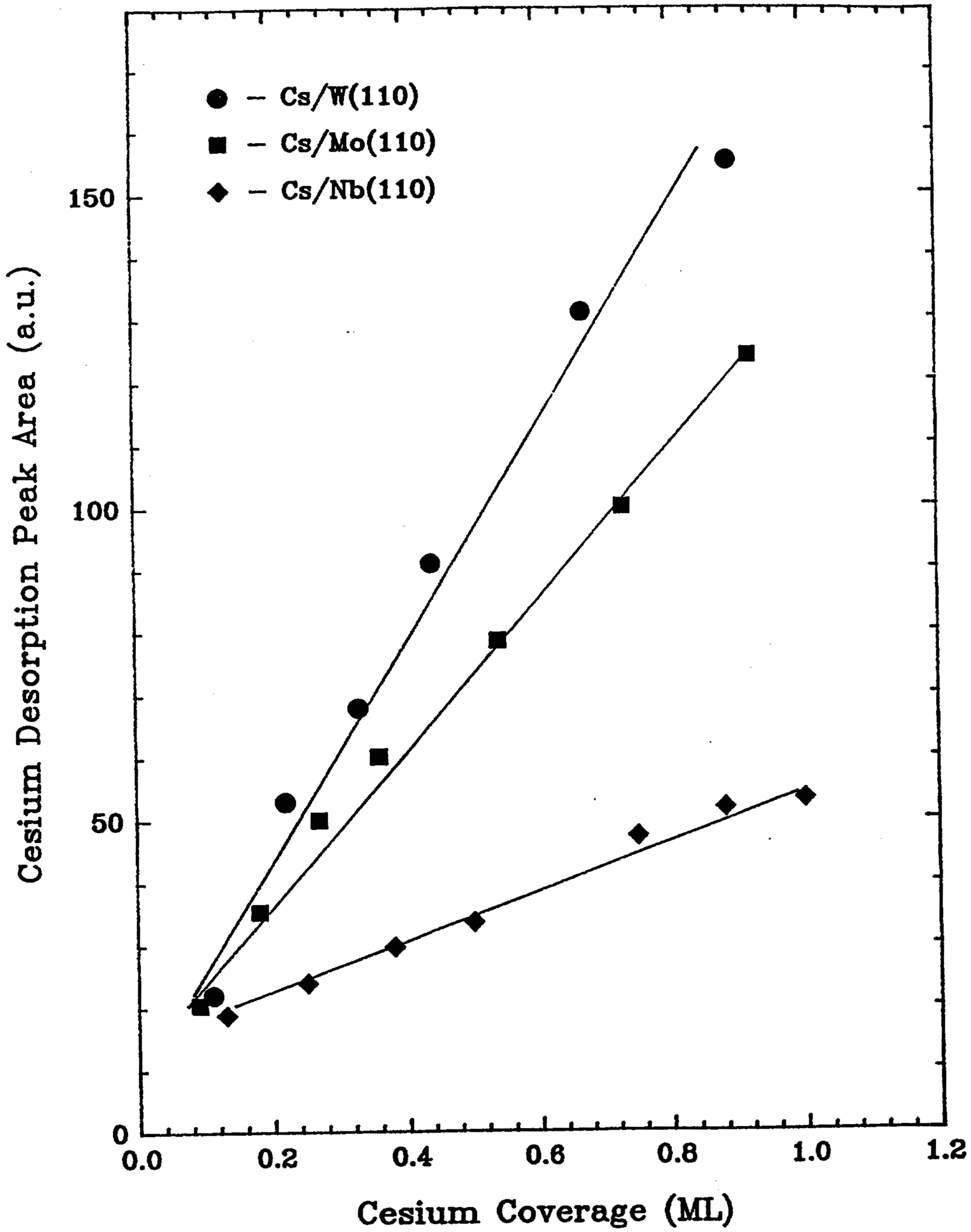

Figure 6.08. Amount of cesium thermally desorbed, monitored by the QMS, versus cesium coverage.

about the forces among the adatoms and between the adatoms and the neighboring substrate atoms. A knowledge of the surface forces and simple geometry of the adsorbate/metal system is necessary for the formulation of valid theories describing the electronic state of the alkali and alkaline earth metal adatoms on refractory metal surfaces. Analysis of the adlayer structure could also contribute to the interpretation of the kinetics of the adsorption process.

The system configuration used in this investigation did not allow complete analysis of the adlayer surface structure to be undertaken. In order to observe ordered diffraction patterns of either cesium or barium on W(110), Mo(110) or Nb(110), the surface must be cooled to liquid nitrogen temperatures[29,32]. However, changes in the adlayer surface structure have been reported in the literature and have been found to be important to the understanding of work function and activation energy changes caused by the adsorption of alkali and alkaline earth metals. The measurements have been interpreted in terms of the theoretical arguments presented in chapter three and correlated with the experimentally found values of the work function and heat of adsorption for various adsorbate/metal systems. Not all the structural data concerning the adsorption of cesium or barium on W(110), Mo(110) or Nb(110) agree totally but there is a general consensus about the adlayer structural formation. The adlayer atomic structure, work function and bonding mechanism are inherently tied together by the repulsive interaction of the adatoms. Even though we were unable to observe the structural changes first hand, we shall to briefly discuss our work function and desorption data for cesium and barium on W(110), Mo(110) and Nb(110) in terms of models developed in the literature. The discussion should help in developing the description of how alkali and alkaline earth metal adsorption affects the surface properties of refractory metals presented in this report.

The activation energy for desorption versus cesium and barium coverage are rather smooth curves, which corresponds to smooth transitions in the surface structure, although we do detect some structure related changes in the work function versus adsorbate coverage curves, especially for barium on tungsten and molybdenum. The changes are evident in the slight slope changes that occur in the work function versus coverage curve. Gorodetsky and Melnik[29]and Fedorus, *et al.*[21] found that linear segments in the work function versus barium coverage on the

W(110) and the Mo(110) surfaces coincide with certain structural development and that the appropriate diffraction patterns appear at the breakpoints. According to Ref. 6 and 21, barium forms the structures illustrated in Fig. 6.09 with increasing adsorption on W(110) and Mo(110). For small coverages (<1.2 × 10^{14} atoms/cm^2), barium forms an incoherent structure, but as the barium coverage increases, there is an appearance of a *c*(6×2) coherent diffraction pattern. As the coverage is further increased, the barium adatoms are compressed and a slightly shifted intermediate (2×3) diffraction pattern begins to be seen, however it is quickly displaced by the formation of *c*(2×2) structural arrangement. The work function minimum coincides with the diffraction pattern c(2×2). It is interesting to point out that the noticeable slope change in the Ba/Mo(110) work function curve (Fig. 5.14) corresponds to a barium adatom concentration of approximately 1.2 × 10^{14} atoms/cm^2 ($n_{sat} = 6.0 \times 10^{14}$ atoms/cm^2) which is the concentration corresponding to the appearance of the c(6×2) adlayer structure. At a monolayer coverage, the barium adlayer is arranged in a hexagonal close-packed (hcp) structure. The diffuse rings we see in our LEED data for high coverages of barium correspond to the formation of the hcp structure even though we cannot see the diffraction spots for the individual barium adatoms.

The LEED results for cesium adsorption onto W(110), Mo(110) and Nb(110) do not seem to show the distinct intermediate surface structures at submonolayer coverages which have been associated with barium adsorption, although compressing and orientation changes of the cesium adatoms as the coverage increased have been suggested by Fedorus and Naumovets[21]. Their scheme of the diffraction spot locations is illustrated in Fig. 6.10. The figure shows that the cesium adatoms are arrayed in a hexagonal structure throughout all stages of deposition. As the cesium coverage increases, the diffraction spots continuously move away from the center of the pattern which indicates a gradual decrease in the adlayer lattice constant. It was noted by Fedorus that the hexagonal adlayer structure orientation changes by 30° relative to the substrate when the work function passes through the minimum value. This happens rather quickly and corresponds to pattern d in Fig. 6.10. After the minimum work function is reached, the diffraction pattern continuously moves away from the center substrate diffraction spot (the adatoms are being compressed closer and closer together) until the hcp diffraction pattern is formed. In the hcp structure,

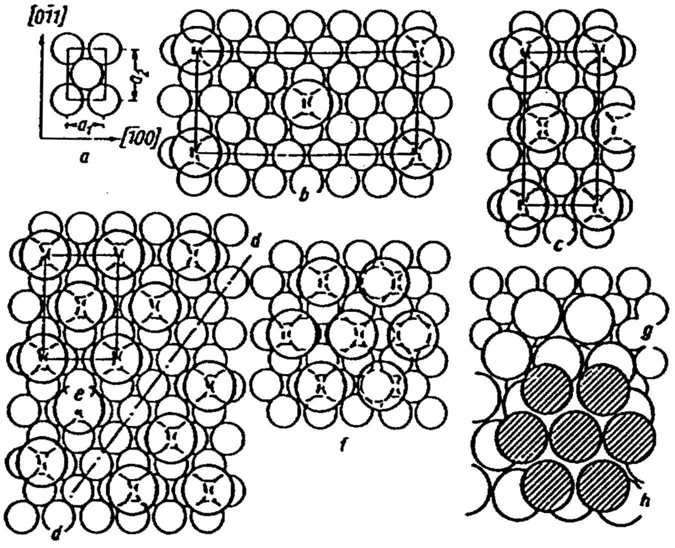

Figure 6.09. Models of the surface structure for barium on W(110) and Mo(110). Models a thru h correspond to diffraction patterns observed in Ref. 6 and 21. a) (1×1) sturcture of Mo(110), b) c(6×2), c) (2×3), d) out of phase boundary, e) c(2×2), f) hexagonal structure coherent with the [110] direction, g) close-packed monolayer, h) hexagonal structure of the second monolayer islands. [Ref. 6]

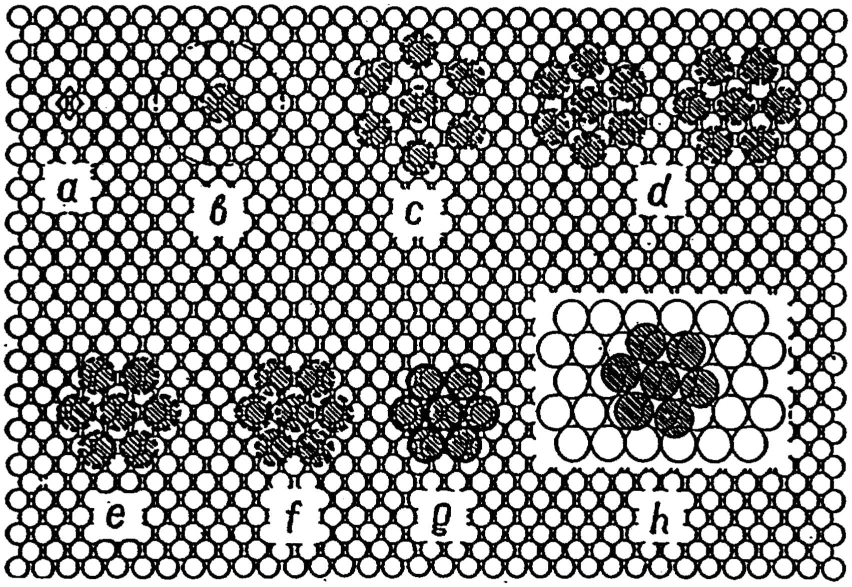

Figure 6.10. Models of the surface structure of the Cs/W(110) system. The models a thru h correspond to the patterns given in Ref. 6. a) (1×1) structure of W(110), b) the first coordination circle at n = 1.7 × 1014 atoms/cm-2 and long range order disturbed, d) orientation at optimal coverage, g) close-packed monolayer, h) the second layer of cesium atoms on the first cesium monolayer. [Ref. 21]

the shortest adatom spacing was determined to be 11% less than the cesium atom diameter[6]. A similar result was found by Gerlach and Rhodin[27] in their study of cesium on Ni(011). They account for this fact by assuming the cesium adatom is partially ionized. In Ref. 2, it was found that the lattice spacing for sodium adatoms on W(110) was approximately equal to the diameter of the sodium atom. This is apparently due to the higher ionization energy associated with sodium. Hence, there is probably even much less compression for the barium adatoms on W(110).

References

1 A. G. Fedorus and A. G. Naumovets, Surf. Sci. 21 (1970) 426.

2 V. K. Medvedev, A. G. Naumovets and A. G. Fedorus, Fiz. Tverd. Tela 12 (1970) 375.

3 V. K. Medvedev and A. I. Yakivchuk, Fiz. Tverd. Tela 16 (1971) 981.

4 Yu. M. Konoplev, A. G. Naumovets and A. G. Fedorus, Fiz. Tverd. Tela 14 (1972) 326.

5 J. W. Gadzuk, Phys. Rev. B 1 (1970) 2110.

6 A. G. Fedorus, A. G. Naumovets and Yu. Vedula, Phys. Stat. Sol. (a) 13 (1970) 445.

7 E. V. Klimenko and A. G. Naumovets, Sov. Phys. Tech. Phys. 24 (1979) 710.

8 J.-L. Desplat and C. A. Papageorgopoulos, Surf. Sci. 92 (1980) 79.

9 V. M. Gavrilyuk, Yu. S. Vedula, A.G. Naumovets and A. G. Fedorus, Fiz. Tverd. Tela 9 (1981) 881.

10 D. A. Gorodetsky and Yu. P Melnik, Surf. Sci. 62 (1977) 647.

11 A. U. MacRae, K. Muller, J. J. Lander and j. Morrison, Surf. Sci. 15 (1969) 483.

12 S. Andersson and U. Jostell, Solid State Commun. 13 (1973) 833.

13 E. Wimmer, A.J. Freeman, J. R. Hiskes and A. M. Karo, Phys. Rev. B 28 (1983) 3074.

14 B. V. Bondarenko and V. I. Makhov, Fiz. Tverd. Tela 12 (1970) 1912.

15 B. M. Zykov and V. K. Tskhakaya, Sov. Phys. Tech. Phys. 24 (1979) 948.

16 J. Psarouthakis, Surf. Sci. 17 (1969) 316.

17 V. G. Bazanov, N. G. Ban'kovskii and O. M. Mul'tanovskaya, Sov. Phys. Solid State 10 (1968) 397.

18 J. P. Muscat and D. M. Newns, Surf. Sci. 74 (1978) 355.

19 R. W. Gurney, Phys. Rev. 47 (1935) 479.

20 J. W. Gadzuk, Surf. Sci. 6 (1967) 133.

21 A. G. Fedorus and A. G. Naumovets, Surf. Sci. 21 (1970) 426.

22 P. A. Redhead, Vacuum 12 (1962) 203.

23 C. J. Todd and T. N. Rhodin, Surf. Sci. 42 (1974) 156.

24 V. M. Gavriljuk, Yu. S. Vedula, A. G. Naumovets and A. G. Fedorus, Fiz. Tverd. Tela 9 (1967) 1127.

25 L. D. Schmidt and R. Gomer, J. Chem. Phys. 45 (1966) 1605.

26 K. F. Wojciechowski, Acta Phys. Polon. 33 (1968) 363.

27 R. L. Gerlach and T. N. Rhodin, Surf. Sci. 17 (1969) 32.

Chapter 7

Conclusion

The results presented here provide the fundamental data needed for the comparison of the characteristics of adsorbed cesium layers and barium layers on model thermionic converter electrode surfaces W(110), Mo(110) and Nb(110). There has been numerous studies[1] completed on the effects of alkali metal and alkaline earth metal adsorption on the surface properties of single crystal refractory metals. These studies have confirmed many surface phenomenon characteristic to the adsorption of alkali and alkaline earth metals. The most established doctrines being the characteristic work function versus coverage curve and the lowering of the near zero coverage desorption energy associated with increased coverage. The behavior of the work function and desorption energy along with the surface structure formation given in this investigation are in good agreement with many of these theoretical and experimental studies. A summary of the results of this investigation can be found in Table 7.00.

The work function and the thermal desorption results barium on W(110), Mo(110) and Nb(110) show that barium adsorption would be more suitable than cesium for modifying the surface properties of surfaces at high temperatures. The binding energy of barium is much higher than that of cesium for the surfaces investigated, while low coverages of barium produce a favorable reduction in the work function. The low work function, high temperature surface should offer certain advantages when used as a thermionic converter electrode. These advantages include greater interelectrode spacing, lower vapor pressures and higher efficiency. The high binding energy of barium also causes some problems with thermionic converters used in some applications. For mixed vapor thermionic converters, the work function of a bariated surface versus cesium coverage curves show that only low work functions can be achieved on surfaces that are operated at temperature high enough to maintain barium coverages below 0.5

Substrate	**W(110)**		**Mo(110)**		**Nb(110)***	
Adsorbate	**Cesium**	**Barium**	**Cesium**	**Barium**	**Cesium**	**Barium**
Work Function Minimum	1.54 eV	2.21 eV	1.50 eV	2.20 eV	1.47 eV	2.21 eV
Adsorbate Coverage at Work Function Minimum	0.56 ML	0.5 ML	0.55 ML	0.5 ML	0.5 ML	0.4 ML
Near Zero Coverage Desorption Energy	3.08 eV	4.35 eV	2.85 eV	3.85 eV	3.08 eV	3.72 eV
Near Zero Coverage Desorption Energy Peak Temperature	1200 K	1650 K	1100 K	1500 K	950 K	1420 K
Near Zero Coverage Dipole Moment	6.02 Debye	7.26 Debye	6.01 Debye	7.18 Debye	5.49 Debye	5.78 Debye

* The values for the Nb(110) surface due to the adsorption of cesium and barium may be affected by the residual oxygen present on the Nb(110) surface.

Table 7.00. Experimental data for the adsorption of cesium and barium on W(110), Mo(110) and Nb(110).

barium and consequently have a work function of bulk barium (2.7 eV). For example, a Nb(110) surface would have to be above 1200 K.

Although a mixed vapor thermionic converter has its limitations, it seems to be a positive approach to obtaining better performance for high temperature thermionic converter applications. The vast amount of fundamental data found in this thesis for the adsorption of cesium and barium on various substrates offers some support of such a statement. The work function, desorption energy and structure formation data show that all three substrates investigated could be viable electrode materials for a barium-cesium thermionic converter. The fundamental data shown here along with investigations by Henne[2] and Psarouthakis[3] into the practical aspects of a barium-cesium converter show that the introduction of alkaline earth metals into cesium-only converters could improve performance in certain applications.

References

1 The reader is referred to the numerous articles cited at the end of chapters 3, 4, 5 and 6.

2 R. Henne, Thesis, Univ. of Stuttgart, West Germany, 1975.

3 I. Psarouthakis, Thesis, Univ. of Maryland, USA, 1965.

VITA

The author of this dissertation was born on June 23, 1966 in Missoula, Montana. He later moved, with his family, to Enterprise, Oregon where he started his formal education. He graduated from Enterprise High School in May of 1985. He then attended Linfield College in McMinnville, Oregon and graduated in May of 1989 with Bachelor of Science degree in Applied Physics/Electronics. He enrolled in graduate school in September of 1989 at the Oregon Graduate Center (now the Oregon Graduate Institute of Science & Technology) and performed his thesis work under the direction of Dr. Paul Davis. The requirements for a Doctor of Philosophy in Electrical Engineering were completed in October of 1995.